VNIVERSITAT DE VALÈNCIA

DEPARTAMENTO DE FÍSICA APLICADA Y ELECTROMAGNETISMO
FACULTAD DE FÍSICA

PROGRAMA DE DOCTORADO EN FÍSICA

OPTOELECTRONIC DEVICES BASED ON CAESIUM LEAD HALIDE PEROVSKITE NANOCRYSTALS

Juan Navarro Arenas

Dirigida por el Prof. Dr. Juan Pascual Martínez Pastor y
el Dr. Isaac Suárez Álvarez

Valencia, septiembre de 2020

Juan Pascual Martínez Pastor, Catedrático del Departamento de Física Aplicada y Electromagnetismo, e **Isaac Suárez Álvarez**, Profesor ayudante doctor del Departamento de Ingeniería Electrónica

Certifican:

Que la presente memoria "**Optoelectronic devices based on caesium lead halide perovskite nanocrystals**" ha sido realizada bajo su dirección en el Departamento de Física Aplicada y Electromagnetismo de la Universidad de Valencia por **Juan Navarro Arenas**, y constituye su Tesis para optar al grado de Doctor en Física por la Universidad de Valencia (RD99/2011).

Y para que así conste, en cumplimiento de la legislación vigente, firman el presente certificado.

Valencia, a 29 de Julio de 2020,

Isaac Suárez Álvarez — Firmado digitalmente por Isaac Suárez Álvarez Fecha: 2020.07.30 13:52:01 +02'00'

Isaac Suárez Álvarez

JUAN PASCUAL|MARTINEZ|PASTOR — Firmado digitalmente por JUAN PASCUAL|MARTINEZ|PASTOR Nombre de reconocimiento (DN): cn=JUAN PASCUAL|MARTINEZ|PASTOR, serialNumber=74214044J, givenName=JUAN PASCUAL, sn=MARTINEZ PASTOR, ou=CIUDADANOS, o=ACCV, c=ES Fecha: 2020.07.28 23:19:15 +01'00'

Juan Pascual Martínez Pastor

A mi padre.

Este proyecto no hubiese podido ver la luz sin el consejo, las orientaciones y el trabajo de mis directores, Juan P. Martínez Pastor e Isaac Suárez Álvarez, a quienes siempre agradeceré la confianza que durante estos años me han brindado. También quisiera agradecer a mis compañeros del grupo: fue una gran decisión trasladarme del semisótano a la tercera planta para compartir todos estos buenos años con vosotros. Esta tesis doctoral también tiene una deuda con mis amigos y familia, en particular con Mélanie, Miguel y Pablo, a quienes doy las gracias por sus ánimos y por su paciencia. Os regalo estas páginas sobre nanocristales y dispositivos optoelectrónicos;

es lo mejor que tengo hasta ahora.

Table of Contents

ABSTRACT

Traditionally, the implementation of active materials in photonic integrated circuits (PICs) has been developed by using III-V semiconductors and glasses and ferroelectrics doped by rare earth ions. However, there is a cost-efficient alternative based on (nano)materials synthetized by colloidal chemistry techniques. The fabrication of solution-processed nanomaterials provides semiconductors with tailor-made optical properties (light emission, absorption, scattering, bandgap) that can be engineered during the synthesis. In addition, their colloidal nature allows a straightforward integration into any optical architecture by coating or printing techniques. In this context, all-inorganic $CsPbX_3$ (with X = Cl, Br, I) perovskite nanocrystals (PNCs) have recently emerged as an outstanding material with fascinating optical properties, including a high efficiency of absorption, a quantum yield of emission exceeding 90 % at room temperature, a tunable band gap depending on chemical composition—or size and shape tuning—, and high nonlinear optical coefficients. Considering the aforementioned background, the project of this Ph.D. Thesis intends to harness the potential of PNCs as an active material for optoelectronics, from both the point of view of the fundamental science and the applications. A first research objective involves the fabrication of PNC-based photodetectors enhanced by a solid-state ligand-exchange procedure that yields a superior device performance via increased inter-mobility between the PNCs. In this first step, the technology to assemble bulk nanomaterials (thin films) from PNC building blocks is stablished. A second objective is focused on the fundamental physics behind the generation of optical gain in PNCs. This study allows to determine the physical mechanisms involved, and also to stablish the role of different excitonic species, to explain the stimulated emission in these nanocrystals. In particular, the presented investigations demonstrate that the amplified spontaneous emission (ASE) in these materials is generated by the recombination of single excitons, and that the threshold of optical gain is determined only by optical losses. In line with this research, a novel all-fiber hollow-core amplification device, prepared by filling the fiber with PNCs, is properly fabricated and characterized. This device demonstrates a thresholdless gain effect at room temperature that can be attributed to a third order non-linear optical mechanism achieved by strong modal confinement. Finally, in order to further exploit the modal confinement strategy, layers of PNCs are integrated in a waveguide structure that was properly designed to enhance the generation of photoluminescence (PL) when the structure is optically pumped. In particular, this configuration was chosen to study the propagation of the secondary flow of photons resulting from the reabsorption of the PL. This effect, the photon recycling, results in spectral redshift and increased lifetimes for the photons extracted from the output of the waveguide. The photon recycling effect has important implications in the performance of solar cells, light-emitting diodes, among other optoelectronic devices. Considering the aforementioned results, this Ph. D. Thesis concludes that colloidal PNCs are promising candidates to pave the road towards a new generation of active optoelectronic devices.

1 INTRODUCTION

Materials with perovskite lattice have gained interest within a large community of researchers around the world. Their importance lies in their outstanding properties: their mechanical and electrical properties, such as pyro and piezo electricity; their dielectric and superconducting properties; their high nonlinear coefficients and potential electrooptic effects. Therefore, this family of materials proves to be a suitable candidate for a wide range of applications [1].

Despite the relative simplicity of its crystal structure, ABX_3, the perovskite lattice spans a huge collection of compounds [2] due to all the possible crystallographic variations and chemical diversity. Most of them are oxides and fluorides, but also chlorides, hydrides, oxynitrides, and sulfides [3]. The evolution of perovskite materials was developed in three phases. First, ceramic materials with the perovskite-type structure ABO_3 (like in the compounds $LiNbO_3$, $LiTaO_3$, $BaTIO_3$, etc.) started to be thoroughly studied since the Second World War, leading to the development of piezoelectrics and ferroelectrics amongst other modern applications [4]. Meanwhile, a second phase of hybrid organic-inorganic perovskites, in which the A- or X-sites of the crystal structure are replaced by organic cations, found many applications, mainly in photovoltaics (PV), but also in light-emitting devices and other optoelectronic technologies such as memory devices, photodetectors and X-ray detection, to name a few applications [5]. Hybrid perovskites often contain lead and other toxic heavy metals. For this reason, scientists started a third phase in perovskite research, lead-free perovskites, as inexpensive, non-toxic, earth-abundant materials for the next generation of optoelectronic applications. Quite recently, lead-free perovskites were reported to show faint ferroelectric properties, which in some cases tend to preclude potential applications [6].

This Ph. D. Thesis has been mainly focused on the development of optoelectronic and photonic devices based on lead halide perovskite (LHP) nanocrystals. LHPs have

the general formula of $APbX_3$ (see a rendered representation of the LHP unit cell in Figure 1.1), where A is a monovalent cation (organic or inorganic) and X is the halide (Cl, Br or I). Methylammonium (MA) and Formamidinium (FA) are among the most common monovalent organic cations currently being used in the synthesis of LHPs. If the organic cation is replaced by an inorganic cation, a fully inorganic LHP is formed. In terms of available size inside the perovskite structure, the caesium cation (Cs) results a suitable choice, forming the caesium lead halide perovskite family ($CsPbX_3$). Each cation has a series of advantages over the others; for example, the FA is sometimes chosen in the fabrication of single-junction solar cells because of the redshifted position of its bandgap and improved thermal stability at room temperature. However, the large size of the FA molecule deforms the perovskite, showing poor thermal stability at temperatures higher than room temperature [7]. Superior stability under thermal and humidity attacks in comparison with organic cation-based hybrids is offered by the all-inorganic $CsPbBr_3$ perovskites [8]. Lately, several groups have started to mix the cation position (i.e. the CsFA-, or MAFA- double cation mixtures), producing films with much improved thermal stability and optoelectronic properties, among other unanticipated effects [9]. The mixing approach makes a nearly endless family of possible LHP compounds, and the technological feasibilities of this kind of material are still growing. Since the first publication in 2009 by Kojima et. al. [10] of the first hybrid LHP dye synthetized solar cell, the interest of halide perovskites has experienced an exponential growth. In 2020, according to the WOS (Web of Science), the topic "halide perovskites" comprises more than five thousand scientific papers in the last three years. Besides their suitability for photovoltaics, LHPs also hold a great potential as a material for Integrated Optics. Soon after the discovery of exceptional gain in 2014 [11], other LHP devices such as lasers and light-emitting diodes have also been rapidly developed. LHP photodetectors are another prominent example and expected to have important applications in Integrated Optics.

Considering the aforementioned background, in this Ph. D. Thesis we will concentrate on the use of the colloidal nanocrystal version of all-inorganic LHPs, which preserve the unique features of their bulk counterparts. Since the synthetic achievement of all-inorganic LHP nanocrystals [12] with defined shape, size, and surface chemistry, new optoelectronic properties are enabled for a variety of new applications. In the next sections of the Introduction chapter we will discuss why we chose this all-inorganic perovskite nanocrystals (PNCs) as the building blocks to achieve the objectives of this Thesis.

1.1 PEROVSKITE NANOPARTICLES

Since the first publication of perovskite NCs in 2014 [13], this material has been extensively studied by many researchers around the world. Lead halide PNC are synthesized in a similar fashion to more traditional NCs systems, by a technique known as the hot-injection method detailed in Section 3.1.1 of this Thesis. The synthetic approach allows to precisely tune the size and shape of the NCs so that bulklike NCs (particles exhibiting low quantum confinement), or zero-dimensional quantum dots (QDs) can be selectively fabricated [14]. Also, other nanostructures with dimensions significantly below the exciton Bohr radius, like nanowires and nanoplatelets, can be tailor-made by adjusting the reaction parameters [15]. The composition of the PNCs can also be tuned not only during the synthesis, but also post synthesis through, for example, ion exchange treatments [16].

The interesting optical properties of PNCs include a high efficiency of absorption, a quantum yield of emission exceeding 90 % at room temperature and a tunable band gap depending on chemical composition [14]. Besides, solution processability enables inkjet printing compatible manufacturing; PNCs can be processed into films on a large variety of optical architectures or substrates by standard coating techniques [17]. In this context, all-inorganic $CsPbX_3$ PNCs have recently emerged as outstanding materials for integrated optics [18]. Consequently, since the first publication from Kovalenko's group in 2015 [12], PNCs have been extensively studied as active materials, with demonstrated applications in light emitting diodes, lasers or optical amplifiers [19].

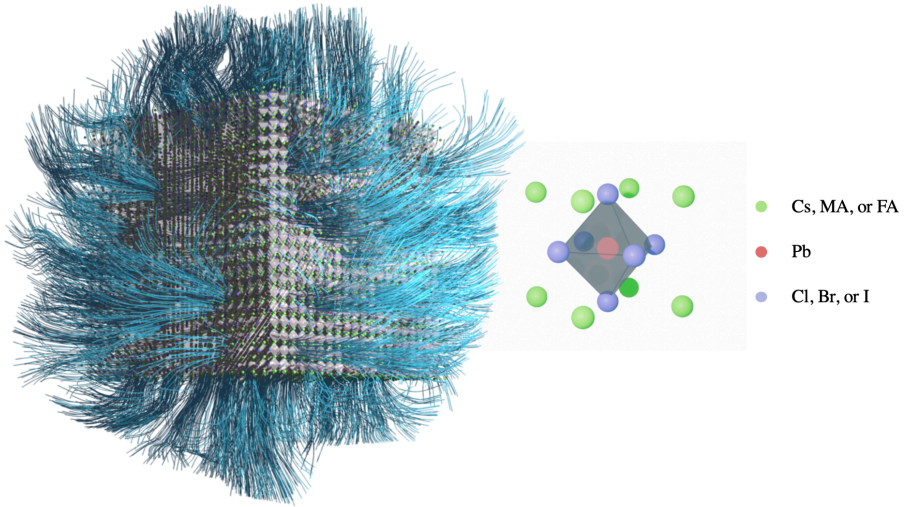

Figure 1.1. Render of a perovskite NC on the left and the unit cell of the LHP family on the right.

The basic anatomy of a semiconductor nanocrystal, including the capping ligands surrounding the crystal structure of the perovskite, is illustrated in Figure 1.1. These ligands (blue filaments in Figure 1.1) play a crucial role in the solubility, colloidal stability, and interactions between nanocrystals and their surrounding media. Furthermore, ligands introduce a potential barrier for charge-carrier transfer and transport in PNC close-packed films. Also, surface passivation is drastically improving the quantum yield by reducing the surface defects, thus preventing defect-assisted non-radiative recombination. In this Ph.D. Thesis, the effect of ligands over the electrical and optical properties will be also studied.

1.2 INTEGRATED OPTICS AND PEROVSKITE NANOCRYSTALS

Over 50 years ago Stewart E. Miller elucubrated that the integration of multiple photonic components in a common chip would emulate the stablished *modus operandi* of the microelectronics [20]. At this time, the year 1969, Miller was the head of the Bell's guided wave research laboratory, the laser revolution had already begun [21], and the very first commercial IC operational amplifier had just been launched in the market (the μA709 by Fairchild Semiconductor). Thus, the idea of utilizing lasers as a power source into miniaturized optical circuits was a natural step towards joining microelectronics and photonics technologies. In Miller's paper, the use of photolithographic techniques was proposed to mass-produce optical circuits like in the integrated-circuit industry, suggesting embedded miniature forms of lasers, modulators and hybrid devices.

Since at that time the low-loss signal propagation along optical fibers had not yet been achieved, and the coupling efficiency of light inside the optical chips was very low, much of the researcher's effort was devoted to the realization of efficient miniature optical waveguides and to the application of thin-film technology to the formation of optical devices and circuits. P. K. Tien, also working for Bell Labs, soon revealed a way to fabricate optical chips capable of coupling the laser power with low losses [22], expanding the realizations of integrated optics into a new breed of optical devices: switches, detectors, prisms, lenses, and polarizers with unprecedented efficiencies [23].

Today, a large assembly of photonic integrated circuits (PICs) are available on the market. The integrated optics community has reached the consumer-grade technology in the industry of telecommunications. Since metropolitan and wide area networks rely on optical telecommunications, integrated optics is receiving the limelight from the research community in a market of ever-increasing demand; the integrated optics allows

the direct implementation of all-optic networks, overcoming the limitations introduced by optical-electronic-optical conversion stages, the evolution towards this technology is much desirable. In any case, the development of purely photonic circuits, as well as hybrids of both PICs and ICs, are impetus stems for the promise of technologies past the microelectronics age, expanding the limits of an already well-established industries as computing or telecommunications [24]. Their implementation is performed over a huge diversity of material platforms and technologies (silica, silicon nitrides, polymers, sol-gels, lithium niobate, indium phosphide, gallium arsenide, etc.) depending on the specific application of the chip [25]. The components can be divided into two subspecies: active and passive. In a few words, active components are those capable of generating light when they are externally excited by optical pumping or electrical injection [26].

In this context, PNCs have been proposed as active materials, because these nanocrystals demonstrate a low threshold for stimulated emission together with a straightforward integration in optical architectures [27]. We believe that they are promising candidates for future integrated sources or amplifiers. This Ph. D. Thesis is mainly focused in studying the active properties of perovskite nanocrystals and their eventual integration in PIC systems. The devices studied comprise passive and active waveguides, as well as lasers and photodetectors.

1.2.1 WAVEGUIDES

Optical waveguides are spatially inhomogeneous structures that confine and propagate the light. There are a variety of waveguides and waveguide components including the conventional index-guided waveguides and the recent implementations based on wave interference. The former structures are based on the principle of total internal reflection (TIR), explained in Section 2.2 of this Thesis. An example of an interference-based waveguide is the antiresonant reflecting optical waveguide (ARROW), which is used in Chapter 5 of this Thesis.

We will mainly focus on index-guided waveguides. These waveguides are usually fabricated with dielectric materials in the form of enclosed stripes (channel or ridge) [28] or planar films [29], which are based on the confinement of light in a material with higher refractive index (core) surrounded by a low index cladding. In PIC systems, the components can be manufactured of the same material as the waveguide and can couple light directly into the waveguide, allowing high operational efficiencies.

In the field of Integrated Optics there is always an interest in the fabrication of active devices capable of adding new functionalities to existing material platforms. In this

context, colloidal quantum dots or, in general, photoluminescent nanocrystals, are a suitable choice as a material for light generation, as stated above. The idea of doping waveguides with NCs has been implemented since decades now [30], providing reliable solutions for specific technological problems. For example, NIR-emitting PbS QDs can be embedded in glass or polymer matrix to create a waveguided potential gain medium for the development of wavelength-tunable lasers and broadband fiber amplifiers suitable for telecom applications [31,32]. With a similar prospect, integrated devices can be built with NCs operating at visible wavelengths, such as II-VI semiconductor nanocrystals [33]. The integration of NCs in the waveguide can be carried out by different strategies. For example, one could simply process the colloidal NC into close-packed thin films of desired thickness and then grow the cladding layers of low index material around it. This structure may be referred in literature sometimes as a sandwich-type active waveguide [34]. In addition, the NCs can be embedded into a solid-state matrix, creating a blend which is often called nanocomposite [35]. Polymers offer many advantages over glass, such as the solution processability, the integration with a large variety of substrates, even flexible ones, and the possibility to perform micro- and nano-patterning with UV or e-beam lithographic techniques.

In the present Ph.D. Thesis, we fabricated nanocomposite and sandwich type structures based on PNCs. We focused our research on the sandwich type structure because it offers better photoluminescence generation efficiency. The base polymer was PMMA and the whole structure was built on a SiO_2/Si substrate. Firstly, the waveguides were fabricated following standard thin-film deposition techniques, and then optically characterized to stablish their advantages and potential applications. Here, waveguides are not only interesting from a technological point of view, but also because they serve as optimum platforms for optical experimentation: the high confinement of light in the core of the waveguide provides the required power density to reach the stimulated emission threshold or to activate the nonlinear properties, among other applications.

1.2.2 Optical Fibers

Optical fibers are cylindrical and flexible optical waveguides that can potentially be very long (on the kilometers scale). Optical fibers operate under the same principles of total internal reflection and wave interference governing the light propagation in rectangular waveguides. In the 60 and 70 decades, optical fibers reached two important milestones that have revolutionized the telecommunication networks. First of all, the

reduction of the attenuation in silica type fibers, down to 20 dB/km, and secondly the implementation of Erbium Doped Fibers Amplifiers (EDFA). These achievements significantly increased the transmission distance over hundreds of km, and nowadays optical fibers have become the skeleton of the global telecommunication networks. Currently, light at 1550 nm (third optical window) is transmitted with an attenuation smaller than 0.2 dB/km while being efficiently amplified by EDFAs. With the EDFAs started the optical wiring of the U.S. in the 80's. At that time, systems operated at 90 Mb/s. In the coming years, the early 1990's, as Internet was becoming widespread, the transmission capacity became a major concern. Technologies such as the wavelength-division multiplexing (WDM), a technique that enables multiple communication links to use a common transmission fiber, were developed in an effort to escalate the transport capacity with bit rates, up to 8–10 Gb/s, over country-wide distances [36].

Nowadays, the multiplexing possibilities of the single-mode fiber have been largely exploited. Internet traffic keep increasing exponentially and the spectral efficiency of the backbone network lurks the Shannon capacity limit [37]. Thus, a photonic integrated circuit that packages multiple optical parallelism strategies into compact components with a small footprint is considered a promising solution to alleviate the bandwidth saturation and power scaling global network situation [38].

Hollow-core fibers (HCFs) makes a good candidate for novel multiplexing techniques [39]. While glass fibers guide the light using total internal reflection effect, HCFs confine the light using a periodical cladding structure. Since light propagates through air instead of glass, the absorption coefficient is orders of magnitude lower than in a conventional single-mode fiber. HCF technology promises applications in different areas because of their unique optical properties, hitherto unknown in conventional optical fiber materials: high damage threshold, reduced non-linearity coefficients, potentially low loss in transmission, lower latency etc. However, state-of-the-art HCFs still have a loss several times higher than standard single-mode fibers. Nevertheless, recent reports demonstrated that losses can be reduced to the 1 dB/km mark, or even lower, in a hollow-core fiber, which represents an important breakthrough [40].

Although telecom industry is the main application field for silica optical fibers, they have also been opened for optical sensing. The advantages of fiber optical sensors include the possibility of monitoring several physical parameters avoiding the necessity of positioning many discreet sensors, the arrangement in various configurations for distributed sensing of strain, the characterization of temperature or pressure, and a large range of other potential applications, such as chemo-/bio-sensing [41].

In the framework of this Thesis, hollow-core fibers will serve as hosts, working as a lab-on-a-fiber for the study of optical properties of materials. In Chapter 5 it is shown how PNCs were incorporated into HCFs to construct a novel optical device that enhances the emission of light by PNCs [42], and can be a useful workbench for the implementation of different tasks, such as signal regeneration, modulation, multiplexing or demultiplexing, among others [43].

1.2.3 COMPACT LASERS FOR INTEGRATED OPTICS

The invention of the laser in 1960 at Hughes Research Laboratories leaded to a major technological revolution. Nevertheless, the construction of lasers components in the silicon photonics platform is difficult to accomplish due to the indirect band gap nature of this material. Thus, the integrated technology depends on III-V/Si heteroepitaxy to fabricate lasers within this platform. However, in the last decades there have been significant advances in colloidal QD lasers. The low-dimensional semiconductor structures can moderate the sensitivity of lasing threshold to the temperature due to their delta-function-like density of states profile [44]. Furthermore, size of the QDs can be tuned to produce lasing at wavelengths not accessible with standard semiconductor laser diodes. Indeed, recently, colloidal semiconductor QDs or NCs have been chosen as active core material to fabricate VCSELs [27].

In this Thesis we attempted to produce distributed feedback lasers (DFBs), as well as VCSELs operating at room temperature, but the research effort diverted towards more fundamental questions. Nevertheless, ongoing progress towards this end are summarized in Chapter 6, in which the characteristic resonances of random lasing could be identified.

1.2.4 PHOTODETECTORS

Photodetectors are optoelectronic devices that convert the light into an electrical signal. Depending on the specific application, the photodetector has to accomplish different requirements. When this device is integrated in a chip, it usually needs to measure a range of specific wavelengths under relatively low input power level conditions, sometimes demanding high performance requirements into a small footprint for a high density of integration.

Thus, to achieve monolithically integrated optoelectronics, a high level of manufacturing sophistication is required. The growth on crystalline substrates using lattice-matched semiconductors, implemented together with read-out circuitry, becomes challenging for many laboratories. Nevertheless, solution process materials, such as colloidal QDs can be readily integrated on other integrated circuits by using a plethora of low-cost techniques (i.e. inkjet printing, spin-coating or spray-casting techniques). For example, colloidal QDs or NCs can be embedded into conductive polymers to fabricate micrometric photodetectors on Si substrates or directly into nano-gaps between metal nano-contacts [45]. Additionally, the tunable optical absorption and emission spectra, together with the comparatively high quantum efficiencies, are some very special characteristics of PNCs, which result useful for integrated optics applications.

1.3 THESIS OBJECTIVES

The main objective of the present Ph.D. Thesis is the incorporation of PNCs emitting in visible (or near-infrared) wavelengths in photonic structures to construct novel integrated optical devices. For this purpose, the outstanding optoelectronic properties of PNCs are implemented to bring different functionalities, such as light generation, light amplification or photodetection, into various optoelectronic devices. Following this lead, we may divide the main objective in two secondaries:

Objective 1. It is mandatory to examine the physical mechanisms responsible for amplified spontaneous emission in PNCs. First, thin films of PNCs will be used as basic building blocks from which integrate more complex architectures; being able to generate ASE in thin films of PNCs and completely characterize its dependence with excitation fluency and temperature, as well as its dynamics, it is an important milestone in the achievement of this objective. Once the ideal conditions for optical amplification are stablished in thin films, the PNCs can be integrated in hollow-core fibers, used as a host for the nanocrystals, allowing signal amplification while bringing non-linear effects into discussion. A third landmark will be the integration PNCs into a waveguide structure that enhances the generation of light and minimizes the propagation losses. This will allow us to demonstrate under which conditions the photons can be reabsorbed and reemitted by the active PNC layer, the so-called *photon recycling* effect. All these results provide a novel knowledge on the possible use of caesium lead halide PNCs as an active material and can pave the road of new optoelectronic devices based on PNCs.

Therefore, this research is essential to achieve more ambitious objectives such as lasing under continuous wave (CW) optical excitation, or electrical injection, at room temperature.

Objective 2. In addition, the effects of altering the surface chemistry of PNC thin films need to be investigated in order to further improve the performance of the material for some optoelectronic applications. For this purpose, a solid-state ligand-exchange technology is proposed to develop a photoconductor and a phototransistor device. This achievement will represent a step forward in the processability of films based on PNCs, allowing to fabricate heterojunctions between PbS QDs (lead sulfide semiconductor operating at telecom wavelengths) and PNCs. Such devices not only can act as receivers in a photonic circuit, enabling chip-to-chip interconnection, but also open the door for a wide range of applications such as visible-NIR cameras, multiwavelength LEDs for integrated photonics, solar cells, etc.

1.4 THESIS OUTLINE

The present Ph.D. Thesis comprises several investigation fields related with the use of PNCs as an active material for optoelectronics. The structure of this manuscript contains three introductory chapters to describe all the theoretical concepts needed to fully understand the experimental results, which are summarized in the other chapters. Finally, this report is finished with a general conclusion chapter.

Chapter 1: Introduction.

This chapter includes a brief description of the history and recent state of the art of integrated optics, with a particular emphasis on the applicability of NCs, and the main objectives of the present Ph.D. Thesis.

Chapter 2: Theoretical Introduction.

In this section, a brief summary of the theoretical aspects, needed to follow the discussion of the core experimental chapters, are presented. In particular, it comprises

the photophysical aspects of semiconductor nanocrystals and the theory of photodetectors.

Chapter 3: Experimental Methods.

The purpose of this chapter is to describe the fabrication and characterization techniques involved in the development of the research.

Chapter 4: PNC Photodetectors and solid-state ligand exchange strategies.

This chapter presents the project of PNC-based photodetectors. In this work, $CsPbBr_3$ NCs thin films are engineered and enhanced via a solid-state ligand-exchange procedure. The extraction of the figures of merit of the detector serves a benchmark, revealing photoresponsivities up to 0.1 A/W, with open circuit voltages around 0.6-0.8 V, with short circuit currents of 1 to 3 mA/cm^2 and detectivities as high as 8×10^{10} jones. A photoconductor and a FET (Field Effect Transistor) chip device were also built in order to measure the electrical and electro-optical properties of this material, substantiating that the ligand exchange with MPA yields a superior device performance via increased inter-mobility between the PNCs. This work serves as a building block for other realizations with PNCs since the film deposition strategy was established in the development of this one.

Chapter 5: Optical amplification in Hollow-Core fibers doped with PNCs.

In this chapter, a hollow-core negative-curvature fiber (HC-NCF) optical signal amplifier was fabricated by the filling of the microchannels of the fiber with all-inorganic $CsPbBr_3$ PNCs. The optimum fabrication conditions were found to enhance the optical gain, up to +3 dB in the best device. The experimental results were approximately reproduced by means of a gain assisted mechanism based on the nonlinear optical properties of the PNCs, indicating that signal regeneration can be achieved under low pump powers, much below the threshold of stimulated emission. The results can pave the road for new functionalities of the HC-NCF technology with PNCs, such as optical amplification, nonlinear frequency conversion and liquid and gas chemo- bio-sensing.

Chapter 6: Amplified Spontaneous Emission in Thin Films of PNCs.

Here, we analyze the formation of optical gain in PNCs of three different bandgaps ($CsPbBr_3$, $CsPbBr_{1.5}I_{1.5}$ and $CsPbI_3$). The PNCs are processed into films by a layer-by-layer technique. The fabrication was optimized to minimize the threshold of stimulated emission. Our characterization reveals the physical mechanism responsible for the optical gain in these materials. Experimental results are properly reproduced by a physical model that reproduces the limiting impact of self-absorption effect over the generation of ASE.

Chapter 7: Photon recycling effect in $CsPbBr_3$-PMMA waveguides.

In this chapter, we propose the use of a waveguide structure containing $CsPbBr_3$ PNCs thin films (<200 nm) between poly(methyl methacrylate) (PMMA) layers. This sandwich configuration enhances the reabsorption and emission efficiency of the PNCs. Reabsorption and reemission of the photoluminescence (PL) emitted by a semiconductor, or photon recycling (PR) effect, adds a degree of freedom to control the carrier density in semiconductor thin films. Thus, the PR effect can enhance different optoelectronic properties of the material. We propose an experimental set-up based on the frequency modulation spectroscopy and a stochastic Monte Carlo model to provide an appropriate characterization of this effect inside waveguiding structures.

Chapter 8: Conclusions.

A closing chapter that draws together the conclusions and future perspectives resulting from the present Ph.D. work.

1.5 REFERENCES

1. Ortega-San-Martin, L. Introduction to Perovskites: A Historical Perspective BT - Revolution of Perovskite: Synthesis, Properties and Applications. In; Arul, N.S., Nithya, V.D., Eds.; Springer Singapore: Singapore, 2020; pp. 1–41 ISBN 978-981-15-1267-4.
2. Lu, S.; Zhou, Q.; Ouyang, Y.; Guo, Y.; Li, Q.; Wang, J. Accelerated discovery of stable lead-free hybrid organic-inorganic perovskites via machine learning. *Nat. Commun.* **2018**, *9*, 3405.
3. Kageyama, H.; Hayashi, K.; Maeda, K.; Attfield, J.P.; Hiroi, Z.; Rondinelli, J.M.; Poeppelmeier, K.R. Expanding frontiers in materials chemistry and physics with multiple anions. *Nat. Commun.* **2018**, *9*, 772.
4. Watthage, S.C.; Song, Z.; Phillips, A.B.; Heben, M.J. Chapter 3 - Evolution of Perovskite Solar Cells. In; Thomas, S., Thankappan, A.B.T.-P.P., Eds.; Academic Press, 2018; pp. 43–88 ISBN 978-0-12-812915-9.
5. Brenner, T.M.; Egger, D.A.; Kronik, L.; Hodes, G.; Cahen, D. Hybrid organic—inorganic perovskites: low-cost semiconductors with intriguing charge-transport properties. *Nat. Rev. Mater.* **2016**, *1*, 15007.
6. Wang, H.; Liu, H.; Zhang, Z.; Liu, Z.; Lv, Z.; Li, T.; Ju, W.; Li, H.; Cai, X.; Han, H. Large piezoelectric response in a family of metal-free perovskite ferroelectric compounds from first-principles calculations. *npj Comput. Mater.* **2019**, *5*, 17.
7. Leijtens, T.; Bush, K.; Cheacharoen, R.; Beal, R.; Bowring, A.; McGehee, M.D. Towards enabling stable lead halide perovskite solar cells; interplay between structural, environmental, and thermal stability. *J. Mater. Chem. A* **2017**, *5*, 11483–11500.
8. Mehrabian, M.; Dalir, S.; Mahmoudi, G.; Miroslaw, B.; Babashkina, M.G.; Dektereva, A. V; Safin, D.A. A Highly Stable All-Inorganic CsPbBr3 Perovskite Solar Cell. *Eur. J. Inorg. Chem.* **2019**, *2019*, 3699–3703.
9. Saliba, M. Polyelemental, Multicomponent Perovskite Semiconductor Libraries through Combinatorial Screening. *Adv. Energy Mater.* **2019**, *9*, 1803754.
10. Kojima, A.; Teshima, K.; Shirai, Y.; Miyasaka, T. Organometal Halide Perovskites as Visible-Light Sensitizers for Photovoltaic Cells. *J. Am. Chem. Soc.* **2009**, *131*, 6050–6051.
11. Xing, G.; Mathews, N.; Lim, S.S.; Yantara, N.; Liu, X.; Sabba, D.; Grätzel, M.; Mhaisalkar, S.; Sum, T.C. Low-temperature solution-processed wavelength-tunable perovskites for lasing. *Nat. Mater.* **2014**, *13*, 476–480.
12. Protesescu, L.; Yakunin, S.; Bodnarchuk, M.I.; Krieg, F.; Caputo, R.; Hendon, C.H.; Yang, R.X.; Walsh, A.; Kovalenko, M. V Nanocrystals of Cesium Lead Halide Perovskites (CsPbX3, X = Cl, Br, and I): Novel Optoelectronic Materials Showing Bright Emission with Wide Color Gamut. *Nano Lett.* **2015**, *15*, 3692–3696.
13. Schmidt, L.C.; Galian, R.E.; Pertegás, A.; Agouram, S.; González-Carrero, S.; Bolink, H.J.; Pérez-Prieto, J.; Malinkiewicz, O.; Mínguez Espallargas, G. Nontemplate Synthesis of CH 3 NH 3 PbBr 3 Perovskite Nanoparticles . *J. Am. Chem. Soc.* **2014**, *136*, 850–853.
14. Protesescu, L.; Yakunin, S.; Bodnarchuk, M.I.; Krieg, F.; Caputo, R.; Hendon, C.H.; Yang, R.X.; Walsh, A.; Kovalenko, M. V. Nanocrystals of Cesium Lead Halide Perovskites (CsPbX3, X = Cl, Br, and I): *Nano Lett.* **2015**, *15*, 3692–3696.
15. Chakrabarty, A.; Satija, S.; Gangwar, U.; Sapra, S. Precursor-Mediated Synthesis of Shape-Controlled Colloidal CsPbBr3 Perovskite Nanocrystals and Their Nanofiber-Directed Self-Assembly. *Chem. Mater.* **2020**, *32*, 721–733.

16. Chiba, T.; Hayashi, Y.; Ebe, H.; Hoshi, K.; Sato, J.; Sato, S.; Pu, Y.-J.; Ohisa, S.; Kido, J. Anion-exchange red perovskite quantum dots with ammonium iodine salts for highly efficient light-emitting devices. *Nat. Photonics* **2018**, *12*, 681–687.
17. Suárez Alvarez, I. Active photonic devices based on colloidal semiconductor nanocrystals and organometallic halide perovskites. *Eur. Phys. J. Appl. Phys.* **2016**, *75*, 30001.
18. Kovalenko, M. V; Protesescu, L.; Bodnarchuk, M.I. Properties and potential optoelectronic applications of lead halide perovskite nanocrystals. *Science (80-.).* **2017**, *358*, 745–750.
19. Li, Y.-F.; Feng, J.; Sun, H.-B. Perovskite quantum dots for light-emitting devices. *Nanoscale* **2019**, *11*, 19119–19139.
20. Miller, S.E. Integrated optics: An introduction. *Bell Syst. Tech. J.* **1969**, *48*, 2059–2069.
21. Hecht, J. Short history of laser development. *Opt. Eng.* **2010**, *49*, 1–23.
22. Tien, P.K.; Ulrich, R. Theory of Prism - Film Coupler and Thin-Film Light Guides. *J. Opt. Soc. Am.* **1970**, *60*, 1325–1337.
23. Tien, P.K. Integrated optics and new wave phenomena in optical waveguides. *Rev. Mod. Phys.* **1977**, *49*, 361–420.
24. Chovan, J.; Uherek, F. Photonic Integrated Circuits for Communication Systems. *Radioengineering* **2018**, *27*, 357–363.
25. Eldada, L. Optical communication components. *Rev. Sci. Instrum.* **2004**, *75*, 575–593.
26. Kogelnik, H. An Introduction to Integrated Optics BT - Optical Information Processing: Volume 2. In; Barrekette, E.S., Stroke, G.W., Nesterikhin, Y.E., Kock, W.E., Eds.; Springer US: Boston, MA, 1978; pp. 349–389 ISBN 978-1-4615-7545-0.
27. Huang, C.Y.; Zou, C.; Mao, C.; Corp, K.L.; Yao, Y.C.; Lee, Y.J.; Schlenker, C.W.; Jen, A.K.Y.; Lin, L.Y. CsPbBr3 Perovskite Quantum Dot Vertical Cavity Lasers with Low Threshold and High Stability. *ACS Photonics* **2017**, *4*, 2281–2289.
28. Ebeling, K.J. Strip Waveguides - Integrated Optoelectronics: Waveguide Optics, Photonics, Semiconductors. In; Ebeling, K.J., Ed.; Springer Berlin Heidelberg: Berlin, Heidelberg, 1993; pp. 75–108 ISBN 978-3-642-78166-7.
29. Signoretto, M.; Zink-Lorre, N.; Suarez, I.; Font-Sanchis, E.; Sastre-Santos, Á.; Chirvony, V.S.; Fernandez-La zaro, F.; Martínez-Pastor, J.P. Efficient optical amplification in a sandwich-type active-passive polymer waveguide containing perylenediimides. *ACS Photonics* **2017**, *4*, 114–120.
30. Dong, G.; Wang, H.; Chen, G.; Pan, Q.; Qiu, J. Quantum Dot-Doped Glasses and Fibers: Fabrication and Optical Properties. *Front. Mater.* **2015**, *2*, 13.
31. Pang, F.; Sun, X.; Guo, H.; Yan, J.; Wang, J.; Zeng, X.; Chen, Z.; Wang, T. A PbS quantum dots fiber amplifier excited by evanescent wave. *Opt. Express* **2010**, *18*, 14024–14030.
32. Huang, X.; Fang, Z.; Kang, S.; Peng, W.; Dong, G.; Zhou, B.; Ma, Z.; Zhou, S.; Qiu, J. Controllable fabrication of novel all solid-state PbS quantum dot-doped glass fibers with tunable broadband near-infrared emission. *J. Mater. Chem. C* **2017**, *5*, 7927–7934.
33. Gordillo, H.; Suárez, I.; Abargues, R.; Rodríguez-Cantó, P.; Martínez-Pastor, J.P. Color Tuning and White Light by Dispersing CdSe, CdTe, and CdS in PMMA Nanocomposite Waveguides. *IEEE Photonics J.* **2013**, *5*, 2201412.
34. Suárez, I.; Larrue, A.; Rodríguez-Cantó, P.J.; Almuneau, G.; Abargues, R.; Chirvony, V.S.; Martínez-Pastor, J.P. Efficient excitation of photoluminescence in a two-dimensional waveguide consisting of a quantum dot-polymer sandwich-type structure. *Opt. Lett.* **2014**, *39*, 4962–4965.

35. Bueno, A.; Suarez, I.; Abargues, R.; Sales, S.; Pastor, J.P.M. Temperature Sensor Based on Colloidal Quantum Dots–PMMA Nanocomposite Waveguides. *IEEE Sens. J.* **2012**, *12*, 3069–3074.
36. Brackett, C.A. Dense wavelength division multiplexing networks: principles and applications. *IEEE J. Sel. Areas Commun.* **1990**, *8*, 948–964.
37. Liu, X. Chapter 3 - Challenges and Opportunities in Future High-Capacity Optical Transmission Systems. In; Zyskind, J., Srivastava, A.B.T.-O.A.W.D.M.N., Eds.; Academic Press: Oxford, 2011; pp. 47–82 ISBN 978-0-12-374965-9.
38. Zhou, D.; Sun, C.; Lai, Y.; Yu, Y.; Zhang, X. Integrated silicon multifunctional mode-division multiplexing system. *Opt. Express* **2019**, *27*, 10798–10805.
39. Hayashi, T. Multi-core Fibers for Space Division Multiplexing BT - Handbook of Optical Fibers. In; Peng, G.-D., Ed.; Springer Singapore: Singapore, 2018; pp. 1–46 ISBN 978-981-10-1477-2.
40. Bradley, T.D.; Hayes, J.R.; Chen, Y.; Jasion, G.T.; Sandoghchi, S.R.; Slavik, R.; Fokoua, E.N.; Bawn, S.; Sakr, H.; Davidson, I.A.; et al. Record Low-Loss 1.3dB/km Data Transmitting Antiresonant Hollow Core Fibre. In Proceedings of the European Conference on Optical Communication, ECOC; 2018; Vol. 2018-September.
41. Lu, P.; Lalam, N.; Badar, M.; Liu, B.; Chorpening, B.T.; Buric, M.P.; Ohodnicki, P.R. Distributed optical fiber sensing: Review and perspective. *Appl. Phys. Rev.* **2019**, *6*, 41302.
42. Navarro-Arenas, J.; Suárez, I.; Martínez-Pastor, J.P.; Ferrando, A.; Gualdrón-Reyes, A.F.; Mora-Seró, I.; Gao, S.-F.; Wang, Y.-Y.; Wang, P.; Sun, Z.; et al. Optical Amplification in Hollow-Core Negative-Curvature Fibers Doped with Perovskite CsPbBr3 Nanocrystals. *Nanomaterials* **2019**, *9*, 868.
43. Agrawal, G.P. (Govind P.. *Applications of nonlinear fiber optics*; Elsevier, 2008; ISBN 9780080568768.
44. Roh, J.; Park, Y.-S.; Lim, J.; Klimov, V.I. Optically pumped colloidal-quantum-dot lasing in LED-like devices with an integrated optical cavity. *Nat. Commun.* **2020**, *11*, 271.
45. Gui, P.; Chen, Z.; Li, B.; Yao, F.; Zheng, X.; Lin, Q.; Fang, G. High-Performance Photodetectors Based on Single All-Inorganic CsPbBr3 Perovskite Microwire. *ACS Photonics* **2018**, *5*, 2113–2119.

2 THEORETICAL BACKGROUND

2.1 SEMICONDUCTOR COLLOIDAL NANOCRYSTALS

The notion of “quantum dot” (QD) was introduced first by Alexey Ekimov at the coming of 1980 [1], enunciating the possibility to confine charge carriers in "microscopic semiconductors" due to the localized nature of the potential energy distribution in spatially reduced structures. During the last decades, colloidal QDs have attracted the attention of the scientific community, mostly due to their remarkable electronic [2], optical [3] and catalytic [4] properties. Furthermore, fabrication through synthetic routes offers unseen advantages; the possibility to manipulate the quantum confinement in QDs, and hence their optical and electric properties, by tuning the size, shape, surface states or chemical composition allows to produce tailor-made materials that perform specific optoelectronic applications [5].

A central characteristic of semiconductors is the energy band gap (E_g), which defines the minimum energy required to promote an electron from the valence band (VB) to the conduction band (CB). When an electron is promoted to the CB, a positively charged hole is generated in the VB. The electron-hole bound state is called exciton and it can be described with hydrogenic energy states. Within this model, the most probable electron-hole distance in its ground state is the so-called Bohr radius. This length can be calculated for any semiconductor system assuming the effective mass approximation by scaling the hydrogen Bohr radius $a_0 \approx 52.9\, pm$ with the following equation:

$$a_B = \varepsilon \frac{m_0}{m^*} a_0 \tag{2.1}$$

Here, ε is the dielectric constant of the semiconductor and $m^{*-1} = m^{*-1}_e + m^{*-1}_h$ is the electron-hole reduced mass. Depending on the semiconductor, the value of a_B in state-of-the-art QD systems have a wide range of variability. For instance, the cadmium-based QDs of groups II-VI, namely CdS, CdSe and CdTe, have an excitonic a_B of 2, 4 and 5 nm, respectively [6]. In the other side of the spectrum, IV-VI lead salts of PbS, PbSe and PbTe have much larger excitonic Bohr radius (21, 55 and 104 nm,

respectively) [6]. In this way, strong quantum confinement regime can be achieved with PbTe QDs with 30 nm of diameter due to its large excitonic radius. In the case of caesium lead halide perovskite nanocrystals (PNCs), the calculated Bohr radii of $CsPbCl_3$, $CsPbBr_3$ and $CsPbI_3$ is around 2.5, 3.5, and 6 nm, respectively [5]. Given that PNCs can be synthesized slightly in the range of sizes very close to those Bohr radii, strong confinement is not expected, although smaller NC sizes with significant 3D quantum size confinement can be reached in some cases [7]. Other nanostructures, like 2D perovskite nanosheets with monolayer-thickness control show strong quantum confinement effects [8]. Certainly, it is not the case for the cubic PNCs used in this PhD because they present edge lengths higher than the Bohr radii (8-14 nm as TEM imaging reveals). Thus, when referring to our PNCs we opted to drop the QD label as the term implies a significant degree of quantum confinement.

2.1.1 PHOTOPHYSICS OF SEMICONDUCTOR NANOCRYSTALS

In semiconductor nanocrystals (NCs) the most important photophysical processes involved in the description of the physical system behavior are the exciton generation, the relaxation, the charge recombination and carrier trapping [9]. A variety of different excitations appear after a photoexcitation event: free electrons and holes, excitons and phonons are generated inside NCs when a photon with energy higher than the bandgap is absorbed. The Coulomb interaction between electrons and holes rules over the formation of excitons, bound states defined by the hydrogenic system quantized energies converging to the electron-hole continuum. When a short pulse of photons with mean energy $h\nu_{ph}$ is absorbed by the semiconductor NC, the excess energy $h\nu_{ph}$ - E_g is added to the carriers in the form of kinetic energy and the semiconductor ceases to be in thermal equilibrium. Then, the NC undertakes several temporally overlapping relaxation processes that bring the carrier thermal distribution into equilibrium again:

(i) In the coherent regime, the excitations generated in the semiconductor have a well-defined phase relationship with the excitation photons. During this initial stage, a period typically in the femtosecond domain, the scattering processes quickly destroy the coherence (in perovskite NCs it has been reported to last a period no longer than 80 ps [10]), leading to

(ii) the hot-carrier regime, where carriers and excitons thermalize (carriers and excitons species can be described with a single temperature-dependent

distribution) to lattice temperature by scattering among their own species (carrier-carrier or exciton-exciton scattering processes) in period lasting hundreds of femtoseconds (excitons) or picoseconds (carriers). The thermalized carriers reach lattice temperatures in hundreds of picoseconds by exchanging energy interaction with lattice phonons. When all the species (carriers, excitons and phonons) share a common temperature distribution, it comes the

(iii) isothermal regime, where the excess of electron-hole pairs recombine, radiatively or non-radiatively, until the semiconductor restores its thermal equilibrium.

In this Thesis we will mainly focus on the isothermal regime of the semiconductor. Specifically, we will study the radiative recombination of excitons in a time window ranging from a few hundred of picoseconds to tens of nanoseconds. This time scale overlaps with the perovskite NC's recombination time, which is clocks around the nanosecond [11]. The excitonic quasi-particles and their many body interactions have a prominent role in the absorption and emission spectra of PNCs and their understanding can provide means to enhance their optoelectronic properties. Carrier recombination is a process by which electron and hole annihilate each other. The electrons promoted to the conduction band (CB) occupy the holes in the valence band (VB). If a band-to-band recombination occurs, a photon with the energy of the bandgap is generated. However, the process can take more steps than one: the hot-carriers may decay first to the lowest energy level of their band before band-to-band recombination. This intra-band processes can be radiative or non-radiative. During the hot-carrier relaxation, if the electron-hole pair has an energy greater than twice the bandgap, more excitons could be generated by taking the excessive energy in a process called the multi-exciton generation (MEG).

If multiple carriers or excitons are involved, the occurring many-body interaction mainly follows the biexcitonic or trionic Auger recombination path. This is a non-radiative channel in which the exciton transfers its energy to a third particle that is excited to a higher energy level. Because part of the excitonic energy is lost in the form of heat, this process hampers the PL efficiency of the NC. Thus, in the development of photoluminescent devices, the Auger recombination must be avoided [12]. To reduce Auger scattering, the average number of photoexcitations per nanocrystal and the carrier density must be kept below a certain threshold [13]. Nonetheless, for certain applications such as the laser, the excitation must be strong enough to reach the lasing threshold. This gives rise to one of the fundamental tribulations with NC optical gain media, mainly

when Auger becomes the dominant relaxation process. In the case of PNCs this issue is investigated in Chapter 6 of this Thesis.

In semiconductor NCs there is yet another recombination channel to explore; the trap-assisted recombination, when a carrier is trapped into an energy level located within the bandgap. This intra-band states can be either shallow traps or deep traps. Shallow traps involve a comparatively small difference of energy from the respective CB/VB band edge, while deep traps lay near the middle of the semiconductor bandgap. A carrier occupying the trap can fence into an empty valence band state after a certain amount of time, the trapping lifetime, that usually depends on the depth of the trap within the bandgap, the temperature and other specific parameters. The effect of trap states in the carrier dynamics depends on the depth of the energy level. Shallow traps only obstruct the free carrier transport through trapping and detrapping processes; deep traps, however, having longer lifetimes and equal proximity to semiconductor bands, facilitate non-radiative recombination pathways. We will refer to this process as Shockley-Read-Hall (SRH) recombination [13]. The origin of traps in PNCs is discussed in Chapter 4, but they are mostly caused by structural defects at the surface of the NC [14]. Trap assisted recombination in low-dimensional semiconductors is a critical effect due to the large surface-to-volume ratio in a NC. Thus, the chemistry of the NC surface can have a direct impact on the optoelectronic properties of the semiconductor. The NC surface contains a large number of impurity levels and electrically active dangling bonds that can act as recombination centres. Surface defects in NCs can also be generated due to an incomplete ligand substitution or charge imbalance between the ligand and the surface states [15]. These surface defects in NCs are dependent on the length and the chemical structure of the capping ligands surrounding and interconnecting the NCs [16]. Furthermore, they introduce trapping states energetically located within the NC band gap that modify the photoconductivity kinetics [17].

2.2 WAVEGUIDES

A waveguide is an optical structure that confines and propagates the light. For this purpose, a waveguide is composed of dielectric materials with different refractive indexes. Typically, a high-index core is surrounded by a low-index cladding. In this configuration, the higher refractive index of the core of the waveguide compared to those of the cladding results in the confinement of the light by total internal reflection (TIR). In particular, all rays with an incidence angle smaller than the critical acceptance light cone

are launched and confined into the structure. From the electromagnetic point of view, only a discrete set of angles (or parallel wave vectors) satisfies the phase matchings conditions given by the geometrical parameters and refractive indexes of the involved materials. This set of characteristic solutions are wavelength-dependent and receive the name of *propagation modes*. Modes have the particular feature of maintaining the same polarization and field transverse distribution across the propagation axis.

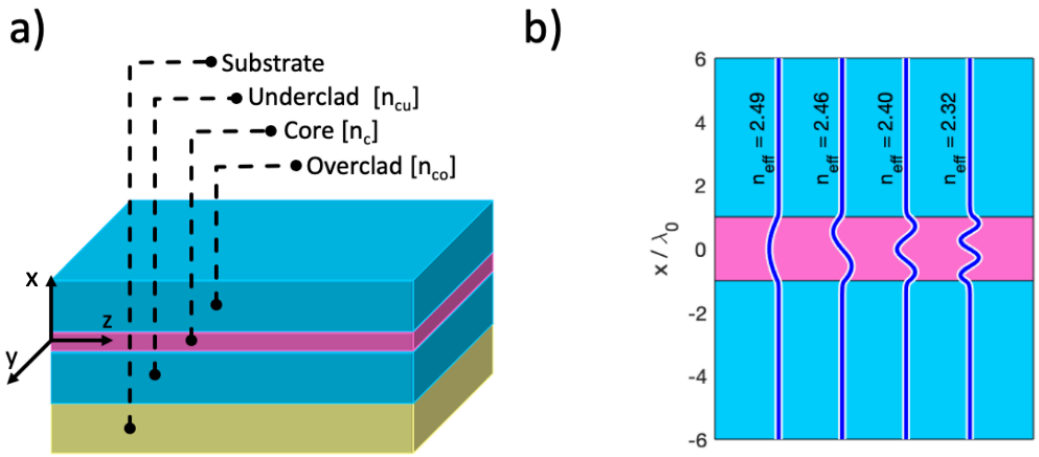

Figure 2.1. a) Schematic illustration of a slab waveguide where the pink area surface represents the core (with higher index n_c) and the blue area represents the cladding surface (with lower index n_{cu} and n_{co}). b) First four TE modes of the symmetrical slab waveguide ($n_{cu} = n_{co}$) with and index of 2.5 in the core and 1.5 in the cladding calculated by the finite-difference analysis method. The x axis was normalized to the free space wavelength λ_0.

An example of this is shown for the slab waveguide architecture of Figure 2.1b, in which the first four TE modes were calculated with the finite-difference method [18]. In this Thesis, the transfer matrix theory of multilayer optics was used to solve the modes of waveguides for their effective indices and field distributions [19].

2.3 OPTICAL GAIN

In this Section the fundamental processes of light amplification at optical frequencies will be presented.

2.3.1 AMPLIFIED SPONTANEOUS EMISSION

Amplified spontaneous emission (ASE), or sometimes called superluminescence, is an optical process in which spontaneous emission is amplified via the stimulated emission. The process of ASE is typically described in a cylindrical geometry with an energy diagram consisting of several population levels in which the lower level has a negligible occupation and the upper state is densely populated (population inversion). In this scenario, the variation of the spectral intensity I along the propagation axis *z* is given by the following differential equation [20]:

$$\frac{\partial I_v}{\partial z} = \sigma \mathrm{N} I_v + \frac{\Omega}{4\pi} N A_v h\nu \tag{2.2}$$

Here σ is the stimulated emission cross section, the term *N* is the upper state population, *A* is the spectral rate of spontaneous emission, and the factor solid angle $\Omega/4\pi$ measures the projection of the differential element *dz* over the complete solid angle 4π.

Integrating Equation 2.2 under the correct approximations for homogeneous line broadening produces the Svelto (1998) equation [20]:

$$\frac{I}{I_\mathrm{s}} = \phi \frac{\Omega}{4\pi} \frac{(G-1)^{3/2}}{(\pi G \ln\, G)^{1/2}} \tag{2.3}$$

Here, G = exp($g_0 L$) = exp(σNL) is the optical unsaturated gain coefficient, where *L* is the length of the active medium; $I_\mathrm{s} = h\nu_0/\sigma\tau$ is the saturation intensity; τ is the radiative lifetime and ν_0 the transition frequency; and $\phi = \tau A$ is the fluorescence quantum yield. This expression is used to predict the intensity of the ASE for low saturated regime, 5<$g_0 L$<8; in the case of reaching the saturation regime ($I \gg I_s$), $g_0 L$>15, this asymptotic approximation is valid:

$$I/I_s = \phi g_0 L/2 \tag{2.4}$$

Following the Gaussian approximation, the normalized ASE linewidth can be calculated as follows:

$$\Delta\nu_{\mathrm{ASE}} = (\ln\ 2)^{1/2}\left(\frac{G-1}{G\ln\ G}\right)^{1/2}\Delta\nu_0 \qquad (2.5)$$

With $\Delta\nu_0$ defined as the spontaneous emission linewidth. The approximation given by these formulas can be compared to the calculation in which saturation is taken exactly (green line in Figure 2.2a).

This analysis allows to identify the ASE emission spectral features:

(i) the ASE narrows with respect to the spontaneous emission bandwidth,

(ii) the ASE signal grows superlinearly above a gain threshold.

The intensity versus gain (pump power) curve presents a characteristic S-shape which allows to identify the ASE regime and the saturation regime as two inflection points in such plots.

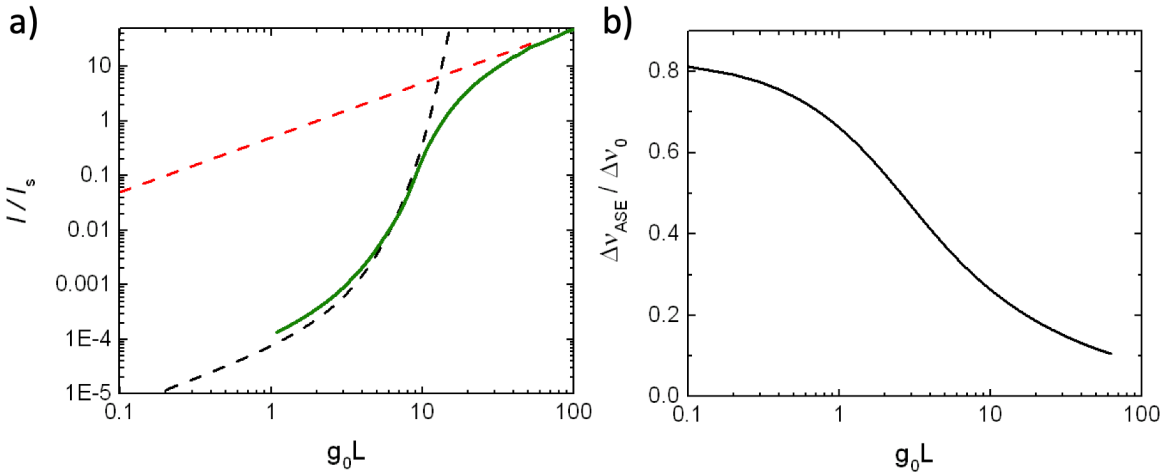

Figure 2.2. a) Normalized ASE intensity versus g_0L for homogeneous line broadening and solid angle $\boldsymbol{\Omega/4\pi\ =\ 10^{-4}}$. The black discontinuous line is the Svelto approximation (Equation 2.2, the red discontinuous line is the asymptotic approximation (Equation 2.4) and the solid green line is the exact numerical integration of Equation 2.2. b) Normalized ASE linewidth versus g_0L calculated from Equation 2.5.

Another characteristic of ASE emission lifetime is that the lifetimes associated with the photons emitted under ASE regime present shorter lifetimes than the spontaneous emission lifetime. The appearances of this particular spectral and dynamic behavior allow to characterize the generation of gain in nanocrystal thin films.

2.3.2 FIBER AMPLIFIERS

2.3.2.A DOPED FIBER AMPLIFIERS

The optical gain inside an optical fiber filled with PNCs can be calculated by coupling the power and rate equations for a two-lever energy system [21]. Here, an analytical solution of the power propagation equations is deduced, obtaining an expression that is commonly used in similar problems (namely, in erbium-doped fiber amplifiers) under small-signal single-pass amplification conditions. The model reproduces input-output characteristics for any length of the amplifying system if strong-signal saturation processes are not present. We limit our discussion to the case of a signal beam and N pump beams with frequency v_k propagating in the positive direction (reflections from the end of the fiber are discarded), which are treated identically in the formalism. In a two-level system, the population fractions for the fundamental and the excited level, $N_1(z,t)$ and $N_2(z,t)$ respectively, hold the relation of $N_1(z,t)+ N_2(z,t) = 1$, and follow the present differential equation:

$$\frac{\partial N_2(z,t)}{\partial t} = -\frac{N_2(z,t)}{\tau} - \sum_{k=1}^{N} \frac{\phi_k}{\varrho A h v_k} \frac{\partial P_k(z,t)}{\partial z} \tag{2.6}$$

Here, ϕ_k is the emission quantum efficiency, h is the Plank constant, hv_k is the energy of the *kth* beam, and ϱ is the cross-sectional density of NCs in the fiber. For simplicity, the pump and the doping concentration are considered homogeneous over the area A of the core. Moreover, under steady state conditions, the population of the upper level is independent of time and can be expressed by the following equation:

$$N_2(z) = -\sum_{k=1}^{N} \frac{\tau \phi_k}{\varrho A h v_k} \frac{\partial P_k(z,t)}{\partial z} \tag{2.7}$$

Taking this equations into account, the power propagation equation for the *kth* beam ($P_k(z,t)$) can be denoted with the following expression:

$$\frac{\partial P_k(z,t)}{\partial z} = \varrho \Gamma_k [N_2(z,t)\sigma_k^e - N_1(z,t)\sigma_k^a] P_k(z,t) \tag{2.8}$$

Where σ_k^a and σ_k^e are the absorption and emission cross sections for the *kth* beam, respectively; Γ_k is the confinement factor. Then, combining Equations 2.6 and 2.7, the problem can be expressed by the differential equation.

$$\frac{\partial P_k(z,t)}{\partial z} = \varrho\Gamma_k[(\sigma_k^a + \sigma_k^e)\sum_{k=1}^{N}\frac{\tau\phi_k}{\varrho A h\nu_k}\frac{\partial P_k(z,t)}{\partial z} - \sigma_k^a]P_k(z,t) \tag{2.9}$$

If the following definitions are introduced, α_k and P_k^{sat}, the absorption constant and the saturation power,

$$\alpha_k = \varrho\Gamma_k\sigma_a^k \tag{2.10}$$

$$P_k^{sat} = \frac{h\nu_k A}{(\sigma_k^e + \sigma_k^a)\tau\phi_k} \tag{2.11}$$

and the Equation 2.9 is integrated across all the fiber length L, we obtain the output power for the kth beam as a function of the input power:

$$P_k^{out} = P_k^{in} e^{-\alpha_k L + P_a/P_k^{sat}} \tag{2.12}$$

where P_a is the absorbed power:

$$P_a = \sum_{k=1}^{N}(P_k(0) - P_k(L)) \tag{2.13}$$

Thus, by taking logarithms, the gain for the single signal beam at a distance L from the beginning of the amplifier can be expressed as

$$G_s(L) = log(e)\left[\frac{\Gamma_p\,(\sigma_s^e + \sigma_s^a)\tau\phi_p}{h\nu_p A}P_a - \alpha_s L\right] dB \tag{2.14}$$

This theory is distilled enough to enable an easy analysis of the experimental results in Chapter 5, while still giving insight about the physical effects occurring in the system.

2.3.2.B Four Wave Mixing Optical Parametric Amplifiers

The four-wave mixing (FWM) process starts with two pump waves that propagate together into the optical fiber with frequencies ω_{1p} and ω_{2p}. As they propagate, they will continuously beat between each other generating new sidebands inside the fiber. The sidebands are produced at frequencies $\omega_i = \omega_{1p} + (\omega_{1p} - \omega_{2p})$ and $\omega'_i = \omega_{1p} + (\omega_{2p} - \omega_{1p})$. In this example, phase matching conditions would require that the propagation constants

hold the relation $k_{12} = k_{1p} + k_{2p}$. The generated waves can also be cascaded by further combination with other frequencies and gives rise to many possible replicas. In the simplest case, both pump waves having the same frequency, the degenerate FWM process, which holds $\omega_{2p} = \omega_{1p} = \omega$, the following waves are produced: $\omega + \omega = 2\omega$, $\omega + 2\omega = 3\omega$, $3\omega - \omega = 2\omega$, and $2\omega - \omega = \omega$. Yet if a third frequency $\omega_3 = \omega_s$ (the signal wave) is added, a total of nine sidebands would be generated. The amplitude of the sidebands produced by the overlapping of these components will be proportional to the amplitude of the signal. Some of these products will overlap with the signal frequency, in this case ω_1, resulting in a gain of the signal.

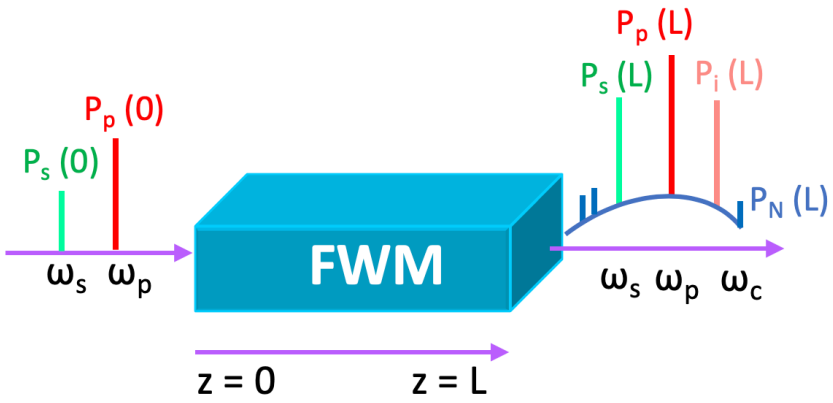

Figure 2.3. Degenerate FWM process in an optical parametric amplifier device of length L. The pump wave with power P_p interacts with the signal wave (with power P_s) producing amplification at the end of the fiber. Other sidebands are produced, consuming the pump wave power. In the graphical representation are depicted as a continuum of cascaded interactions (P_N) and other major contributions named idlers (P_i).

The degenerate FWM process, like the one depicted in Figure 2.3, is best described by the interaction of three stationary copolarized waves with frequencies ω_p, ω_s and ω_i with complex amplitudes $A_p(z)$, $A_s(z)$ and $A_i(z)$. Under these circumstances, the total transverse field E(x,y,z) propagating inside the fiber is described as the product of the transversal mode profile $f(x,y)$ times the complex amplitude of the four mixed waves:

$$E(x,y,z) = f(x,y)[A_p(z)e^{\beta_0 z - i\omega_0 t} + A_s(z)e^{\beta_1 z - i\omega_1 t} + A_i(z)e^{\beta_2 z - i\omega_3 t} + \text{c. c}\,] \quad (2.15)$$

If power loss is neglected, the evolution of the complex amplitude waves inside the fiber with a third-order nonlinearity can be calculated as follows [22]:

$$\begin{aligned}
\frac{dA_p}{dz} = \quad & i\gamma[(|A_p|^2 + 2(|A_s|^2 + |A_i|^2))A_p \\
& +2A_sA_iA_p^*\exp(i\Delta\beta z)] \\
\frac{dA_s}{dz} = \quad & i\gamma[(|A_s|^2 + 2(|A_i|^2 + |A_p|^2))A_s \\
& +A_i^*A_p^2\exp(-i\Delta\beta z)] \\
\frac{dA_i}{dz} = \quad & i\gamma[(|A_i|^2 + 2(|A_s|^2 + |A_p|^2))A_i \\
& +A_s^*A_p^2\exp(-i\Delta\beta z)]
\end{aligned} \tag{2.16}$$

Here $\Delta\beta$ is the phase mismatch term and $\gamma = 2\pi n_2/\lambda A_{eff}$ is the nonlinearity coefficient. The parameter n_2 is the fiber nonlinear coefficient and A_{eff} is the effective modal area of the fiber. An approximate signal gain solution for the Equation 2.16 is given by [23]:

$$G_{dB} = 10\log_{10}\left(1 + \left[\frac{\gamma P_p}{g}\sinh(gL)\right]^2\right) \tag{2.17}$$

The parametric gain coefficient g is given by the set of equations:

$$\begin{gathered}
g^2 = [(\gamma P_{\mathrm{p}})^2 - (\kappa/2)^2] = -\Delta\beta_1\left(\frac{\Delta\beta}{4} + \gamma P_{\mathrm{p}}\right) \\
\Delta\beta = -\frac{2\pi c}{\lambda_0^2}\frac{\mathrm{d}D}{\mathrm{d}\lambda}(\lambda_{\mathrm{p}} - \lambda_0)(\lambda_{\mathrm{p}} - \lambda_{\mathrm{s}})^2 \\
(\kappa = \Delta\beta + 2\gamma P_{\mathrm{p}})
\end{gathered} \tag{2.18}$$

where κ is the total phase mismatch term. The wavelengths λ_{p} and λ_0 are the pump and the fiber's zero-dispersion wavelengths, respectively; λ_{s} is the signal wavelength. The slope $dD/d\lambda$ is the dispersion parameter at the zero-dispersion wavelength, and c is the light velocity in the vacuum.

2.4 PHOTODETECTORS

Within this Ph.D. Thesis we study several photodetection architectures based on thin films of PNCs. Photodetector devices can be classified in two main categories: photoconductors and photodiodes. In this Section, the underlying physical mechanism of such devices will be discussed as well as the figures of merit that are used in literature to extract material's photodetection performances.

2.4.1 PHOTOCONDUCTORS

A two-port photoconductor architecture typically consist of a semiconductor material and two metal ohmic contacts. The absorption of photons by the semiconductor

generates electron–hole pairs drifting across the material by the applied external electric field. In this way, the conductivity of semiconductors increases because of the perturbation introduced ($n = n_0 + \Delta n$) in the carrier density distribution of both, electrons Δn and holes Δp, although in the basic treatment of photoconductivity carried on in this Thesis only the transport of minority excess carriers is considered. Carrier mobility may also increase upon illumination (see the dark conductivity of a semiconductor in Equation 2.19). Both effects contribute to change the response of the biased photoconductor [24].

$$\sigma = e(n\mu_n + p\mu_p) \tag{2.19}$$

In the case of n-type materials, the current density is given by, $\vec{J} = q\mu_e n\vec{E} + qD_e\vec{\nabla}n$, where μ_e and D_e are the electron mobility and diffusivity, respectively. Through this relation, the changes the slope of J-V curves can be translated conductivity changes, which are used in Chapter 4 to describe the behavior of a $CsPbBr_3$ PNC photoconductor.

In photoconductors there is also a photoconductive gain effect, defined as the ratio of circulated carriers per absorbed photon, which can be exploited to increase the performance (amplification factor) of the photoconductor. Prior to the investigations conducted in this Thesis, the candidate participated in the research of photoconductive gain in PbS QDs [24].

2.4.2 PHOTODIODES

Photodiodes are built upon junctions of two different semiconductors (heterojunctions); or a semiconductor material separated in two regions opposite doping (homojunctions); or a semiconductor in contact with a metal barrier (Schottky junctions). The photodiodes fabricated for studies summarized in Chapter 4 are Schottky junctions, a $CsPbBr_3$ PNC thin film capped with an Au gold pad, and a PbS - $CsPbBr_3$ NC thin film heterojunction.

In photodiodes, the excitonic pairs generated by an absorption event are dissociated by the action of the built-in electric potential powered by the junction. When carriers are extracted through the contacts, an absorption event is then registered. Since there are no recirculating currents, the photoconductive gain is not available in photodiodes. This implies that, with most of the materials, the expected efficiency of a photodiode architecture can be potentially lower than the one of a photoconductor, but the temporal response of the device will be much faster since the temporal response of photodiodes is determined by the carriers transit time between contacts instead of their kinetics

(taking into account radiative/non-radiative recombination and eventual carrier trapping/detrapping processes induced by shallow/deep traps).

The photodetection performance is mainly limited by the parasitic noise currents. An important contribution to signal noise is the dark current density. In thin-film based photodiodes, dark current can usually be attributed to either carrier injection from the metal contacts or thermal generation within the active layer. For materials with a substantially large density of defect states or impurity levels, or a relatively small bandgap, thermal dark current can be problematic and may thus require operation at lower temperatures. In reversely biased photodiodes, however, the injected component of dark current can overshadow the detection signal in certain scenarios. In this case, additional engineering is required to design the device; the inclusion of metal-semiconductor interfaces with a band alignment so that electrons or holes are blocked thorough the contact is the usual strategy to reduce the dark current. Such layers receive the name of electron or hole blocking layers (EBLs or HBLs) and examples of which can be found in literature [25]. In Chapter 4 we implemented a device architecture with an ETL consisting of a 20 nm molybdenum trioxide (MoO_3) interlayer placed between the $CsPbBr_3$ PNCs thin film and the Au contact. Similar photodiode structures were also fabricated in our previous publications based on PbS QDs [26].

2.4.3 Figures of Merit of Photodetectors

Figures of merit of photodetectors are used to evaluate and quantitatively compare the performances of various photodetector technologies regardless of their architecture. The figure of merit that it is primarily used to benchmark the performance of a photodetector is the Responsivity. This parameter quantifies the device's electrical signal output per optical power input. This figure of merit characterizes the ratio of photocurrent to incident light power irradiating the active layer of the detector, and it is commonly expressed as follows [27]:

$$R = \frac{I(\lambda)}{P(\lambda)} = \frac{\eta(\lambda) e \lambda}{hc} \tag{2.20}$$

Here, $I(\lambda)$ is the photocurrent, $P(\lambda)$ is the incident optical power at wavelength λ, h the Planck's constant, c the speed of light, e is the electron charge and η the quantum efficiency. The responsivity is proportional to the quantum efficiency, which represents the probability for an incident photon of becoming a charge carrier and being extracted from the device. In the computation of quantum efficiency, the internal reflectance paths

inside the device, scattering and absorbance, are taken into the equation. In general, two types of quantum efficiencies are often considered: The External Quantum Efficiency (EQE), which is computed from the incoming flux of light; and the Internal Quantum Efficiency (IQE), which is computed from the ratio of photons that were already absorbed by the device, discarding the scattered or transmitted photons.

Another principal figure of merit is the noise equivalent power (NEP), a measure of the power sensitivity of the photodetector. The NEP is the minimum optical power that the detector can discern over noise and can be measured experimentally in a direct way (photocurrent as a function of incident power) and estimated from [26]:

$$NEP = \frac{i_n}{R} \tag{2.21}$$

Here *R* is the responsivity and i_n is the noise current. There are several sources of noise in photoconductors (shot noise, Johnson noise, generation–recombination noise, and *1/f* noise) that should be considered. Finally, there is the specific detectivity (*D**), reciprocal of the NEP, but normalized per square root of the photodetector area (*A*) and frequency bandwidth (*B*) [26].

$$D^* = \frac{\sqrt{AB}}{NEP} = \frac{\sqrt{ABR}}{i_n} \tag{2.22}$$

*D** is expressed cm $Hz^{1/2}$ W^{-1} (or Jones units). State-of-the-art values for this figure of merit in the context of this Thesis can be found in Chapter 4.

2.5 REFERENCES

1. Ekimov, A.I.; Efros, A.L.; Onushchenko, A.A. Quantum size effect in semiconductor microcrystals. *Solid State Commun.* **1985**, *56*, 921–924.
2. Kovalenko, M. V Opportunities and challenges for quantum dot photovoltaics. *Nat. Nanotechnol.* **2015**, *10*, 994–997.
3. Frecker, T.; Bailey, D.; Arzeta-Ferrer, X.; McBride, J.; Rosenthal, S.J. Review—Quantum Dots and Their Application in Lighting, Displays, and Biology. *ECS J. Solid State Sci. Technol.* **2015**, *5*, R3019–R3031.
4. Abargues, R.; Navarro, J.; Rodríguez-Cantó, P.J.; Maulu, A.; Sánchez-Royo, J.F.; Martínez-Pastor, J.P. Enhancing the photocatalytic properties of PbS QD solids: The ligand exchange approach. *Nanoscale* **2019**, *11*, 1978–1987.

5. Protesescu, L.; Yakunin, S.; Bodnarchuk, M.I.; Krieg, F.; Caputo, R.; Hendon, C.H.; Yang, R.X.; Walsh, A.; Kovalenko, M. V Nanocrystals of Cesium Lead Halide Perovskites (CsPbX3, X = Cl, Br, and I): Novel Optoelectronic Materials Showing Bright Emission with Wide Color Gamut. *Nano Lett.* **2015**, *15*, 3692–3696.
6. Madelung, O. *Semiconductors: Data Handbook*; Springer Berlin Heidelberg, 2004;
7. Butkus, J.; Vashishtha, P.; Chen, K.; Gallaher, J.K.; Prasad, S.K.K.; Metin, D.Z.; Laufersky, G.; Gaston, N.; Halpert, J.E.; Hodgkiss, J.M. The Evolution of Quantum Confinement in CsPbBr3 Perovskite Nanocrystals. *Chem. Mater.* **2017**, *29*, 3644–3652.
8. Even, J.; Pedesseau, L.; Katan, C. Understanding Quantum Confinement of Charge Carriers in Layered 2D Hybrid Perovskites. *ChemPhysChem* **2014**, *15*, 3733–3741.
9. Zhang, Y.; Wu, G.; Liu, F.; Ding, C.; Zou, Z.; Shen, Q. Photoexcited carrier dynamics in colloidal quantum dot solar cells: insights into individual quantum dots, quantum dot solid films and devices. *Chem. Soc. Rev.* **2020**, *49*, 49–84.
10. Utzat, H.; Sun, W.; Kaplan, A.E.K.; Krieg, F.; Ginterseder, M.; Spokoyny, B.; Klein, N.D.; Shulenberger, K.E.; Perkinson, C.F.; Kovalenko, M. V; et al. Coherent single-photon emission from colloidal lead halide perovskite quantum dots. *Science (80-.).* **2019**, *363*, 1068 LP – 1072.
11. Li, B.; Huang, H.; Zhang, G.; Yang, C.; Guo, W.; Chen, R.; Qin, C.; Gao, Y.; Biju, V.P.; Rogach, A.L.; et al. Excitons and Biexciton Dynamics in Single $CsPbBr_3$ Perovskite Quantum Dots. *J. Phys. Chem. Lett.* **2018**, *9*, 6934–6940.
12. Iveland, J.; Martinelli, L.; Peretti, J.; Speck, J.S.; Weisbuch, C. Direct Measurement of Auger Electrons Emitted from a Semiconductor Light-Emitting Diode under Electrical Injection: Identification of the Dominant Mechanism for Efficiency Droop. *Phys. Rev. Lett.* **2013**, *110*, 177406.
13. Srimath Kandada, A.R.; Neutzner, S.; D'Innocenzo, V.; Tassone, F.; Gandini, M.; Akkerman, Q.A.; Prato, M.; Manna, L.; Petrozza, A.; Lanzani, G. Nonlinear Carrier Interactions in Lead Halide Perovskites and the Role of Defects. *J. Am. Chem. Soc.* **2016**, *138*, 13604–13611.
14. Giansante, C.; Infante, I. Surface Traps in Colloidal Quantum Dots: A Combined Experimental and Theoretical Perspective. *J. Phys. Chem. Lett.* **2017**, *8*, 5209–5215.
15. Jeong, K.S.; Tang, J.; Liu, H.; Kim, J.; Schaefer, A.W.; Kemp, K.; Levina, L.; Wang, X.; Hoogland, S.; Debnath, R.; et al. Enhanced Mobility-Lifetime Products in PbS Colloidal Quantum Dot Photovoltaics. **2012**, 89–99.
16. Colbert, A.E.; Wu, W.; Janke, E.M.; Ma, F.; Ginger, D.S. Effects of Ligands on Charge Generation and Recombination in Hybrid Polymer/Quantum Dot Solar Cells. *J. Phys. Chem. C* **2015**, *119*, 24733–24739.
17. Konstantatos, G.; Sargent, E.H. Colloidal quantum dot photodetectors. *Infrared Phys. Technol.* **2011**, *54*, 278–282.
18. Okamoto, K. Beam propagation method. *Fundam. Opt. Waveguides* 2007, 329–397.
19. Evans, with C.A. Optical waveguides. *Quantum Wells, Wires Dots* 2016, 441–482.
20. Svelto, O.; Taccheo, S.; Svelto, C. Analysis of amplified spontaneous emission: some corrections to the Linford formula. *Opt. Commun.* **1998**, *149*, 277–282.
21. Saleh, A.A.M.; Jopson, R.M.; Evankow, J.D.; Aspell, J. Modeling of gain in erbium-doped fiber amplifiers. *IEEE Photonics Technol. Lett.* **1990**, *2*, 714–717.
22. Stolen, R.; Bjorkholm, J. Parametric amplification and frequency conversion in optical fibers. *IEEE J. Quantum Electron.* **1982**, *18*, 1062–1072.

23. Hansryd, J.; Andrekson, P.A.; Westlund, M.; Li, J.; Hedekvist, P.-. Fiber-based optical parametric amplifiers and their applications. *IEEE J. Sel. Top. Quantum Electron.* **2002**, *8*, 506–520.
24. Maulu, A.; Navarro-Arenas, J.; Rodríguez-Cantó, P.; Sánchez-Royo, J.; Abargues, R.; Suárez, I.; Martínez-Pastor, J. Charge Transport in Trap-Sensitized Infrared PbS Quantum-Dot-Based Photoconductors: Pros and Cons. *Nanomaterials* **2018**, *8*, 677.
25. Kung, P.-K.; Li, M.-H.; Lin, P.-Y.; Chiang, Y.-H.; Chan, C.-R.; Guo, T.-F.; Chen, P. A Review of Inorganic Hole Transport Materials for Perovskite Solar Cells. *Adv. Mater. Interfaces* **2018**, *5*, 1800882.
26. A. Maulu, P.J. Rodríguez-Cantó, J. Navarro-Arenas, R. Abargues, J. F. Sánchez-Royo, Raúl García-Calzada, and Juan P. Martínez Pastor. Strongly-coupled PbS QD solids by Doctor Blading for IR Photodetection. RSC Advances. **2016**, 6, 80201–80212.
27. Wang, H.; Kim, D.H. Perovskite-based photodetectors: materials and devices. *Chem. Soc. Rev.* **2017**, *46*, 5204–5236.

3 EXPERIMENTAL METHODS

This chapter describes the experimental methods used during this Ph.D. Thesis, including the fabrication and characterization techniques. The first part of this chapter summarizes the technologies chosen to the implement the optoelectronic devices developed these years: photodetectors, field-effect transistors, active (amplifying) waveguides and laser cavities, among others, are made of nano-inks containing nanocrystals. In addition, a general overview of the chemical synthesis of quantum dots and perovskite nanocrystals is also included in this part. The second section explains the experimental setups built for the characterization of the devices and materials. These setups allowed the extraction of relevant physical parameters from the materials (carrier mobility, absorption cross-section, photoluminescence lifetime, etc.) and to evaluate performance of a specific device.

3.1 FABRICATION METHODS

3.1.1 SYNTHESIS OF NANOCRYSTALS AND POST-PROCESSING TREATMENTS

Lead halide perovskite nanocrystals (PNCs) were synthetized following the method developed by *Protesescu et al* [1]. This procedure is based on the hot-injection method commonly used to prepare NCs of II–VI, IV–VI, and III–V semiconductor compounds [2]. Here, colloidal $CsPbX_3$ (X = Cl, Br, I) nanocubes with a PLQY (photoluminescence quantum yield) close to 90% at room temperature with a wide color gamut were fabricated to be used as active materials [1]. A similar procedure was also adopted to synthesize of PbS NCs with the aim of implementing photodetectors [3–5].

In brief, the hot injection method (Figure 3.1) consists in the injection of chalcogenide precursors (S, Se, bistrimethylsilyl sulphide, n-dodecanethiol, etc.), metal precursors (metal halides, in the case of PNCs), and specific ligands of high coordinating power (oleylamine, oleic acid, trioctylphosphine, etc.) into another hot coordinating solution with metal-organic precursors in a high-boiling solvent (octadecene). Flasks are kept under an inert N_2 atmosphere and at relatively low temperature, below 200 - 300 °C.

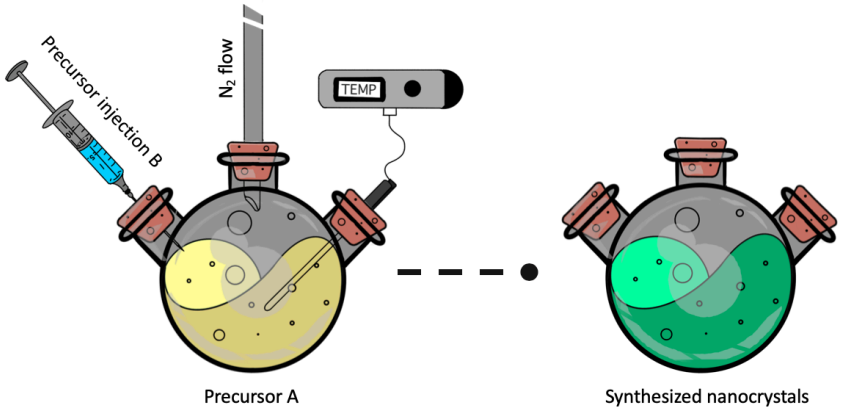

Figure 3.1. Scheme of the hot-injection method for the synthesis of nanocrystals.

Once the precursors are injected, the chemical reaction starts and the first monomer molecules are generated. According to the classical LaMer model [6], the concentration of monomers will super-saturate eventually, leading to the formation of nucleation seeds. The formed nuclei will continue increasing in number while the population of available monomers constantly decreases until a critical point is reached. At this point, there is almost no nucleation occurring due to the low concentration of monomers. Once the nuclei are formed, they will act as the seed for crystal growth; larger nanocrystals will be formed by coalescence of existing ones as described by a process known as Ostwald ripening. Because nucleation of seeds and crystalline growth processes are "coupled", both stages play a role in deciding the final average size and the size distribution of the NCs. There are many strategies to control the growth process and the size distribution of the nanocrystals. The most important parameters are the reaction temperature, the reaction time, the concentration of precursors and the concentration of coordinating solvents.

During the final stages of the NCs synthesis, the resulting NCs are coated with a layer of surfactant molecules (ligands) that provides colloidal stability and passivate surficial defects. However, the as-synthesized NC solution also contain the high-boiling solvent, reaction byproducts, unreacted precursors and ligands. Thus, the crude solution must be purified with a polar/non polar solvent strategy in order to remove the chemical waste, improving the final size distribution and overall rheological properties of the final solution. Typically, the high-boiling solvent is replaced with low molecular weight solvents, such as n-hexane or toluene. The final colloidal solution of NCs, which is ready for film casting, is usually denoted as nano-ink.

In this Thesis, the specific details about the synthesis (reactive, reaction times, etc.) of particular NCs used in each study will be described in the corresponding chapters.

3.1.2 Fabrication of Solid-State Nanocrystal Films

A major concern in the fabrication of efficient optoelectronic devices based on semiconductor nano-inks is the growth of high quality close-packed films made of individual nanocrystals. Such films must preserve the optoelectronic properties shown by the colloidal NCs while in solution. The device operation strongly depends on the charge transport in the case of photodetectors, and in the emission efficiency in the case of light emitting devices. Therefore, parameters such as homogeneous deposition or interparticle distance within the NC ensemble in the film must be optimized to obtain close-packed solids with high mobility, sometimes allowing Bloch-like electronic transport of carriers [7]. To optimize the generation of light, additional treatment can be practiced to passivate the films (capping of defects present at the NC surface), successfully reducing the rate of non-radiative recombination and increasing the overall PLQY [8].

So far, layer-by-layer (LBL) techniques based on solution processing coating methods (dip-coating, spin-coating, spray-coating, etc.) are the state-of-the-art standard techniques for the experimental assembly of devices, such as photodiodes and FETs. This procedure consists of the application of several coating steps on a specific substrate. Consequently, the layer is sequentially grown, allowing the administration of post-treatments (such as ligand-exchange) in-between each layer deposition or at the end of the LBL process. Multistep film growth offers the possibility to fabricate pinhole-free films with controlled thicknesses, up to hundreds of nanometers. Typically, LBL techniques produce close-packed dense films with relatively high conductivity, as compared to single-step fabrication techniques.

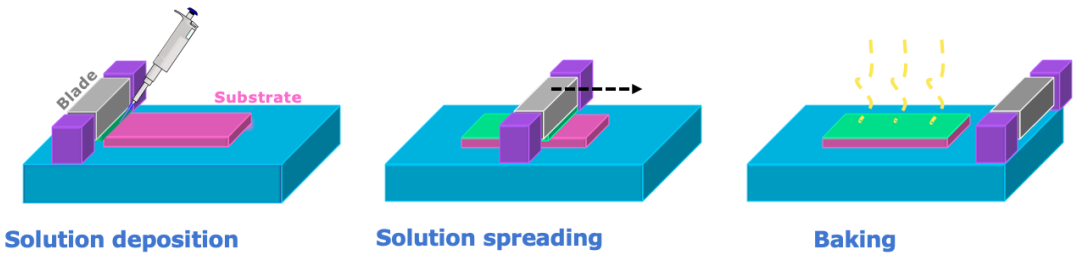

Figure 3.2. Schematic illustration of the doctor blading deposition technique.

LBL is also compatible with the roll-to-roll printing process, enabling low-cost fabrication of large-area optoelectronics, via the Doctor Blade (or tape casting) technique. The term owes its name to the former *doctor* blade mechanical piece, key in the 19th-century printing process known as rotogravure [9].

Doctor blading allows precise thickness control over large areas with minimum material. We have chosen to apply this technique for the fabrication of the films of this thesis because it was proven useful in previous publications dealing with colloidal QD thin layer fabrications [4,5], showing successful results under similar conditions. The processing with a low-concentration, clean and filtered nanocrystal solution benefits to the smoothness of the fabricated layers, producing a film with almost specular reflection.

The three steps of the doctor blading application are summarized in Figure 3.2. Firstly, the ink is loaded in the air gap between the substrate and the blade. The surface tension of the nanoink forms a meniscus between the blade and the wet film on the trailing edge of the blade. Then, the Doctor blade coating machine mechanically spreads the ink uniformly over the substrate. At this point, the blade velocity determines the amount of ink that leaks from the moving meniscus and, depending on the nano-ink concentration, the thickness of the deposited layer. This cycle is repeated until the desired layer thickness is reached. Although the inks are usually formulated with non-polar solvents having low boiling temperatures (hexane, octane, toluene, chloroform) to allow fast evaporation, a baking process is usually carried out between each deposition cycle in order to remove the residual solvent.

Layer-by-layer technique can also include more sophisticated procedures between each deposition to improve the quality of the layer. For example, a polar (such as methanol or ethanol) anti-solvent can be added to the initial ink in low concentrations (<5%) to force nanocrystals to precipitate out of the solution. Then, the nanoparticles may be arranged in ordered self-assembled solid-state materials [4]. In addition, the excess of ligands that surround the nanocrystals can be removed by using the Doctor blade applicator loaded with a polar solvent. In this way, the interparticle distance is reduced and the coupling between nanocrystals is drastically improved [10].

Once the desired thickness is reached, several post-processing treatments can be applied to further improve the performance of the semiconductor film. The solid-state nanocrystal films that are prepared in this Ph. D. Thesis usually undergo a ligand exchange procedure. For example, fabrication of high-quality thin films of perovskite NCs for photodetection applications relies on their efficient charge transport properties and, since the typically used highly insulating organic capping ligands, such as oleylamine and oleic acid, severely affects the performance of devices, they must be replaced. This ligand-exchange process is often carried out after post-deposition of NCs films in the presence of suitable solvents. The films are submerged in a polar solution containing a certain amount of the replacement ligand or spin-coated on top of the film [11]. In

addition, a ligand exchange process that follows a similar procedure as the one described above, the LBL method, can be carried out at the end of each coating deposition. This is particularly helpful in dense-packed and relatively thick layers in which full penetration of the exchange solution was not completely ensured [12].

Regardless of the ligand exchange process, the deposition of perovskite NCs thin films offers multiple advantages in terms of the post-processing treatments available. For example, post-synthetic halide exchange and cation-exchange have been performed in order to achieve a notable efficiency enhancement of photovoltaic devices [13].

Taking into account the aforementioned considerations, the layers of NCs in the present Ph. D. were deposited with the following procedure. Firstly, the substrates were cleaned by rinsing in isopropanol and water and dried under N_2 flow. Depending on the particular device, the substrate was covered by the nanoink or an additional polymer. For example, a thin PEDOT:PSS film was spin-coated onto an ITO coated glass substrate to fabricate photodiodes, or a PMMA film was spin-coated on a solid substrate to fabricate planar waveguides. In all cases, deposition of NCs was always done using a commercial Doctor Blade applicator (Elcometer 4340). The baking times and temperature ranged from 1 minute at 80 °C to 5 minutes at 110 °C, depending on the material. More details relative to the specifics of the material processing can be found in the respective chapters of this Thesis.

3.1.3 PATTERNING

3.1.3.A CONTACT PATTERNING

The thermal evaporation Physical Vapor Deposition (PVD) machine illustrated in in Figure 3.3 was used to deposited contact electrodes or thin metallic mirrors (< 100 nm).

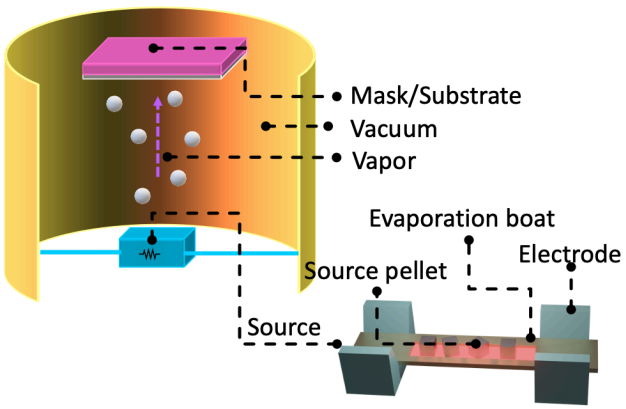

Figure 3.3. Scheme of the Physical Vapor Deposition technique.

PVD is a cost-effective way to deposit pure metals (Ag, Au, Pt), metal alloys and some metal oxides, as thin films ranged between 2 nm to 1000 nm on different substrates (glass, glass/ITO, Si/SiO_2, etc.). In addition, the deposited film can be patterned with a specific geometry by including a shadow mask between the vapor source and the substrate.

The metallization occurs inside a high vacuum chamber (10^{-6} mbar or lower, achieved by a rotary and turbomolecular pumps). The source materials are small pellets that sublimate to atoms or atom groups (molecule fragments, clusters) after the appropriate heat transfer. The evaporation chamber consists of a curved-shape piece of tungsten that drastically increases its temperature up to a few thousands of Kelvin degrees (as a reference, the boiling point of silver is at 962 °C) in order to allow the sublimation of the source. Since tungsten has the lowest coefficient of thermal expansion of any pure metal and the highest boiling point, it proves to be an ideal evaporation material. To achieve a sublimation temperature, the tungsten crucible is short-circuited with a high power (up to 250 A at 6 V) current supply. When the temperature is high enough, the tungsten boat emits blooming-white black-body radiation. Then, the source vapor is diffused in the vacuum chamber and condenses on the target substrate. The boat profile is designed to concentrate the heat towards the center, where the evaporating matter gathers, increasing the homogeneity of deposition on large substrates.

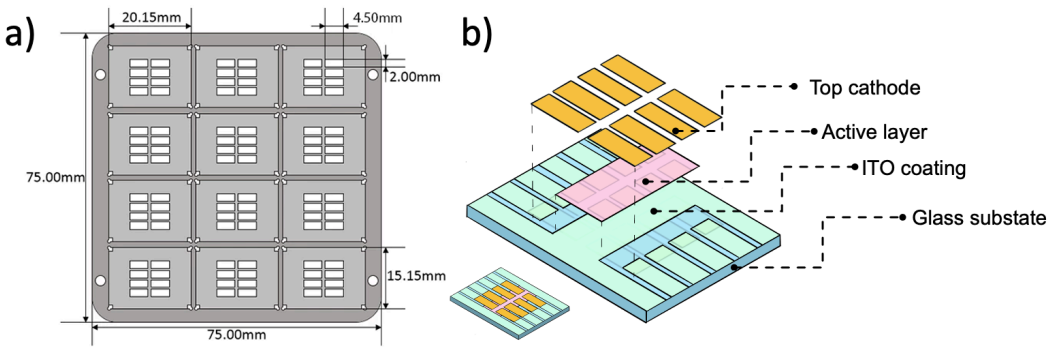

Figure 3.4. a) Mask used for contact patterning on the right. b) Device assembly with the shadow mask

Evaporated films can be easily patterned by placing a mask between the target (substrate) and the source. In the case of photovoltaic devices built for this Thesis, a multi-electrode mask (Figure 3.4a) compatible with the prepatterned ITO substrate purchased from Ossila (Sheffield, UK), shown in Figure 3.4b, is chosen. The device

assembly diagram after using the shadow mask is shown in Figure 3.4b. The active layer and other interlayers are deposited with the techniques described in Section 3.1.2 on top of the ITO anode. The top cathode is evaporated right above it, conforming the final structure of the device. Typical sources for the evaporation process were high purity materials such as silver, gold, molybdenum trioxide, aluminum and chromium.

3.1.3.B UV-PHOTOLITHOGRAPHY AND LIFT-OFF PROCESSING

UV-photolithography is a technique commonly used in Microelectronics and Photonics technology to define patterns down to 1 μm^2 on a resist previously deposited on a flat substrate. Here, a commercial SU-8 resist is chosen to define the photolithographic patterns. This negative photoresist allows UV patterning down to 1 μm with the following procedure [14]. Firstly, a layer of photoresist is spin-coated on top of the substrate and baked at 65 and 95 °C for two minutes (Figure 3.5a). Then, the photomask is aligned on the sample with aid of the mask aligner SUSS MicroTec MJB4, and the sample is exposed to UV illumination for 5 seconds (Figure 3.5b). Finally, the sample is heated again at 65 °C and 95 °C for two minutes and submerged in the developer solution Since SU-8 is a negative photoresist, exposed area become cross-linked, while the unexposed can be removed by using the appropriate solvent. After the development step, the substrate is covered by ridge SU-8 patterns (Figure 3.5c). These patterns can be used as a final device, for example in the ridge waveguides proposed elsewhere [15], or can be used as an intermediate step for a more complicated structure.

Once the SU-8 lithography is performed on the appropriate substrate, the lift off consists of the deposition of a metal film with the PVD system described above and the immersion of the resulting metalized sample in the development solution (Figure 3.5d - 3.5f). In these conditions, the developer removes the SU-8 with the metal deposited on the top, leaving the metal in the regions of the sample where there was not resist. Here, it is necessary to use negative patterns and deposit a SU-8 film three times thicker than the desired thickness for the metal. A photography of the actual results of this technique can be found in Figure 3.6, in which it is shown that the mask blueprint and the transferred interdigitated gold pads are reproduced with micrometric precision. It is worth mentioning that some parameters must be optimized to obtain the highest resolution in the final structure. In particular, it is necessary to control precisely the exposure time: if the exposure dose is too low the resolution can be lost, but if it is too high the patterns can be distorted.

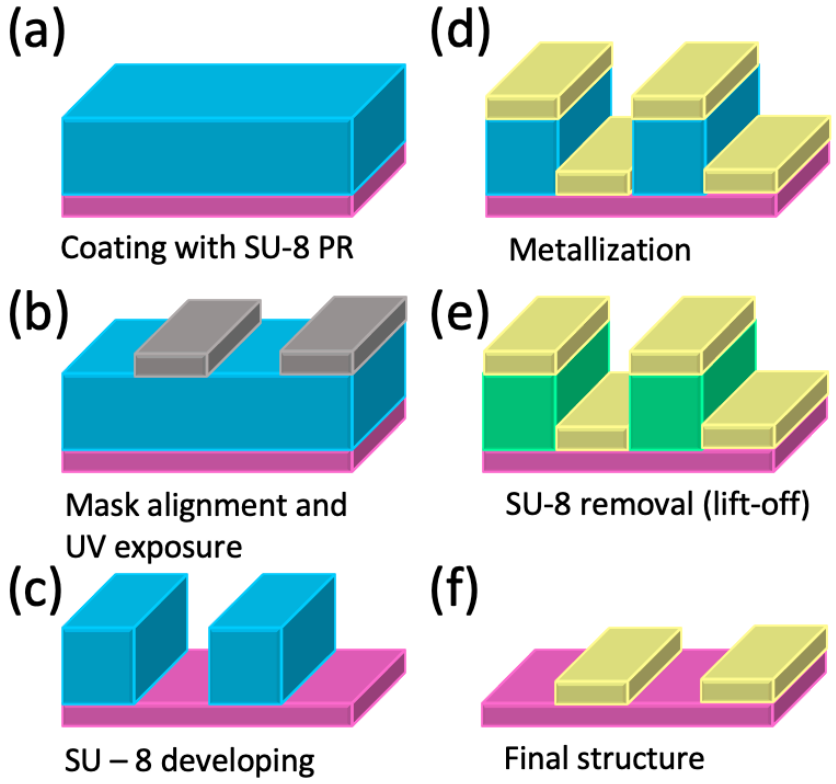

Figure 3.5. Schematic illustration of the SU-8 negative photoresist lift-off procedure.

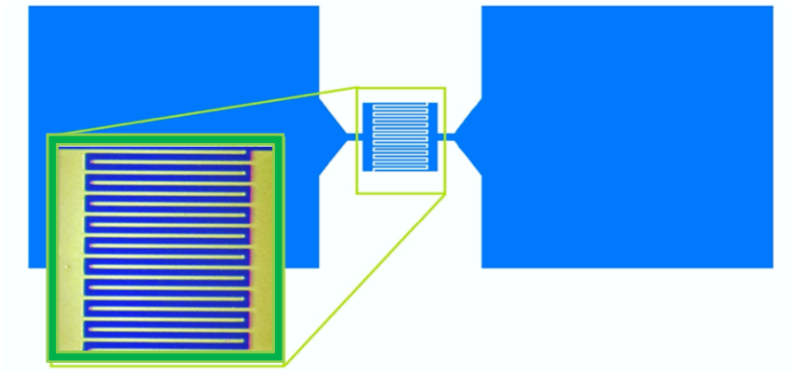

Figure 3.6. Successful result of the technique with a structure of 20 µm interdigitated gold pads and piece of the photomask in blue. The complete mask contains this structure replicated multiple times with different channel lengths (2, 5, 10 and 20 µm).

3.2 CHARACTERIZATION METHODS

In this section, the experimental setups used in the characterization of the materials and devices are properly detailed. These set-ups include not only commercial systems, but also home-made set-ups built in our labs, eventually automated by using Labview (National Instruments).

3.2.1 ELECTRICAL CHARACTERIZATION

3.2.1.A BASIC ELECTRICAL CHARACTERIZATION

The characterization of the Current-Voltage response was carried out by means of a Keithley's Series 2400 Source Measure Unit (SMU). Samples were studied under dark conditions and under illumination with an AM1.5G solar spectra simulator source or under continuous wave (CW) lasers with wavelengths ranged between 405 and 550 nm. While a large portion of the devices were prepared in custom-made substrates and testing platform, the majority of the test substrates were purchased from Ossila. These pre-patterned substrates, like the 8 Pixel Photovoltaic ITO 211/S213 units, are specially prepared to work with the Ossila's Solar Cell I-V Test System, designed to ease the experimental process of electrical characterization. In the setup shown in Figure 3.7, the SMU is wired to the source/drain BNC port of the test board. This technology allowed to increase the available volume of investigation data. Basic electrical characterization of the current-voltage curve of Schottky heterojunctions and photoconductors can be found in Chapter 4 of this Thesis (Figures 4.4 and 4.5 respectively).

The same set-up was used to measure the current-gate voltage curve (transfer characteristics) of FET devices. For this purpose, prepatterned FET test chips were loaded in a compatible high-density FET test board (also from Ossila), designed to reduce leakage current, external noise, and stray capacitance. Drain-source current was measured at 1-V bias using the SMU, and the gate bias was applied using a DC power source connected to the BNC connector board. Measured data was used to extract the carrier mobility of the semiconductor of the FETs. Figure 4.6 shows an example of the application of this setup in FET devices (Chapter 4 of this Ph. D. Thesis).

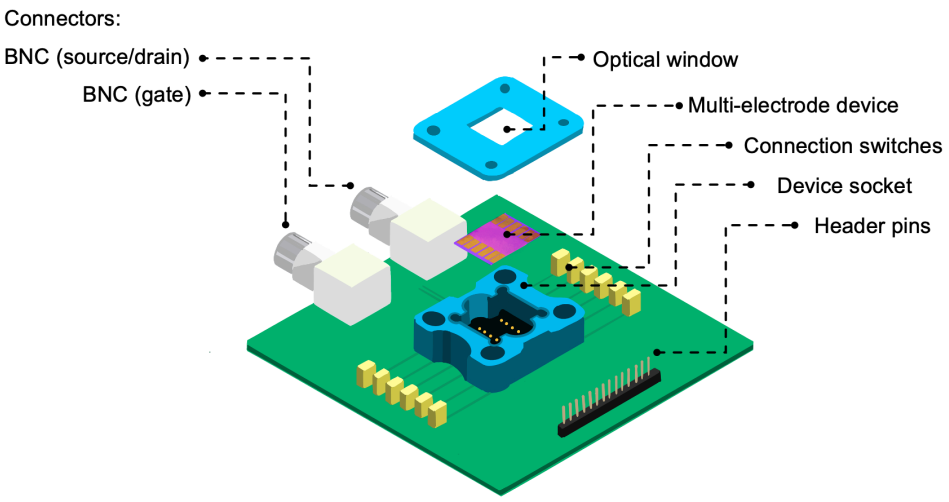

Figure 3.7. Schematics of the basic electrical characterization setup for multi-electrode devices.

Capacitance-Voltage and Capacitance–Frequency responses were obtained by using a 1 MHz LCR Meter QuadTech model 1920. These measurements were helpful to parametrize some properties of the Schottky photodetectors, such as the acceptor concentration, the built in potential and the width of the depletion region, provided the well-known relation for the depletion region formed in the semiconductor (abrupt doping approximation) [16].

3.2.1.B Characterization of Photodetector's Figures of Merit

The electro-optical properties of the photodetectors and photoconductors were measured by a homemade setup based on a halogen lamp (20 W) focused into the input slit of a DeltaNu DNS-300 monochromator with 600 grooves per mm grating. Light at the output slit of the monochromator was modulated up to 1 kHz by a mechanical chopper and focused onto the fabricated photodetector with a 10x objective. The electrical signal of the photodetector was synchronously measured with the modulation by means of a 100 kHz lock-in amplifier (SR830, Stanford Research Systems). An optical filter was used to suppress the second and third order unwanted diffraction coming out of the monochromator. A scheme of this setup is illustrated in Figure 3.8.

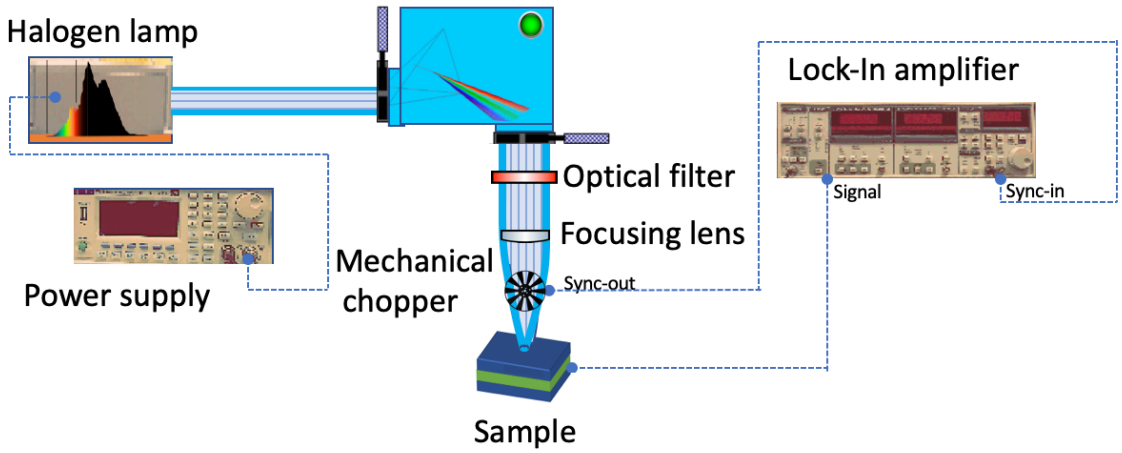

Figure 3.8. Scheme of the experimental setup to characterize photodetectors.

This setup is based on a synchronous detection carried out with a lock-in amplifier. This versatile instrument allows the extraction of signal externally modulated, which results useful to increase the signal to noise ratio, to develop pump and probe measurements, among other experiments. For example, the measurements related to photon recycling effect in PNC waveguides was performed with the 200 MHz lock-in

amplifier SR844, also from Stanford Research Systems, as the basis for a fluorescence spectroscopy technique in the frequency domain.

In this experimental technique, the photodetector is illuminated with a modulated source. This can be achieved, for example, with a mechanical chopper. A TTL synchronizes the Lock-In and the choppers blade rotation to the same reference phase. The Lock-in amplifier allows to extract from the sampled device the amplitude and the phase difference from the device's signal with respect to the modulated source. This technique is especially useful when measuring small amplitude signals in a noisy background.

This set-up provides the figures of merit of the photodiode devices. The Responsivity (R) was extrapolated by comparing the signals detected in the devices under test with that measured by a calibrated photodiode. In particular, Si (Thorlabs) and a Ge (Newport DETL-GE-T-C) photodiodes were used for the characterization of photodiodes containing perovskite NCs and those containing PbS QDs, respectively. Other figures of merit are the noise equivalent power (NEP) and detectivity (D^*). The NEP is defined as the level of incident light power that generates a photocurrent equal to the noise current. The NEP value can be graphically extrapolated to the noise-level baseline from the measured photocurrent - excitation power curve at a particular wavelength (for this one can use a laser or the exit of a monochromator with a white light source coupled at its entry). The value of D^* is then obtained as a function of R and the NEP.

3.2.2 Optical Characterization

3.2.2.A Reflectivity/Transmission and Absorbance

A commercial reflectometer Nanocalc-2000 from Mikropak/Ocean (Figure 3.9) was employed to acquire the reflectivity (R) and transmission (T) spectra of thin films. The UV-visible light of the source lamp (Deuterium + Halogen) illuminates the surface of the sample while a spectrograph records the transmitted or reflected light. Then, transmittance or reflectance are extrapolated from the sample by comparison with the measurements carried out on a reference substrate. This equipment also allowed us to calculate the absorbance (A) by the well-known formula ($A = -log_{10}[T]$).

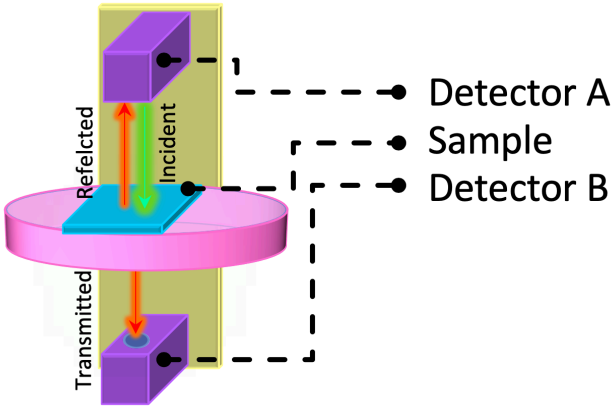

Figure 3.9. Experimental setup for reflectivity and transmittance characterization

Another experimental device used to characterize the absorbance spectra of thin films or colloidal solutions (laying inside a quartz cuvette prepared for UV-visible spectroscopy) is the commercial spectrophotometer UV-2501PC from Shimadzu. This setup equips a UV-visible Xenon lamp and a monochromator operating in the range of 300-900 nm with a resolution of 0.5 nm.

3.2.2.B BACKSCATTERED PHOTOLUMINESCENCE

Photoluminescence (PL) is an optical process from which a material spontaneously emits photons after the absorption of light at a shorter wavelength. Here, PL is measured under backscattering geometry in order to avoid the influence of reabsorption effects and to minimize the flow of the excitation power into the detector system.

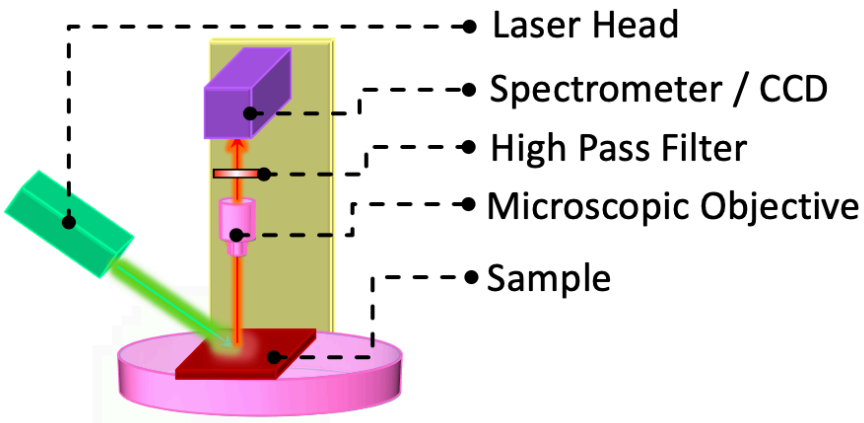

Figure 3.10. Schematic representation of the setup used to measure the backscattered photoluminescence of thin films of NCs.

For this purpose, samples are loaded in a motorized XYZ stage and were illuminated at 45 degrees by a continuous wave (CW) 450 nm laser, as illustrated in Figure 3.10. The PL signal is collected from the surface with a 10x microscope objective and coupled to a multimode fiber wired to a spectrometer (HR4000 Ocean Optics). A high pass filter suppresses the scattered portion of the excitation laser radiation.

3.2.2.C Time Resolved Photoluminescence (TRPL)

Time resolved PL (TRPL) measurements were performed to characterize the PL transients produced in a material after pulsed laser excitation. These measurements require the simultaneous acquisition of the laser pulse and the emitted signal, in order to synchronize the pulsed laser with the emission of PL. For this purpose, the laser pulse is split in two branches, one for the trigger and the other for the sample. A high pass filter is placed before the photodetector or monochromator to avoid the influence of the excitation source.

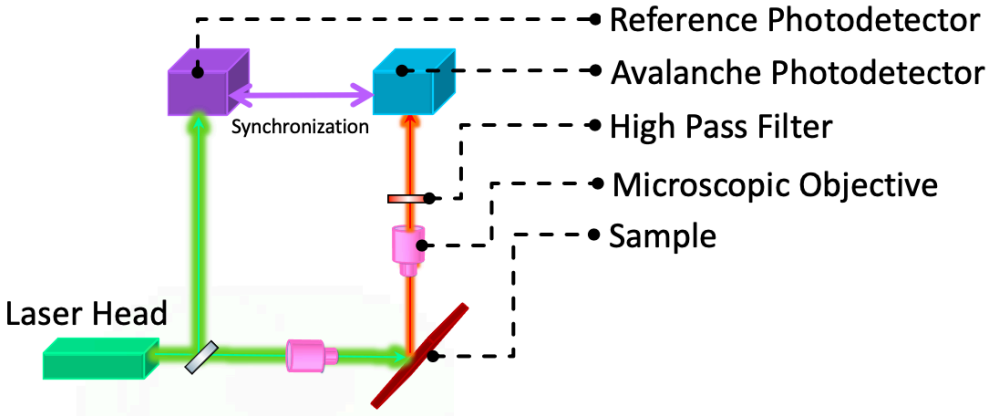

Figure 3.11. Scheme of the TRPL technique in backscattering configuration. The excitation laser pulse is divided in two branches, one of which acts as a gate for the detection of fluorescence light.

The nanosecond time-resolved PL was carried out by using a Q-switched Nd:YAG (1 kHz, 1 ns) laser doubled or tripled at 532 and 355 nm (CRYLAS 6FTSS355-Q4-S). The 355 nm line was used to excite the bromide PNC species while the 532 line was used with the iodide and the iodide-bromide mixed species. The PL was analyzed with a Hamamatsu C5658-3769 avalanche photodetector connected to a BOXCAR DPCS-150 electronics from Becker and Hickl GmbH.

PL under femtosecond pulsed excitation was carried out by using a mode-locked Ti:sapphire laser at a working wavelength of 810 nm, doubled to 405 nm by means of a non-linear BBO crystal. In this case, time-resolved PL measurements was carried out with the Ti:sapphire laser in pulsed mode operation (pulse width 200 fs and 76 MHz of

repetition rate) at the same wavelength. In this case, the emitted light by PNCs is dispersed by a 300 mm monochromator (Acton Research 300i) and collected by means of a Si avalanche photodiode, which is connected to a time-correlated single-photon counting electronic card (Edinburgh Instruments).

3.2.2.D WAVEGUIDES

Waveguides were characterized by end-fire coupling an excitation/probe beam at the input edge of the sample (Figure 3.12a) with the aid of a 40x objective microscope objective with infinite correction and 0.66 numerical aperture. Light at the output edge of the waveguide was collected with another microscope objective (a 20x with 0.35 of numerical aperture) and focused to a multimode optical fiber plugged into an HR4000 Ocean Optics spectrometer. In the case of PNCs, the excitation sources were: a Nd:YAG (1 kHz, 1 ns) laser doubled or tripled at 532 and 355 nm (CRYLAS 6FTSS355-Q4-S) and a 450 nm (XS-450, Changchun New Industries Optoelectronics Tech. Co., Ltd.)

Perpendicular excitation was also carried out for waveguides containing luminescent materials, such as perovskite NCs. The set-up consists of focusing the excitation beam on a straight line on the surface of the sample with the aid of a cylindrical lens. This particular excitation geometry receives the name of the Variable Stripe Length (VSL) method and it is widely used in the characterization of active quantum-dot/quantum-well and perovskite NC based waveguides [17–19]. VSL enables the possibility to accurately characterize the optical gain and the losses of a planar waveguide. Optical gain is characterized by measuring the PL collected at the output edge of the sample as a function of the length of the stripe, while losses are estimated with the dependence of the outcoupled PL as a function of the distance between the stripe and the edge of the sample, respectively.

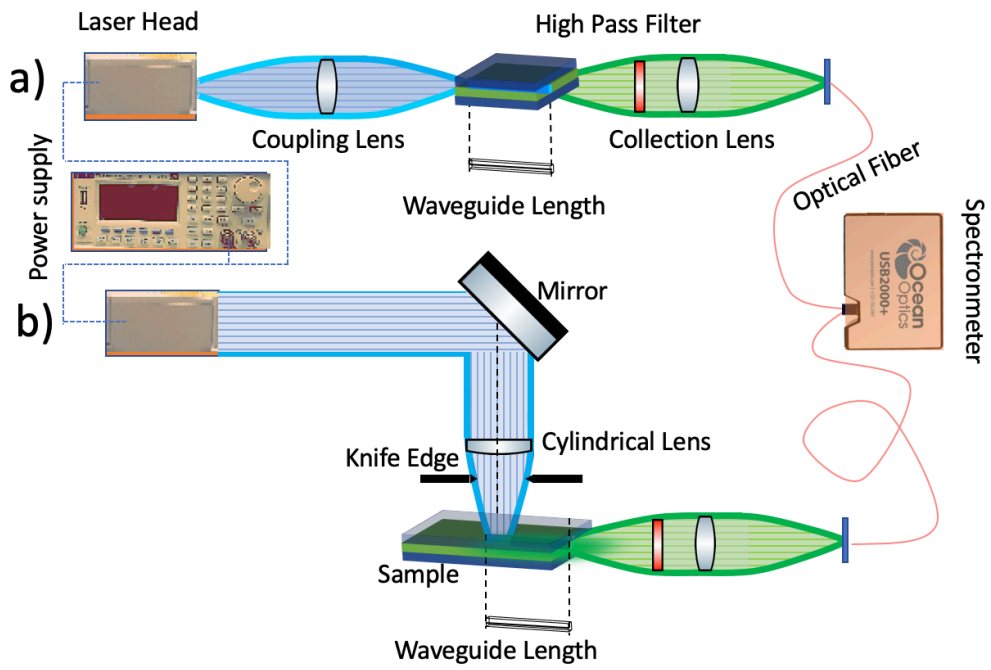

Figure 3.12. a) End-fire coupling setup for optical characterization. b) Setup for the Variable Stripe Length method for optical gain characterization in waveguides.

The variable stripe length method setup is illustrated in Figure 3.12b. The pump beam at 450 nm was focused on an 800x200 μm straight line on the top of the sample with the aid of a cylindrical lens and a slit to cut the borders of the Gaussian tail. Then, waveguided PL is collected from the edge of the waveguide by a 20x microscope objective, focusing the light to the appropriate photodetector after removing the residual pump light with a long pass filter. The laser was mounted on a Z translator in order to study the PL spectra as a function of the distance between the stripe and the edge of the sample. The waveguide is end-fire coupled to a spectrograph (USB-650 Red Tide, Ocean Optics). This technique to easily calculate the gain/loss profile of the waveguide.

3.2.2.E Fiber Optics

Hollow-Core Anti-Resonant Fibers (HC-ARF) are a special class of optical fibers where the cladding is composed by an array of hollow glass tubes surrounding a hollow-core. Hollow-core fibers can also serve as hosts, working as a lab-on-a-fiber for the study of optical properties of materials. In this thesis we purpose the filling of the HC-ARF fibers with $CsPbBr_3$ PNCs as potential all-fiber active optical microdevices. The final device produced small-signal amplification [20].

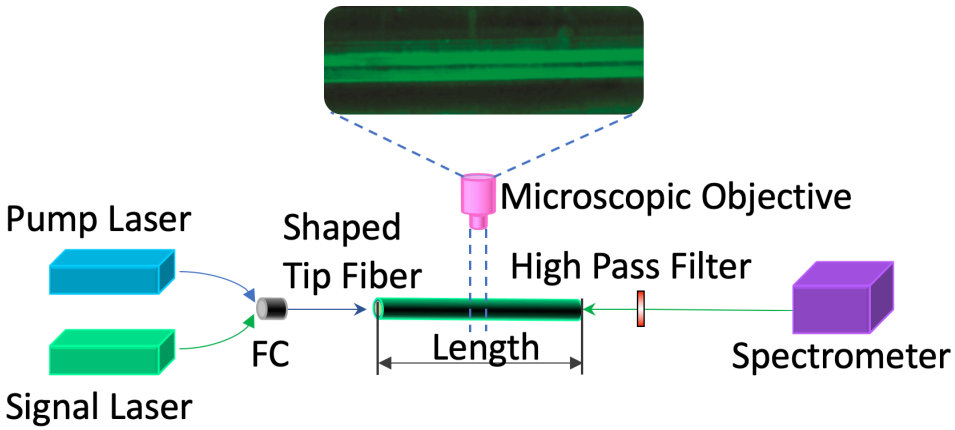

Figure 3.13. Experimental setup for optical gain measurements, consisting of two tip-shaped fibers coupled at both ends of the HC-ARF facets. CW-pump (405 nm) and probe signal (515 nm) beams are combined inside the first fiber by a fused fiber coupler (FC), whereas the second fiber collects light at the output of the HC-ARF into a spectrometer after a 450 nm long-pass filter.

In order to characterize the amplification capabilities of the PNC-doped HC-ARFs, the experimental setup shown in Figure 3.13 was specially built for this task. It consists of two lensed fibers positioned at the input and output ends of the HC-ARF by computer-controlled XYZ piezo translators with micrometric precision. In addition, both tipped fiber couplers are placed on a rotating head with two additional degrees of freedom. A focused fiber coupler (FC) launches both pump (405 nm) and probe signal (515 nm) beams inside the input fiber, while the other fiber tip is coupled to the output end and connected to a spectrometer (Ocean Optics 2000) through a 450 nm long-pass (LP) filter to cut the pump light in the spectrometer. Power of the pump beam is externally controlled up to 3 μW, while probe signal intensity is reduced down to 1 nW.

3.2.2.F Fluorescence Spectroscopy in the Frequency-Domain

In the frequency-domain fluorescence spectroscopy (FD-spectroscopy) technique, the sample is excited by a modulated source of light. The fluorescence emitted by the sample has a similar time-dependent waveform. Since a succession of several events of photon emission and reabsorption by the sample occurs along the propagation path, the emission of a photon is delayed relative to the modulated reference signal. The higher the modulation frequency, the higher the sample fails to precisely match the excitation (due to its finite temporal response), thus limiting the range of frequencies that the material can tolerate. Under favorable experimental conditions, the resulting output signal will be delayed by a certain phase from the source. The amplitude of the outcoming signal will also change by the frequency-modulated signal due to the phase

difference [21]. Thus, from both the amplitude modulation (*M*) and the relative phase difference (ϕ), the time decay associated with the PL signal generated by the sample can be determined.

To extract the relative phase delay from the fluorescence signals, a 200 MHz Lock-In Amplifier (SR844 from Stanford Research Systems) is used. The reference modulation signal is taken as TTL from the function generator used to trigger the modulated laser used in these experiments.

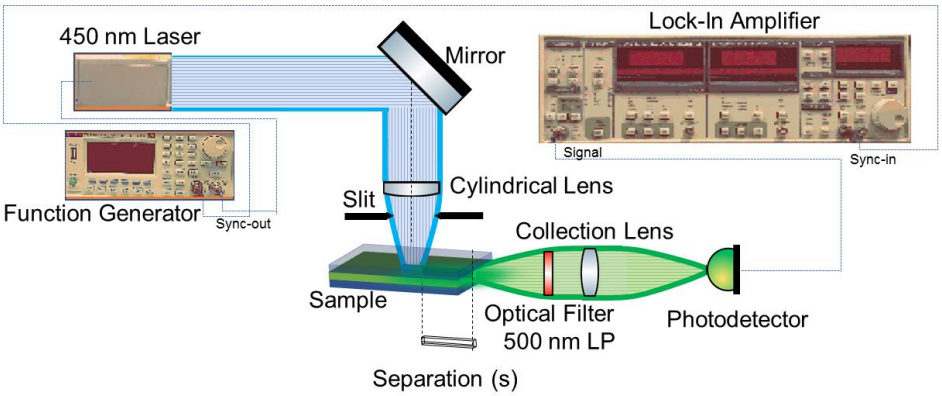

Figure 3.14. Experimental setup for optical photon recycling measurements, consisting a frequency-modulated 450 nm laser head focused vertically to the waveguide sample. An avalanched photodetector measures the phase and amplitude of the photoluminescence generated by the PNPs in the waveguide. The signal is processed with a Lock-In amplifier clocked with the same TTL used to drive the laser. The PL and absorbance of the PNCs is shown in the bottom left corner.

The implementation of this technique in our laboratory consisted of a 50 mW 450 nm laser head (MDL-XS-450, Changchun New Industries Optoelectronics Tech. Co., Ltd.) driven by means of modulated sinusoidal voltage whose frequency is varied in the range from 25 kHz to 3 MHz. A function generation is producing this laser driving voltage as well as the TTL signal used as a reference to clock the SR844 Lock-In Amplifier to the phase of the laser head. A cylindrical lens is used to change the profile of laser beam into a thin line. The Gaussian tail of the conformed beam is suppressed with an adjustable linear diaphragm, defining a rough-shaped 500 x 100 micrometers line. The beam-focusing optics are mounted on a XYZ head that allows to position the spot on any point of the surface of the sample. Once the laser is coupled to the sample, the waveguided PL produced by the sandwiched PNCs is collected at the edge of the sample with a 20x microscopic objective focused at the input face of an optical fiber. In order to cut the residual signal left by the 450 nm pumping laser, a 500 nm cutoff long pass (LP) filter is placed just after the sample. Then, the collection optics launches the signal of the

waveguide into an optical fiber coupled to a Si Avalanche Photodetector (APD120A/M, Thorlabs). Phase and amplitude of the collected signal is finally analyzed by a photodetector connected to a Lock-In Amplifier. Also, the optical fiber can be connected to a spectrograph (USB-650 Red Tide, Ocean Optics) to measure the Stokes Shift.

3.3 STRUCTURAL CHARACTERIZATION

Morphological characterization was performed on NC and thin films in order to obtain the size and size dispersion of the NCs, crystallinity, the identification of the main crystallographic planes, and the thickness of a film.

3.3.1 ELECTRON MICROSCOPY

The classical optics theory defines a limit to the maximum resolution obtainable by any optical microscopy system. This limit, sometimes called the diffraction barrier ($\lambda/2n$), restricts the ability of optical instruments to distinguish between two objects separated by a lateral distance less than hundreds of nanometers. In this context, electron microscopy (EM) allows the characterization of a given material with, ideally, the characteristic De Broglie wavelength of an electron. Most common types of electron microscopes are transmission (TEM) and scanning (SEM) systems. While there are many operational differences between this equipment pieces, the most preeminent one is the spatial resolution that they can achieve. In practice, commercial SEM equipment offers nanometric resolution; TEM can achieve even near atomic resolution [22,23]. On the downside, TEM only allows the loading of thin samples (<150 nm) an requires specific preparations.

In this thesis, the morphology and size distribution of the NCs are characterized by TEM with a JEOL JEM-1010 at 100 kV. For surface morphology, and cross-sectional examination of NC solid films, SEM microscopy is used (Hitachi 4800 microscope at 10 kV of acceleration voltage).

3.3.2 PROFILOMETRY

Profilometry is a technique that allows to characterize the thickness and roughness of deposited thin films. The profilometer used in this Ph. D Thesis (Dektak 150 from Veeco) consisted of a mechanical stylus with a diamond tip that remains in contact with the sample and is moved laterally across the surface. When a change in the contact

force is registered, the tip has encountered a rough vertical feature, the force exerted by the surface in the needle is translated to spatial units by the specialized software. The thickness of a thin film can be estimated by making an incision in the film with a razor blade and the height difference between the film surface and the groove produced by the blade is taken to be the film thickness. The vertical resolution of the Dektack 150 from Veeco unit utilized in this thesis is about 5 nm.

3.4 REFERENCES

1. Protesescu, L.; Yakunin, S.; Bodnarchuk, M.I.; Krieg, F.; Caputo, R.; Hendon, C.H.; Yang, R.X.; Walsh, A.; Kovalenko, M. V Nanocrystals of Cesium Lead Halide Perovskites (CsPbX3, X = Cl, Br, and I): Novel Optoelectronic Materials Showing Bright Emission with Wide Color Gamut. *Nano Lett.* **2015**, *15*, 3692–3696.
2. Chang, J.; Waclawik, E.R. Colloidal semiconductor nanocrystals: controlled synthesis and surface chemistry in organic media. *RSC Adv.* **2014**, *4*, 23505–23527.
3. Abargues, R.; Navarro, J.; Rodríguez-Cantó, P.J.; Maulu, A.; Sánchez-Royo, J.F.; Martínez-Pastor, J.P. Enhancing the photocatalytic properties of PbS QD solids: the ligand exchange approach. *Nanoscale* **2019**, *11*, 1978–1987.
4. Maulu, A.; Rodríguez-Cantó, P.J.; Navarro-Arenas, J.; Abargues, R.; Sánchez-Royo, J.F.; García-Calzada, R.; Martínez Pastor, J.P. Strongly-coupled PbS QD solids by doctor blading for IR photodetection. *RSC Adv.* **2016**, *6*, 80201–80212.
5. Maulu, A.; Navarro-Arenas, J.; Rodríguez-Cantó, P.; Sánchez-Royo, J.; Abargues, R.; Suárez, I.; Martínez-Pastor, J. Charge Transport in Trap-Sensitized Infrared PbS Quantum-Dot-Based Photoconductors: Pros and Cons. *Nanomaterials* **2018**, *8*, 677.
6. Ng, C.K.; Wang, C.; Jasieniak, J.J. Synthetic Evolution of Colloidal Metal Halide Perovskite Nanocrystals. *Langmuir* **2019**, *35*, 11609–11628.
7. Kagan, C.R.; Murray, C.B. Charge transport in strongly coupled quantum dot solids. *Nat. Nanotechnol.* **2015**, *10*, 1013–1026.
8. De Giorgi, M.L.; Krieg, F.; Kovalenko, M. V; Anni, M. Amplified Spontaneous Emission Threshold Reduction and Operational Stability Improvement in CsPbBr3 Nanocrystals Films by Hydrophobic Functionalization of the Substrate. *Sci. Rep.* **2019**, *9*, 17964.
9. Kim, T.-H.; Cho, K.-S.; Lee, E.K.; Lee, S.J.; Chae, J.; Kim, J.W.; Kim, D.H.; Kwon, J.-Y.; Amaratunga, G.; Lee, S.Y.; et al. Full-colour quantum dot displays fabricated by transfer printing. *Nat. Photonics* **2011**, *5*, 176–182.
10. Balazs, D.M.; Rizkia, N.; Fang, H.H.; Dirin, D.N.; Momand, J.; Kooi, B.J.; Kovalenko, M. V.; Loi, M.A. Colloidal Quantum Dot Inks for Single-Step-Fabricated Field-Effect Transistors: The Importance of Postdeposition Ligand Removal. *ACS Appl. Mater. Interfaces* **2018**, *10*, 5626–5632.
11. Suh, Y.-H.; Kim, T.; Choi, J.W.; Lee, C.-L.; Park, J. High-Performance CsPbX3 Perovskite Quantum-Dot Light-Emitting Devices via Solid-State Ligand Exchange. *ACS Appl. Nano Mater.* **2018**, *1*, 488–496.
12. Lin, Q.; Yun, H.J.; Liu, W.; Song, H.-J.; Makarov, N.S.; Isaienko, O.; Nakotte, T.; Chen, G.; Luo, H.; Klimov, V.I.; et al. Phase-Transfer Ligand Exchange of Lead Chalcogenide Quantum Dots for Direct Deposition of Thick, Highly Conductive Films. *J. Am. Chem. Soc.* **2017**, *139*, 6644–6653.

13. Hazarika, A.; Zhao, Q.; Gaulding, E.A.; Christians, J.A.; Dou, B.; Marshall, A.R.; Moot, T.; Berry, J.J.; Johnson, J.C.; Luther, J.M. Perovskite Quantum Dot Photovoltaic Materials beyond the Reach of Thin Films: Full-Range Tuning of A-Site Cation Composition. *ACS Nano* **2018**, *12*, 10327–10337.
14. Pinto, C.V.; Sousa, J.P.; Cardoso, F.V.; Minas, G. Optimized SU-8 Processing for Low-Cost Microstructures Fabrication without Cleanroom Facilities. *Micromachines* 2014, *5*.
15. Gordillo, H.; Suárez, I.; Abargues, R.; Rodríguez-Cantó, P.; Almuneau, G.; Martínez-Pastor, J.P. Quantum-Dot Double Layer Polymer Waveguides by Evanescent Light Coupling. *J. Light. Technol.* **2013**, *31*, 2515–2525.
16. Clifford, J.P.; Johnston, K.W.; Levina, L.; Sargent, E.H. Schottky barriers to colloidal quantum dot films. *Appl. Phys. Lett.* **2007**, *91*, 253117.
17. Chan, Y.; Steckel, J.S.; Snee, P.T.; Caruge, J.-M.; Hodgkiss, J.M.; Nocera, D.G.; Bawendi, M.G. Blue semiconductor nanocrystal laser. *Appl. Phys. Lett.* **2005**, *86*, 73102.
18. Dang, C.; Lee, J.; Breen, C.; Steckel, J.S.; Coe-Sullivan, S.; Nurmikko, A. Red, green and blue lasing enabled by single-exciton gain in colloidal quantum dot films. *Nat. Nanotechnol.* **2012**, *7*, 335–339.
19. Yakunin, S.; Protesescu, L.; Krieg, F.; Bodnarchuk, M.I.; Nedelcu, G.; Humer, M.; De Luca, G.; Fiebig, M.; Heiss, W.; Kovalenko, M. V. Low-threshold amplified spontaneous emission and lasing from colloidal nanocrystals of caesium lead halide perovskites. *Nat. Commun.* **2015**, *6*, 1–8.
20. Navarro-Arenas, J.; Suárez, I.; Martínez-Pastor, J.P.; Ferrando, A.; Gualdrón-Reyes, A.F.; Mora-Seró, I.; Gao, S.-F.; Wang, Y.-Y.; Wang, P.; Sun, Z.; et al. Optical Amplification in Hollow-Core Negative-Curvature Fibers Doped with Perovskite CsPbBr3 Nanocrystals. *Nanomaterials* **2019**, *9*, 868.
21. Time-Domain Lifetime Measurements BT - Principles of Fluorescence Spectroscopy. In; Lakowicz, J.R., Ed.; Springer US: Boston, MA, 2006; pp. 97–155 ISBN 978-0-387-46312-4.
22. Ruska, E. The Development of the Electron Microscope and of Electron Microscopy (Nobel Lecture). *Angew. Chemie Int. Ed. English* **1987**, *26*, 595–605.
23. Shibata, N.; Kohno, Y.; Nakamura, A.; Morishita, S.; Seki, T.; Kumamoto, A.; Sawada, H.; Matsumoto, T.; Findlay, S.D.; Ikuhara, Y. Atomic resolution electron microscopy in a magnetic field free environment. *Nat. Commun.* **2019**, *10*, 2308.

4 PEROVSKITE NANOCRYSTAL PHOTODETECTORS AND SOLID-STATE LIGAND EXCHANGE STRATEGIES

Surface chemistry engineering of nanocrystals offers a direct approach to tune charge carrier dynamics in nanocrystals-based photodetectors. For this purpose, we have investigated the effects of altering the surface chemistry of thin films of $CsPbBr_3$ perovskite nanocrystals produced by the doctor blading technique, via solid state ligand-exchange using 3-mercaptopropionic acid (MPA). The electrical and electro-optical properties of photovoltaic and photoconductor devices were improved after the MPA ligand exchange, mainly due to a mobility increase up to 5×10^{-3} cm^2/Vs. The same technology was developed to build a tandem photovoltaic device based on a bilayer of PbS QDs and $CsPbBr_3$ perovskite nanocrystals. Here, the ligand exchange was successfully carried out in a single step once the bilayers were coated. The photodetector device showed responsivities around 40 and 20 mA/W at visible and near infrared wavelengths, respectively. This strategy can be of interest for future visible-NIR cameras, optical sensors or receivers in photonic devices for future internet-of-things technology. The content of this chapter was published in the scientific journal *Nanomaterials* (journal with impact factor of 4.324 in 2019, ranked in Q2 within the Materials Science Multidisciplinary and Nanoscience & Nanotechnology categories of WoS) during the year 2020 [1].

4.1 INTRODUCTION

All-inorganic caesium lead halide perovskites, with formulation $CsPbX_3$ (X = Cl, Br, I), have been proposed for a large number of optoelectronic applications because of their unique properties, such as a large optical absorption cross section and high photoluminescence quantum yield (PLQY) [2]. Besides, these materials, which were engineered as nanocrystals for the first time in 2015 [3], exhibit a relatively low concentration of defects [4] and enhanced endurance to ambient environment as compared to their organic–inorganic analogues [5], while it also allows for a flexible bandgap tunability with narrow emission lines, being the ideal material for next generation of light-emitting diodes (LEDs) and display applications [6]. In the field of photodetectors, these materials can display high responsivities in the form of nanowires

[6,7], because of their long carrier lifetimes and fast charge transfers [9], and monolayers (or few-layer nanosheets) that use a metal-semiconductor-metal (MSM) configuration [10,11]. The MSM architecture was also applied to the development of optoelectronic devices based on films of nanocrystals (nanocube shape) [12–14]. However, only a few publications explore photodetector architectures based on heterojunctions, as in the case of solar cells. While these configurations are arguably more complex, they facilitate the introduction of functional interfaces, which can increase the charge carrier selectivity at the contacts, enabling potentially higher detection performance.

The use of perovskite nanocrystals (PNCs) in the form of thin films offer additional advantages as compared to the use of perovskite polycrystalline thin films, such as the composition control during the PNC synthesis [2], the self-assembling of PNCs leading to 3D superlattices or supercrystals [15], and the possibility of carrying out a post-synthetic anion or cation exchange, allowing to tune and optimize the resulting bandgap [16]. An ordered assembly of nanocrystals can enable 3D electronic coupling between them, thus enhancing charge carrier transport in the superlattice structure. This kind of structure can be obtained with by inexpensive thin film solution deposition technique such as doctor blading, which allows for a precise thickness control over large areas with a minimum waste of material as it was proven in our previous publications based on PbS quantum dots (QDs) [17,18]. Other deposition techniques, such as spin-coating, spray coating, and dip-coating, have also been employed to fabricate nanocrystal-based optoelectronic devices, some of them with relatively good figures of merit [19]. An important issue involved in the formation of compact high-quality layers of PNCs for optoelectronics originates is the insolubility of the inorganic metal halide in the processing solvents [20]. Besides, the ionic nature of perovskites restricts the use of classical polar/non-polar solvent purification strategies [21]. In this context, ligands become one of the main tools to gain control over the superlattice formation and electronic coupling between nanocrystals [22]. Particularly, when insulating long chain carboxylic acids and amine functional groups, oleic acid (OA) and oleylamine (OAm) are replaced by short chain thiols, a significant improvement was observed in the performance of photovoltaic and photocatalytic devices based on PbS QDs [21,22].

On the basis of previous studies on QDs, when long chain ligands are exchanged by short chain thiols, an improved carrier transport is measured because of the reduced interparticle distance and consequent efficient charge transfer between neighboring PNCs in films. Mercaptopropionic acid (MPA) is a bifunctional linker molecule that is widely used as a ligand because of its potential surface capping ability and remarkable

influence on charge-transport [18,23–25]. In order to remove the insulating ligands from the surface of PNCs, a ligand-exchange strategy was studied in a few reports. Guopeng Li et al. used phenylethylammonium bromide (PEAmBr) in methyl acetate for replacing the conventional OAm/OA surface ligands of $CsPbBr_3$ PNCs, and achieved very bright films and efficient LEDs [26]. L. Zhou et al. used MPA to couple the TiO_2 layer and $CsPbBr_3$ PNCs, resulting in an improved responsivity and detectivity [27]. PNCs are more sensitive to ligand-exchange processes using MPA than conventional IV-VI group QDs because of their ionic surface. M. Gong et al. carried out a surface-engineering process using MPA ligand of a film of $CsPbI_3$ PNCs that resulted in their improved stability by reducing surface traps [28]. High photoresponsivity ($>10^6$ A/W) and high photoconductive gain (3.6×10^6) was obtained with these films in graphene field-effect transistors (GFETs). Moreover, ligand exchange has been proven to be a valid strategy to improve the electrical properties of solid thin films made of nanocrystals/QDs, but also the removal of ligand excess in PNCs by washing the film with ethyl acetate solution have led to an increase of its electro-optical quality [29].

In this work, we propose the use of MPA as a ligand exchange strategy to improve the charge carrier transport in $CsPbBr_3$ PNCs thin films for efficient photodiode detectors. Such films were prepared by doctor blading technique using a well purified solution of $CsPbBr_3$ PNCs. In thin films deposited by layer-stacking of PNCs, the dominant transport mechanism can be assimilated to carrier hopping because of the three-dimensional electronic coupling between PNCs [30]. The Schottky-heterostructure photodevices were fabricated with/without MPA ligand exchange to study the differences in their electro-optical properties. The ligand-exchange is carried out in solid state after the deposition of the PNC thin film. MPA replaces longer OAm ligands and enhances the wave-function overlapping among nanocrystals to improve charge transport via carrier hopping mechanism. The resulting photodiodes exhibited device responsivities ~0.1 A/W and detectivities as high as 8×10^{10} jones (1 jones = 1 cm $Hz^{1/2}$ W^{-1}), other than open circuit voltages 0.6–0.8 V and short circuit currents of 1–3 mA/cm^2 under solar AM1.5G illumination. These values are well above those obtained in reference samples without MPA treatment. Furthermore, we also demonstrated the compatibility and film formation of PbS QDs on top of $CsPbBr_3$ PNCs, together with a ligand exchange in both layers at the same time. Our analysis showed that the thiol group (-SH) of MPA efficiently coordinates to surface Pb(II) atoms to provide a very good passivation of PNCs and QDs while reducing their interparticle spacing in the film. These findings are applied to a

tandem photodetector, which exhibited a broadband responsivity levels of 40 mA/W at visible wavelengths and 20 mA/W around the telecom C-band (1525–1565 nm).

4.2 PREPARATION AND CHARACTERIZATION METHODS OF THE OPTOELECTRONIC DEVICES

4.2.1 SYNTHESIS OF THE PNCS

Synthesis of $CsPbBr_3$ PNCs was performed using the hot-injection method (presented in section 3.1.1 of this Thesis) with the modifications detailed below. In a typical synthesis process, firstly Cs-oleate was prepared by mixing 0.16 g Cs_2CO_3, 10 mL of OA and 10 mL of 1-ODE into a 50 mL three-neck flask by heating at 120 °C in vacuum under a constant stirring. Then, the mixture was allowed to N_2-purging and heated at 150 °C until all of the Cs_2CO_3 was completely dissolved. The solution was further stored under N_2 by keeping the temperature at 100 °C to avoid Cs-oleate precipitation. Meanwhile, 0.55 g $PbBr_2$ was mixed with 20 mL of 1-ODE into a 100 mL three-neck flask. The mixture was heated at 120 °C under vacuum for 1 h, keeping a constant stirring. Then, 5 mL OA and 5 mL of OAm were separately added to the flask under N_2 atmosphere, and rapidly heated to reach 170 °C. At this stage, 10 mL of already prepared Cs-oleate solution was injected into this mixture. Lastly, the flask was immersed into a bath ice for 5 s to quench the reaction mixture. The solution was then centrifuged at 4700 rpm for 10 min and purified using the mixture of antisolvents namely hexane/ethyl acetate to achieve high purity $CsPbBr_3$ PNCs. This washing procedure was key to allow the isolation of the $CsPbBr_3$ PNCs for further processing into thin films by the doctor blading technique. The $CsPbBr_3$ PNCs were separated after discarding the supernatant and re-dispersed in hexane to prepare a colloidal solution with a concentration of 50 mg/mL.

4.2.2 CHARACTERIZATION OF THE PNCS

The absorption spectrum of the colloidal solution with synthesized $CsPbBr_3$ PNCs in toluene exhibits a well-defined excitonic resonance at 482 nm (red curve in Figure 4.1a), whereas the PL spectrum is rather narrow (Full Width at Half Maximum around 25 nm) and centered at 498 nm (black curve in Figure 4.1a). The PLQY of $CsPbBr_3$ PNCs in toluene reached a value of 55%. Transmission electron microscopy (TEM) image of

the prepared $CsPbBr_3$ PNCs given in Figure 4.1b shows that the prepared sample possess cubic morphology with the average size around 8.2 nm. The PL peak and absorbance resonance wavelengths are consistent with this average size, according to published results of $CsPbBr_3$ PNCs similarly synthesized by the hot injection method [3]. In the case of PbS QDs used in Section 4.3.5 of this Chapter absorption and PL spectra (Figure 4.1c) are consistent with their average size of 6.3 nm (Figure 4.1d).

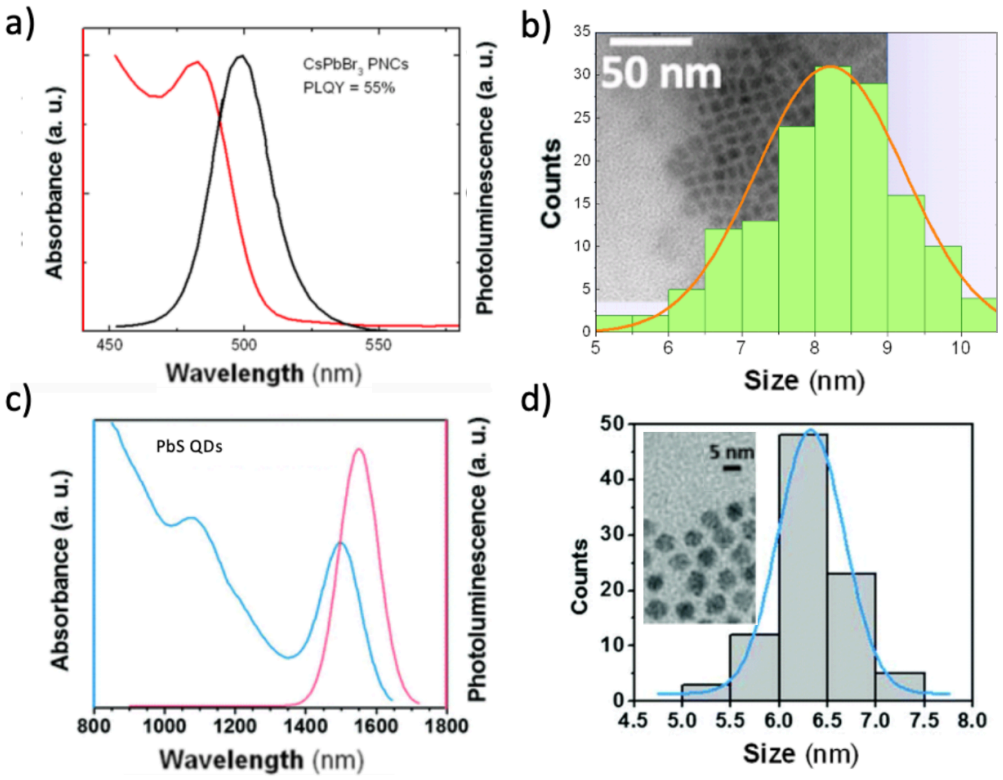

Figure 4.1. PL and absorbance spectra of the synthesized a) $CsPbBr_3$ NCs c) PbS QDs. NCs size distribution and TEM image of b) $CsPbBr_3$ NCs and d) PbS QDs.

4.2.2 Device Fabrication

With the purpose of obtaining a clear picture of the postulated MPA ligand exchange effects on the $CsPbBr_3$ PNCs, three types of opto-electronic devices were fabricated and characterized: Schottky heterostructures, interdigitated photoconductor structures, and OFET (organic field effect transistor) chips. With the analysis of these devices we can obtain different optoelectrical parameters such as mobility, electrical conductivity, and the figures of merit of photodetectors.

For the fabrication of the Schottky heterostructure, a prepatterned ITO substrate (Ossila, Sheffield, UK), a 8-Pixel photovoltaic substrate, was sonicated for 5 minutes in

Hellmanex III (1%) (Ossila) at 70 °C, then rinsed in water/isopropanol and finally exposed to UVO (UV-Ozone) treatment for 20 minutes prior to the deposition of a thin layer (50 nm) of PEDOT: PSS (Sigma-Aldrich). The PEDOT: PSS was spin-coated at a speed of 3000 rpm for 40 seconds. Then, a cleansed 200 micrometer-filtered $CsPbBr_3$ PNCs solution (free of aggregates laying at the bottom of the flask) with an optimal nanocrystal concentration of 30 to 50 mg/mL was casted on top of the PEDOT: PSS film using a commercial doctor blade applicator (model 4340, Elcometer, Manchester, UK). Subsequent layers of $CsPbBr_3$ PNCs layer were deposited with a blade velocity of 1.5 cm/s with an intermediate annealing step of 2 minutes at 100 °C. This process was repeated several times, until a thickness of 350–400 nm was achieved. The thickness was measured by using a stylus profilometer (model Dektak 150, Veeco, Plainview, NY, USA). Finally, the film was annealed at 100 °C for 1 h under vacuum in order to remove the presence of hexane in between the nanocrystals and/or trapped by the ligands' network. This annealing step prevents the NC layer to detach from the substrate during the ligand exchange procedure. For the ligand exchange, the film was dipped during 60 s into a solution of 10% (in volume) MPA in ethyl acetate and then rinsed with ethyl acetate to remove the MPA excess. After the treatment, the layer aspect appeared as a hazy white surface, but after drying with compressed air and annealing at 100 °C under vacuum for 1 h the layer presented a saturated green color.

Finally, a 20-nm thick MoO_3 (molybdenum trioxide) and a 100-nm thick gold layers were deposited by thermal evaporation under high vacuum. The shadow mask used during this thermal process was specially designed to work with these substrates (Ossila, Sheffield, UK). This multi-electrode mask defines up to eight separated devices whose individual active area is 4 mm^2. Here, the MoO_3 interlayer between the thin film of $CsPbBr_3$ PNCs and the Au contact would act as an electron blocking layer. More information regarding the techniques to fabricate these devices were summarized in sections 3.1.2 and 3.1.3 of this Thesis.

Tandem photodevices integrating two stacked films of $CsPbBr_3$ PNCs and PbS QDs were fabricated by using similar procedures described above. PbS QDs were synthetized according to a procedure described in our previous publications [17,30] in which a Schottky heterostructure was built by Doctor Blade to operate at telecom wavelengths (see emission and absorption spectra in Figures 4.1c and 4.1d).

The OFET test chips were purchased from Ossila, whereas metal–semiconductor–metal interdigitated photoconductors were previously fabricated by UV photolithography and lift-off processing (the gold pads were 100 nm thick and consisted of 10 pairs of

fingers spaced 20 μm each). $CsPbBr_3$ PNCs were deposited on both OFET and interdigitated chips with the same doctor blade technique as the one used for the fabrication of Schottky heterostructures.

4.2.3 CHARACTERIZATION OF FILMS AND DEVICES

The PLQY analysis of all samples was carried out by using an integrating sphere (Hamamatsu C9920-02 absolute PL quantum yield measurement system). Transmission electron microscopy (TEM) images were taken using JEOL 1010 microscope (JEOL, Tokyo, Japan) at the operating voltage of 100 kV. The electro-optical properties of the photodetectors and photoconductors were measured by a homemade setup based on a halogen lamp (25 mW/cm^2 of white light intensity) focused onto a multimode optical fiber (800 μm of core diameter) attached to the entry of a DNS-300 monochromator (DeltaNu, Laramie, WY, USA), whose output was modulated at 1 kHz by means of a mechanical chopper and focused onto the fabricated photodetector by a 10x objective. We used a grating with 1200 (600) grooves per mm and blaze at 500 (1200 nm) nm for visible (near-infrared) wavelengths. For example, if the output slit of the monochromator was opened to 1 mm, a power of 18 nW was measured at a wavelength of 500 nm. The electrical signal of the photodetector was synchronously measured by a lock-in amplifier. The lamp spectrum at the monochromator's output was measured using a calibrated Si photodetector and responsivity of tested photodetectors were determined by using the calibrated table of that Si photodetector. The current-voltage (J-V) characteristics under dark and AM1.5G illumination conditions were measured using a Keithley's Series 2400 Source Measure Unit (SMU) and a solar simulator based on a 150 W Xe lamp (Zolix, model GLORIA-X150A) with an AM1.5G air mass filter (Newport). Light intensity was adjusted with a calibrated solar cell of silicon. The photocurrent transient times were measured with a triggered oscilloscope. More details about the setup can be found in Section 3.2.1.B of this Thesis.

The Ossila OFET test chips were loaded for characterization on a high-density OFET test board (also from Ossila), designed to reduce leakage current, external noise, and stray capacitance. Drain-source current was measured at 1-V bias using the SMU, and the gate bias was applied using a DC power source connected to a BNC connector board. The optical properties of the layers, absorbance and photoluminescence (PL), were determined by means of a spectrograph (HR4000, Ocean Optics, Largo, FL, USA). The details of the corresponding setup can be found in Section 3.2.2.A of the Thesis.

4.3 RESULTS AND DISCUSSION

For the purpose of obtaining a clear picture of the postulated MPA ligand exchange effects on the $CsPbBr_3$ PNCs, three types of opto-electronic devices were fabricated and characterized: Schottky heterostructures, interdigitated photoconductor structures and OFET (Organic Field Effect Transistor) chips. With the analysis of these devices we can obtain different electro-optical parameters such as mobility, electrical conductivity and the photodetector's figures of merit described in section 2.4.3 of this Thesis.

4.3.1 THIN FILMS OF PNCS

Thin films of $CsPbBr_3$ PNCs with a thickness of 400 nm were deposited on borosilicate glass to measure PL (Figure 4.2a) and absorbance (Figure 4.2b) spectra before (red lines) and after (blue lines) the MPA ligand exchange. The PL spectra are very similar in shape, but significantly shifted to the red, from 502 to 517 nm, after the MPA treatment (see Figure 4.2a). A similar shift is observed for the exciton absorption resonance (Figure 4.2b). This clear redshift can be ascribed to a strong reduction in the inter-particle spacing among $CsPbBr_3$ PNCs; the NCs probably merged into bigger particles (or agglomerates), losing part of their (weak) quantum confinement characteristics [17].

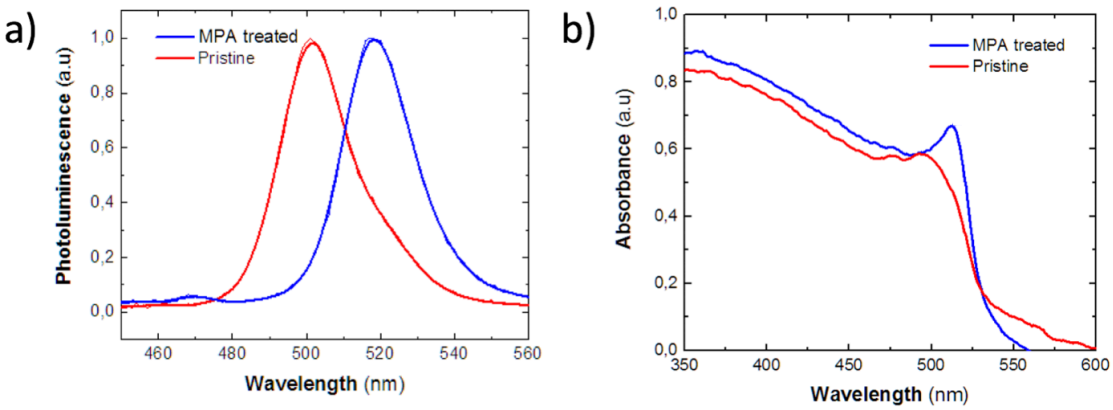

Figure 4.2. Optical characterization of the 350 - 400 nm $CsPbBr_3$ PNCs 400 nm layers before (red curves) and after MPA ligand exchange (blue curves). a) Photoluminescence, measured by backscattering and collecting to a spectrograph. b) UV-Vis absorbance spectra.

4.3.2 Electro-Optical Characterization of Schottky Heterostructures

A Schottky-heterostructure (Figure 4.3a) samples, (before and after ligand exchange) with and without MPA-treatment, was fabricated in order to explore the effects of the ligand exchange on the optoelectronic properties of the films constituted of $CsPbBr_3$ PNCs. In the band diagram shown in Figure 4.3b (energy levels extracted from references [31–33]) it can be observed how the charge separation is provided by the structure. As in other devices, the MoO_3 oxide interlayer plays the role of high-energy electron blocking layer [34], while allowing hole transfer towards the gold electrode.

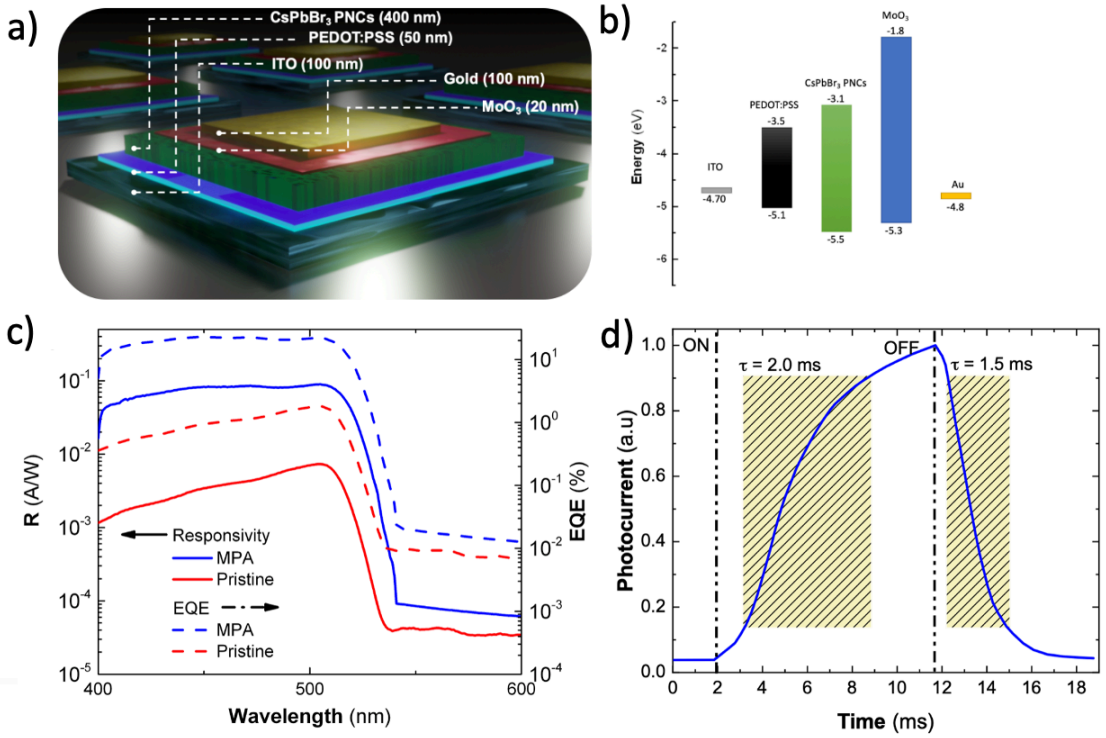

Figure 4.3. a) Schematic representation of the device architecture. b) Schematic energy level diagram of a complete photovoltaic device based on the light absorbing layer of $CsPbBr_3$ PNCs. c) Responsivity curve at 0 V bias of the Schottky photodiodes prepared with MPA ligand exchanged (blue solid line) and pristine (red solid line) $CsPbBr_3$ NCs. The calculated EQE is represented by discontinued lines. d) One response cycle of the MPA treated photodetector when illuminated under 50 Hz chopped white light at measured at 0 V bias.

The measured responsivity has a maximum at 500 nm of around 100 mA/W in the MPA-treated devices (blue solid curve in Figure 4.3a), as compared to the 7 mA/W of the pristine ones (red solid curve in Figure 4.3a), i.e., more than 14 times of

enhancement. The external quantum efficiency (EQE) and the specific detectivity (D^*) can be calculated following the usual expressions (see Section 2.4.3) [35]. EQE (dotted curves in Figure 4.3a) and D^* in our MPA-treated photodiodes reach values up to 20 % and 8 × 10^{10} jones (1 jones = 1 cm $Hz^{1/2}$ W^{-1}), respectively, as compared to 1 % and 4 × 10^9 jones in the pristine ones.

A typical photocurrent transient curve for the MPA treated photodetectors is illustrated in Figure 4.3b. The temporal response of the photocurrent was evaluated by using a white light halogen lamp source with intensity around 25 mW/cm^2 chopped at 50 Hz. Rise and decay time constants of 2.0 and 1.5 ms are estimated from the time intervals required for photocurrent to reach 90% or to decay until 10% of the photocurrent peak value, respectively. These photocurrent time constants are comparable to other values found in recently reported photodevices (see Table 4.1 for an updated list of relevant publications) [36,37]. The relatively long response times are attributed to charge trapping and detrapping processes that originate from relatively shallow defect levels at the surface of the PNCs, as demonstrated and discussed in literature [38,39].

Type	Architecture	Material	R (A/W)	D^* (jones)	Rise/Decay (ms)	Year	Ref
MSM	ITO/$CsPbCl_3$/ITO	0D	1.89	-	41/43	2017	[40]
MSM	Au/$CsPbBr_3$/Au	Thin films	55	-	0.43/0.318	2017	[36]
MSM	Au/$CsPbBr_3$ – TiO_2 /Au	0D	3.5	-	> 1000	2017	[41]
MSM	Au/$CsPbBr_3$/Au	2D	1.33	0.86 × 10^{12}	20.9/24.6	2018	[42]
FET	$CsPbBr_3$/MoS_2	0D/2D	4.4	2.5 × 10^{10}	0.72/1.01	2018	[37]
FET	$CsPbBr_3$/MoS_2	0D/2D	4 × 10^4	-	7.5/8	2019	[43]
Photodiode	ITO/$CH_3NH_3PbI_3$/Au	2D	0.036	-	320/330	2017	[44]
Photodiode	FTO/TiO_2/$CsPbBr_3$/Spiro-OMeTAD/Au	0D	3	1 × 10^{14}	-	2018	[45]
Photodiode	ITO/PEDOT:PSS/$CsPbBr_3$ /MoO_3/Au	0D	0.1	8× 10^{10}	2/1.5	2020	Here

Table 4.1. Comparison of caesium lead halide nanocrystal perovskite-based photodetectors.

In order to gain insight on the physical magnitudes determining charge transport and charge separation in our the Schottky-heterostructure devices, we focus on their J-V curves and the observed changes after ligand exchange. The J-V curves provide a reliable benchmark for the evaluation of charge transport properties through the many parameters than can be derived from the fitting of the data. Specifically, the series resistance considers directly the carrier mobility and conductivity, the shunt resistance accounts for the recombination losses and the saturation current density includes carrier

generation-recombination mechanism inside the device. Since the ligand exchange directly affects the performance of the hopping transport within the PNC film, these parameters are expected to shed light on the effects introduced by the MPA ligand exchange.

Despite the device stack configuration is not the optimal one for photovoltaic conversion, their respective parameters can be used to extract useful information. Figures 4.4a-b shows the J-V curves for both MPA-treated and pristine best-devices (averaged values listed in Table 4.2) where it can be seen a noticeable improvement of the photodiode properties due to the ligand exchange. The short-circuit current density J_{sc} is increased from 7×10^{-3} to 2.9 mA cm^{-2}, more than 400-fold. The open-circuit voltage was also increased from 0.2 to 0.7 V. The relatively low values of V_{oc} as compared to the bandgap of the PNCs, 2.25 eV [46], can be attributed to the lack of engineering in the ETL (electron transport layer)/perovskite and perovskite/HTL(hole transport layer) interfaces, which become significant sources of non-radiative recombination. In any case, measured values of J_{sc} and V_{oc} for MPA-capped $CsPbBr_3$ PNCs devices are comparable with previously published results. For instance, Hoffman et al. [47] reported 300 nm Layer-by-Layer PNCs solar cells with V_{oc} of around 1.2 V and J_{sc} 4 mA cm^{-2}; Akkerman et. al. [48] reports a similar device a V_{oc} of 1.5 V and a J_{sc} of 5 mA cm^{-2} and finally Yang et. al. [49] matches those results with a photodetector operating with an V_{oc} of 1.2 V and J_{sc} of 1 mA cm^{-2} at room temperature. It should be noted that the new MPA ligand may result in a different electronic work function, as demonstrated for PbS QD solids, in which the work function can vary several hundreds of meVs depending on the ligand post-treatment applied [18,50].

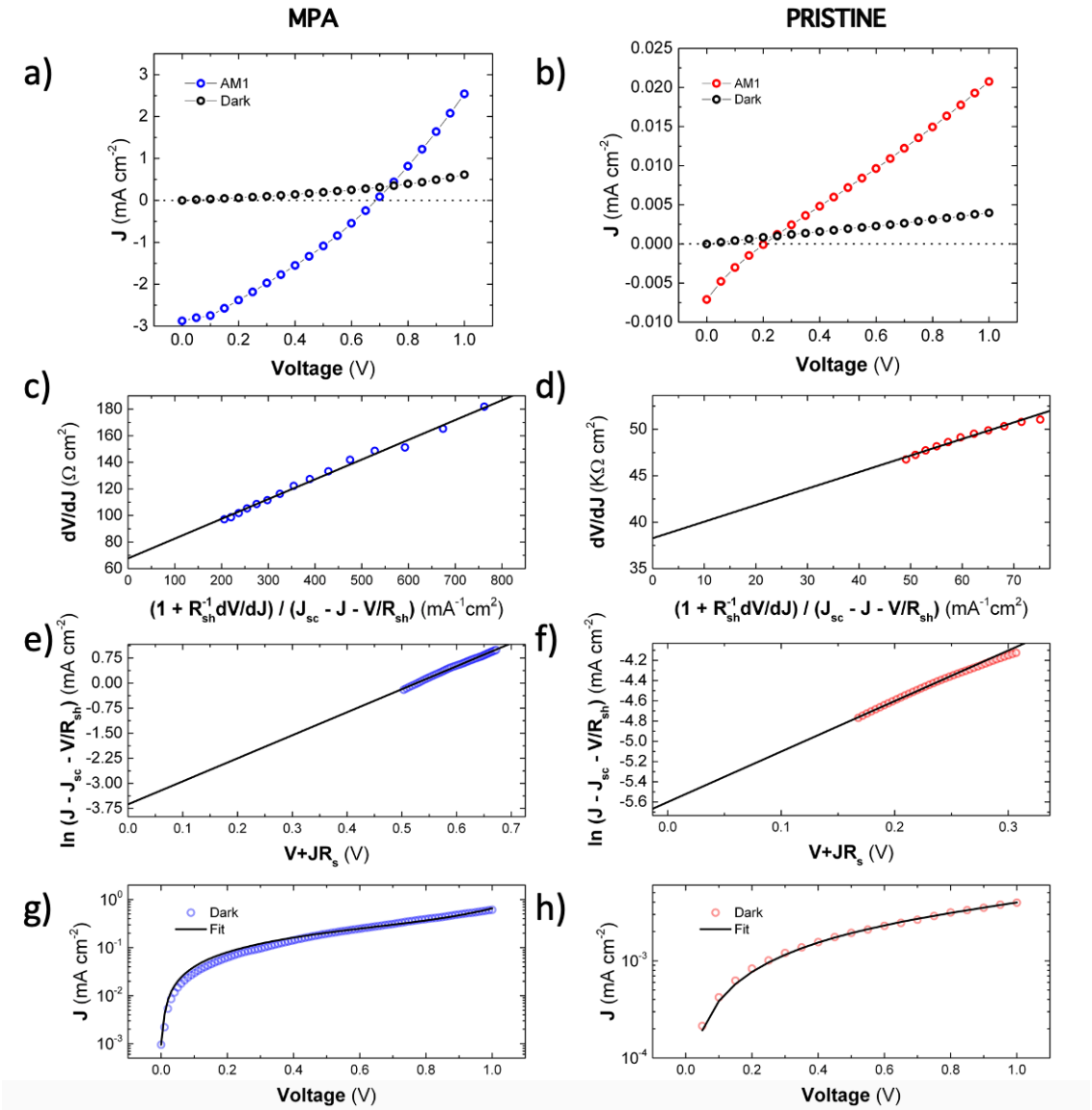

Figure 4.4. J-V curves for planar PNC photodiodes using ITO/PEDOT:PSS/$CsPbBr_3$ PNCs/MoO_3/Au architecture. The measurements are carried out in dark and under AM1 for MPA ligand-exchanged (a) and pristine (b) devices. Fitting curves (continuous black lines) using Equations 4.4 - 4.5 for J-V curves under AM1 illumination for MPA (c-e) and pristine (d-f) devices, and Equation 4.7 for J-V under dark conditions in MPA (g) and pristine (h) cases.

The real diode equivalent circuit limited by the presence of the internal series resistance (R_s) and the leakage current governed by the shunt parallel resistance (R_{sh}) would be:

$$J = J_{sc} - J_0\left(e^{\frac{q(V+JR_s)}{mKT}}\right) - \frac{V + JR_s}{R_{sh}} \tag{4.1}$$

where the parameter m is the ideality factor, J_{sc} is the short-circuit current density and J_0 is the reverse saturation current density. The latter represents the electron thermionic emission, which is related to the recombination rate of the diode and its open-circuit voltage (V_{oc}). The fitting of Equation 4.1 to the experimental data is not

straightforward, because photodiodes based on QDs often show linear or superlinear instead of saturation-type behavior, whose main feature is related to large ideality factors (m > 2) [38,51]. That is, the carrier recombination mechanism within such regions needs descriptions that go beyond the Shockley–Read–Hall (SRH) model approximation. While the SRH recombination at deep trap states predicts $m \leq 2$ [52], diodes based on nanostructured metal halide perovskites usually deviate from this behavior, with $m >> 2$ at relative low voltages (< 1 V) [49,53].

The high value of the *m*-parameter may be the result of a broad energy tail of superficial trapping states present on the light-soaked PNCs [54] or simply due to the presence of leaking currents introduced by a certain random distribution of pinholes throughout the thin films. For thick samples or studies made under high illumination intensities, the effect of shallow traps of such energy tail is attenuated by state filling [55]. Thus, describing the photovoltaic device as two PN heterojunctions in series, instead of a single PN junction [56,57], is a more heuristic approach to explain a J-V curve with a large *m*-parameter. The equivalent electrical circuit of the double heterojunction model [56] is used here to obtain the photodiode parameters of the MPA-treated photodiodes and the pristine cells:

$$J = J_{sc} - J_0\left(e^{\frac{q(V+JR_s)}{(m_1+m_2)KT}}\right) - \frac{V+JR_s}{R_{sh}} \tag{4.2}$$

$$\frac{V_1}{m_1} = \frac{V_2}{m_2} = \frac{V+JR_s}{m_1+m_2} \tag{4.3}$$

where the parameters J_{sc}, J_0, R_s and R_{sh} correspond to the whole structure while V_j and m_j (j = 1,2) apply for a single heterojunction. These equations hold true considering the approximation $J_{01} \cong J_{02} = J_0$. Moreover, if both heterojunctions are ruled by the SRH mechanism ($m \leq 2$), the sum of the ideality factors $m_1 + m_2$ should be as high as 4, allowing again the SRH mechanism to describe the recombination in both heterojunctions. In order to avoid the non-linear fitting of data to Equation 4.2, the following useful transformations can be practiced

$$-\frac{dV}{dJ} = \frac{(m_1+m_2)kT}{q}\left(\frac{1+\frac{1}{R_{sh}}\frac{dV}{dJ}}{J_{sc}-J-\frac{V}{R_{sh}}}\right) + R_s \tag{4.4}$$

$$\ln(J_{sc} - J - V/R_{sh}) = \frac{q}{(m_1 + m_2)kT}(V + JR_s) + \ln J_0 \quad (4.5)$$

These equations allow now to extract the ideality factors $m_1 + m_2$ and R_s with a linear regression (Equation 4.4), if $\left(1 + \frac{1}{R_{sh}}\frac{dV}{dJ} \Big/ J_{sc} - J - \frac{V}{R_{sh}}\right)$ is taken as the x-variable. Equation 4.5 allows to easily extract current J_0 from the y-intercept and using the best fitting value of $m_1 + m_2$ previously obtained through Equation 4.4. The fitting curves (black continuous lines) using Equations 4.4 - 4.5 to experimental data (coloured symbols) are shown in Figures 4.4c, 4.4d for MPA-treated and Figures 4.4d, 4.4f for pristine photovoltaic devices.

The ideality factors extracted from these fittings are large for both the MPA ($m1 + m2 = 5 \pm 1$) and the pristine (6 ± 2) photodiodes (the uncertainty associated with the *m* factor was estimated from the standard deviation of fitting parameters deduced from all measured photodiodes), but still compatible with the SRH recombination mechanism under the hypothesis of the double-heterojunction. The reverse saturation current densities in the best devices were 2 × 10^{-1} mA cm^{-2} (MPA) and 4 × 10^{-3} mA cm^{-2} (pristine), with average values (1.5 ± 1.0) × 10^{-1} (MPA) and (2 ± 1) × 10^{-3} mA cm^{-2} (Pristine), as listed Table 4.2. From these relatively high values, the barrier height can be related with J_0 with the thermionic emission theory for the Schottky diode:

$$\phi_b = \frac{kT}{q} ln\left(\frac{A^* T^2}{J_0}\right) \quad (4.6)$$

Here, $A^* = A(m^*/m_0)$ is the effective Richardson constant with A = 120 A cm^{-1} K^{-2}, where an electron effective mass m^* = 0.126 m_0 can be adopted from literature [58]. The barrier height can be estimated from Equation 4.6: 0.51 V for the MPA-treated and 0.58 V for the pristine device, which are around 0.2 V lower than other similar devices in literature [49,59]. The relatively high value of the ideality factors combined with the low values for ϕ_b suggests that there is still room for the improvement of the MPA-treated devices, especially in the enhancement of the Schottky-heterojunction interfaces and their corresponding energy alignments.

In addition, the J-V curves under dark conditions allows us to obtain the recombination current density J_r, the diffusion current density J_d and the shunt resistance R_{sh} (it was taken as a fixed parameter in Equations 4.4 and 4.5) with a non-linear fitting by using the following double heterojunction equation [56]:

$$J = \frac{V}{R_{sh}} + J_r\left(e^{\frac{qV}{m_r kT}} - 1\right) + J_d\left(e^{\frac{qV}{m_d kT}} - 1\right) \quad (4.7)$$

Here the ideality factor m_r is associated with the dual recombination current model, hence $m_r = m_{r1} + m_{r2} \leq 4$ (m_{r1} and m_{r2} ideality factors for both heterojunctions); whereas $m_d = m_{d1} + m_{d2}$ corresponds to the dual diffusion current model and hence can be as high as 2.

Recombination currents J_r(MPA) = 4 × 10^{-5} mA/cm^2 (Figure 4.4g) and J_r(pristine) = 5 × 10^{-8} mA/cm^2 (Figure 4.4h) (average 4 ± 1 × 10^{-5} for MPA and 5 ± 2 × 10^{-8} mA cm^{-2} for Pristine, as listed in Table 4.2) were obtained after fitting the J-V curves under dark conditions through Equation 4.7. The difference between pristine and MPA-treated devices is mainly attributed to the strong difference between dark conductivities. The dark recombination current of the pristine device is similar to those with similar Schottky-heterostructures in the literature [49]. From the same fitting procedure, we obtained a diffusion current density (J_d) of around 5 x 10^{-8} mA cm^{-2} (average (5 ± 3) × 10^{-8} mA cm^{-2}) for the pristine devices, a value consistent with the large turn-on diffusion voltage (V_{bias} > 1 V), as observed in Figures 4a-b. The diffusion component in MPA-treated devices doesn't play any role in the fitting of the curves and, thus, can be considered zero.

	R_{sh}(MΩcm^{-2})	R_s (Ω cm^{-2})	$(m_1 + m_2)$	J_r (mA cm^{-2})	J_d (mA cm^{-2})	J_0 (mA cm^{-2})	ϕ_b (eV)
Pristine	4 ± 2	(3 ± 1) × 10^4	6 ± 2	(5 ± 2) × 10^{-8}	(5 ± 3) × 10^{-8}	(2 ± 1) × 10^{-3}	(5 ± 1) × 10^{-1}
MPA	8 ± 3	50 ± 20	5 ± 1	(4 ± 1) × 10^{-5}	0	(1.5 ± 1.0) × 10^{-1}	(5 ± 1) × 10^{-1}

Table 4.2. Average parameters of the device performances of the prepared thin film $CsPbBr_3$ PNCs based photodetectors, as obtained from the different fittings.

Low dark recombination current is an essential requirement for a photodetector to have a high responsivity figure of merit. In spite of the relatively high values of dark J_0 discussed above, the photodiodes can still reach a good responsivity level when compared with other reported in recent literature [12,14,60]. Overall, the extracted figures of merit of our MPA-treated photovoltaic device are comparable or better than those found in other photodetectors based on thin films of $CsPbBr_3$ PNCs, as listed in Table 4.1, but still worse than in similar photodevices based on QDs (0.2 A/W for NIR light was obtained by our previously developed PbS QD photodetectors using doctor

blade deposition [61]). In this sense, if the charge injection/extraction of the photodiode was improved, photovoltaic devices would be more suitable for solar conversion. In any case, we have demonstrated the positive and potential benefit of the MPA ligand exchange for developing conductive thin films of $CsPbBr_3$ PNCs as the basis for photovoltaic detectors. In next sections of this paper additional electronic transport properties will be obtained for future optimization of MPA-treated photodevices.

4.3.3 Electro-Optical Characterization of the Photoconductors

A simpler MSM structure was adopted to characterize photoconductive properties of the thin films based on $CsPbBr_3$ PNCs. In this way, a 300 nm thick absorbing perovskite layer was deposited by doctor blading onto the interdigitated pads. This structure is widely adopted for perovskites [14,28,36,62], because it provides a reliable testing workbench for new strategies with solution processed PNCs.

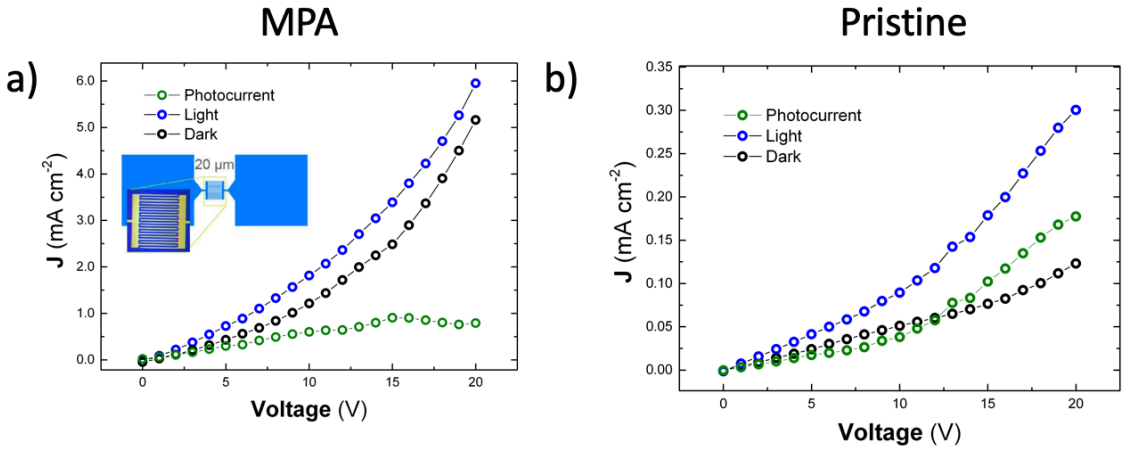

Figure 4.5. J–V characteristics of the device in dark conditions and under illumination with 25 mW cm^{-2} white light for a) MPA-treated devices and b) pristine devices. The total photocurrent (difference between the light and the dark curves) is plotted in green color. The inset shows one test chip blueprint and optical microscopic image before the deposition of the $CsPbBr_3$ PNCs.

The current-versus-voltage characteristic curves (0 to 20 V) of the MSM interdigitated photodetectors are shown in Figure 4.5. The curves display the behavior of the pristine and MPA-treated films of PNCs under dark conditions and white-light illumination (25 mW/cm^2). Noticeably, MPA-treated $CsPbBr_3$ PNC films (Figure 4.5a) display higher dark current levels (black data symbols) and larger photocurrent (green data symbols) than the pristine ones (Figure 4.5b). The difference can be explained in terms of photo-sensitivities, defined as $S = (J_L - J_D)/J_L = \Delta\sigma/(\sigma_0 + \Delta\sigma)$. Here, the current densities J_L and J_D are measured under illumination and dark conditions at a

given voltage, whereas σ_0 and $\Delta\sigma$ are the conductivity under dark conditions and the photoconductivity, respectively.

Dark conductivity and photoconductivity listed in Table 4.3 are extracted from linear fits to the corresponding experimental curves in Figure 4.5 in the 0-10 V region. For higher voltages the J-V curves deviates from the linear law to a quadratic behavior. This nonlinear behavior originates from the space-charge-limited current (SCLC) effect that occurs when uncompensated charge carriers are injected into the material from the MSM contacts. In this condition, the mobility (μ) can be approximately estimated in the SCLC region ($J \sim V^2$) under dark conditions by using the Mott–Gurney law [63]:

$$\mu = \frac{8 J_D L^3}{9 \varepsilon \varepsilon_0 V^2} \tag{4.8}$$

Here, L is the channel length (20 μm), ε_0 is the permittivity of vacuum and ε is the relative dielectric constant of $CsPbBr_3$, which is in the order of ~24 [64]. As listed in Table 4.3, the dark conductivity of the MPA-treated films (25 $\mu S/cm$) increases by more than one order of magnitude with respect to the value in the pristine ones (1 $\mu S/cm$), which is in line with results reported above for Schottky-heterojunctions, a difference that it is mostly due to the increase in the effective carrier mobility for the ligand-exchanged film for which we estimate $\sim 10^{-3}\ cm^2/Vs$, as compared to the value found in pristine films, which is $\sim 10^{-4}\ cm^2/Vs$, with a certain contribution of the background carrier concentration. That is, MPA is possibly doping $CsPbBr_3$ PNCs (n_0 around 6×10^{14} cm^{-3}) over the background carrier concentration of PNCs with original ligands (n_0 around 3×10^{14} cm^{-3}).

	$\sigma_0(\mu S/cm)$	$\Delta\sigma\ (\mu S/cm)$	$S_{10V} = (J_L - J_D)/J_L$	$\mu_{SCLC}\ (cm^2/Vs)$
MPA	0.8	0.33	0.35	10^{-3}
Pristine	0.03	0.03	0.40	10^{-4}

Table 4.3. Dark conductivity (σ_0), photoconductivity (Δσ), photoconductive sensitivity (S), and Mott–Gurney mobility (μ), extracted with Equation 4.8, of MSM photodetectors based on $CsPbBr_3$ PNCs. The pristine and MPA-treated thin films parameters were extracted from J–V curves in Figure 4.5.

4.3.4 CHARACTERIZATION OF THE FET DEVICES

Although the Mott–Gurney law is commonly used to extract the charge-carrier mobility in films of Metal Halide Perovskites, the application of Equation 4.8 is only valid in trap-independent space-charge limited regime [65]. For this reason, the extraction of this parameter needs to be supported with additional analysis, for example from J-V characteristics measured in FET transistors based on films of $CsPbBr_3$ PNCs. This architecture allows to extract the mobility from the field-effect model.

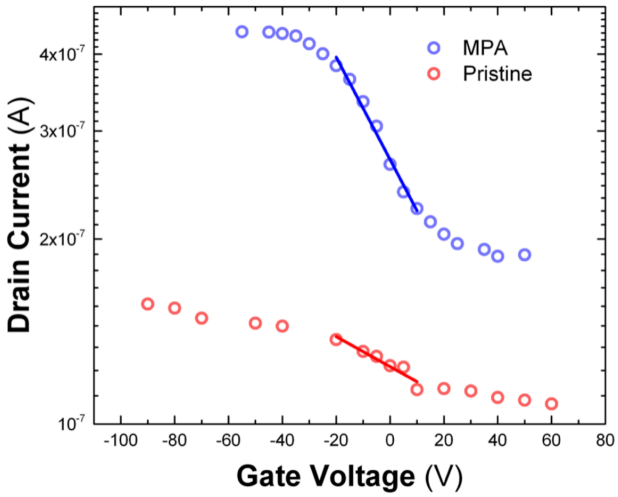

Figure 4.6. Transfer FET curves of processed $CsPbBr_3$ PNCs based FET devices treated with MPA (blue curve) and pristine (red curve).

The FET-mobility in the linear regime was determined using the characteristic output curves of the field-effect transistor, given by the plot of drain-source current (I_{DS}) versus gate voltage (V_{GS}) for a given drain voltage (V_{DS}) bias (Figure 4.6). The transfer curves can be divided into two regions: the linear region and the saturation region. The slope of the linear region can be used to obtain the charge-carrier mobility using the following equation:

$$\frac{\partial I_{DS}}{\partial V_{GS}} = \frac{W}{L}\mu C_S V_{DS} \tag{4.9}$$

Here *L* is the channel length (10 μm), W is the channel width (1 mm) and C_S = 1.15 × 10^{-8} F cm^{-2} is the capacitance of the SiO_2 insulating layer (300 nm thick) in Ossila substrates. The drain-source voltage was set at 1V. In these conditions, the FET-mobility is found to be 0.005 cm^2/Vs for the MPA-treated $CsPbBr_3$ PNCs thin films and 5 × 10^{-4} cm^2/Vs for the pristine ones. These values are a factor 5 greater than those obtained through the analysis performed in previous section on MSM photoconductors in the SCLC regime, but we measure an increase of one order of magnitude after the MPA treatment of the film of PNCs.

4.3.5 TANDEM PbS-PNC PHOTODIODES

Once the effectiveness of the MPA ligand-exchange on the $CsPbBr_3$ PNCs thin films has been proved to render almost a 10-fold increase in the majority of the photodetector figures of merit, we propose here a step forward by demonstrating the processability of a heterojunction between both layers, PbS QDs and $CsPbBr_3$ PNCs, with a ligand exchange processing step after their doctor blade deposition. Given that PbS QDs operate at telecom wavelengths (1550 nm), their integration with $CsPbBr_3$ PNCs would enable the optimized photodetection over a large region of optical frequencies. This kind of heterojunction has well established precedents in literature. Tandem heterostructures are a great promise for overcoming the Shockley–Queisser limit, while the solution processability of colloidal nanocrystals allows to keep the production costs well very low [66]. In the particular case of metal halide perovskite solar cells, the PbS QDs can be used as co-sensitizers. The addition of PbS QDs into $CH_3NH_3PbI_3$ ($MAPbI_3$) precursors was found to be beneficial for the crystallization of perovskites [67]. Also, the processing of PbS QDs as hole transporter layers (HLT) for planar heterojunction perovskite solar cells was recently demonstrated [39]. PbS QDs can readily substitute the spiro-type HTLs, while offering an increased absorption range of the solar spectrum and/or multi-wavelength LEDs due to possible exciplex states between the perovskite and QDs [68]. In the case of photodetectors, the benefits of this hybridization were also demonstrated in another study of $CsPbBr_3$ bulk perovskite layers and PbS QDs based phototransistors with a wide response spectrum, from 400 to 2100 nm [69]. From the point of view of the device fabrication, both PbS QDs and CsPbBr3 NCs are fully compatible since they are formulated in hexane using OAm as ligand. Moreover, both deposition and ligand exchange for QDs and PNCs follow the same procedure.

Figure 4.7 shows the responsivity curve of our tandem-like prototype photodiode (layer and energy band alignment schemes are shown in the inset of Figure 4.7) in the visible and near-infrared spectral regions. The MPA ligand exchange was carried out to the whole structure after the deposition of both PNC and QD films with the same parameters used in the case of Schottky-heterostructure based on single layers of $CsPbBr_3$ PNCs.

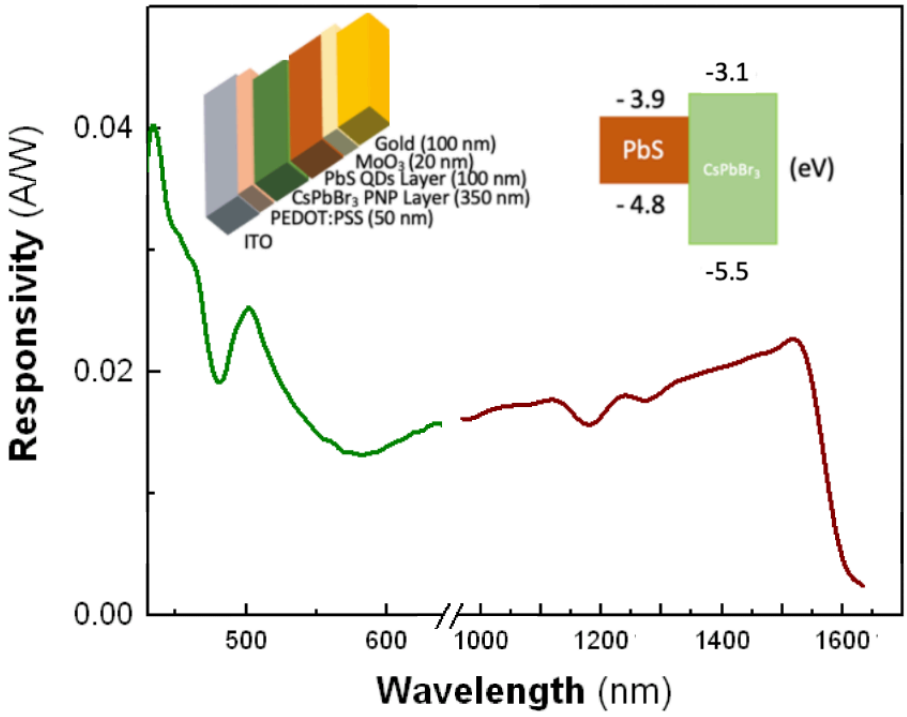

Figure 4.7. Responsivity curve of the MPA ligand-exchanged PbS QDs-$CsPbBr_3$ PNCs heterojunction photodiode. Device architecture is represented in the top inset. The red solid curve represents the extended responsivity range added by the PbS QDs layer while the green solid curve characterizes the responsivity part of the spectrum dominated by $CsPbBr_3$ PNCs. The gap in between the two curves (800 – 900 nm) is due to the switching between reference photodiodes: calibrated Si and Ge detectors and different gratings for measuring in visible and near-infrared windows.

The highest responsivity is around 40 and 25 $mA \cdot W^{-1}$ at visible wavelengths, 430 nm and at the exciton absorption resonance of $CsPbBr_3$ PNCs (green curve in Figure 4.7), respectively. The tandem photodetector reaches a maximum of 20 $mA \cdot W^{-1}$ at the near-infrared spectral region dominated by light absorption of PbS QDs (red curve in Figure 4.7). While it is true that the responsivity obtained in this spectral range is one order of magnitude smaller than previously reported results in single PbS QD-Schottky heterojunctions fabricated in a similar way [17], let note that the PbS layer thickness in our tandem photodevice is significantly thinner (≈100 nm). It is worth mentioning that the present device is a proof of concept of the feasible implementation of two complementary nanomaterials in a single device that must be further optimized in a number of different ways (tandem thicknesses, PNC and PbS bandgaps, photodiode architecture, …) according to the application (optical sensors, visible-NIR cameras, photoreceivers or multiwavelength LEDs for integrated photonics, solar cells, ...).

4.4 CONCLUSIONS

We have presented here a solid-state ligand exchange procedure to replace the original long-chained surface ligands (long-chain aliphatic molecules like oleic acid) of $CsPbBr_3$ PNCs with much shorter MPA ligand molecules. Thin films of densely packed $CsPbBr_3$ PNCs were deposited by means of a layer-by-layer method, up to an optimal thickness of 300 - 400 nm. As a result, Schottky-based heterojunction photodetectors were achieved using doctor blade deposition technique. The resulting devices exhibited and enhanced photovoltaic detection performances. In this way, the short inter-particle distance imposed by MPA ligands led to mobilities in the order of $5 \times 10^{-3}\ \mathrm{cm^2/Vs}$, as determined by FET mobility measurements, which are and order of magnitude greater than those measured in pristine films (without ligand exchange), $5 \times 10^{-4}\ \mathrm{cm^2/Vs}$. This mobility enhancement is the most important parameter that determines the 20-fold higher photoconductivity and the responsivity increase from 7 to 100 mA/W (and a detectivity as high as 8 x 10^{10} jones) measured in our Schottky-based heterostructures. In order extend the applicability of the MPA solid-state ligand exchange, a tandem structure was integrated in the same photovoltaic architecture: a film of PbS QDs on top of a first film made of $CsPbBr_3$ PNCs. The resulting device has a wide spectral response, ranging from the UV to the NIR due to absorption of light and carrier photogeneration in thin solid films formed of $CsPbBr_3$ PNCs and PbS QDs, offering responsivity levels of 40 mA/W at visible wavelengths and 20 mA/W around the telecom C-band (1525-1565 nm). These results can be basis of future photodiode array or CMOS-like cameras operating simultaneously at visible and NIR wavelengths or low-cost applications in the fields of IOT and optical sensing.

4.5 REFERENCES

1. Navarro Arenas, J.; Soosaimanickam, A.; Pashaei Adl, H.; Abargues, R.; P. Boix, P.; Rodríguez-Cantó, P.J.; Martínez-Pastor, J.P. Ligand-Length Modification in CsPbBr3 Perovskite Nanocrystals and Bilayers with PbS Quantum Dots for Improved Photodetection Performance. *Nanomaterials* **2020**, *10*.
2. Kovalenko, M. V; Protesescu, L.; Bodnarchuk, M.I. Properties and potential optoelectronic applications of lead halide perovskite nanocrystals. *Science (80-.).* **2017**, *358*, 745–750.
3. Protesescu, L.; Yakunin, S.; Bodnarchuk, M.I.; Krieg, F.; Caputo, R.; Hendon, C.H.; Yang, R.X.; Walsh, A.; Kovalenko, M. V Nanocrystals of Caesium Lead Halide Perovskites (CsPbX3, X = Cl, Br, and I): Novel Optoelectronic Materials Showing Bright Emission with Wide Color Gamut. *Nano Lett.* **2015**, *15*, 3692–3696.

4. Wu, K.; Liang, G.; Shang, Q.; Ren, Y.; Kong, D.; Lian, T. Ultrafast Interfacial Electron and Hole Transfer from $CsPbBr_3$ Perovskite Quantum Dots. *J. Am. Chem. Soc.* **2015**, *137*, 12792–12795.
5. Colbert, A.E.; Wu, W.; Janke, E.M.; Ma, F.; Ginger, D.S. Effects of Ligands on Charge Generation and Recombination in Hybrid Polymer/Quantum Dot Solar Cells. *J. Phys. Chem. C* **2015**, *119*, 24733–24739.
6. Huang, H.; Polavarapu, L.; Sichert, J.A.; Susha, A.S.; Urban, A.S.; Rogach, A.L. Colloidal lead halide perovskite nanocrystals: synthesis, optical properties and applications. *NPG Asia Mater.* **2016**, *8*, e328–e328.
7. Chen, Y.; Wu, X.; Chu, Y.; Zhou, J.; Zhou, B.; Huang, J. Hybrid Field-Effect Transistors and Photodetectors Based on Organic Semiconductor and CsPbI3 Perovskite Nanorods Bilayer Structure. *Nano-Micro Lett.* **2018**, *10*, 1–9.
8. Yang, T.; Zheng, Y.; Du, Z.; Liu, W.; Yang, Z.; Gao, F.; Wang, L.; Chou, K.-C.; Hou, X.; Yang, W. Superior Photodetectors Based on All-Inorganic Perovskite $CsPbI_3$ Nanorods with Ultrafast Response and High Stability. *ACS Nano* **2018**, *12*, 1611–1617.
9. Zhang, D.; Yang, Y.; Bekenstein, Y.; Yu, Y.; Gibson, N.A.; Wong, A.B.; Eaton, S.W.; Kornienko, N.; Kong, Q.; Lai, M.; et al. Synthesis of Composition Tunable and Highly Luminescent Cesium Lead Halide Nanowires through Anion-Exchange Reactions. *J. Am. Chem. Soc.* **2016**, *138*, 7236–7239.
10. Yang, D.; Fang, H.; Dong, A.; Liu, L.; Hu, W.; Xu, Y.; Zhang, X.; Luo, W.; Lv, L.; Xu, F.; et al. Generalized colloidal synthesis of high-quality, two-dimensional cesium lead halide perovskite nanosheets and their applications in photodetectors. *Nanoscale* **2016**, *8*, 13589–13596.
11. Song, J.; Xu, L.; Li, J.; Xue, J.; Dong, Y.; Li, X.; Zeng, H. Monolayer and Few-Layer All-Inorganic Perovskites as a New Family of Two-Dimensional Semiconductors for Printable Optoelectronic Devices. *Adv. Mater.* **2016**, 4861–4869.
12. Ramasamy, P.; Lim, D.H.; Kim, B.; Lee, S.H.; Lee, M.S.; Lee, J.S. All-inorganic cesium lead halide perovskite nanocrystals for photodetector applications. *Chem. Commun.* **2016**, *52*, 2067–2070.
13. Jang, D.M.; Kim, D.H.; Park, K.; Park, J.; Lee, J.W.; Song, J.K. Ultrasound synthesis of lead halide perovskite nanocrystals. *J. Mater. Chem. C* **2016**, *4*, 10625–10629.
14. Dong, Y.; Gu, Y.; Zou, Y.; Song, J.; Xu, L.; Li, J.; Xue, J.; Li, X.; Zeng, H. Improving All-Inorganic Perovskite Photodetectors by Preferred Orientation and Plasmonic Effect. *Small* **2016**, *12*, 5622–5632.
15. Tong, Y.; Yao, E.-P.; Manzi, A.; Bladt, E.; Wang, K.; Döblinger, M.; Bals, S.; Müller-Buschbaum, P.; Urban, A.S.; Polavarapu, L.; et al. Spontaneous Self-Assembly of Perovskite Nanocrystals into Electronically Coupled Supercrystals: Toward Filling the Green Gap. *Adv. Mater.* **2018**, *30*, 1801117.
16. Hazarika, A.; Zhao, Q.; Gaulding, E.A.; Christians, J.A.; Dou, B.; Marshall, A.R.; Moot, T.; Berry, J.J.; Johnson, J.C.; Luther, J.M. Perovskite Quantum Dot Photovoltaic Materials beyond the Reach of Thin Films: Full-Range Tuning of A-Site Cation Composition. *ACS Nano* **2018**, *12*, 10327–10337.
17. Maulu, A.; Rodríguez-Cantó, P.J.; Navarro-Arenas, J.; Abargues, R.; Sánchez-Royo, J.F.; García-Calzada, R.; Martínez Pastor, J.P. Strongly-coupled PbS QD solids by doctor blading for IR photodetection. *RSC Adv.* **2016**, *6*, 80201–80212.
18. Abargues, R.; Navarro, J.; Rodríguez-Cantó, P.J.; Maulu, A.; Sánchez-Royo, J.F.; Martínez-Pastor, J.P. Enhancing the photocatalytic properties of PbS QD solids: the ligand exchange approach. *Nanoscale* **2019**, *11*, 1978–1987.
19. Ji, G.; Zhao, W.; Wei, J.; Yan, L.; Han, Y.; Luo, Q.; Yang, S.; Hou, J.; Ma, C.Q.

12.88% efficiency in doctor-blade coated organic solar cells through optimizing the surface morphology of a ZnO cathode buffer layer. *J. Mater. Chem. A* **2019**, *7*, 212–220.
20. Huang, H.; Lin, H.; Kershaw, S. V; Susha, A.S.; Choy, W.C.H.; Rogach, A.L. Polyhedral Oligomeric Silsesquioxane Enhances the Brightness of Perovskite Nanocrystal-Based Green Light-Emitting Devices. *J. Phys. Chem. Lett.* **2016**, *7*, 4398–4404.
21. Cai, Y.; Wang, L.; Zhou, T.; Zheng, P.; Li, Y.; Xie, R.-J. Improved stability of CsPbBr3 perovskite quantum dots achieved by suppressing interligand proton transfer and applying a polystyrene coating. *Nanoscale* **2018**, *10*, 21441–21450.
22. Boles, M.A.; Engel, M.; Talapin, D. V Self-Assembly of Colloidal Nanocrystals: From Intricate Structures to Functional Materials. *Chem. Rev.* **2016**, *116*, 11220–11289.
23. Fu, W.; Shi, Y.; Qiu, W.; Wang, L.; Nan, Y.; Shi, M.; Li, H.; Chen, H. High efficiency hybrid solar cells using post-deposition ligand exchange by monothiols. *Phys. Chem. Chem. Phys.* **2012**, *14*, 12094–12098.
24. Crisp, R.W.; Kroupa, D.M.; Marshall, A.R.; Miller, E.M.; Zhang, J.; Beard, M.C.; Luther, J.M. Metal Halide Solid-State Surface Treatment for High Efficiency PbS and PbSe QD Solar Cells. *Sci. Rep.* **2015**, *5*.
25. Baker, D.R.; Kamat, P. V. Tuning the emission of CdSe quantum dots by controlled trap enhancement. *Langmuir* **2010**, *26*, 11272–11276.
26. Li, G.; Huang, J.; Zhu, H.; Li, Y.; Tang, J.-X.; Jiang, Y. Surface Ligand Engineering for Near-Unity Quantum Yield Inorganic Halide Perovskite QDs and High-Performance QLEDs. *Chem. Mater.* **2018**, *30*, 6099–6107.
27. Zhou, L.; Yu, K.; Yang, F.; Cong, H.; Wang, N.; Zheng, J.; Zuo, Y.; Li, C.; Cheng, B.; Wang, Q. Insight into the effect of ligand-exchange on colloidal CsPbBr3 perovskite quantum dot/mesoporous-TiO2 composite-based photodetectors: Much faster electron injection. *J. Mater. Chem. C* **2017**, *5*, 6224–6233.
28. Gong, M.; Sakidja, R.; Goul, R.; Ewing, D.; Casper, M.; Stramel, A.; Elliot, A.; Wu, J.Z. High-Performance All-Inorganic CsPbCl3 Perovskite Nanocrystal Photodetectors with Superior Stability. *ACS Nano* **2019**, *13*, 1772–1783.
29. Balazs, D.M.; Rizkia, N.; Fang, H.H.; Dirin, D.N.; Momand, J.; Kooi, B.J.; Kovalenko, M. V.; Loi, M.A. Colloidal Quantum Dot Inks for Single-Step-Fabricated Field-Effect Transistors: The Importance of Postdeposition Ligand Removal. *ACS Appl. Mater. Interfaces* **2018**, *10*, 5626–5632.
30. Maulu, A.; Navarro-Arenas, J.; Rodríguez-Cantó, P.; Sánchez-Royo, J.; Abargues, R.; Suárez, I.; Martínez-Pastor, J. Charge Transport in Trap-Sensitized Infrared PbS Quantum-Dot-Based Photoconductors: Pros and Cons. *Nanomaterials* **2018**, *8*, 677.
31. Hori, T.; Moritou, H.; Fukuoka, N.; Sakamoto, J.; Fujii, A.; Ozaki, M. Photovoltaic Properties in Interpenetrating Heterojunction Organic Solar Cells Utilizing MoO3 and ZnO Charge Transport Buffer Layers. *Materials (Basel).* **2010**, *3*, 4915–4921.
32. Golubev, T.; Liu, D.; Lunt, R.; Duxbury, P. Understanding the impact of C60 at the interface of perovskite solar cells via drift-diffusion modeling. *AIP Adv.* **2019**, *9*, 35026.
33. Moyen, E.; Kanwat, A.; Cho, S.; Jun, H.; Aad, R.; Jang, J. Ligand removal and photo-activation of CsPbBr3 quantum dots for enhanced optoelectronic devices. *Nanoscale* **2018**, *10*, 8591–8599.
34. Ng, C.H.; Ripolles, T.S.; Hamada, K.; Teo, S.H.; Lim, H.N.; Bisquert, J.; Hayase, S. Tunable Open Circuit Voltage by Engineering Inorganic Cesium Lead Bromide/Iodide Perovskite Solar Cells. *Sci. Rep.* **2018**, *8*, 2482.

35. Li, Y.; Shi, Z.-F.; Li, X.-J.; Shan, C.-X. Photodetectors based on inorganic halide perovskites: Materials and devices. *Chinese Phys. B* **2019**, *28*, 017803.
36. Li, Y.; Shi, Z.F.; Li, S.; Lei, L.Z.; Ji, H.F.; Wu, D.; Xu, T.T.; Tian, Y.T.; Li, X.J. High-performance perovskite photodetectors based on solution-processed all-inorganic CsPbBr3 thin films. *J. Mater. Chem. C* **2017**, *5*, 8355–8360.
37. Song, X.; Liu, X.; Yu, D.; Huo, C.; Ji, J.; Li, X.; Zhang, S.; Zou, Y.; Zhu, G.; Wang, Y.; et al. Boosting Two-Dimensional MoS_2 /$CsPbBr_3$ Photodetectors via Enhanced Light Absorbance and Interfacial Carrier Separation. *ACS Appl. Mater. Interfaces* **2018**, *10*, 2801–2809.
38. Yao, Y.; Zhang, B.; Green, M.A.; Conibeer, G.; Shrestha, S.K. Photovoltaic effect in Ge nanocrystals/c-silicon heterojunctions devices. In Proceedings of the 2010 35th IEEE Photovoltaic Specialists Conference; 2010; pp. 1889–1893.
39. Hu, L.; Wang, W.; Liu, H.; Peng, J.; Cao, H.; Shao, G.; Xia, Z.; Ma, W.; Tang, J. PbS colloidal quantum dots as an effective hole transporter for planar heterojunction perovskite solar cells. *J. Mater. Chem. A* **2015**, *3*, 515–518.
40. Zhang, J.; Wang, Q.; Zhang, X.; Jiang, J.; Gao, Z.; Jin, Z.; Liu, S. (Frank) High-performance transparent ultraviolet photodetectors based on inorganic perovskite $CsPbCl_3$ nanocrystals. *RSC Adv.* **2017**, *7*, 36722–36727.
41. Zhou, L.; Yu, K.; Yang, F.; Zheng, J.; Zuo, Y.; Li, C.; Cheng, B.; Wang, Q. All-inorganic perovskite quantum dot/mesoporous TiO2 composite-based photodetectors with enhanced performance. *Dalt. Trans.* **2017**, *46*, 1766–1769.
42. Li, Y.; Shi, Z.; Lei, L.; Zhang, F.; Ma, Z.; Wu, D.; Xu, T.; Tian, Y.; Zhang, Y.; Du, G.; et al. Highly Stable Perovskite Photodetector Based on Vapor-Processed Micrometer-Scale $CsPbBr_3$ Microplatelets. *Chem. Mater.* **2018**, *30*, 6744–6755.
43. Lin, R.; Li, X.; Zheng, W.; Huang, F. Balanced Photodetection in Mixed-Dimensional Phototransistors Consisting of $CsPbBr_3$ Quantum Dots and Few-Layer MoS_2. *ACS Appl. Nano Mater.* **2019**, *2*, 2599–2605.
44. Li, P.; Shivananju, B.N.; Zhang, Y.; Li, S.; Bao, Q. High performance photodetector based on 2D $CH_3NH_3PbI_3$ perovskite nanosheets. *J. Phys. D. Appl. Phys.* **2017**, *50*, 094002.
45. Yang, Z.; Wang, M.; Li, J.; Dou, J.; Qiu, H.; Shao, J. Spray-Coated $CsPbBr_3$ Quantum Dot Films for Perovskite Photodiodes. *ACS Appl. Mater. Interfaces* **2018**, *10*, 26387–26395.
46. Huang, H.; Bodnarchuk, M.I.; Kershaw, S. V.; Kovalenko, M. V.; Rogach, A.L. Lead Halide Perovskite Nanocrystals in the Research Spotlight: Stability and Defect Tolerance. *ACS Energy Lett.* 2017, *2*, 2071–2083.
47. Hoffman, J.B.; Zaiats, G.; Wappes, I.; Kamat, P. V. CsPbBr3Solar Cells: Controlled Film Growth through Layer-by-Layer Quantum Dot Deposition. *Chem. Mater.* **2017**, *29*, 9767–9774.
48. Akkerman, Q.A.; Gandini, M.; Di Stasio, F.; Rastogi, P.; Palazon, F.; Bertoni, G.; Ball, J.M.; Prato, M.; Petrozza, A.; Manna, L. Strongly emissive perovskite nanocrystal inks for high-voltage solar cells. *Nat. Energy* **2017**, *2*, 16194.
49. Yang, Z.; Wang, M.; Li, J.; Dou, J.; Qiu, H.; Shao, J. Spray-Coated CsPbBr3 Quantum Dot Films for Perovskite Photodiodes. *ACS Appl. Mater. Interfaces* **2018**, *10*, 26387–26395.
50. Zhang, Y.; Wu, G.; Liu, F.; Ding, C.; Zou, Z.; Shen, Q. Photoexcited carrier dynamics in colloidal quantum dot solar cells: insights into individual quantum dots, quantum dot solid films and devices. *Chem. Soc. Rev.* **2020**, *49*, 49–84.
51. Kirchartz, T.; Deledalle, F.; Tuladhar, P.S.; Durrant, J.R.; Nelson, J. On the Differences between Dark and Light Ideality Factor in Polymer:Fullerene Solar Cells. *J. Phys. Chem. Lett.* **2013**, *4*, 2371–2376.

52. Breitenstein, O.; Altermatt, P.P.; Ramspeck, K.; Schenk, A. The Origin of Ideality Factors n > 2 of Shunts and Surfaces in the Dark I-V Curves of Si 625 Solar Cells 2006.
53. Zolfaghari, Z.; Hassanabadi, E.; Pitarch-Tena, D.; Yoon, S.J.; Shariatinia, Z.; van de Lagemaat, J.; Luther, J.M.; Mora-Seró, I. Operation Mechanism of Perovskite Quantum Dot Solar Cells Probed by Impedance Spectroscopy. *ACS Energy Lett.* **2019**, *4*, 251–258.
54. Tress, W.; Yavari, M.; Domanski, K.; Yadav, P.; Niesen, B.; Correa Baena, J.P.; Hagfeldt, A.; Graetzel, M. Interpretation and evolution of open-circuit voltage, recombination, ideality factor and subgap defect states during reversible light-soaking and irreversible degradation of perovskite solar cells. *Energy Environ. Sci.* **2018**, *11*, 151–165.
55. Zhang, Z.-Y.; Wang, H.-Y.; Zhang, Y.-X.; Hao, Y.-W.; Sun, C.; Zhang, Y.; Gao, B.-R.; Chen, Q.-D.; Sun, H.-B. The Role of Trap-assisted Recombination in Luminescent Properties of Organometal Halide CH3NH3PbBr3 Perovskite Films and Quantum Dots. *Sci. Rep.* **2016**, *6*, 27286.
56. Liao, P.; Zhao, X.; Li, G.; Shen, Y.; Wang, M. A New Method for Fitting Current-Voltage Curves of Planar Heterojunction Perovskite Solar Cells. *Nano-micro Lett.* **2018**, *10*, 5.
57. Cappelletti, M.A.; Casas, G.A.; Cédola, A.P.; Peltzer y Blancá, E.L.; Marí Soucase, B. Study of the reverse saturation current and series resistance of p-p-n perovskite solar cells using the single and double-diode models. *Superlattices Microstruct.* **2018**, *123*, 338–348.
58. Yang, Z.; Surrente, A.; Galkowski, K.; Miyata, A.; Portugall, O.; Sutton, R.J.; Haghighirad, A.A.; Snaith, H.J.; Maude, D.K.; Plochocka, P.; et al. Impact of the Halide Cage on the Electronic Properties of Fully Inorganic Cesium Lead Halide Perovskites. *ACS Energy Lett.* **2017**, *2*, 1621–1627.
59. Dong, R.; Fang, Y.; Chae, J.; Dai, J.; Xiao, Z.; Dong, Q.; Yuan, Y.; Centrone, A.; Zeng, X.C.; Huang, J. High-Gain and Low-Driving-Voltage Photodetectors Based on Organolead Triiodide Perovskites. *Adv. Mater.* **2015**, *27*, 1912–1918.
60. Algadi, H.; Mahata, C.; Woo, J.; Lee, M.; Kim, M.; Lee, T. Enhanced Photoresponsivity of All-Inorganic (CsPbBr3) Perovskite Nanosheets Photodetector with Carbon Nanodots (CDs). *Electronics* **2019**, *8*, 678.
61. Clifford, J.P.; Konstantatos, G.; Johnston, K.W.; Hoogland, S.; Levina, L.; Sargent, E.H. Fast, sensitive and spectrally tuneable colloidal-quantum-dot photodetectors. *Nat. Nanotechnol.* **2009**, *4*, 40–44.
62. Li, Y.; Shi, Z.; Lei, L.; Ma, Z.; Zhang, F.; Li, S.; Wu, D.; Xu, T.; Li, X.; Shan, C.; et al. Controllable Vapor-Phase Growth of Inorganic Perovskite Microwire Networks for High-Efficiency and Temperature-Stable Photodetectors. *ACS Photonics* **2018**, *5*, 2524–2532.
63. Haruta, Y.; Ikenoue, T.; Miyake, M.; Hirato, T. Fabrication of (101)-oriented $CsPbBr_3$ thick films with high carrier mobility using a mist deposition method. *Appl. Phys. Express* **2019**, *12*, 085505.
64. Zhang, P.; Zhang, G.; Liu, L.; Ju, D.; Zhang, L.; Cheng, K.; Tao, X. Anisotropic Optoelectronic Properties of Melt-Grown Bulk $CsPbBr_3$ Single Crystal. *J. Phys. Chem. Lett.* **2018**, *9*, 5040–5046.
65. Herz, L.M. Charge-Carrier Mobilities in Metal Halide Perovskites: Fundamental Mechanisms and Limits. *ACS Energy Lett.* **2017**, *2*, 1539–1548.
66. Karani, A.; Yang, L.; Bai, S.; Futscher, M.H.; Snaith, H.J.; Ehrler, B.; Greenham, N.C.; Di, D. Perovskite/Colloidal Quantum Dot Tandem Solar Cells: Theoretical Modeling and Monolithic Structure. *ACS Energy Lett.* **2018**, *3*, 869–874.

67. Han, J.; Luo, S.; Yin, X.; Zhou, Y.; Nan, H.; Li, J.; Li, X.; Oron, D.; Shen, H.; Lin, H. Hybrid PbS Quantum-Dot-in-Perovskite for High-Efficiency Perovskite Solar Cell. *Small* **2018**, *14*, 1801016.
68. Sanchez, R.S.; de la Fuente, M.S.; Suarez, I.; Muñoz-Matutano, G.; Martinez-Pastor, J.P.; Mora-Sero, I. Tunable light emission by exciplex state formation between hybrid halide perovskite and core/shell quantum dots: Implications in advanced LEDs and photovoltaics. *Sci. Adv.* **2016**, *2*, e1501104.
69. Yu, Y.; Zhang, Y.; Jin, L.; Chen, Z.; Li, Y.; Cao, M.; Che, Y.; Yao, J.; Li, Q. Highly photosensitive vertical photodetectors based on CsPbBr3 and PbS quantum dot layered heterojunction. In Proceedings of the Optoelectronic Devices and Integration VII; Li, B., Yu, C., Zhang, X., Zhang, X., Eds.; SPIE, 2018; Vol. 10814, p. 38.

5 OPTICAL AMPLIFICATION IN HOLLOW-CORE FIBERS DOPED WITH PNCS

In this chapter, hollow-core negative-curvature fibers (HC-NCF) are thoroughly investigated as a potential platform for light amplification. For this purpose, the air microchannels of the fiber are filled by $CsPbBr_3$ perovskite nanocrystals (PNCs) described in the previous sections. The excitation of the PNCs by a laser pump beam at 405 nm demonstrates an enhancement of a laser probe beam at 515 nm coupled into the fiber. In particular, optical gain was found in the best device with an excitation power as low as 100-200 nW. Experimental data can be nicely reproduced by a model based on parametric oscillators, indicating that the gain assisted mechanism could be based on a nonlinear process. In this way, the present chapter converges with the main topic of the thesis related with the implementation of photonic functionalities. Indeed, the proposed device could be useful in a broad range of applications including signal regeneration or gas sensors. Experimental results are also interesting from the point of view of material science: the demonstration of signal regeneration under CW low excitation fluencies, much below the threshold of stimulated emission, represents an important milestone in the current state of art of the perovskite NCs.

The main results of the present chapter were published in *Nanomaterials* (journal with impact factor of 4.324 in 2019, ranked in Q2 within the Materials Science Multidisciplinary and Nanoscience & Nanotechnology categories of WoS) [1]. The work was carried out during a research stay in the Department of Electronics and Nanoengineering of the Aalto University (Helsinki, Finland) under the supervision of Prof. Zhipei Sun. The synthesis of the PNCs was carried out by Andrés F. Gualdrón-Reyes and Iván Mora-Seró, both members of the Institute of Advanced Materials (INAM) in the University Jaime I (Castellón, Spain). The hollow-core fiber was fabricated by Shou-Fei Gao, Ying-Ying Wang and Pu Wang at the Beijing Engineering Research Centre of Laser Technology (Beijing, China). Experimental results and modelling were carried out by Juan Navarro-Arenas under the supervision of Isaac Suárez and Juan P. Martínez Pastor.

5.1 INTRODUCTION

Hollow-core negative-curvature fibers (HC-NCF) are a special class of optical fibers in which the cladding is composed by an array of hollow glass tubes surrounding a hollow-core [2]. NCFs are also referred to *hypocycloid-shaped hollow-core fibers* [3], *revolver fibers* [4], *tube lattice fibers* [5] or *hollow-core anti-resonant fibers* [6,7]. In all these fibers, the curvature of the normal surface in the region surrounding the central hollow-core is negative with respect to the radial unit vector. HC-NCFs allow for antiresonant reflecting optical waveguiding mechanism [8], and differ from hollow-core photonic crystal fibers (HC-PCF), formed by a two-dimensional periodic cladding structure [9]. The degrees of freedom introduced by the core-shape boundary in HC-NCFs allow to define realizable fiber arrangements that can provide improved performance in terms of leakage and bending losses compared to standard fibers [10]. In this way, since their appearance in 2002, with the Kagome-type broadband hollow-core fiber [11], the HC-NCFs have attracted significant attention of the photonics community; as such fibers are expected to reach new frontiers in the fiber optics field and serve as a workbench for developing new technologies. These fibers support extremely large transmission bandwidths and low field dielectric overlap, avoiding a significant decrease of the absorption loss with respect to other fiber designs and the presence of non-linearities such as the Kerr effect, making them excellent waveguides for high pulse delivery and other high optical density applications [12]. Examples of practical applications include the development of high-power diode-pumped alkali lasers [13] or the signal splitting in optical telecommunications networks [14,15]. More recently, HC-ARFs have been also suggested as a potential platform for supermode excitation, enabling a broader range of integrated applications [16,17].

Hollow-core fibers can also serve as hosts for fluids or nanoparticles, working as a *lab-on-a-fiber* for the study of optical properties of infiltrated nanomaterials. In this way, filling air holes with different nanomaterials exhibiting different functionalities allows a large range of potential applications, such as chemo-/bio-sensing [18]. Given the relatively youth of this kind of microstructured fibers, only a few amount of research works have been developed in this direction, as optofluidic lasers [19] and sensors [20]. Thus far, the combination of emitting materials with HC-NCFs has not been examined, although we can find a few HC-PCFs demonstrations of lasing at visible wavelengths by using CdZnS/ZnS core-shell colloidal Quantum Dots (QDs) [21–23], and optical amplification at telecommunication wavelengths with PbS colloidal QDs [24,25].

In this chapter, we present the inclusion of $CsPbBr_3$ PNCs in HC-NCFs as potential all-fiber active optical microdevices. For this purpose, the air holes of the micro-structured silica fiber are filled with colloidal PNCs by capillary forces. The method for infiltrating PNCs into the HC-NCF was properly optimized to obtain a homogeneous adhesion of the nanocrystals to their walls along tens of centimeters. In the resulting active photonic structure that was modeled by COMSOL Multiphysics software, a probe beam coupled at the input facet of the HC-NCF is enhanced up to +3 dB under 405 mm Continuous Wave (CW) optical pumping. Although this optical amplification can be phenomenologically modeled by the standard theory of Erbium-doped fiber amplifiers [26], stimulated emission conditions are not reached under the low power CW laser pumping used in our experiments. Alternatively, we suggest a nonlinear mechanism to explain the experimentally observed amplification, even if further investigation is needed to elucidate the ultimate origin for this mechanism.

These results not only represent a thresholdless gain assisted mechanism for HC-NCFs, but also pave the road of integrating a broad range of functionalities within these fibers. In particular, it is well known that nonlinear processes are necessary to develop a full optical signal processing in a telecommunication system [27]. Thus, the nonlinear mechanism proposed here could be useful in the implementation of different photonic tasks, such as signal regeneration, modulation, multiplexing or demultiplexing, among others [27]. In addition, the particular structure of HC-NFCs is an excellent platform for sensing of high-toxicity gases [28]. In these conditions, since PNCs also demonstrate a high sensitivity to different gas or liquid compounds [29], the insertions of PNCs in the HC-NFCs is expected to enhance sensitivity with gas and liquid samples and hence serving as the basis to develop high throughput optical chemo-/bio-sensors.

5.2 FABRICATION OF THE PNC-DOPED HC-NCF FIBERS

5.2.1 $CsPbBr_3$ NANOCRYSTAL SYNTHESIS

$CsPbBr_3$ nanocrystals were synthetized following the hot-injection method (presented in section 3.1.1 of this Thesis) with the modifications detailed below. All the reactants were used as received without additional purification process. Briefly, a Cs-oleate solution was prepared by mixing 0.41 g Cs_2CO_3 (Sigma-Aldrich, Madrid, Spain, 99.9%), 1.25 mL of oleic acid (OA, Sigma Aldrich, Spain, 90%) and 20 mL of 1-octadecene (1-ODE, Sigma-Aldrich, Spain, 90%) into a 50 mL three-neck flask at 120 °C

under vacuum for 1 h, stirring constantly. Then, the mixture was N_2-purged and heated at 150 ˚C until the Cs_2CO_3 was completely dissolved. The solution was stored under N_2, keeping the temperature at 100 ˚C to prevent the Cs-oleate precipitation. For the synthesis of $CsPbBr_3$ nanocrystals, 0.69 g $PbBr_2$ (ABCR, Spain, 99.999%) was mixed with 50 mL of 1-ODE into a 100 mL three-neck flask. The mixture was heated at 120 ˚C under vacuum for 1 h, keeping a constant stirring. Then, 5 mL of both OA and oleylamine (OLA, Sigma-Aldrich, Spain, 98%) were separately added to the flask under N_2 atmosphere, and rapidly heated to reach 170 ˚C, injecting quickly 4 mL of Cs-oleate solution. Lastly, the flask was immersed into a bath ice for 5 s to quench the reaction mixture. For the isolation of PNCs, the colloidal solutions were centrifuged at 4700 rpm for 10 min. The PNCs were separated after discarding the supernatant and re-dispersed in hexane to prepare a colloidal solution with a concentration of 50 mg/mL. The absorption spectrum of this colloidal solution exhibits a well-defined excitonic edge around 505 nm, whereas the PL spectrum is rather narrow (24.8 nm) and centered at 514 nm (see Figure 5.1a). Absorption/PL data are in agreement with previously published results for cubic-shape PNCs of similar size (10 nm in average, as shown in Figure 5.1b) [30].

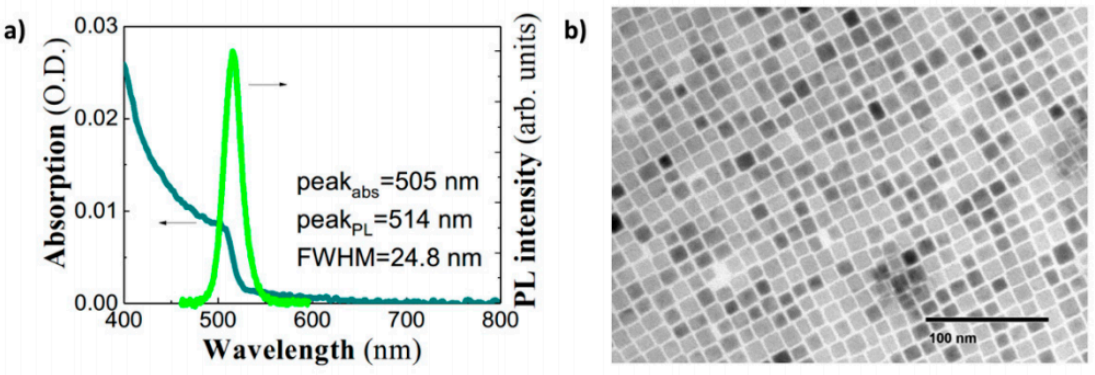

Figure 5.1. (a) Absorbance (blue continuous line) and PL (green continuous line) spectra of $CsPbBr_3$ PNCs dispersed in hexane; and (b) TEM image of cubic $CsPbBr_3$ PNCs. The average cube side is around 10 nm.

5.2.2 Fabrication and Characteristics of the HC-NCFs

The Hollow-Core fiber was fabricated by the stack-and-draw technique. This fiber is quite similar with the one published in reference [31]: a HC fiber with seven untouched capillary tubes built around the hollow-core. The HC-NCF was properly designed to span the transmission window between 400 to 780 nm in order to present low attenuation at both the emission wavelength of the PNCs (515 nm) and the pump beam wavelength (405 nm). Indeed, propagation losses of the fundamental air mode at the pass band are

reduced down to 0.04 dB·cm^{-1} and 0.14 dB·cm^{-1} at 514 nm and 405 nm, respectively. Testing fibers where cleaved with a fiber cleaver (CT-101, Fujikura). An optical microscope (WITec alpha300) was used to map the backscattered PL light of the PNCs infiltrated in the HC-NCF.

5.2.3 FABRICATION AND SIMULATION OF HC-NCFS DOPED WITH PNCS

A short piece of HC-NCF is submerged inside the colloidal solution of PNCs to load the fiber's air tubes (of radii 3 μm and radially distributed with a period of 10 μm beneath the cladding of the HC-NCF, as shown in Figure 5.1) with PNCs by capillary action. Since the size of the PNCs (10 nm) is much smaller than these holes, the colloidal solution easily infiltrates through the SiO_2-air hole walls, where PNCs are deposited, as demonstrated below. The length, *h*, covered by the liquid inside the air capillary can be calculated by applying the Jurin's law, which relates the radius *r* of the fiber microtube with the surface tension γ of the PNC-colloidal solution [32]:

$$\mathrm{h} = \frac{2\gamma\cos(\Theta)}{\rho g r} \qquad (5.1)$$

Here *g* is the gravitational acceleration, ρ the liquid density and Θ the contact angle between the liquid and the capillary wall. Since the concentration of PNCs in the solvent is relatively low (see below), γ and ρ can be approximated by the values reported for hexane, 18 dyn/cm and 0.659 g/mL [33], respectively. In these conditions, and assuming a contact angle of $\Theta = 0$ (to estimate the upper limit for *h*), Jurin's law predicts that h is much longer than used fiber lengths (0.6-1.4 cm). The optimum concentration of the colloidal solution containing the $CsPbBr_3$ PNCs was around 1 mg/mL, being the dipping process maintained over 1 day to get a uniform loading of the HC-NCF. A careful cleaving procedure (CT-101, Fujikura) was carried out in order to smooth the fiber facets before characterization and gain experiments.

As expected, PNC-loaded HC-NCFs show an uniform PL along 140 mm, as shown in Figure 5.2b (image of the whole 140 mm long fiber and zoom of a 0.8 mm long fragment). In addition, PL cross section images measured at the input (Figure 5.2c) and middle (Figure 5.2d) faces of the PNC-loaded HC-NCF clearly demonstrate that light emission is concentrated in the air tube walls and maintained along the fiber (also visible in Figure 5.2b).

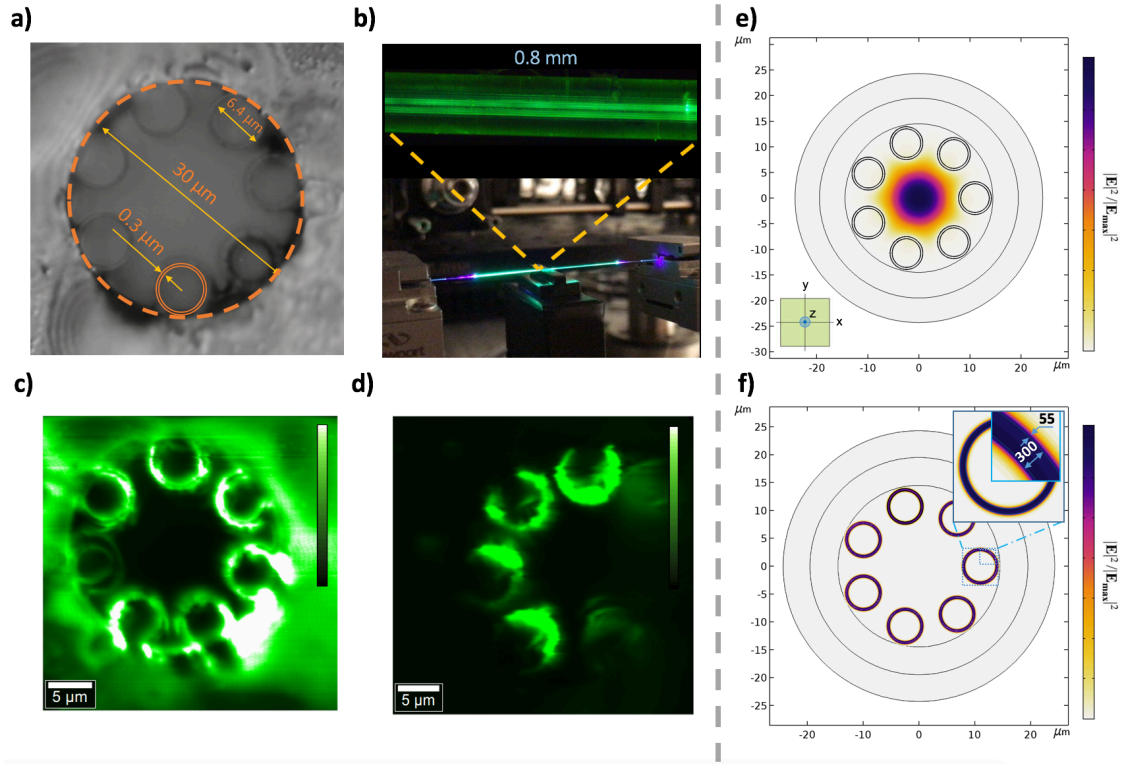

Figure 5.2. (a) Cross section of an undoped fiber taken with optical microscopy. (b) Picture of the whole doped HC-NCF being pumped with the 405 nm CW laser and zoomed axial fragment (this image was registered with an optical microscope that assists the experimental setup described in the section 3.2.2.E of this thesis). (c) and (d) PL cross-section images at input and intermediate (after cleaving) faces of the HC-NCF, respectively. (e) Simulation of the modal field distribution of the 7-tube HC-NCF fiber operating at a wavelength of 515 nm in the absence of PNCs. Z-axis corresponds to the propagation direction. (f) Modal field distribution of the HC-NCF doped with PNCs concentrated on the tube walls after considering a PNC layer with 55 nm thickness.

The HC-NCF was simulated with COMSOL Multiphysics software by using the finite element method with a circular Perfectly Matched Layer (PML) applied to the outermost ring of the structure geometry (see Figure 5.2e-f). First of all, simulation of the unloaded membrane showed the central HE_{11}-core mode (this mode is depicted in Figure 5.2e) with an effective index of 0.99984 reported from this type of fibers [31]. However, the adhesion of the PNCs on both sides of the walls of the fiber allows the propagation of modes through the walls of the HC-NCF. The PNCs are considered to be attached to both sides of the walls. In particular, a supermode composed by seven degenerated cladding modes are supported with an effective index of 1.4574 (Figure 5.2f). Indeed, the calculated modal distributions corroborate the experimental PL-map shown in Figure 5.2c-d. These simulations were carried out by considering seven non-touching SiO_2 capillary membranes with a thickness of 300 nm surrounded by two coating layers (the inner and the outer) of PNCs with a thickness of 55 nm. The PNC film thickness was estimated from the optical images (Figure 5.2c-d) and contrasted with profilometry

measurements from dip-coated PNC films prepared on top of a SiO_2 substrate. In both cases the thickness was carefully controlled by the right concentration of PNCs in the solvent (from 1 to 50 mg/mL). Also, the uniform deposition of PNCs along the fiber was checked by sampling the cross section of the loaded HC-NCF device at different lengths (1, 2 and 3 cm from one of the open ends), obtaining a mean thickness of around 60±10 nm. The operation wavelength was set equal to 500 nm (since there is not too much difference in the 400-550 nm range), the refractive index of membrane was fixed to 1.46 (SiO_2), and the refractive index of the PNCs was considered in the range of n_p = 1.8 – 2.2, as reported elsewhere [34].

Therefore, the adhesion of PNCs strongly modifies the light propagation properties of the HC-NCF for both pumping and probe laser beams. Indeed, the super-mode distribution depends on the thickness of PNCs deposited at the capillary walls. For this purpose, we evaluate the mode confinement of the super-mode as a function of the PNC-doped thickness through the following overlap integral Γ_p:

$$\Gamma_p = \frac{\iint_{\text{PNC Rings}} |\langle S_z(x,y)\rangle| dxdy}{\iint_{-\infty}^{\infty} |\langle S_z(x,y)\rangle| dxdy} \quad (5.2)$$

Here, the modulus of the time-averaged normal component of the Poynting vector is integrated in the area occupied by the nanocrystals and compared to the whole extension of the modal field distribution. In particular, Γ_p = 0.2 is calculated from a thickness of PNCs of 55 nm, as determined from the optical images.

5.3 RESULTS AND DISCUSSION

5.3.1 OPTICAL AMPLIFICATION IN THE HC-NCF DOPED WITH PNCS.

Optical amplification in the PNC-doped HC-NCFs was characterized by coupling pump and probe signal beams at the input facet of the HC-NCF, as commonly used in erbium-doped fiber optical amplifiers [26]. The details of experimental setup are described in section 3.2.2.E of this thesis. Optical amplification can be observed as an enhancement of the probe signal by increasing pump power. Experimental spectra recorded for different excitation fluencies (data symbols in Figure 5.3a) were deconvoluted by the sum of two Gaussian functions (solid lines in Figure 5.3a) in order to study the propagation of the PL generated by the CW-laser pump (405 nm) and the

probe signal light (515 nm), independently. On the one hand, the integrated PL of PNCs exhibits a sharp increase under low excitation regime (i.e. < 0.5 μW of absorbed pump power) and PL saturates above this value (brown solid circles in Figure 5.3b), whereas the probe signal increases linearly in the entire range of absorbed pump power (green solid circles in Figure 5.3b). Here, since the excitation light coupled in the cladding modes will be strongly attenuated by the absorption of the PNCs, the pump beam is considered to be propagated through the fundamental air mode. In these conditions, the observed saturation effect can be attributed to propagation losses of the pump beam along the HC-NCF core (0.14 dB/cm). Obviously, these losses are quite low and the propagation of the pump beam is assured through the entire length of the fiber, hence being effective the excitation of PL from PNCs by the evanescent field of the HC-NCF HE_{11}-core mode (Figure 5.2e). Indeed, a similar co-propagation of pump and PL was already exploited in planar waveguide amplifiers [35,36]. From these experiments we deduce a signal amplification or gain P_{out}/P_{in} (ratio of probe signal at the output facet of the fiber over that at the input one) that increases with the absorbed pump power and with the HC-NCF length (Figure 5.3c). Consequently, the probe signal might well be enhanced by the pump-activated amplification, due to the interaction with the infiltrated PNCs in the fiber.

The full gain of the HC-NCF can be calculated by:

$$G_{dB} = 10\log_{10}\left(\frac{I_{Probe}(P_{abs})}{I_{Probe}(0)}\right) \tag{5.3}$$

Here $I_{probe}(P_{abs})$ is the output signal intensity at the probe light wavelength as a function of the absorbed pump power (P_{abs}). In this way, a signal amplification P_{out}/P_{in} = 2 (3 dB gain) is demonstrated for the highest pump power in a 140 mm long HC-NCF (black solid squares in Figure 5.3c). The optical amplification is significantly reduced for shorter fibers, 80 and 60 mm long, where less than 2 and 1 dB is measured (blue and red solid squares in Figure 5.3c), respectively. The observed optical amplification as a function of the HC-NCF length follows the $e^{(g \cdot L)}$ law commonly observed in waveguide or fiber optical amplifiers [37]. The saturation observed in P_{out}/P_{in}, especially for short fibers, can be explained by the attenuation of the pump beam, as explained above. It is worth noting that these three HC-NCFs in Figure 5.3c were doped by using the same PNC-solution with a concentration of 1 mg/mL, which is the optimum value for the fabrication process described in Section 5.2.2 of this Thesis. A minimum amount of PNCs deposited

in the HC-NCF are required, in agreement with previous results of waveguides doped with colloidal nanocrystals or dyes [36].

5.3.2 MODELLING THE OPTICAL AMPLIFICATION

The optical gain generated in a waveguide is usually simulated by a rate equation model coupled with the propagation equation [38]. Here, an analytical solution of the power propagated in the HC-NCF can be obtained by using the formalism developed in erbium-doped fiber amplifiers, applicable under small-signal (<20 dB) amplification [39]. This model reproduces the signal and gain generated in an optical amplifier with amplification of the spontaneous emission (ASE). The discussion is limited to a signal beam (s) and a pump beam (p), identically treated in the formalism. In addition, the pump and the PNC-doping concentration are considered homogeneous over the cross-section area A of the core, whereas the propagation losses for the signal beam are considered negligible. In these conditions, the gain of the signal beam fulfils the analytical equation derived in Section 2.3.2.A of this thesis based on previous fiber amplifier literature [40]:

$$G_s(L) = 10\log_{10}(e)\left[\frac{\Gamma_p\,(\sigma_s^e + \sigma_s^a)\tau\phi_p}{h\nu_p A}P_a - \alpha_s L\right]dB \tag{5.4}$$

where $\alpha_s = \varrho\Gamma_s\sigma_s^a$ is the signal absorption constant and the saturation power, ϱ is the concentration of PNCs per unit volume, τ is the radiative lifetime of the PNCs, σ_s^a and σ_s^e are the absorption and emission cross sections for the signal beam, Γ_p is the modal confinement factor calculated for the pump (or the signal beam) through Equation 5.2, P_a is the absorbed laser pumping power and the area A refers to the cross section of the HC-NCF.

Here, the area A was set 7.5 μm^2, τ was fixed to τ = 15 *ns* as reported elsewhere for this kind of nanocrystals [41], Γ_p = 0.2 was obtained from the COMSOL simulation described in Section 5.2.1, and ν_p is the pump frequency. The quantum efficiency of the emitters was set to be around ϕ_p = 0.85, as reported for these PNCs [42]. Although it is well known that this parameter decreases in thin films [43], it does not show a critical impact in the simulation results, and can be ranged between 0.5 and 0.85, as we measured in previous publications.

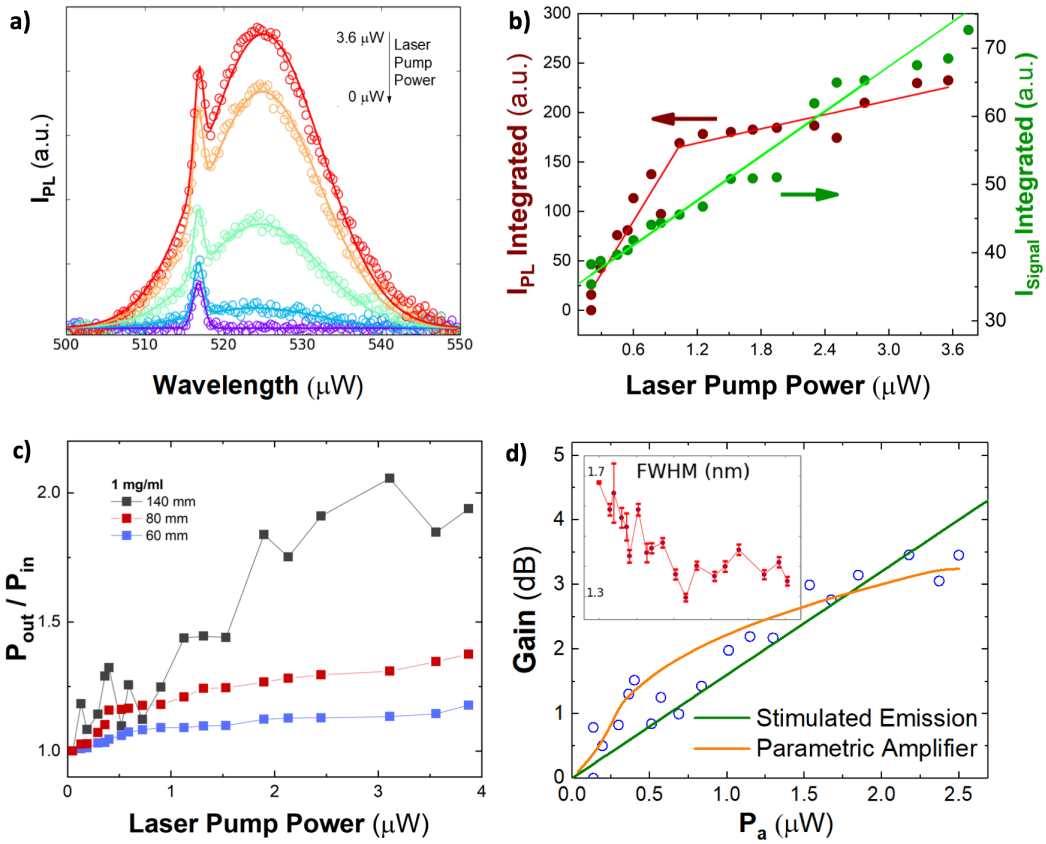

Figure 5.3. (a) Spectra recorded at the extreme of a 140 mm long HC-NCF filled with PNCs (concentration of 1 mg/ml) for different laser pumping powers.; symbols correspond to the experimental data and solid lines to the fitting by the sum of two Gaussian lineshapes (the PL of the PNCs and the regenerated 515nm laser line, or probe). (b) Integrated intensity of the PL (brown circles) and probe (green circles) signals deconvoluted from the spectrum in (a) for the 140 mm long HC-NCF, and (c) optical amplification ratio P_{out}/P_{in} for different HC-NCF lengths, as a function of the laser pumping power. (d) Gain in dB as a function of the excitation in the 140 mm long HC-NCF doped with colloidal PNCs. Continuous curves stand for calculated ASE gain (green line) and parametric amplification (orange line). The inset shows the FWHM of the probe signal with error bars as extracted from fitting experimental curves in (a) (the x-axis range is the same as in the main figure).

In these conditions, absorption and emission cross sections can be deduced by fitting to Equation 5.4 the experimental results presented in Figure 5.3d (from data in Figure 5.3c) for the 140 mm long PNC-doped HC-NCF (blue hollow squares). For this purpose, σ^a and σ^e can be related with McAmber theory [44] by $\sigma^e = \sigma^a \exp((\mathrm{E} - \mathrm{h}\nu_s)/k_B\mathrm{T})$, where the energy $k_B\mathrm{T}$ = 25.7 meV, the energy E corresponds to the energy associated with the absorption edge (i.e zero phonon energy) and $\mathrm{h}\nu_s$ is the signal transition energy. Thus, the McAmber theory yields coefficient of σ^e/σ^a = 5.6. In this way a value of $\sigma^a = (5 \pm 2)\ 10^{-14}$ cm² is the best fitting parameter in the calculated curve in Figure 5.3d (green continuous line) that is in good agreement with that reported in literature, $2 \cdot 10^{-14}$ cm² [45].

However, although an optical gain model can reproduce our experimental data, there are no physical evidences of stimulated emission in the experimental results presented here. An optical gain process through the HC-NCF should be manifested in the observation of ASE in PL spectrum under sufficiently high power pumping conditions, whose physical evidence is the collapse of the PL spectrum (around 20 nm wide) in Figure 5.3a into a much narrower line (below 2 nm wide) under high excitation powers, and a superliner growth of its intensity above a certain threshold [46]. In spite of a slight narrowing observed in the probe signal linewidth (inset in Figure 5.3d), any remarkable change is observed for the main PL band by increasing laser pumping power (see Figure 5.3a - b), hence none of above given conditions are fulfilled. That is, the observed enhancement of the probe signal can be phenomenologically explained by a stimulated emission process, even if the pumping laser power coupled to PNCs is below the ASE threshold. Other possible gain assisted mechanisms include the superposition of the PL-beam produced by the laser pump and the probe signal or scattered light. However, the former is discarded by the deconvolution performed in the analysis of recorded spectra at the exit of the fiber, while the latter would follow a linear dependence on the laser pump power.

Alternatively, third order non-linear effects in PNCs may also explain the experimental results presented here, at least to be considered as another phenomenological model until being confirmed by other different experiments. In previous works, we have already demonstrated that similar pumping conditions can change the effective refractive index of colloidal QDs integrated in plasmonic [44] or dielectric waveguides [47] due to a nonlinear interaction of pump plus probe beams with QDs. On the other hand, a Four Wave Mixing (FWM) third order nonlinear process (see Section 2.3.2.B of this Thesis) has been commonly proposed to provide parametric gain in Fiber-based optical devices [48] or the generation of high energy femtosecond pulses [49]. The four wave mixing and can be exploited to generate optical parametric gain at the created wavelengths when it correctly is tuned. In these conditions, the parametric gain generated by this process can be described by the following equation if the operative range of wavelengths (the difference between the pump and the signal wavelengths) does not exceed a band of 100 nm [50]:

$$G_{dB} = 10 \log_{10} \left(1 + \left[\frac{\gamma P_a}{g} \sinh (gL) \right]^2 \right) \tag{5.5}$$

Here G is the normalized output signal ($G = P_{out}/P_{in}$) produced though a length L; the factor $\gamma = 2\pi n_2/\lambda A_{\text{eff}}$ is the effective nonlinear optical coefficient, where n_2 is the fiber nonlinear parameter. The parametric gain coefficient g is given by:

$$g^2 = -\Delta\beta\left(\frac{\Delta\beta}{4} + \gamma P_p\right) \tag{5.1}$$

where the phase mismatch Δβ is given by:

$$\Delta\beta = \beta(\omega_s) + \beta(\omega_i) - 2\beta(\omega_p) \tag{5.2}$$

Under resonant conditions, $\Delta\beta \approx 0$ ang also, $g \approx 0$. If we calculate the first terms of the Taylor expansion for low gL values, it follows that:

$$\begin{aligned} G_{dB} &= 10\log_{10}\left(1 + (\gamma P_p L)^2\left[1 + \frac{gL^2}{6} + \frac{gL^4}{120} + \cdots\right]^2\right) \\ &\approx 10\log_{10}\left(1 + (\gamma P_p L)^2\right) \end{aligned} \tag{5.8}$$

In this way, the experimental data in Figure 5.2d can be also nicely fitted to Equation 5.8, the orange continuous line, with $n_2 = 3.8\ 10^{-10}$ m²/W and phase mismatch values $\Delta\beta < 1°$. Therefore, the model suggests that a material with a large Kerr effect would influence the propagation of a probe signal beam. Since the reported values of the silica nonlinear refractive index are limited to 10^{-20} m²/W under nanosecond excitation, we believe that nonlinear optical properties of PNCs can be responsible of the mechanism proposed here. Indeed, similar measurements with an unloaded HC-NCF did not show any signal enhancement. Although the application of PNCs in optical nonlinear devices is currently at its very beginning, the few experimental studies show promising properties [51]. The values reported for colloidal solution of $CsPbBr_3$ materials are about $2{\cdot}10^{-17}$ m²/W [51] and $1.2{\cdot}10^{-16}$ m²/W [52] for femtosecond and nanosecond excitation, respectively, but it is necessary to take into account that the concentration of PNCs in such colloidal solutions is usually low. Therefore, the nonlinear optical parameters can be much higher in thin films, as it is in our device. In any case, further research is needed to elucidate the ultimate origin of the nonlinear optical properties of PNCs under CW pumping and if they are sufficient to support a parametric gain mechanism.

5.4 CONCLUSIONS

In the present chapter, a novel HC-NCF optical amplifier is demonstrated by doping the fiber with highly luminescent $CsPbBr_3$ nanocrystals. The PNCs were infiltrated by capillary forces producing a 55 nm thick layer on the air tube walls of the fiber, producing a change in the optical modes at the wavelengths of emitted light by PNCs (510-540 nm), whereas the pumping laser is guided in the main optical mode of the HC-NCF (central hollow-core). A gain figure of merit of 3 dB was obtained for a 140 mm long fiber. Given the absence of ASE in $CsPbBr_3$ PNCs under continuous wave laser pumping at room temperature, the observed amplification by the PNC-doped HC-NCF can be alternatively explained by means of a third order non-linear optical mechanism. This kind of promising device is expected to be a source of new and interesting applications in high power optical fiber lasers, optical telecommunications or chemo-/bio-sensing, and what is more important, a workbench for the study of high order optical nonlinear optics, combining the light confinement properties of HC-NCFs and the optical properties of the perovskite nanocrystals, which would be of great importance for both fundamental physics investigation and practical multiphoton applications.

5.5 REFERENCES

1. Navarro-Arenas, J.; Suárez, I.; Martínez-Pastor, P.J.; Ferrando, A.; Gualdrón-Reyes, F.A.; Mora-Seró, I.; Gao, S.-F.; Wang, Y.-Y.; Wang, P.; Sun, Z. Optical Amplification in Hollow-Core Negative-Curvature Fibers Doped with Perovskite CsPbBr3 Nanocrystals. *Nanomater.* 2019, *9*.
2. Yu, F.; Knight, J.C. Negative Curvature Hollow-Core Optical Fiber. *IEEE J. Sel. Top. Quantum Electron.* **2016**, *22*, 146–155.
3. Wang, Y.Y.; Wheeler, N. V.; Couny, F.; Roberts, P.J.; Benabid, F. Low loss broadband transmission in hypocycloid-core Kagome hollow-core photonic crystal fiber. *Opt. Lett.* **2011**, *36*, 669.
4. Bufetov, I.; Kosolapov, A.; Pryamikov, A.; Gladyshev, A.; Kolyadin, A.; Krylov, A.; Yatsenko, Y.; Biriukov, A.; Bufetov, I.A.; Kosolapov, A.F.; et al. Revolver Hollow Core Optical Fibers. *Fibers* **2018**, *6*, 39.
5. Vincetti, L.; Setti, V. Waveguiding mechanism in tube lattice fibers. *Opt. Express* **2010**, *18*, 23133.
6. Bache, M.; Habib, M.S.; Markos, C.; Lægsgaard, J. Poor-man's model of hollow-core anti-resonant fibers. *J. Opt. Soc. Am. B* **2019**, *36*, 69.
7. Habib, M.S.; Antonio-Lopez, J.E.; Markos, C.; Schülzgen, A.; Amezcua-Correa, R. Single-mode, low loss hollow-core anti-resonant fiber designs. *Opt. Express* **2019**, *27*, 3824.
8. Archambault, J.-L.; Black, R.J.; Lacroix, S.; Bures, J. Loss calculations for antiresonant waveguides. *J. Light. Technol.* **1993**, *11*, 416–423.
9. West, J.A. Photonic crystal fibers. In Proceedings of the LEOS 2001. 14th Annual Meeting of the IEEE Lasers and Electro-Optics Society (Cat. No.01CH37242); 2001; Vol. 1, pp. 14–15 vol.1.
10. Gao, S.; Wang, Y.; Ding, W.; Jiang, D.; Gu, S.; Zhang, X.; Wang, P. Hollow-core conjoined-tube negative-curvature fibre with ultralow loss. *Nat. Commun.* **2018**, *9*, 2828.
11. Benabid, F.; Knight, J.C.; Antonopoulos, G.; Russell, P.S.J. Stimulated Raman Scattering in Hydrogen-Filled Hollow-Core Photonic Crystal Fiber. *Science (80-.).* **2002**, *298*, 399 LP – 402.
12. Michieletto, M.; Lyngsø, J.K.; Jakobsen, C.; Lægsgaard, J.; Bang, O.; Alkeskjold, T.T. Hollow-core fibers for high power pulse delivery. *Opt. Express* **2016**, *24*, 7103.
13. Sintov, Y.; Malka, D.; Zalevsky, Z. Prospects for diode-pumped alkali-atom-based hollow-core photonic-crystal fiber lasers. *Opt. Lett.* **2014**, *39*, 4655.
14. Malka, D.; Peled, A. Power splitting of 1 × 16 in multicore photonic crystal fibers. *Appl. Surf. Sci.* **2017**.
15. Malka, D.; Katz, G. An Eight-Channel C-Band Demux Based on Multicore Photonic Crystal Fiber. *Nanomater. (Basel, Switzerland)* **2018**, *8*.
16. Li, L.; Xiao, L. Plasmonic Nodeless Hollow-Core Photonic Crystal Fibers for In-Fiber Polarizers. *J. Light. Technol.* **2019**, *37*, 5199–5211.
17. Huang, X.; Zang, J.; Yoo, S. Multiple hollow-core anti-resonant fiber as a supermodal fiber interferometer. *Sci. Rep.* **2019**, *9*, 9342.
18. Algorri, J.F.; Zografopoulos, D.C.; Tapetado, A.; Poudereux, D.; Sánchez-Pena, J.M. Infiltrated photonic crystal fibers for sensing applications. *Sensors (Switzerland)* **2018**, *18*, 1–32.
19. Yu, J.; Liu, Y.; Wang, Y.; Wang, Z.; Zhang, X.; Liu, X.; Gao, S.; Wang, X.; Wang, P. Optofluidic laser based on a hollow-core negative-curvature fiber. *Nanophotonics* **2018**, *7*, 1307–1315.

20. Huang, X.; Zang, J.; Yoo, S. Sensing applications of double hollow-core anti-resonant fiber based modal interferometer. In Proceedings of the Conference on Lasers and Electro-Optics; OSA: Washington, D.C., 2018; p. AF1M.3.
21. Wang, Y.; Leck, K.S.; Ta, V.D.; Chen, R.; Nalla, V.; Gao, Y.; He, T.; Demir, H.V.; Sun, H. Blue Liquid Lasers from Solution of CdZnS/ZnS Ternary Alloy Quantum Dots with Quasi-Continuous Pumping. *Adv. Mater.* **2015**, *27*, 169–175.
22. Kazes, M.; Lewis, D.Y.; Ebenstein, Y.; Mokari, T.; Banin, U. Lasing from Semiconductor Quantum Rods in a Cylindrical Microcavity. *Adv. Mater.* **2002**, *14*, 317–321.
23. Hu, Z.; Gao, P.; Xie, K.; Liang, Y.; Jiang, H. Wavelength control of random polymer fiber laser based on adaptive disorder. *Opt. Lett.* **2014**, *39*, 6911–6914.
24. Wang, Z.; Shang, Y.; Pang, F.; Liu, H.; Chen, N.; Wu, Y.; Kang, Y. PbS Quantum Dots Filled Photonic Crystal Fiber for All-fiber Amplifier. *J. Phys. Conf. Ser.* **2017**, *844*, 12060.
25. Dai, Y.; Pang, F.; Wang, T. Gain property analysis of a quantum dot doped inner cladding fiber. *Passiv. Components Fiber-Based Devices VIII* **2011**, *8307*, 830709.
26. Giles, C.R.; Desurvire, E. Modeling erbium-doped fiber amplifiers. *J. Light. Technol.* **1991**, *9*, 271–283.
27. Willner, A.E.; Khaleghi, S.; Chitgarha, M.R.; Yilmaz, O.F. All-Optical Signal Processing. *J. Light. Technol.* **2014**, *32*, 660–680.
28. Silva, A.A.; Barea, L.A.M.; Spadoti, D.H.; Francisco, C.A. De Hollow-core negative curvature fibers for application in optical gas sensors. *Opt. Eng.* **2019**, *58*, 1–7.
29. Enhessari, M.; Salehabadi, A. *Perovskites-based nanomaterials for chemical sensors, progresses in chemical sensor*; Wen Wang, Ed.; INTECH, 2016; Vol. 4;.
30. Protesescu, L.; Yakunin, S.; Bodnarchuk, M.I.; Krieg, F.; Caputo, R.; Hendon, C.H.; Yang, R.X.; Walsh, A.; Kovalenko, M. V Nanocrystals of Cesium Lead Halide Perovskites (CsPbX3, X = Cl, Br, and I): Novel Optoelectronic Materials Showing Bright Emission with Wide Color Gamut. *Nano Lett.* **2015**, *15*, 3692–3696.
31. Gao, S.; Wang, Y.; Liu, X.; Hong, C.; Gu, S.; Wang, P. Nodeless hollow-core fiber for the visible spectral range. *Opt. Lett.* **2017**, *42*, 61.
32. Caupin, F.; Cole, M.W.; Balibar, S.; Treiner, J. Absolute limit for the capillary rise of a fluid. *{EPL} (Europhysics Lett.* **2008**, *82*, 56004.
33. Rusanov A.I, Levichev S.A, T.V.Y. Composition of the Surface Layer in the n-Hexane-Acetone System. *Vestn.Leningr.Univ.* **1966**, *121–127*.
34. Yakunin, S.; Protesescu, L.; Krieg, F.; Bodnarchuk, M.I.; Nedelcu, G.; Humer, M.; De Luca, G.; Fiebig, M.; Heiss, W.; Kovalenko, M. V Low-threshold amplified spontaneous emission and lasing from colloidal nanocrystals of caesium lead halide perovskites. *Nat. Commun.* **2015**, *6*, 8056 EP-.
35. Suárez Alvarez, I. Active photonic devices based on colloidal semiconductor nanocrystals and organometallic halide perovskites. *Eur. Phys. J. Appl. Phys.* **2016**, *75*, 30001.
36. Signoretto, M.; Zink-Lorre, N.; Suarez, I.; Font-Sanchis, E.; Sastre-Santos, Á.; Chirvony, V.S.; Fernandez-La zaro, F.; Martínez-Pastor, J.P. Efficient optical amplification in a sandwich-type active-passive polymer waveguide containing perylenediimides. *ACS Photonics* **2017**, *4*, 114–120.
37. Agrawal, G.P. Applications of Nonlinear Fiber Optics. In *Applications of Nonlinear Fiber Optics*; Academic Press: Burlington, 2008; pp. 179–244 ISBN 978-0-12-374302-2.
38. Saleh, B.E.A.; Teich, M.C.; Wiley, C.J. *Fundamentals of Photonics*; 1991; ISBN 0471839655.
39. Saleh, A.A.M.; Jopson, R.M.; Evankow, J.D.; Aspell, J. Modeling of gain in erbium-doped fiber amplifiers. *IEEE Photonics Technol. Lett.* **1990**, *2*, 714–717.

40. Mackechnie, C.J.; Pask, H.M.; Carman, R.J.; Barber, P.R.; Tropper, A.C.; Hanna, D.C.; Dawes, J.M. Ytterbium-doped silica fiber lasers: versatile sources for the 1-1.2 μm region. *IEEE J. Sel. Top. Quantum Electron.* **2002**, *1*, 2–13.
41. Wang, Y.; Li, X.; Nalla, V.; Zeng, H.; Sun, H. Solution-Processed Low Threshold Vertical Cavity Surface Emitting Lasers from All-Inorganic Perovskite Nanocrystals. *Adv. Funct. Mater.* **2017**, *27*, 1–7.
42. Protesescu, L.; Yakunin, S.; Bodnarchuk, M.I.; Krieg, F.; Caputo, R.; Hendon, C.H.; Yang, R.X.; Walsh, A.; Kovalenko, M. V. Nanocrystals of Cesium Lead Halide Perovskites (CsPbX3, X = Cl, Br, and I): *Nano Lett.* **2015**, *15*, 3692–3696.
43. Talgorn, E.; Gao, Y.; Aerts, M.; Kunneman, L.T.; Schins, J.M.; Savenije, T.J.; van Huis, M.A.; van der Zant, H.S.J.; Houtepen, A.J.; Siebbeles, L.D.A. Unity quantum yield of photogenerated charges and band-like transport in quantum-dot solids. *Nat. Nanotechnol.* **2011**, *6*, 733.
44. Yan, J.H.; Wang, C.G.; Zhang, H.; Cheng, C. Evaluation of emission cross section of CdSe quantum dots for laser applications. *Laser Phys. Lett.* **2012**, *9*, 529–531.
45. Ye, S.; Yan, W.; Zhao, M.; Peng, X.; Song, J.; Qu, J. Low-Saturation-Intensity, High-Photostability, and High-Resolution STED Nanoscopy Assisted by CsPbBr3 Quantum Dots. *Adv. Mater.* **2018**, *30*, 1800167.
46. Suárez, I.; Juárez-Pérez, E.J.; Bisquert, J.; Mora-Seró, I.; Martínez-Pastor, J.P. Polymer/Perovskite Amplifying Waveguides for Active Hybrid Silicon Photonics. *Adv. Mater.* **2015**, *27*, 6157–6162.
47. Hervás, J.; Suárez, I.; Pérez, J.; Cantó, P.J.R.; Abargues, R.; Martínez-Pastor, J.P.; Sales, S.; Capmany, J. MWP phase shifters integrated in PbS-SU8 waveguides. *Opt. Express* **2015**, *23*, 14351–14359.
48. Hansryd, J.; Andrekson, P.A. Broad-band continuous-wave-pumped fiber optical parametric amplifier with 49-dB gain and wavelength-conversion efficiency. *IEEE Photonics Technol. Lett.* **2001**, *13*, 194–196.
49. Aguergaray, C.; Andersen, T. V; Röser, F.; Rademaker, K.; Limpert, J.; Cormier, E.; Tünnermann, A. High power, ultra-short pulses from fiber laser pumped optical parametric amplifier. In Proceedings of the Proc.SPIE Commercial and Biomedical Applications of Ultrafast Lasers VII; San Jose, California, United States, 2007; Vol. 6460.
50. Hansryd, J.; Andrekson, P.A.; Westlund, M.; Li, J.; Hedekvist, P.-. Fiber-based optical parametric amplifiers and their applications. *IEEE J. Sel. Top. Quantum Electron.* **2002**, *8*, 506–520.
51. Ferrando, A.; Martínez Pastor, J.P.; Suárez, I. Toward Metal Halide Perovskite Nonlinear Photonics. *J. Phys. Chem. Lett.* **2018**, *9*, 5612–5623.
52. Suárez, I.; Vallés-Pelarda, M.; Gualdrón-Reyes, A.F.; Mora-Seró, I.; Ferrando, A.; Michinel, H.; Salgueiro, J.R.; Pastor, J.P.M. Outstanding nonlinear optical properties of methylammonium- and Cs-PbX3 (X = Br, I, and Br–I) perovskites: Polycrystalline thin films and nanoparticles. *APL Mater.* **2019**, *7*, 41106.

6 AMPLIFIED SPONTANEOUS EMISSION IN THIN FILMS OF PNCS

In this chapter, the generation of optical gain in $CsPbX_3$ perovskite nanocrystals (PNCs) films are analysed. We establish the intrinsic mechanisms underlying ASE in PNCs of three different bandgaps ($CsPbBr_3$, $CsPbBr_{1.5}I_{1.5}$ and $CsPbI_3$) and the conditions to minimize the threshold of stimulated emission. Among the possible physical mechanisms responsible for ASE (single excitions, biexcitons or free carriers) our characterization reveals that the optical gain in these materials is produced by the formation of single excitons. In these conditions, inverted population can be reached under small thresholds (as low as 5 $\mu J/cm^2$) only limited by the self absorption losses, which becomes stronger for thicker layers. We believe that these conclusions will pave the road to more ambitious targets like lasing under continuous wave optical or electrical excitation, and the development of a new generation of active devices based on PNCs. Most of the results presented have been published in a peer reviewed scientific *Journal of Physical Chemistry Letters* (journal with impact factor of 6.71 in 2019, ranked in Q1 within the Materials Science Multidisciplinary and Q2 in Nanoscience & Nanotechnology categories of WoS). The synthesis of the PNCs was carried out by Andrés F. Gualdrón-Reyes and Iván Mora-Seró, both members of the Institute of Advanced Materials (INAM) in the University Jaime I (Castellón, Spain). Experimental results and modelling were carried out by Juan Navarro-Arenas under the supervision of Isaac Suárez and Juan P. Martínez Pastor, and with the help of Vladimir Chirvony.

6.1 INTRODUCTION

Colloidal quantum dots (CQD) have been extensively studied as a cheap alternative to epitaxial III-V semiconductors for optical gain purposes [1,2]. Since the first demonstration of the amplified spontaneous emission (ASE) in CQD in 2000 [3], a significant progress has been achieved [2] including the demonstration of lasing under continuous wave operation in 2017 [4] and, more recently, under electrical pumping in 2018 [5]. In particular, several important milestones have been achieved in the study of optical gain mechanisms of optically excited CQDs: (i) the problem of Auger

recombination was partially circumvented by employing femtosecond (fs) excitation and densely packed QD films [6]; (ii) understand the impossibility of obtaining gain in neutral (uncharged) core-only QDs within single exciton regime [7]; (iii) increase of absorption cross-section using large-volume nanostructures [8]; and (iv) introduction of permanent charges for reducing the gain threshold due to partial blocking of ground state absorption [9].

In previous chapters, PNCs have been introduced as a potential material with demonstrated applications in light emitting diodes, optical amplifiers and lasers [10]. Particularly, PNC-based films exhibited reduced ASE thresholds of the order of 1 $\mu J/cm^2$ [11], which are smaller than those measured in polycrystalline perovskite thin films [12] or conventional CQDs (from groups II-VI, III-V, IV-VI, …) [2]. For this reason, we believe that PNC-based films can be promising candidates for future integrated optical sources or amplifiers. Over the past 3-4 years, many reports have been focused on the study of the mechanism of optical amplification in $CsPbX_3$ (X = Br, I) PNCs [2,11,13–32]. Most of these works, however, still required femtosecond (fs) excitation pulses to avoid or reduce Auger recombination mechanism under high excitation conditions. Hence, further investigations are needed to achieve more ambitious objectives such as lasing under CW operation or electrical pumping. Indeed, the intrinsic mechanism underlying the optical gain in PNCs remains poorly studied. It is still under debate whether single exciton, biexciton or free carrier (electron-hole plasma) recombination regimes can be dominant in the stimulated emission process in PNCs [33]. In addition, it is not clear what is the role of self-absorption in ASE, how the inhomogeneous broadening of photoluminescence (PL) spectra can affect ASE spectra, and what are the gain saturation mechanisms. Finally, according to the data published in different papers [11,15,17,23], ASE spectra significantly broaden at high excitation fluencies, although this behavior has not been explained yet.

In CQDs, the two-fold degeneracy of the band-edge states requires that, for achieving optical gain, at least a part of the excited CQDs must contain multiple excitons (that is, the average number of excitons per dot, $\langle N \rangle$, should be higher than 1) [1]. Regardless of this, there is experimental evidence of single-exciton gain regime achieved with high-quality CQD samples possessing low optical losses [6]. The single-exciton gain regime is the most favorable in order to minimize losses because the non-radiative exciton-exciton annihilation (Auger recombination) should be absent in this scenario. In the case of PNCs, where the quantum confinement is very weak (tens of meV), the two-fold degeneracy of the band-edge states was also discussed in literature

[14], and the most frequent conclusion is that biexciton mechanism is responsible for the observed ASE in PNCs at excitation fluencies around threshold of stimulated emission [23,29,34,35].

As our literature analysis shows, the biexciton origin of ASE in PNCs was argued either on the basis of analysis of the observed PL transients, without spectral evidences [29], or due to the presence of a long-wavelength shift of the ASE peak relative to the spontaneous emission position [35], or because of the quadratic dependence of the ASE intensity upon the excitation fluency [23]. Here we show that the aforementioned features can not necessarily be the markers of the biexciton mechanism of ASE. In particular, we demonstrate that the size dispersion present in an ensemble of closely packed PNCs results in the reabsorption of the high energy photons emitted by the smallest nanocrystals of the ensemble that leads to the observed redshift of the ASE spectra (dominated by low energy photons emitted by the biggest nanocrystals of the ensemble). This is experimentally demonstrated by using PNC-based films of different thicknesses. Finally, we propose a model explaining the ASE profile broadening at high excitation densities as a result of the joint influence of PNC size dispersion and the consequent PL inhomogeneous broadening. The study is performed by using thin films of PNCs with three different compositions (i.e., effective bandgaps): $CsPbBr_3$, $CsPbBr_{1.5}I_{1.5}$ and $CsPbI_3$, whose PLQY is very close to unity at cryogenic temperatures. Our results enable us to conclude that the observed optical gain at threshold pumping conditions is due to single exciton emission.

6.2 Preparation and Characterization Methods of PNC Thin Films

6.2.1 Synthesis of colloidal solution

$CsPbX_3$ (X=Br, $Br_{0.5}I_{0.5}$, I) were grown following the hot-injection method (detailed in section 3.1.1 of this thesis) developed by Kovalenko and coworkers [36] with minor modifications. The PNCs exhibit a cubic shape [36] (see TEM images in Figures 6.1a and 6.1b) with an average size (L) of 11.8 nm ($CsPbBr_3$) and 13.8 nm ($CsPbI_3$), with an average size dispersion of about 7 %, as shown in Figures 6.1c and 6.1d, respectively. Since the Bohr radius (a_0) of these PNCs ranges between 7 ($CsPbBr_3$) and 12 nm ($CsPbI_3$), the ratio $L/2a_0$ (L is the nanocube edge size) varies from 0.84 to 0.58, respectively, which corresponds to a weak quantum confinement regime in both cases.

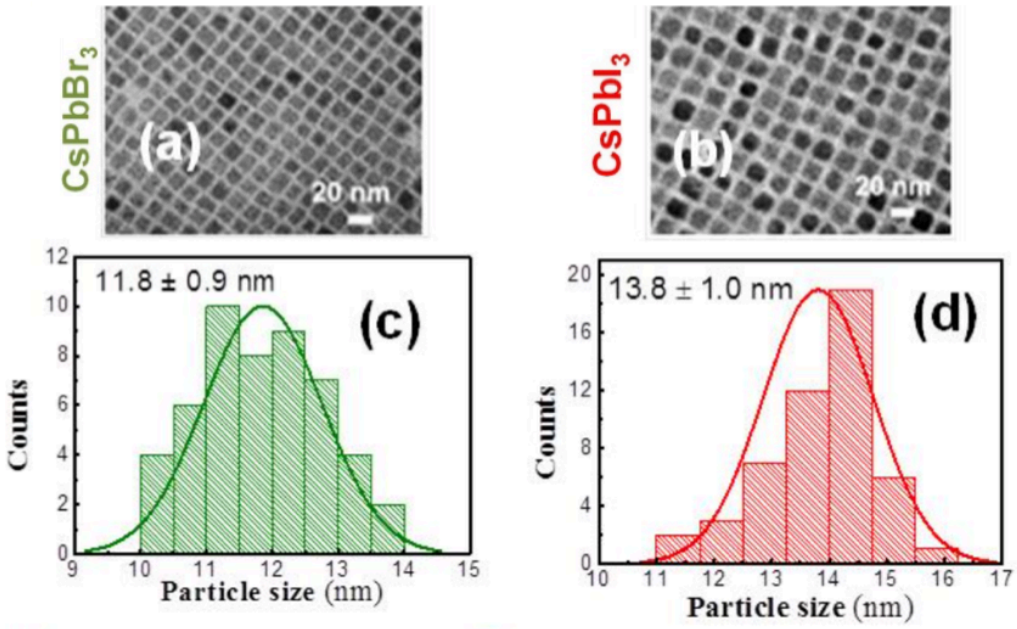

Figure 6.1. TEM images of (a) $CsPbBr_3$ and (b) $CsPbI_3$ NCs. Size dispersion for (c) $CsPbBr_3$ and (d) $CsPbI_3$ NCs.

6.2.2 Sample Preparation and Optical Characterization

PNCs were deposited on a commercial borosilicate substrate by using a commercial Doctor Blade applicator (Elcometer 4340) and post-baking at 100 °C for 1 minute (see Section 3.1.2 for details). These steps have been sequentially repeated until the film of PNCs reached the desired thickness within the range from 20 nm to 1 µm. Prior to the deposition of these films, the substrates were carefully cleaned with acetone, ethanol and isopropanol during 10 minutes in an ultrasound bath.

A commercial NanoCalc-2000 reflectometer (Mikropack) was used the absorption spectra at room temperature of $CsPbX_3$ films deposited on borosilicate substrates (see Section 3.2.2.A for details about this setup).

6.2.3 Low Temperature PL and TRPL

Samples were held in a cold finger of a closed-cycle He cryostat, which can be cooled down to 10K. PL was measured by using a Q-switch Nd:YAG (1 kHz, 1 ns) laser doubled or tripled at 532 nm and 355 nm (CRYLAS 6FTSS355- Q4-S), respectively. The PL signal was dispersed by a double 0.3 m focal length grating spectrograph and detected with a Si CCD camera (Andor Newton EMCCD). Time-resolved PL was carried out by using the same pumping laser, but analyzing the PL with a Hamamatsu

C5658–3769 avalanche photodetector connected to a BOXCARDPCS-150 electronics from Becker and Hickl GmbH. PL under femtosecond operation was carried out by using PL a Ti:sapphire mode locked laser at a wavelength of 405 nm doubled by a BBO crystal. In this case, Time-resolved PL have been carried out with the Ti:sapphire laser in pulsed mode operation (pulse width 200 fs and 76 MHz of repetition rate) at the same wavelength. The emitted light was dispersed by a monochromator with 300 mm of focal length and detected by a Si avalanche photodiode connected to a time correlated single photon counting electronics (electronic card TCC900 from Edinburgh Instruments). For more details and explanations about this technique, consult the Section 3.2.2.C.

6.3 ASE IN PNC BASED THIN FILMS: RESULTS AND DISCUSSION

The photoluminescence (PL) of the PNCs layer as a function of the excitation fluency was studied by holding the samples on a cold finger of a closed-cycle He cryostat cooled down to 15K (see Figure 6.2a for the scheme of the experimental set-up) with the intention to prevent the influence of nonradiative channels. The cryostat presented two glass windows confronted to the top and the bottom of the sample in order to allow the excitation from both faces. In particular, absorption was deduced from the sample transmittance measured at low temperatures by using a Xe lamp taking into account the influence of the windows and the substrate, and the PL was measured in backscattering geometry by pumping the nanocrystals with the Q-switch pulsed at 532 nm or 355 nm, depending on the PNC bandgap. The excitation wavelength was chosen according to the absorption band edge measured for PNCs at cryogenic temperature (see blue symbols in Figures 6.2b and 6.2c): 500 nm (2.35 eV) and 685 nm (1.81 eV) for $CsPbBr_3$ and $CsPbI_3$, respectively.

6.3.1 EVOLUTION OF ASE WITH EXCITATION FLUENCY

The evolution of the PL+ASE spectra in films of PNCs with the excitation fluency (P_{exc}) are shown in 3D plots for 300 nm thick films of $CsPbBr_3$ (Figure 6.2d), $CsPbI_{1.5}Br_{1.5,}$ (Figure 6.2e) $CsPbI_3$ (Figure 6.2f) PNCs films. The evolution of the displayed spectra indicates that more than one physical mechanism participates in the optical gain formation, as will be explained below.

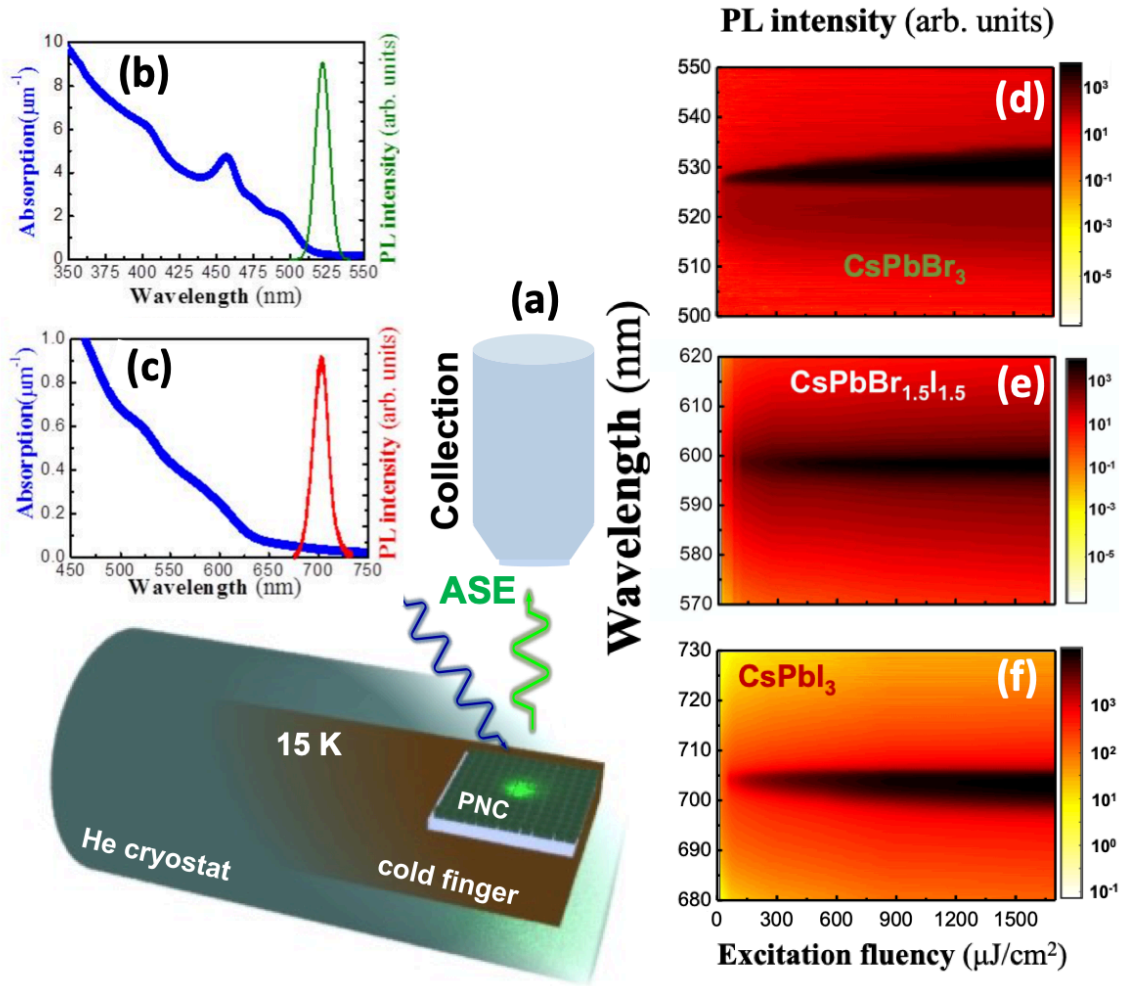

Figure 6.2. (a) Experimental set-up. Absorption (blue and left axis) and PL (green/red and right axis) of (b) $CsPbBr_3$ and (c) $CsPbI_3$. 3D image of PL as a function of excitation fluency for (d) $CsPbBr_3$ (e) $CsPbBr_{1.5}I_{1.5}$ and (f) $CsPbBI_3$. All PL and absorption characterizations were performed at 15 K.

The behavior of thin films of $CsPbBr_3$ PNCs excited at 355 nm under increasing excitation fluency (P_{exc}, see Figure 6.2a) clearly demonstrates three different regions. When $P_{exc} < 3$ μJ/cm², the PL shows a Gaussian shape centered at 522.4 nm (2.3768 eV) with a FWHM of about 10 nm (50 meV). Similar spectral shape has been reported in literature for these PNCs at cryogenic temperatures [17,37] and it can be ascribed to the spontaneous emission due to the exciton recombination (labeled as X in Figure 6.3a). When P_{exc}= 10 μJ/cm², a narrow stimulated emission band (labelled as ASE in Figure 6.3a) appears on the long-wavelength side (526.6 nm) of the spontaneous emission, which is in agreement with results previously reported for this material at room [11] and cryogenic [25] temperatures. Then, as P_{exc} increases above 10 μJ/cm² (and below 48 μJ/cm²), the ASE bandwidth progressively narrows down to 1.37 nm (6.1 meV) and slightly redshifts up to 527.3 nm. With a further increase of P_{exc} (>48 μJ/cm²) the ASE

band continues to redshift, but its linewidth broadens, with an ASE peak wavelength at 530 nm (2.3409 eV) and FWHM of 7 nm (30.1 meV) at $P_{exc} \approx 1.6$ mJ/cm^2.

In order to extract precise information about the generation of ASE spectra in the spectra of Figure 6.3a, the PL curves were fitted by a Voigt + Gaussian function as shown in Figure 6.3b. The deconvolution allows us to extract the integrated PL intensities (I_{SE}), the Full Width at Half Maximum (FWHM) and the centroids of the PL distributions (Figure 6.3c). As the excitation fluency is increased, the three different regions can also be identified in Figure 6.3c). In the case of the bromide PNCs, for low P_{exc} (<10 μJ/cm^2), I_{SE} obeys a linear dependence $I_{SE} \propto P_{exc}$ due to the spontaneous emission process. However, above the threshold at P_{exc} >= 10 μJ/cm^2, I_{SE} exhibits a superlinear dependence ($I_{SE} \propto P_{exc}^{2.3}$) followed by a saturation above $P_{exc} \approx 50$ μJ/cm^2 which can be phenomenologically fitted (solid green line) by the expression $\log(I_{SE}) = 0.65+0.95\cdot\log(P_{exc}) - 0.52\cdot\log^2(P_{exc})$. Taking into account the absorption coefficient at the excitation wavelength (355 nm) shown in Figure 6.2b (9.25 μm^{-1}) and the nanocube edge size (L) of the PNCs, the absorption cross section (σ) can be estimated as $\sigma = \alpha\cdot L^3 = 1.5\cdot10^{-13}$ cm^2, which nicely agrees with results previously reported for this material [38,39]. At these conditions, the average number of excitons per nanocrystal per pulse can be estimated by the formula $\langle N\rangle = P\cdot\sigma/h\nu$ as equal to the value about 2 at the threshold excitation fluency. It does not mean, however, that biexciton recombination is the mechanism responsible for the ASE observed in thin films of $CsPbBr_3$ PNCs (see discussion below).

In the case of thin films of $CsPbI_3$ PNCs (see Figure 6.3d, excitation at 532 nm) the PL dependence on P_{exc} demonstrates three similar regions. For P_{exc}<10 μJ/cm^2 the spectrum is well described by a Gaussian shape centred at 703.6 nm (1.76 eV) with a FWHM of 18.4 nm (46.1 meV), which approximately corresponds to the spontaneous emission band of this material at cryogenic temperatures [37]. When P_{exc} >10 μJ/cm^2 the spectra start narrowing down to 3 nm (7.5 meV) at $P_{exc} \approx 80$ μJ/cm^2; and, with a further increase of P_{exc} the ASE band progressively broadens up to 7.7 nm (19.3 meV) at P_{exc} =1.6 mJ/cm^2. Again, spectra can be simulated by the sum of Gaussian and Voigt distributions (Figure 6.3e). Figure 6.3f shows the evolution of the FWHM and the integrated intensity as a function of P_{exc} with blue and red symbols, respectively. Again, this log-log plot clearly distinguishes the three regions commented above: spontaneous emission ($I_{SE} \propto P_{exc}$) for P_{exc}<10 μJ/cm^2, stimulated emission ($I_{SE} \propto P_{exc}^{1.8}$) above the threshold of P_{exc} =10 μJ/cm^2, and saturation ($I_{SE} \propto P_{exc}^{0.3}$) for P_{exc} > 78 μJ/cm^2. There are, however, some interesting differences when compared with the behaviour presented for

thin films of $CsPbBr_3$ PNCs: (i) ASE band is centered at the peak wavelength of the spontaneous emission band, hence the ASE band is not redshifted as compared to the spontaneous emission; (ii) the boundary region between ASE and saturation is sharper here; (iii) in agreement with previous publications [14], the absorption coefficient at the excitation wavelength (0.54 μm^{-1}) is lower than that measured for $CsPbBr_3$ films, as observed in Figure 6.2c). Due to this, the estimate for <N> at the threshold excitation fluency decreases to 0.5 excitons per nanocrystal per pulse, approximately.

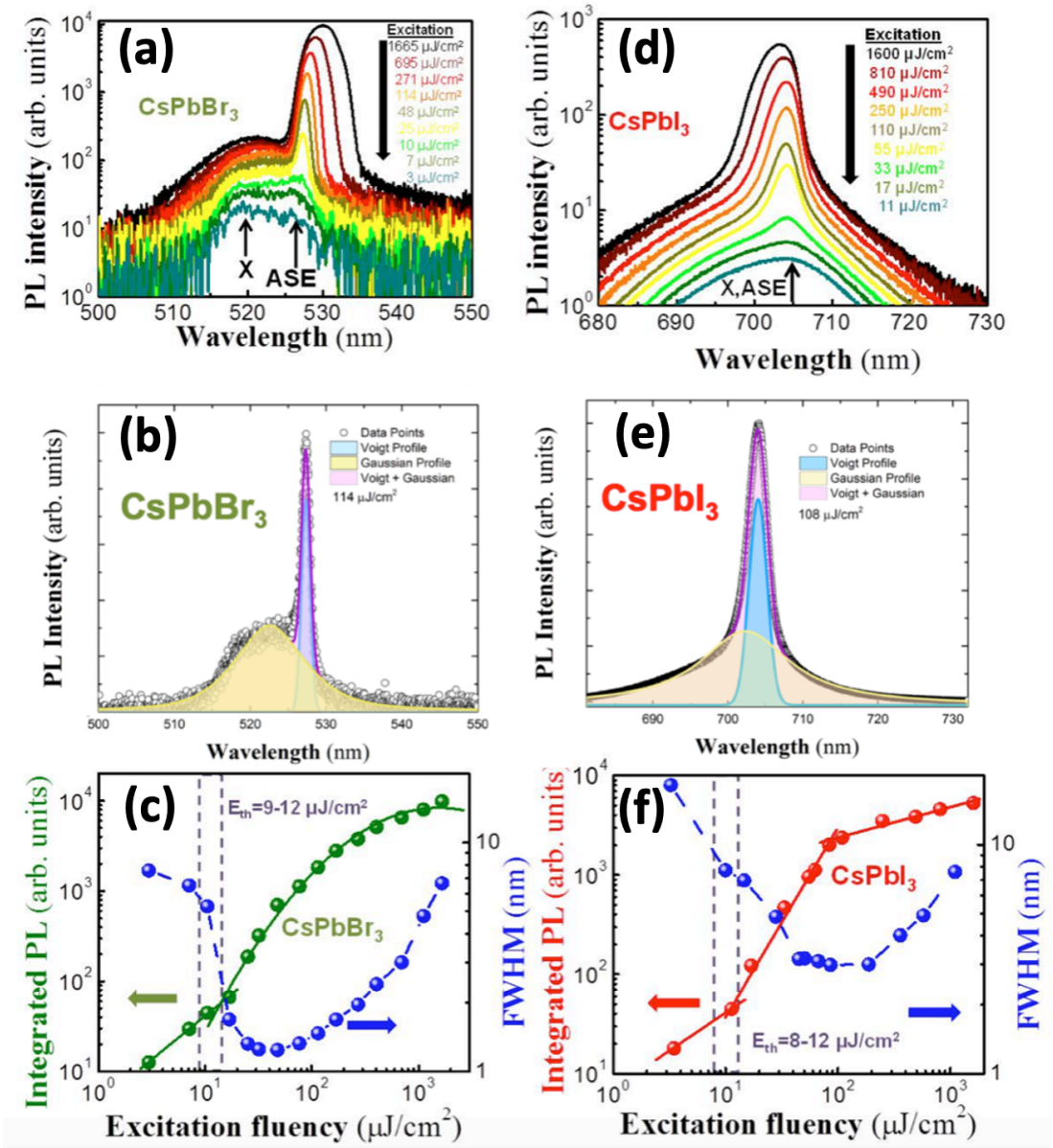

Figure 6.3. Analysis of PL of 300 nm thick (a, b, c) $CsPbBr_3$ and (d, e, f) $CsPbI_3$ PNC layers. (a, d) PL spectra (b, e) spectral deconvolution and (c, f) integrated PL intensity (green/red symbols) and FWHM (blue symbols) at different excitation fluencies.

Discussion of the physical mechanism behind ASE

As the analysis of literature data on optical gain in PNCs reveals, it is very inviting to say that the observed ASE can be explained by the so-called biexcitonic emission (biexciton - exciton cascade recombination) [13], at least for $CsPbBr_3$ PNCs. Indeed, it is commonly accepted for semiconductor quantum dots (QDs) such as CdSe among others, that the optical gain in these nanostructures may be only due to the biexciton-exciton transition that is a result of the double degeneracy for electronic states [3,7]. The biexcitonic ASE band usually appears at energies (E_{XX}) lower than the single-exciton emission energy E_X due to the direct Coulomb and exchange interactions. The energy difference $E_{bXX} = E_X - E_{XX}$ is the so-called "biexciton binding energy". In our results with $CsPbBr_3$ layers the energy difference between the PL (spontaneous emission) and the ASE peak energies at the ASE threshold (Figure 6.3a) is around 20.8 meV, that well correlates with values reported in other works [14,29]. Such a shift of ASE relative to the spontaneous PL is usually considered as the main evidence of the biexciton-exciton transition as the mechanism of ASE in PNCs. As another proof of the biexciton nature of the ASE band, a quadratic dependence of the ASE integral intensity on the excitation density is also considered [7,23]. In fact, we have such a dependence for both $CsPbBr_3$ and $CsPbI_3$ PNCs samples, see Figure 6.3c and 6.3f. Therefore, from the point of view of common proofs usually used in literature, our experimental data also point to the prevalent idea about the biexcitonic origin of the ASE band.

However, we have evidences supporting another interpretation of these results. Indeed, the essential property of the biexciton-exciton transition is that two excitons form one biexciton, which then decays to one exciton and one photon. Thus, the scheme of the process can be presented as exciton + exciton = exciton + photon [40], that is an interaction of two excitons does not result in any non-radiative losses of energy as in case of exciton-exciton annihilation due to Auger recombination. Namely, this lossless character of the biexciton-exciton transition is its principal sign, but not other (secondary) characteristics such as ASE band spectral position, quadratic dependence of ASE intensity on excitation density, and even the number of excitons per QD per pulse near the ASE threshold are considered. We believe that one of the first characteristics that should be checked to confirm or reject the biexciton-exciton nature of an optical transition is the dependence of the PL quantum yield (QY) on the excitation intensity. If the observed ASE band is due to the biexciton–exciton transition, then the PLQY should not drop for excitation fluencies providing $\langle N \rangle$ between 1 and 2. However, for both our PNCs we discovered a continuous monotonic drop of the relative PLQY values with increasing

P_{exc} (see Figure 6.4). This observation corresponds well to the case of the exciton–exciton annihilation due to Auger recombination [41], but not to the case of the biexciton-exciton optical transition.

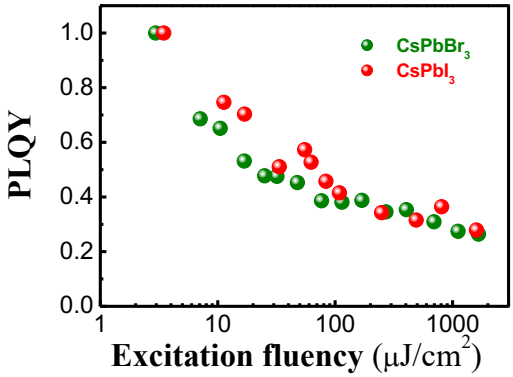

Figure 6.4. QY as a function of the excitation fluency for $CsPbBr_3$ (green symbols) and $CsPbI_3$ (red symbols). QY is calculated by the ratio of the total integrated intensity with the excitation fluency.

Concerning the other commonly accepted proofs of the biexciton-exciton transition in application to our PNCs, we have to say the following. In case of films of $CsPbI_3$ PNCs, the ASE band appears exactly at the maximum of the single-excitonic PL band (Figure 6.3d). Therefore, it would imply that the biexciton binding energy E_{bXX} would be zero, which is not consistent with the biexciton nature of ASE emission. Secondly, the dependence of $I_{SE} \propto P_{exc}^2$ (Figure 6.3f) is well correlated with the narrowing of the spectra, i.e., the characteristic always ascribed to the single-exciton ASE [33].

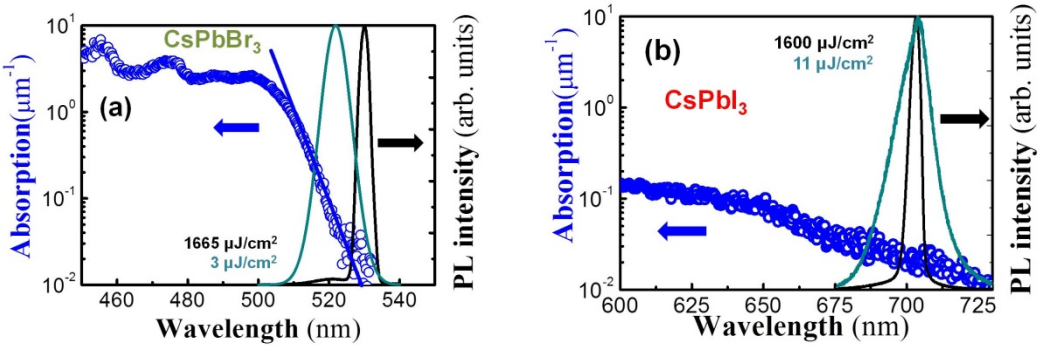

Figure 6.5. Absorption (in log scale, blue symbols) and PL spectra measured at 10 μJ/cm² (cyan) and 1600 mJ/cm² (black) excitation densities for (a) $CsPbBr_3$ and (b) $CsPbI_3$ layers of 300 nm thickness.

Finally, the overlap of the absorption band edge with the PL emission suggests that the self-absorption effect should play an important role (Figure 6.5). In the case of $CsPbBr_3$ layers (see Figure 6.5a) the absorption exhibits a sharp Urbach tail (blue

symbols) overlapping with the spontaneous emission spectrum (cyan line), similarly to the results reported in literature [14,38,42]. As a consequence, the spontaneous PL spectrum experiences an asymmetric attenuation (10^{-2} and 10^{-1} μm^{-1} for the longest and shortest wavelength tails, respectively) and the ASE line, observed under sufficiently high excitation (black line), appears at the long wavelength side of the PL spectrum (>530 nm) where reabsorption is practically negligible (< 10^{-2} μm^{-1}). In the case of $CsPbI_3$ layers (see Figure 6.5b) we measure an absorption attenuation as low as 10^{-2} μm^{-1} (blue symbols) at the PL band wavelengths (cyan line), which is in agreement with other reports [14]. This weak reabsorption ability makes possible to observe the ASE (black line) and spontaneous PL spectra peaked at the same wavelength, i.e., $E_X - E_{ASE} = 0$. In addition, the weaker reabsorption results in the generation of ASE with lower <N>. Then, $CsPbI_3$ layers present similar ASE threshold as $CsPbBr_3$, despite their lower absorption cross section.

6.3.2 SELF-ABSORPTION EFFECT

After the above given discussion, further ASE spectra measurements implemented for different thicknesses of $CsPbBr_3$ PNC films unambiguously demonstrate that the difference $E_X - E_{ASE}$ notably decreases with the film thickness reduction, as clearly observed in Figures 6.6a-c. Of course, such a decrease is again inconsistent with the biexciton ASE emission picture from one side and, contrarily, well agrees with the hypothesis of a self-absorption effect determining the observed redshift of the ASE band with respect to the spontaneous PL peak. It is well known in literature that lead halide perovskites exhibit strong self-absorption effect, which well manifests itself in photon recycling in perovskite devices [43]. Especially favourable for reabsorption is the geometry of thin films, where the high confinement of light can enhance the intrinsic absorption and/or gain effects [44]. The reabsorption effect will lead to a redshift of the PL peak wavelength [45], which is even more drastic for the case of ASE [44], because it is very sensitive to optical losses. If we consider the propagation of PL through the PNC film, thicker films will clearly lead to more intensive PL reabsorption (see the model below for further details). Consequently, the expected reduction of ASE threshold for thicker layers as deduced from the FWHM reduction (Figure 6.6d) strongly correlates with the redshift of the ASE peak (Figure 6.6e).

Therefore, the sample thickness dependence (Figure 6.6a-c) unambiguously evidences that $E_X - E_{ASE}$ is practically zero for a single-monolayer (20 nm) PNC film (Figure 6.6e). Consequently, the redshift of about 6 nm measured for the thickest film

(1000 nm) between the ASE band and the spontaneous emission at the threshold excitation is due to self-absorption of emitted photons, which introduces important losses at wavelengths where PL and absorption edge overlap. This full-optical approach perfectly explains our results without introduction of the biexcitonic emission under near-threshold excitation powers as the origin of ASE. It implies that single-exciton recombination is responsible for the observed ASE. It is suggested for conventional semiconductor QDs that such single-exciton ASE is impossible for neutral (uncharged) QDs due to the double-degeneracy of the neutral exciton state, but it is possible for charged species (negative and positive trions) [14]. We consider that there are two possible explanations of the observed single-exciton gain in the case of lead halide PNCs: i) photo-charging of nanocrystals due to the well-known effect of carrier trapping by non-quenching shallow traps [46,47], or ii) the state filling model used for QDs with strong quantum confinement (where Coulomb interaction is weak) does not hold for PNCs (where Coulomb interaction is of the order of the quantum confinement) [48].

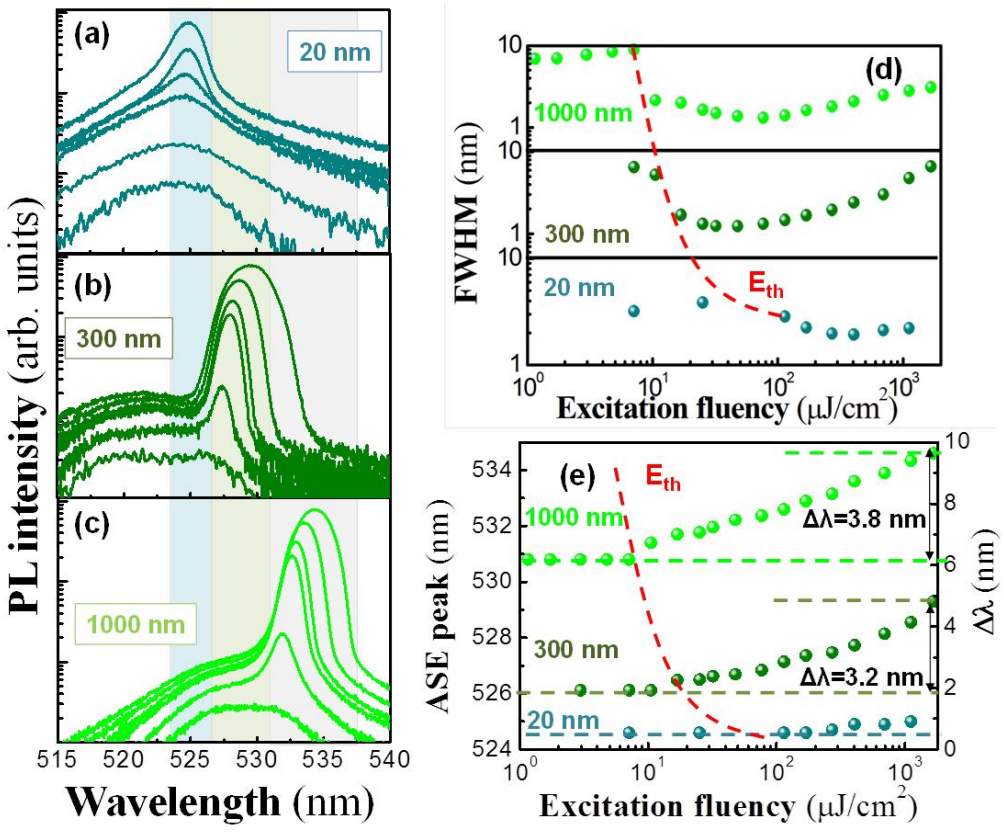

Figure 6.6. (a-c) PL spectra of $CsPbBr_3$ layers as a function of the excitation fluency measured for layers with different thickness: (a) 20 nm, (b) 300 nm, and (c) 1000 nm. (d) FWHM as a function of the excitation fluency for the three different thicknesses, observing a decrease of E_{th} with the increase of thickness, see dashed red line as a guide for the eyes. (e) Shift of the ASE peak wavelength as a function of the excitation fluency and thickness of the sample.

Thus, we believe that in the case we studied, the threshold value of ⟨N⟩, which was around 0.7 for both $CsPbBr_3$ and $CsPbI_3$, is not necessarily related to the mechanism of ASE formation. ASE is formed as a result of competition between stimulated emission by a single-exciton mechanism and parasitic reabsorption of PL under a given geometry of experiment. In fact, an increase of ⟨N⟩ above threshold should lead to reduction of the PL lifetime due to Auger recombination that is observed experimentally (see 15 K curve in figures Figure 6.10c and 6.10d). On the other hand, a growth of ⟨N⟩ up to the formal values of ⟨N⟩ = 10–20 is accompanied by a narrowing of the ASE band (Figure 6.3e–6.3f), which clearly indicates a single-exciton recombination regime for ASE generation even for such high excitation densities. It is worth noting that the peak position of ASE can vary if it is measured in either pristine or sintered $CsPbBr_3$ nanocrystal films [25], which can be easily explained on the basis of absorption spectra reported by the authors of Ref. [25], where a difference in the PL reabsorption for these two kinds of layers is observed.

Note also that the optical excitation with sufficiently long laser pulses, the duration of which is comparable with the exciton lifetime and much longer than the time of exciton-exciton annihilation by Auger processes, should not result in the formation of a large concentration of excitons in a single PNC. For example, formal calculations may result in photogenerated exciton concentrations significantly exceeding the Mott density at which excitons should dissociate (10^{17} cm^{-3}) [33], but all these excitations are not formed simultaneously in an individual PNC and annihilate during the excitation pulse. In general, long excitation pulse conditions turn to be favourable for the detailed investigation of near-threshold spectral manifestations of single-exciton ASE, whereas the investigation of higher density mechanisms of the optical gain, such as the electron-hole plasma recombination, require femtosecond excitation.It is interesting to note here that experiments developed with our PNC films at higher temperatures leaded to ASE thresholds increasing with temperature, which correlates with the increasing influence of excitonic nonradiative recombination (see Section 6.3.3).

Another important point of discussion is the reason of the ASE band broadening, which starts when excitation fluency exceeds 75-100 $\mu J/cm^2$, as observed in Figure 6.3. We believe that, regardless of the nature of the ASE band, a change in its shape could be the result of two effects: the PL inhomogeneous broadening (PL bands in Figures 6.2b-6.2c), which is associated with the nanocrystal size dispersion (Figures 6.1c-6.1d), [49,50] and the gain saturation effect [50,51]. This saturation occurs in optical amplifiers [43] due to the lack of empty excited states along the optical path, whereas in PNCs

would take place for the nanocrystals emitting at around the PL peak (i.e. those corresponding to the average nanocrystal size). In this way, the higher the PL intensity, the earlier the saturation is achieved when excitation fluency increases. Therefore, when the gain saturation region is reached, the spectral edges of the ASE band would grow in intensity faster with excitation intensity than its central part. In the case of $CsPbBr_3$ films, the reabsorption will impact the range of wavelengths of the ASE broadening in such a way that inhibits the growth of the ASE band in the short wavelength range (Figure 6.3a), while the negligible self-absorption in $CsPbI_3$ films practically allows the ASE emission at the whole PL spectrum (Figure 6.3b). Nevertheless, since the quantum yield of emission should be enhanced for small sizes of PNCs [52], the ASE spectrum at high excitation fluencies is slightly asymmetric towards the short wavelength region.

Modeling the self-absorption effect

We have developed a model that incorporates the optical mechanisms discussed in previous section (single exciton gain, emitted light reabsorption, gain saturation and inhomogeneous broadening) in order to corroborate our experimental findings and conclusions. For this purpose, we consider that the excitation beam homogeneously illuminates a circular area of the PNC film with a diameter of 100 μm. The beam is exponentially attenuated along the z direction until the bottom of the film is reached due to the Beer-Lambert law (see the illustration in Figure 6.7a);

$$Pexc = P_0 e^{-\alpha_{355}(L-z)} \tag{6.1}$$

The number of electron hole-pairs (N_{eh}) at each propagation step is given by:

$$N_{eh}(z) = \frac{\alpha_{355} \cdot P_{exc}(z)}{h\nu} \tag{6.2}$$

where α is the absorption coefficient at the excitation wavelength (355 nm and 532 nm for films based on $CsPBr_3$ and $CsPI_3$ PNCs, respectively). Then, the PL is generated isotropically through this cylinder,

$$PPL(zi, \lambda) = QY(Pexc) \cdot N_{eh}(zi) \cdot PL(\lambda) \tag{6.3}$$

where QY is defined as the ratio of the integral PL intensity to the excitation intensity, which decreases continuously with increasing the excitation energy density, and *PL(λ)*

is the spectral shape of the spontaneous emission assumed as a Gaussian distribution centered at 520 nm (2.37 eV) with a FWHM of 10 nm (45.5 meV):

$$PL(E) = \frac{PL_0}{w_{in}\cdot\sqrt{\pi/2}} \cdot e^{-2\frac{(E-E_0)^2}{w_{in}^2}} \tag{6.4}$$

Here, if considering an inhomogeneous broadening of the PL associated with the PNC ensemble, one can assume that this Gaussian PL is the result of the sum of single PNC emitters represented by Lorentzian functions of the type (we consider in our model 130 single PNCs whose PL peak energies are separated 1 meV and characterized by a homogeneous linewidth w = 2 meV) [39]:

$$L(E_k) = PL(E) \cdot \frac{1}{4\cdot(E-E_k)^2+w^2} \tag{6.5}$$

where the sum of the emission of all PNCs gives *PL(E)* (≡ *PL(λ)*). In this way, each PNC will emit light at each propagation step according to the following rate equations:

$$\frac{dN}{dt} = G - \sum_k \frac{N}{\tau} \cdot \frac{1}{w_{in}\cdot\sqrt{\pi/2}} \cdot e^{-2\frac{(E-E_0)^2}{w_{in}^2}} \tag{6.6}$$

$$\frac{dn_k}{dt} = N_k - \frac{n_k}{\tau_r} - \frac{n_k^2}{\tau_{xx}} - (n_k - N_0) \cdot \sigma \cdot \frac{S}{h\cdot\vartheta} \tag{6.7}$$

$$N_k = \frac{N}{\tau} \cdot \frac{1}{w_{in}\cdot\sqrt{\pi/2}} \cdot e^{-2\frac{(E_k-E_0)^2}{w_{in}^2}} \tag{6.8}$$

Here G is the number of electron-hole pairs per pulse, N the number of carriers in excited states, n_k is the number of excitons with energy k, τ_r its radiative recombination time, τ_{xx} the time of formation of biexcitons, N_0 the threshold of stimulated emission, σ the emission cross section, S the signal fluency and $h\nu$ the photon energy of the signal. Here, a saturation condition is introduced to include that the density of nanocrystals (i.e. inverse volume) is correlated with the inhomogeneous size.

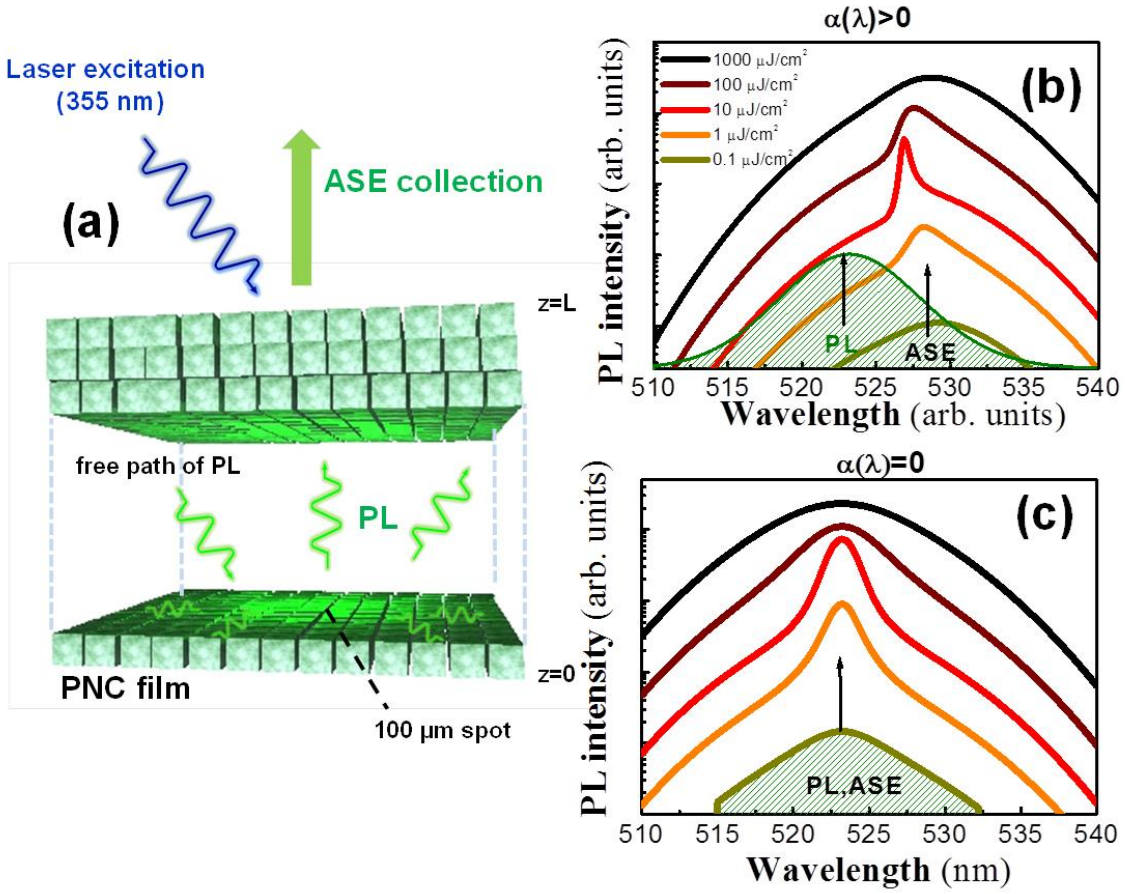

Figure 6.7. Modelling of the SE band broadening due to gain saturation effect: (a) schematic presentation of the experiment geometry; (b) results when self-absorption is included in calculations; (c) results with negligible reabsorption effect.

Finally, the evolution of the signal along the optical path is obtained by solving the propagation equation with a Runge-Kutta algorithm:

$$\frac{dS}{dz} = (g - \alpha) \cdot S + N_{eh} \cdot PL \cdot \tau_r \cdot \delta \tag{6.9}$$

where PL is the shape of the spontaneous emission, δ a fitting parameter and g the gain given by:

$$g_k = \sigma \cdot n_k \cdot S_{norm} \tag{6.10}$$

Here S_{norm} is the normalized shape of the ASE of S obtained in the previous step. The introduction of the wavelength dependent absorption losses (reabsorption effect), α > 0 (at the signal wavelengths), clearly results in a redshift of the ASE spectrum, as observed in Figure 6.7b, while in case of α = 0 the ASE band does not exhibit any redshift, see Figure 6.7c. In both cases, the model reproduces the gain saturation

mechanism proposed here for both $CsPbBr_3$ ($\alpha > 0$) and $CsPI_3$ ($\alpha = 0$). The inhomogeneous broadening of the spontaneous emission band due to the PNC size dispersion is also the main contribution to the broadening of the ASE line towards the tails of the PL line (towards the red in the case of $CsPBr_3$ due to reabsorption), when the PNC films are pumped under high excitation fluencies (Figures 6.7b-6.7c).

6.3.3 EVOLUTION OF ASE WITH TEMPERATURE

In order to provide deeper understanding of ASE generation of PNPs, PL spectra was studied as a function of temperature (T) at an excitation fluency of 0.4 mJ/cm^2 (355 nm laser) in the case of the bromide PNPs and 0.36 mJ/cm^2 (532 nm laser) for the iodide ones, as presented in Figure 6.8. The normalized PL spectra of figures 6.8a-b can also be examined in the maps of Figure 6.8c-d. In these maps, the PL intensity was normalized to the peak maximum at all temperatures. The ASE peak position in the bromide PNCs (see de discontinued black line in Figure 6.8c) experiences a blue shift of 0.8 nm (5 meV) from the initial position of 533.5 nm at T = 15 K to 532.7 at T = 80 K. Then, PL spectrum becomes constant until T = 250 K, when the ASE band shows a significant nonradiative quenching, and the spontaneous emission becomes dominant in the PL spectra. In the case of the iodide PNCs (Figure 6.8d), the blue shift is even more pronounced than that found for bromide PNCs. The ASE band peak shifts up to 6 nm (15 meV) from 703.5 nm at T = 15 K to 697.5 nm at T = 75 K. Then, the PL exhibits a negligible variation until T = 150 K, where again, the optical gain cannot overcome the thermal losses, and the ASE band experience a significant quenching.

The analysis presented above reveals that ASE peak on PNCs presents a blueshift slope from 20 K to 80 K. Since phase crystalline transitions in PNCs were only reported at much higher T (around 361 K and 403 K for $CsPbBr_3$ polycrystalline films) [53], this effect need to be explained by another mechanism. More singularities can be observed in Figures 6.9.

(i) 20-80 K the emission is predominantly radiative and PL (ASE dominant) intensity increases because of the initial activation of traps that contribute to the filling of the excitonic ground state, as detailed in the model below. The slight blue shift (Figures 6.8c-d) is typically related to the formation of emitting species in the high wavelength range of the spectra, causing the blue shifting of the PL peak [17].

(ii) 80-200 K the PL (ASE) intensity decreases because shallow traps are activated and trapping/detrapping mechanism compete with radiative exciton recombination, as proposed in Refs. [47,56,57], other than nonradiative recombination paths opened from these shallow traps. Simultaneously, the constant ASE peak position does not move, possibly because of the opposite effects of the bandgap energy increase and the broadening of the absorption band edge with temperature.

(iii) Above 200 K, non-radiative recombination is more and more effective because it is being activated by deeper traps (Shockley-Read-Hall mechanism). In this regime, we observe a simultaneous important increase of the ASE threshold fluency (Figure 6.9b).

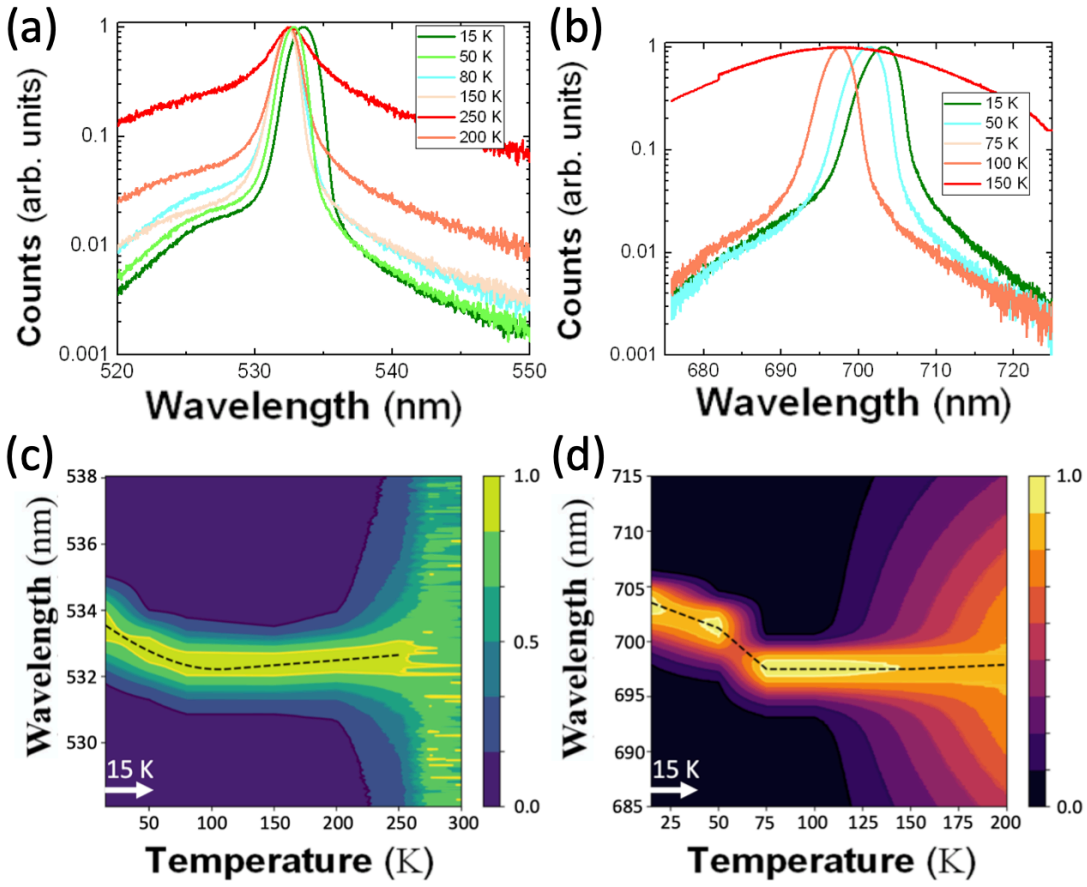

Figure 6.8. PL spectra of (a)$CsPbBr_3$ (0.4 mJ/cm^2) and (b)$CsPbI_3$ 0.36 (mJ/cm^2) at several temperatures and fixed pump fluency. Map of the normalized PL spectra as a function of the temperature and fixed fluency (specified above) for (c) $CsPbBr_3$ PNPs (d) and $CsPbI_3$ PNPs. Dark dashed lines show the positions of the PL spectra centroids.

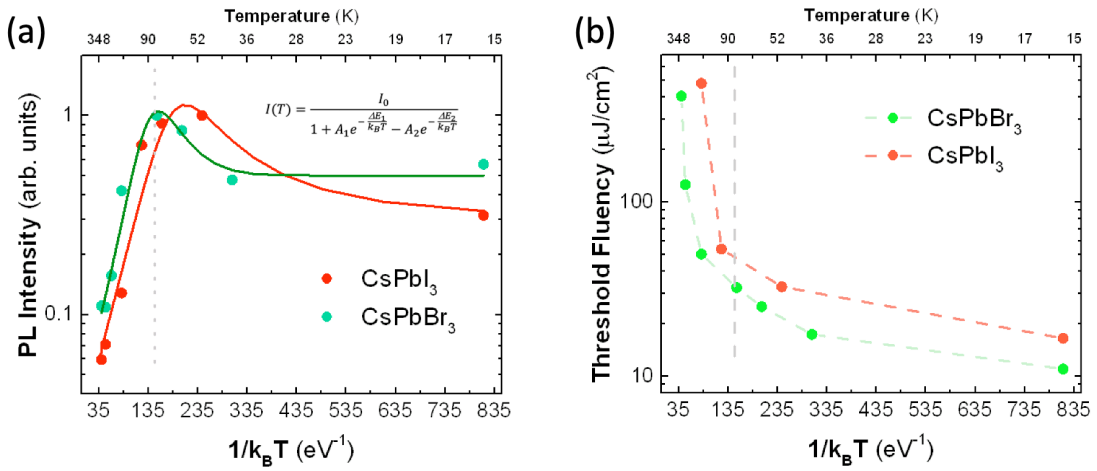

Figure 6.9. (a)Integrated PL intensity at different temperatures with a fixed excitation fluency of 0.4 mJ/cm² (355 nm laser) in the case of the $CsPbBr_3$ PNCs and 3.6 mJ/cm² (532 nm laser) for the $CsPbI_3$ PNCs. The continuous line represents the fitting to the model Equation 6.12 with the specified activation energies. (b) ASE threshold evolution with temperature for $CsPbBr_3$ and $CsPbI_3$ PNCs.

Since there the PL intensity initially suffers an increase (T < 80 K) and then a drop (T > 80 K), there are must two kinds of trap states that get activated with temperature: the one that contributes to the excitonic ground state by detrapping processes and the one that depletes the excitonic ground state (nonradiative recombination). A fitting equation that reproduces this kind of temperature dependence is given by:

$$I(T) = \frac{I_0}{1 + A_1 e^{-\frac{\Delta E_1}{k_B T}} - A_2 e^{-\frac{\Delta E_2}{k_B T}}} \tag{6.11}$$

with A_1 and A_2 as fitting constants and I_0 as the intensity at an asymptotic temperature of 0 K. The results of the fitting of the data (solid lines in Figure 6.9a) for $CsPbBr_3$PNCs (green line) reveals a filling trap state (the term A_2 weighting with a minus sign) with an activation energy of ΔE_2= 11.0 meV and a quenching trap state with a higher activation energy of ΔE_1=17.2 meV. In the same way, $CsPbI_3$ PNPs exhibit similar activation energies ΔE_2= 10.2 meV and ΔE_1 = 18.1 meV (the fitting weights are given in Table 1). Indeed, our results agree with those presented in the literature [57].

Film	A_1	A_2	ΔE_1 (meV)	ΔE_2 (meV)
$CsPbBr_3$	22	11	17.2	11.0
$CsPbI_3$	20	10	18.1	10.2

Table 6.1. Fitting parameters of Equation 6.11 in the data of Figure 6.9a.

This model is common in literature and it has been already been used to study the temperature dependence of the ASE band in $CsPbBr_3$ films [57]. In the carrier density rate equation (Equation 6.12), R(t) is the pump rate; τ_r is the radiative lifetime; ΔE_1 and ΔE_2 the activation energy the nonradiative processes. The energy ΔE_1 corresponds to the activation energy of a nonradiative process, whereas ΔE_2 is the activation energy corresponding to the emission of trapped electrons (for this reason the term has a minus sign in Eq. 6.11) towards the exciton level.

$$\frac{dn}{dt} = R(t) - \frac{n}{\tau_r} - \frac{n}{\tau_{nr1}} e^{-\frac{\Delta E_1}{k_B T}} + \frac{n}{\tau_{\Delta E_2}} e^{-\frac{\Delta E_2}{k_B T}} \tag{6.12}$$

Assuming that the PL intensity I(T) is given by $I(T) = n(T)/\tau_r$, when solving this equation in the stationary case we get the Equation 6.11 used to reproduce I_{PL} in Figure 6.9a.

PL recombination dynamics as a function of T agree with the conclusions obtained with the PL spectra. The TRPL decay curves are fitted to a biexponential curve (Figure 6.10a and 6.10b) $I(T) = I_0 + A_1 e^{-t/\tau_1} + A_2 e^{-t/\tau_2}$, in which τ_1 is a short decay time associated with the exciton lifetime (including radiative and nonradiative paths) and τ_2 is a long decay time associated with the carrier (electron) trapping/detrapping processes from shallow traps, with corresponding weights A_i (i = 1, 2) [47]. The long component does not present a significant variation with the excitation fluency, contrary to the case of the short component that exhibits a noticeable reduction, as shown in Figures 6.10c and 6.10d for $CsPbBr_3$ and $CsPbI_3$, respectively. In both PNC films, the short component of the PL decay decreases with the excitation fluency, because of the influence of stimulated emission (see section 6.3.2). On the contrary, τ_1 slightly increases with T, as expected from the increase of radiative exciton lifetime under low excitation conditions (spontaneous emission). At high excitation conditions (above the ASE threshold) the increase of τ_1 is more important, because in this case the observed decay contains the contribution of the radiative exciton lifetime, but also the stimulated emission rate, which is larger by increasing excitation fluency (observed time decay reduction) and smaller by increasing temperature (due to the increase of the ASE threshold fluency).

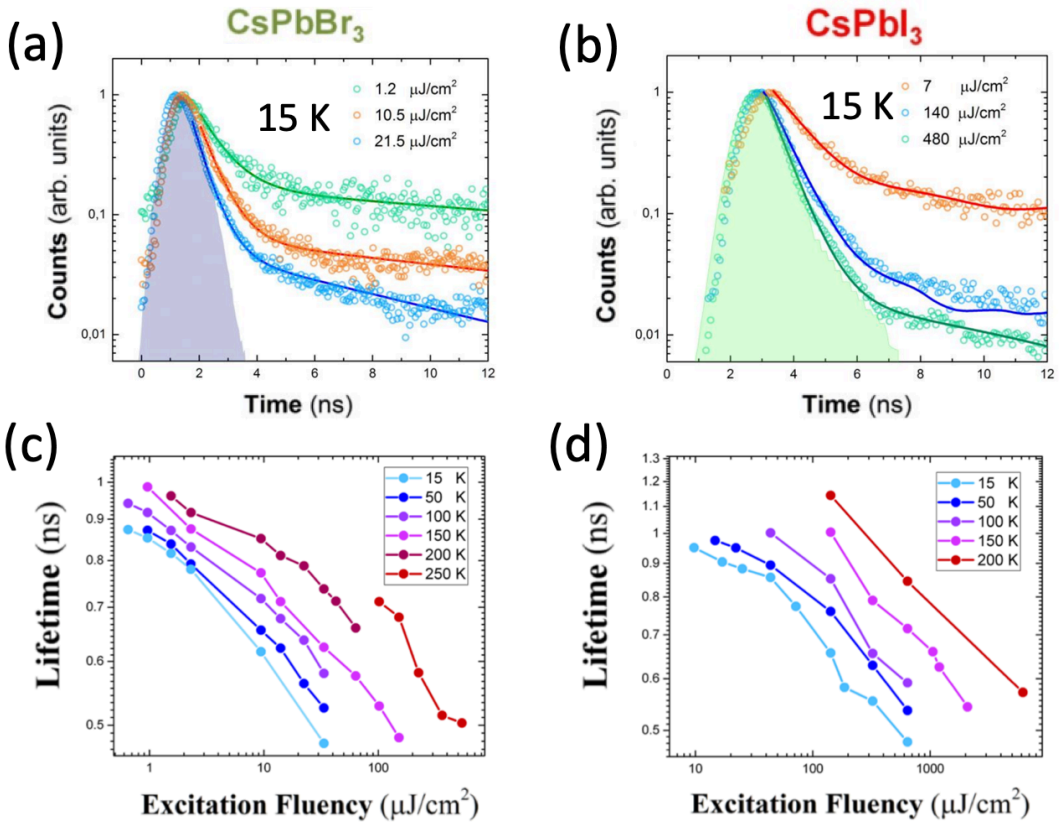

Figure 6.10. Kinetics of the (a) $CsPbBr_3$ and (b) $CsPbI_3$ films at 15 K experimental data (hollow dots) and fit (solid lines). The system response is represented with a shadowed area. Extracted short component recombination times of the (c) $CsPbBr_3$ and (d) $CsPbI_3$ films. The experimental data was extracted with the Q-switch Nd:YAG (1 kHz, 1 ns) laser.

6.4 RANDOM LASING IN PNC THIN FILMS

In a mirrorless random scattering medium, the lasing feedback is provided by constructive interference of the light scattered during its propagation in the active medium. The PNCs or PNC-agglomerates of the film would act as scattering centers, producing random closed loops determining the resonance wavelengths visible in the spectra [58].

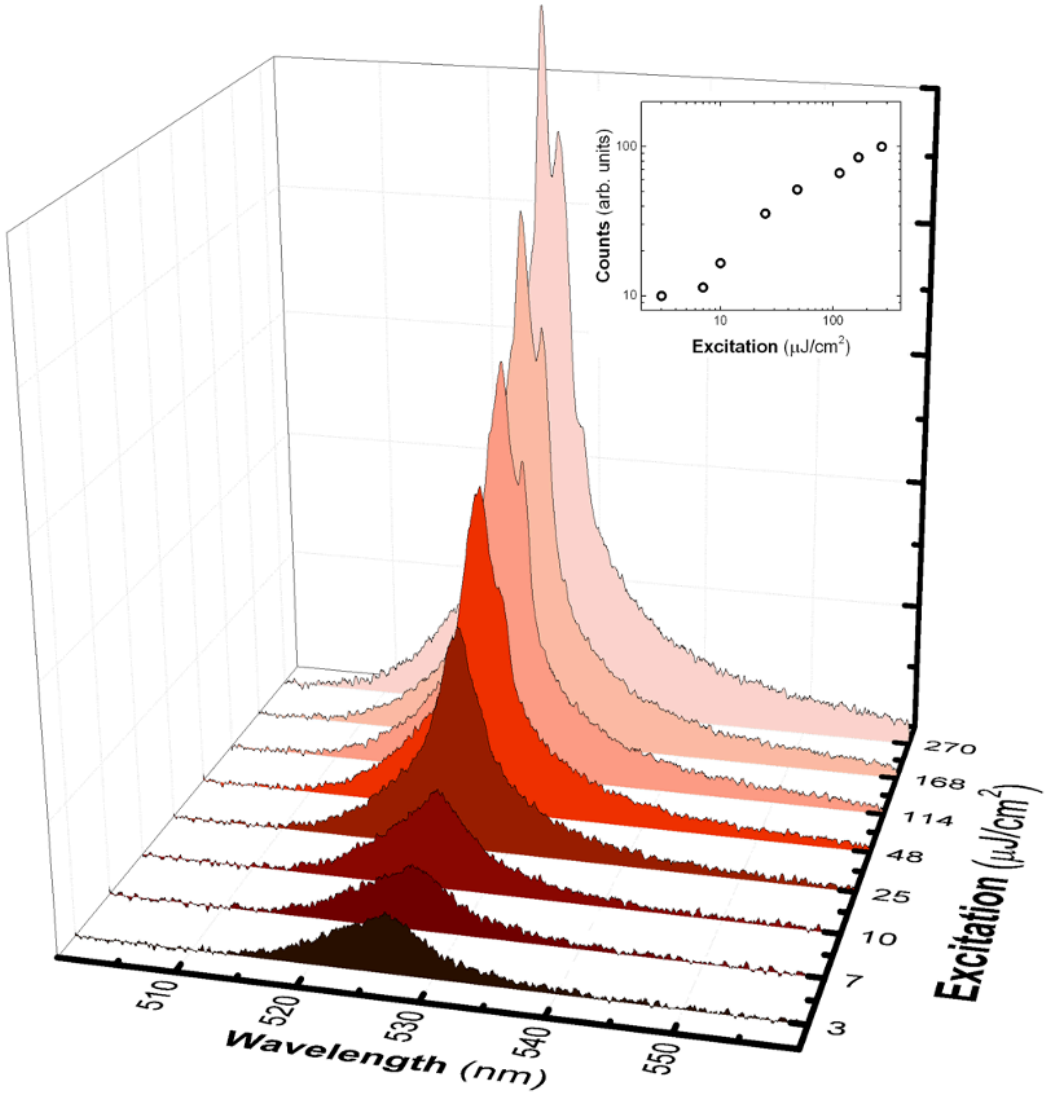

Figure 6.11. Evolution of emission spectra of a 300 nm $CsPbBr_3$ PNC film under different pump intensities and measured at 15 K temperature. The insert shows the evolution of the main peak intensity spectra under low pump powers.

In the realization of the low temperature experiments to characterize ASE depicted in this chapter, random lasing phenomena was often observed when focusing the pumping laser at arbitrary points of the sample surface. The appearance of these phenomena occurred unintentionally, but could be found more frequently in the corners of the sample substrates, where surface morphology often present defects acting as highly scattering centers. In the results reported in Figure 6.11, there can be identified one main resonance, located at 525 nm, and two minor ones at 527 and 529 nm (specially noticeable at higher excitation powers). Similar spectral shapes are attributed to random lasing modes realized in weak scattering regimes in other publications dealing with PNC based thin films [59,60].

6.5 CONCLUSIONS

In summary, we stablished the role of different species (mainly exciton and biexcitons) and physical mechanisms (reabsorption effect, inhomogeneous broadening of the spontaneous emission spectrum, gain saturation) in the formation of optical gain in PNCs. Although biexcitonic emission is usually the preferred mechanism to explain the stimulated emission in these nanocrystals, our experimental data evidence that ASE is produced by single exciton recombination. In particular, we have demonstrated that the experimental redshift observed for ASE is highly dependent on the PNC-layer thickness, which is incompatible with the biexcitonic emission and points out to the influence of reabsorption effects. In addition, we have established the influence of the size distribution of PNCs in the layers as the origin of the inhomogeneous PL spectrum, which results in the gain saturation at the most intense luminescent nanocrystals and the consequent broadening of the ASE spectra under high excitation fluencies. All these physical effects were introduced in a rate equation model able to reproduce the experimental ASE spectra and its evolution with the increase of the optical excitation density. We have also examined the evolution of the process of the formation of ASE with the temperature and the influence of trap states limiting ASE generation, because of non-radiative recombination of excitons and carriers (from trap states). These results are the basis for understanding the generation of ASE in PNCs, which paves the road towards the future development of emitting devices under continuous wave optical (or electrical) operation. Finally, we have found evidence of a random lasing effect naturally occurring in thin films of $CsPbBr_3$ PNCs due to random scattering by them (or PNC-agglomerates). Investigation following this trend could led to new applications of perovskite materials, particularly the development of micro-nano lasers for integrated optics.

6.5 REFERENCES

1. Pietryga, J.M.; Park, Y.S.; Lim, J.; Fidler, A.F.; Bae, W.K.; Brovelli, S.; Klimov, V.I. Spectroscopic and device aspects of nanocrystal quantum dots. *Chem. Rev.* **2016**, *116*, 10513–10622.
2. Suárez Alvarez, I. Active photonic devices based on colloidal semiconductor nanocrystals and organometallic halide perovskites. *Eur. Phys. J. Appl. Phys.* **2016**, *75*, 30001.

3. Klimov, V.I.; Mikhailovsky, A.A.; Xu, S.; Malko, A.; Hollinngsworth, J.A.; Leatherdale, C.A.; Eisler, H.J.; Bawendi, M.G. Optical Gain and Stimulated Emission in Nanocrystal Quantum Dots. *Science (80-.).* **2000**, *290*, 314–317.
4. Fan, F.; Voznyy, O.; Sabatini, R.P.; Bicanic, K.T.; Adachi, M.M.; McBride, J.R.; Reid, K.R.; Park, Y.S.; Li, X.; Jain, A.; et al. Continuous-wave lasing in colloidal quantum dot solids enabled by facet-selective epitaxy. *Nature* **2017**, *544*, 75–79.
5. Lim, J.; Park, Y.S.; Klimov, V.I. Optical gain in colloidal quantum dots achieved with direct-current electrical pumping. *Nat. Mater.* **2018**, *17*, 42–48.
6. Dang, C.; Lee, J.; Breen, C.; Steckel, J.S.; Coe-Sullivan, S.; Nurmikko, A. Red, green and blue lasing enabled by single-exciton gain in colloidal quantum dot films. *Nat. Nanotechnol.* **2012**, *7*, 335–339.
7. Klimov, V.I.; Ivanov, S.A.; Nanda, J.; Achermann, M.; Bezel, I.; McGuire, J.A.; Piryatinski, A. Single-exciton optical gain in semiconductor nanocrystals. *Nature* **2007**, *447*, 441–446.
8. Garcia-Santamaria, F.; Chen, Y.; Vela, J.; Schaller, R.D.; Hollingsworth, J.A.; Klimov, V.I. Suppressed auger recombination in “Giant” nanocrystals boosts optical gain performance. *Nano Lett.* **2009**, *9*, 3482–3488.
9. Woo, C.; CJ Wang; Guyot-Sionnest, P.; Wehrenberg, B. Light emission and amplification in charged CdSe quantum dots. *J. Phys. Chem. B* **2004**, *108*, 9027–9031.
10. Li, Y.-F.; Feng, J.; Sun, H.-B. Perovskite quantum dots for light-emitting devices. *Nanoscale* **2019**, *11*, 19119–19139.
11. Yakunin, S.; Protesescu, L.; Krieg, F.; Bodnarchuk, M.I.; Nedelcu, G.; Humer, M.; De Luca, G.; Fiebig, M.; Heiss, W.; Kovalenko, M. V. Low-threshold amplified spontaneous emission and lasing from colloidal nanocrystals of caesium lead halide perovskites. *Nat. Commun.* **2015**, *6*, 1–8.
12. Xing, G.; Mathews, N.; Lim, S.S.; Yantara, N.; Liu, X.; Sabba, D.; Grätzel, M.; Mhaisalkar, S.; Sum, T.C. Low-temperature solution-processed wavelength-tunable perovskites for lasing. *Nat. Mater.* **2014**, *13*, 476–480.
13. Zhao, W.; Qin, Z.; Zhang, C.; Wang, G.; Huang, X.; Li, B.; Dai, X.; Xiao, M. Optical Gain from Biexcitons in CsPbBr 3 Nanocrystals Revealed by Two-dimensional Electronic Spectroscopy. *J. Phys. Chem. Lett.* **2019**, *10*, 1251–1258.
14. Makarov, N.S.; Guo, S.; Isaienko, O.; Liu, W.; Robel, I.; Klimov, V.I. Spectral and dynamical properties of single excitons, biexcitons, and trions in cesium-lead-halide perovskite quantum dots. *Nano Lett.* **2016**, *16*, 2349–2362.
15. Chen, S.; Nurmikko, A. Stable Green Perovskite Vertical-Cavity Surface-Emitting Lasers on Rigid and Flexible Substrates. *ACS Photonics* **2017**, *4*, 2486–2494.
16. Wang, Y.; Li, X.; Nalla, V.; Zeng, H.; Sun, H. Solution-Processed Low Threshold Vertical Cavity Surface Emitting Lasers from All-Inorganic Perovskite Nanocrystals. *Adv. Funct. Mater.* **2017**, *27*, 1–7.
17. Balena, A.; Perulli, A.; Fernandez, M.; De Giorgi, M.L.; Nedelcu, G.; Kovalenko, M. V; Anni, M. Temperature Dependence of the Amplified Spontaneous Emission from CsPbBr 3 Nanocrystal Thin Films. **2018**.
18. Sutherland, B.R.; Sargent, E.H. Perovskite photonic sources. *Nat. Photonics* **2016**, *10*, 295–302.
19. Wang, Y.; Li, X.; Zhao, X.; Xiao, L.; Zeng, H.; Sun, H. Nonlinear Absorption and Low-Threshold Multiphoton Pumped Stimulated Emission from All-Inorganic Perovskite Nanocrystals. *Nano Lett.* **2016**, *16*, 448–453.
20. Veldhuis, S.A.; Boix, P.P.; Yantara, N.; Li, M.; Sum, T.C.; Mathews, N.; Mhaisalkar, S.G. Perovskite Materials for Light-Emitting Diodes and Lasers. *Adv. Mater.* **2016**, 6804–6834.

21. Zhang, Q.; Su, R.; Liu, X.; Xing, J.; Sum, T.C.; Xiong, Q. High-Quality Whispering-Gallery-Mode Lasing from Cesium Lead Halide Perovskite Nanoplatelets. *Adv. Funct. Mater.* **2016**, *26*, 6238–6245.
22. Park, K.; Lee, J.W.; Kim, J.D.; Han, N.S.; Jang, D.M.; Jeong, S.; Park, J.; Song, J.K. Light-Matter Interactions in Cesium Lead Halide Perovskite Nanowire Lasers. *J. Phys. Chem. Lett.* **2016**, *7*, 3703–3710.
23. Wang, Y.; Li, X.; Song, J.; Xiao, L.; Zeng, H.; Sun, H. All-Inorganic Colloidal Perovskite Quantum Dots: A New Class of Lasing Materials with Favorable Characteristics. *Adv. Mater.* **2015**, *27*.
24. Tang, X.; Hu, Z.; Chen, W.; Xing, X.; Zang, Z.; Hu, W.; Qiu, J.; Du, J.; Leng, Y.; Jiang, X.; et al. Room temperature single-photon emission and lasing for all-inorganic colloidal perovskite quantum dots. *Nano Energy* **2016**, *28*, 462–468.
25. Papagiorgis, P.; Manoli, A.; Protesescu, L.; Achilleos, C.; Violaris, M.; Nicolaides, K.; Trypiniotis, T.; Bodnarchuk, M.I.; Kovalenko, M. V.; Othonos, A.; et al. Efficient Optical Amplification in the Nanosecond Regime from Formamidinium Lead Iodide Nanocrystals. *ACS Photonics* **2018**, *5*, 907–917.
26. Pan, J.; Sarmah, S.P.; Murali, B.; Dursun, I.; Peng, W.; Parida, M.R.; Liu, J.; Sinatra, L.; Alyami, N.; Zhao, C.; et al. Air-Stable Surface-Passivated Perovskite Quantum Dots for Ultra-Robust, Single- and Two-Photon-Induced Amplified Spontaneous Emission. *J. Phys. Chem. Lett.* **2015**, *6*, 5027–5033.
27. Tong, Y.; Bladt, E.; Aygüler, M.F.; Manzi, A.; Milowska, K.Z.; Hintermayr, V.A.; Docampo, P.; Bals, S.; Urban, A.S.; Polavarapu, L.; et al. Highly Luminescent Cesium Lead Halide Perovskite Nanocrystals with Tunable Composition and Thickness by Ultrasonication. *Angew. Chemie - Int. Ed.* **2016**, *55*, 13887–13892.
28. Xu, Y.; Chen, Q.; Zhang, C.; Wang, R.; Wu, H.; Zhang, X.; Xing, G.; Yu, W.W.; Wang, X.; Zhang, Y.; et al. Two-Photon-Pumped Perovskite Semiconductor Nanocrystal Lasers. *J. Am. Chem. Soc.* **2016**, *138*, 3761–3768.
29. Castañeda, J.A.; Nagamine, G.; Yassitepe, E.; Bonato, L.G.; Voznyy, O.; Hoogland, S.; Nogueira, A.F.; Sargent, E.H.; Brito Cruz, C.H.; Padilha, L.A. Efficient Biexciton Interaction in Perovskite Quantum Dots Under Weak and Strong Confinement. *ACS Nano* **2016**, *10*, 8603–8609.
30. Yumoto, G.; Tahara, H.; Kawawaki, T.; Saruyama, M.; Sato, R.; Teranishi, T.; Kanemitsu, Y. Hot Biexciton Effect on Optical Gain in CsPbI3 Perovskite Nanocrystals. *J. Phys. Chem. Lett.* **2018**, *9*, 2222–2228.
31. Nagamine, G.; Rocha, J.O.; Bonato, L.G.; Nogueira, A.F.; Zaharieva, Z.; Watt, A.A.R.; De Brito Cruz, C.H.; Padilha, L.A. Two-Photon Absorption and Two-Photon-Induced Gain in Perovskite Quantum Dots. *J. Phys. Chem. Lett.* **2018**, *9*, 3478–3484.
32. Wang, Y.; Zhi, M.; Chang, Y.Q.; Zhang, J.P.; Chan, Y. Stable, Ultralow Threshold Amplified Spontaneous Emission from CsPbBr3 Nanoparticles Exhibiting Trion Gain. *Nano Lett.* **2018**, *18*, 4976–4984.
33. Geiregat, P.; Maes, J.; Chen, K.; Drijvers, E.; De Roo, J.; Hodgkiss, J.M.; Hens, Z. Using Bulk-like Nanocrystals to Probe Intrinsic Optical Gain Characteristics of Inorganic Lead Halide Perovskites. *ACS Nano* **2018**, *12*, 10178–10188.
34. Yumoto, G.; Tahara, H.; Kawawaki, T.; Saruyama, M.; Sato, R.; Teranishi, T.; Kanemitsu, Y. Hot Biexciton E ff ect on Optical Gain in CsPbI 3 Perovskite Nanocrystals. *J. Phys. Chem. Lett.* **2018**.
35. Zhao, W.; Qin, Z.; Zhang, C.; Wang, G.; Huang, X.; Li, B.; Dai, X.; Xiao, M. Optical Gain from Biexcitons in CsPbBr 3 Nanocrystals Revealed by Two-dimensional Electronic Spectroscopy. *J. Phys. Chem. Lett.* **2019**, 1251–1258.

36. Protesescu, L.; Yakunin, S.; Bodnarchuk, M.I.; Krieg, F.; Caputo, R.; Hendon, C.H.; Yang, R.X.; Walsh, A.; Kovalenko, M. V Nanocrystals of Cesium Lead Halide Perovskites (CsPbX3, X = Cl, Br, and I): Novel Optoelectronic Materials Showing Bright Emission with Wide Color Gamut. *Nano Lett.* **2015**, *15*, 3692–3696.
37. Diroll, B.T.; Zhou, H.; Schaller, R.D. Low-Temperature Absorption, Photoluminescence, and Lifetime of CsPbX3 (X = Cl, Br, I) Nanocrystals. *Adv. Funct. Mater.* **2018**, *28*, 1800945.
38. Chen, J.; Žídek, K.; Chábera, P.; Liu, D.; Cheng, P.; Nuuttila, L.; Al-Marri, M.J.; Lehtivuori, H.; Messing, M.E.; Han, K.; et al. Size- and Wavelength-Dependent Two-Photon Absorption Cross-Section of CsPbBr 3 Perovskite Quantum Dots. *J. Phys. Chem. Lett.* **2017**, *8*, 2316–2321.
39. Maes, J.; Balcaen, L.; Drijvers, E.; Zhao, Q.; De Roo, J.; Vantomme, A.; Vanhaecke, F.; Geiregat, P.; Hens, Z. Light Absorption Coefficient of CsPbBr3 Perovskite Nanocrystals. *J. Phys. Chem. Lett.* **2018**, *9*, 3093–3097.
40. Lai, Y.Y.; Chou, Y.H.; Lan, Y.P.; Lu, T.C.; Wang, S.C.; Yamamoto, Y. Crossover from polariton lasing to exciton lasing in a strongly coupled ZnO microcavity. *Sci. Rep.* **2016**, *6*, 20581.
41. Eperon, G.E.; Jedlicka, E.; Ginger, D.S. Biexciton Auger Recombination Differs in Hybrid and Inorganic Halide Perovskite Quantum Dots. *J. Phys. Chem. Lett.* **2018**, *9*, 104–109.
42. She, C.; Fedin, I.; Dolzhnikov, D.S.; Demortière, A.; Schaller, R.D.; Pelton, M.; Talapin, D. V Low-threshold stimulated emission using colloidal quantum wells. *Nano Lett.* **2014**, *14*, 2772–7.
43. Stranks, S.D.; Hoye, R.L.Z.; Di, D.; Friend, R.H.; Deschler, F. The Physics of Light Emission in Halide Perovskite Devices. *Adv. Mater.* **2018**, *1803336*, 1–11.
44. Suárez, I.; Juárez-Pérez, E.J.; Bisquert, J.; Mora-Seró, I.; Martínez-Pastor, J.P. Polymer/Perovskite Amplifying Waveguides for Active Hybrid Silicon Photonics. *Adv. Mater.* **2015**, *27*, 6157–6162.
45. Gordillo, H.; Suarez, I.; Abargues, R.; Rodriguez-Canto, P.; Martinez-Pastor, J.P. Color Tuning and White Light by Dispersing CdSe, CdTe, and CdS in PMMA Nanocomposite Waveguides. *IEEE Photonics J.* **2013**, *5*, 2201412–2201412.
46. Rivas, D.; Muñoz-Matutano, G.; Canet-Ferrer, J.; García-Calzada, R.; Trevisi, G.; Seravalli, L.; Frigeri, P.; Martínez-Pastor, J.P. Two-color single-photon emission from InAs quantum dots: Toward logic information management using quantum light. *Nano Lett.* **2014**, *14*, 456–463.
47. Chirvony, V.S.; González-Carrero, S.; Suárez, I.; Galian, R.E.; Sessolo, M.; Bolink, H.J.; Martínez-Pastor, J.P.; Pérez-Prieto, J. Delayed Luminescence in Lead Halide Perovskite Nanocrystals. *J. Phys. Chem. C* **2017**, *121*.
48. Muñoz-Matutano, G.; Rivas, D.; Ricchiuti, A.L.; Barrera, D.; Fernández-Pousa, C.R.; Martínez-Pastor, J.; Seravalli, L.; Trevisi, G.; Frigeri, P.; Sales, S. Time resolved emission at 1.3 μm of a single InAs quantum dot by using a tunable fibre Bragg grating. *Nanotechnology* **2014**, *25*.
49. Tan, C.L.; Wang, Y.; Djie, H.S.; Ooi, B.S. The role of optical gain broadening in the ultrabroadband InGaAs/GaAs interband quantum-dot laser. *Comput. Mater. Sci.* **2008**, *44*, 167–173.
50. Kim, J.; Meuer, C.; Bimberg, D.; Eisenstein, G. Effect of Inhomogeneous Broadening on Gain and Phase Recovery of Quantum-Dot Semiconductor Optical Amplifiers. *IEEE J. Quantum Electron.* **2010**, *46 SRC-*, 1670–1680.
51. Rosencher, E.; Vinter, B. *Optoelectronics*; Press, C.U., Ed.; 2002; ISBN 0511034237.
52. Droseros, N.; Longo, G.; Brauer, J.C.; Sessolo, M.; Bolink, H.J.; Banerji, N. Origin of the Enhanced Photoluminescence Quantum Yield in MAPbBr3 Perovskite with Reduced Crystal Size. *ACS Energy Lett.* **2018**, *3*, 1458–1466.

53. Hirotsu, S.; Harada, J.; Iizumi, M.; Gesi, K. Structural Phase Transitions in CsPbBr3. *J. Phys. Soc. Japan* **1974**, *37*, 1393–1398.
54. Savenije, T.J.; Ponseca, C.S.; Kunneman, L.; Abdellah, M.; Zheng, K.; Tian, Y.; Zhu, Q.; Canton, S.E.; Scheblykin, I.G.; Pullerits, T.; et al. Thermally Activated Exciton Dissociation and Recombination Control the Carrier Dynamics in Organometal Halide Perovskite. *J. Phys. Chem. Lett.* **2014**, *5*, 2189–2194.
55. Du, W.; Zhang, S.; Shi, J.; Chen, J.; Wu, Z.; Mi, Y.; Liu, Z.; Li, Y.; Sui, X.; Wang, R.; et al. Strong Exciton–Photon Coupling and Lasing Behavior in All-Inorganic CsPbBr3 Micro/Nanowire Fabry-Pérot Cavity. *ACS Photonics* **2018**, *5*, 2051–2059.
56. Gauthron, K.; Lauret, J.-S.; Doyennette, L.; Lanty, G.; Al Choueiry, A.; Zhang, S.J.; Brehier, A.; Largeau, L.; Mauguin, O.; Bloch, J.; et al. Optical spectroscopy of two-dimensional layered (C6H5C2H4-NH3)2-PbI4 perovskite. *Opt. Express* **2010**, *18*, 5912–5919.
57. Luisa De Giorgi, M.; Perulli, A.; Yantara, N.; Boix, P.P.; Anni, M. Amplified Spontaneous Emission Properties of Solution Processed CsPbBr3 Perovskite Thin Films. *J. Phys. Chem. C* **2017**, *121*, 14772–14778.
58. Luan, F.; Gu, B.; Gomes, A.S.L.; Yong, K.-T.; Wen, S.; Prasad, P.N. Lasing in nanocomposite random media. *Nano Today* **2015**, *10*, 168–192.
59. De Giorgi, M.L.; Anni, M. Amplified Spontaneous Emission and Lasing in Lead Halide Perovskites: State of the Art and Perspectives. *Appl. Sci.* 2019, *9*.
60. Fan, T.; Lü, J.; Chen, Y.; Yuan, W.; Huang, Y. Random lasing in cesium lead bromine perovskite quantum dots film. *J. Mater. Sci. Mater. Electron.* **2019**, *30*, 1084–1088.

7 PHOTON RECYCLING EFFECT IN SANDWICH TYPE PNC-PMMA WAVEGUIDES

The reabsorption and reemission events of primarily emitted photons by a semiconductor, or photon recycling (PR), represents an outstanding mechanism to enhance the carrier density in semiconductor thin films. Indeed, it is well demonstrated that efficient PR can significantly improve the performances of solar cells, as well as potentially other optoelectronics devices, as light emitting devices. PR effect in a semiconductor would be originated if it have both a high absorption coefficient and a high emission quantum yield. Furthermore, we can achieve a stronger PR effect if the semiconductor is integrated in a photonic architecture that promotes the confinement of light in a long (unidirectional) path. In this Chapter, we propose the use of a waveguide structure containing, for the first time, a $CsPbBr_3$ perovskite nanocrystal (PNCs) thin film (< 200 nm) between poly(methyl methacrylate) (PMMA) layers. This sandwich configuration couples the excellent absorption and efficiency of emission properties of the PNCs with a strong confinement of the TE_0 (TM_0) mode within the active layer. Therefore, with geometrical parameters properly optimized to increase the efficiency of reabsorption, this structure is the ideal candidate to study the PR effect; it was properly characterized by measuring the redshift and the decay time of the photons collected at the one of the waveguide, after a certain propagation length. To this end, we propose an experimental set-up based on a frequency modulated spectroscopy technique to extract the decay time and other physical parameters. Finally, experimental results were properly validated by a stochastic Monte Carlo model that reproduces the propagation of emitted light in the waveguide structure by introducing random reabsorption/reemission events.

7.1 INTRODUCTION

Photon recycling (PR) is a physical mechanism that takes place when a fraction of the photons radiatively generated in a semiconductor is sequentially (re)absorbed and (re)emitted before being extracted [1]. Such multiple (re)absorption/(re)emission cycles

give rise to a gas of "recycled photons" densely concentrated in the semiconductor thin film. Consequently, PR provides another degree of freedom to control the carrier density of a semiconductor [2], and with it, a way to tailor-made its optoelectronics properties [3,4]. Demonstrated applications of PR include semiconductor diodes with extremely high open circuit voltages and light modulators [2].

In this context, PR has been recently related to metal halide perovskites (MHP), in order to explain the excellent conversion efficiencies and emission rates reported for this family of semiconductors [5,6]. Indeed, the strong absorption coefficient above the bandgap [7,8], the small Stokes Shift (energy separation between the PL peak and exciton resonance of the absorption spectrum) [9,10] and the high efficiency of light emission (namely, the PLQY) [11,12] that are characteristic of MHPs are clearly favorable for PR. In this way, over the last 3-4 years, different experimental and theoretical papers have analyzed the efficiency of PR in MHPs and the potential benefits for solar cells or light emitting diodes, among other devices [13,14]. In particular, studies on $CH_3NH_3PbX_3$ (X = Cl, Br, I) polycrystalline thin films [14,15], $CH_3NH_3PbX_3$ single crystals [10,16,17], or $CsPbBr_3$ microwires [18,19] mainly conclude that photogenerated PL experiences a redshift and an suffer an elongation of its decay time after traversing some microns of the MHP material, which are clearly signatures for the PR effect [2]. Moreover, the theoretical analysis of PR predicts that it dominates over diffusion of carriers [15], and that multiple photon absorption and emission events increase the effective lifetime of the collected photons [20]. Although there has been a controversy about the impact of PR in the efficiency of solar cells [16], recent studies on perovskite single crystals [6] confirm that PR is the dominant energy transport mechanism, whereas other theoretical and experimental works demonstrate a measurable enhancement of the open circuit voltage in solar cells when PR is optimized [15,21,22].

Here, the use of an optical waveguide provides another degree of freedom to increase the PR efficiency. Examples include the use of MHP nanofilms/microwires as a waveguide for the emitted photons [15], scattering with silver nanoparticles to increase the path for the emitted photons [23], or the enhancement of outcoupled light from the photonic structure [24,25]. In particular, the ideal photonic structure should confine the PL in the MHP, enable a long path for the emitted photons and allow an efficient of light outcoupling.

In this work we propose a photonic architecture that fulfills all necessary conditions to optimize PR on MHP films. This structure consists of a thin (50-200 nm) semiconductor sandwiched between two (passive) poly(methyl methacrylate) (PMMA) layers. This

elegant planar waveguide configuration efficiently exploits the light emission properties of the semiconductor by the high confinement of the light within the active layer, propagates the light with a reduced attenuation due to the absence of losses in the polymer, and allows an efficient extraction of the PL by end fire coupling methods. Indeed, we have already demonstrated similar structures that enhance the generation of PL on close packed CdSe/ZnS quantum dots (QD) films [26] or generate optical amplification on organic compounds [27]. Here, $CsPbBr_3$ perovskite nanocrystals (PNC) films are chosen as nanocrystals with demonstrated high reabsorption and excellent efficiency of emission. In fact, since the first publication by Kovalenko's group in 2015 [12], layers of PNCs have shown excellent efficiencies for light emission [28], optical amplification [29–31] and conversion performances [32]. Thus, although PR within these nanocrystals has not been studied up to now, they present optimum properties to enhance this mechanism. In this way, our PMMA/PNC/PMMA waveguide structure results an excellent configuration that demonstrates an increased lifetime for the collected photons with the length of the waveguide, up to 10 ns for the optimum device. For this purpose, this lifetime is properly characterized by modulated PL spectroscopy technique in the frequency domain [33], which, to the best of our knowledge, is the first time that is applied to study the PR mechanism in MHPs. This set-up allows the extraction of the PL decay time without expensive ultrafast photodiodes or time correlated single photon counting cards. Indeed, we believe that this technique will be very soon the basis of a light-to-light impedance spectroscopy able to extrapolate the different recombination parameters (traps, diffusion, non radiative channels...) of the PL, in analogy to the impedance spectroscopy used for the electrical characterization of solar cells [34]. The accuracy of this experimental set-up is clearly demonstrated with a correlation of the Stokes shift of the PL and the geometrical parameter of the waveguides. Finally, experimental results will be validated by simulations carried out with a stochastic Monte Carlo model that consider a sequence of random (re)absorption/(re)emission events.

7.2 MEASURING THE PHOTON RECYCLING EFFECT

7.2.1 SYNTHESIS OF COLLOIDAL SOLUTION AND SAMPLE PREPARATION

$CsPbBr_3$ PNCs were grown following the hot-injection method (described in section 3.1.1 of this Thesis) developed by Kovalenko et al., [12] with the modifications detailed

elsewhere [31]. Then, PNC-PMMA sandwich waveguide was fabricated on a commercial SiO_2/Si substrate by the following steps: (i) cleaning the wafer sequentially with acetone, ethanol and isopropanol, (ii) spin coating the bottom PMMA cladding at 3000 rpm and post baking at 80 ºC and 150 ºC for two minutes each, (iii) deposition of a close packed film of PNCs with the aid of a commercial Doctor Blade applicator (Elcometer 4340) and postbaking at 80 ºC for 2 minutes, (iv) spin coating the top PMMA cladding at 3000 rpm and post baking at 80 ºC and 150 ºC for two minutes each. Step (iii) was sequentially repeated until the film of PNCs reached the desired thickness (50 - 200 nm). Here, the thickness was accurately characterized with a profilometer after scratching several zones of the sample.

7.2.2 Experimental Setup

Photon recycling can be characterized by measuring the Stokes shift of the PL with respect to the propagation distance. The information regarding photon dynamics (specially the (re)absorption/(re)emission events) can be extracted by the frequency domain spectroscopy (FD-spectroscopy) of waveguided PL, as demonstrated below. For the Stokes-Shift of PL, a modified version of the Variable Stripe Length method (VSL) set-up was used [35], as it was described in Section 3.2.2.D. Similarly, the FD-spectroscopy was also partially described in Section 3.2.2.F.

7.2.3 Sample Description

After the synthesis, $CsPbBr_3$ PNCs exhibit a cubic shape (see Figure 7.1a) with an average edge size (L) of 9 nm and a dispersion of 1.5 (see Figure 7.1b). The ratio $L/2a_0$ (L is the nanocube edge size and a_0 de Bohr radius) results 1.3, which corresponds to a weak quantum confinement regime. The characteristic absorption spectra of $CsPbBr_3$ PNC layers used in this work show an excitonic resonance at 509 nm (blue line in Figure 7.1c), in agreement with results reported in previous publications for similar PNCs [12,31]. In the same way, the PL spectrum (green line in Figure 7.1c) of these layers measured under back scattering geometry under low excitation power is centered at 522 nm with a full width at half maximum (FWHM) of about 20 nm. Clearly, the absorption presents a sharp Urbach tail (blue symbols) overlapping the PL, similarly to results recently reported elsewhere [31].

The waveguide geometry used in this work consists of the PNC-PMMA sandwich structure deposited on a commercial SiO_2/Si (2 µm of SiO_2) wafer, as illustrated in Figure

7.1d. The thickness of PMMA (d_2) was fixed to d_2 = 500 nm, while the thickness of the PNC (d_1) was ranged between 50 and 200 nm, as measured by profilometry (this technique was described in Section 3.3.2). The waveguide structure is based on the different index contrast (at 520 nm) between air (n = 1), PMMA (n = 1.4930) [36], PNC (n = 1.9 – 0.23i) [37], SiO_2 (n = 1.4613) [36] and Si (4.1882 – 0.0377i) [36]. In these conditions, the analysis carried out with a transfer matrix algorithm reveals that the waveguide supports one mode highly confined in the PNC layer in both transverse electric (TE) and transverse magnetic (TM) polarizations. Figure 7.1e shows the mode distribution of the TE_0 mode, which is mostly confined in the PNC layer of 100 nm (TM polarization presents a similar distribution). This mode presents an effective index (N_{eff}) of 1.64185 – 0.05504i, while their counterpart of the waveguides with d_1=*50 nm* and d_1=*200 nm* are N_{eff}=1.54591 – 0.02395i and N_{eff}=1.77275-0.08061i, respectively. Both real and imaginary parts of N_{eff} increase with the thickness of the PNC layer, indicating that the thicker the films, the higher the confinement of the light in the active layer.

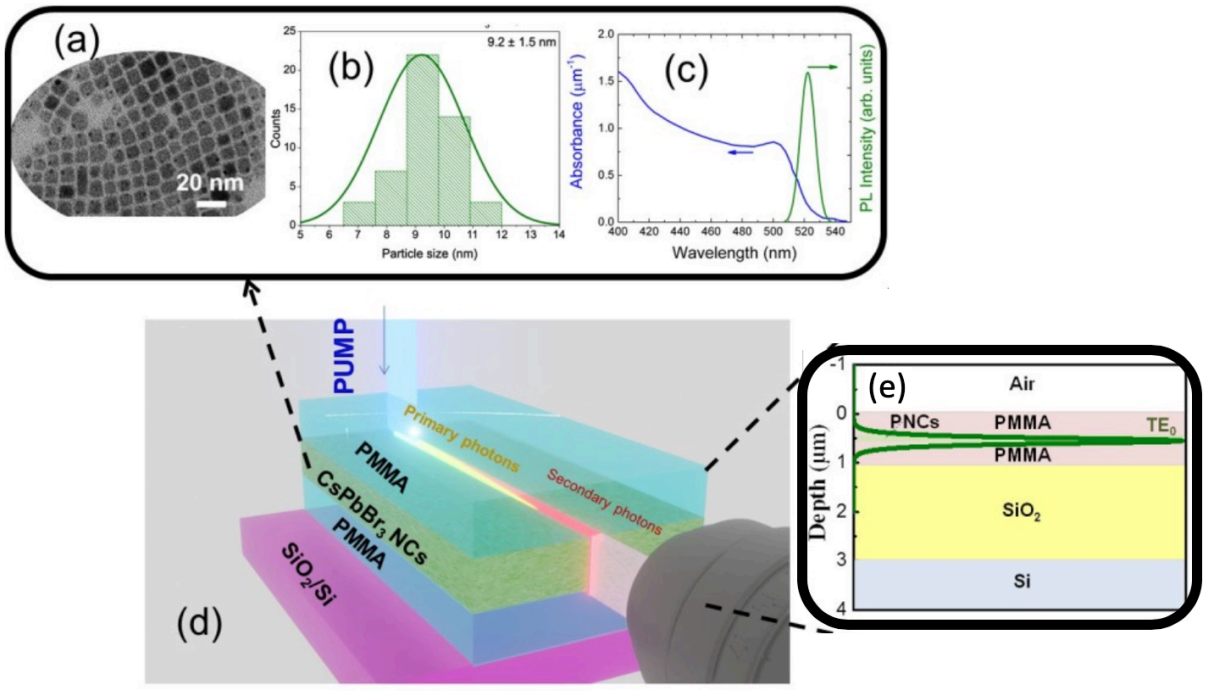

Figure 7.1. Analysis of the waveguide structure: (a) TEM images of the $CsPbBr_3$ NCs. (b) Statistics of the size. (c) Absorption (blue line and left axis) and PL (green line and right axis) of the PNCs layers. (d) Scheme of the sample. A $CsPbBr_3$ close-packed thin (d_1=50-200 nm) film is sandwiched between two PMMA films (d_2=500 nm). (e) SEM image of the sample cross section. (f) Power distribution of the TE_0 mode in a waveguide with d_1=100 nm.

7.3 RESULTS AND DISCUSSION

7.3.1 SPECTRAL SIGNATURE OF THE PHOTON RECYCLING EFFECT

The large overlap between the absorption band edge and PL spectra (see Figure 7.1c) indicates that layers of PNCs would present a large reabsorption effect required for a noticeable PR effect. Indeed, reported values in the literature shows attenuation of around ≈ 10^{-1} μm^{-1} at the PL peak (520 nm) [31], which results on propagation lengths of around ≈ 100 nm for the PL photons traversing a PNC film. Since the quantum yield of the PNCs synthesized in our laboratory is of 40% - 50%, the reabsorption by a given PNC of emitted photons by a different PNC is expected to promote new emitted photons of longer wavelengths. Consequently, photons extracted from a thick film of PNCs at distances much longer than 100 nm will come from the two different contributions illustrated in Figure 7.1d: a flow of secondary photons generated from multiple (re)absorption and (re)emission processes is superimposed to the primary photons not absorbed by the film. The ratio between both photon fluxes depends on the propagation distance and the overlap between the propagation modes and the active material. In particular, this waveguide geometry, where the PL is highly confined in the active layer through the TE_0 (TM_0) mode, would give rise a long path for the photons before extraction and promote an efficient generation of secondary photons. Figures 7.2a - 7.2c present the PL spectra decoupled at the output edge of the waveguide for different separations between the excitation line and the edge of the waveguide (*s*), and thicknesses of the PNC layer of $d_1 =$ 50 nm (Figure 7.2a), $d_2 =$ 100 nm (Figure 7.2b), $d_3 =$ 200 nm (Figure 7.2c). For $d_1 =$ 50 nm (Figure 7.2a) the PL spectra are identical for all separations (*s*) or waveguided traveling distance. Indicating a negligible PL redshift. This is due to the fact that the confinement of the fundamental mode within the PNC region (Γ) is reduced to ≈ 20 % of the total power distribution for this thin layer. However, for thicker layers, Γ increases up to ≈ 80 %, and the PL spectra now shifts to long wavelengths (Figure 7.2b and 7.2c). In particular, for $d_1 =$ 50 nm the PL peak is centered at 521-523 nm for all separations (blue symbols in Figure 7.2d), while the PL peak exhibits a monotonous redshift up to 533 nm for $s =$ 3 mm for $d_1 =$ 100-200 nm (green and brown symbols in Figure 7.2d). The redshift observed in the different samples is correlated with the attenuation of the PL presented in Figure 7.2e. The PL intensity (I_{PL}) measured as a function of *s* obeys the equation: [35]

$$I_{PL} = A_0 \cdot e^{-s/L_{p0}} + A_1 \cdot e^{-s/L_{p1}} \tag{7.1}$$

where I_0 is the intensity at $z = 0$, A_i the relative intensity of the mode i, and L_{pi} the propagation length of the i^{th} mode. In this way, I_{PL} measured as a function of z follows two exponential decays. The first one is characterized by $L_{p1} = 180 \pm 10$ µm, $L_{p1} = 100 \pm 20$ µm and $L_{p1}=150 \pm 20$ for $d_1=50$ nm, $d_1=100$ nm and $d_1=200$ nm, respectively; and corresponds to the fundamental mode. The second propagation length is about $L_{p2} = 750 \pm 250$ μm for all samples and only represents a 20-25 % ($A_1/(A_0+A_1)$) of the PL intensity.

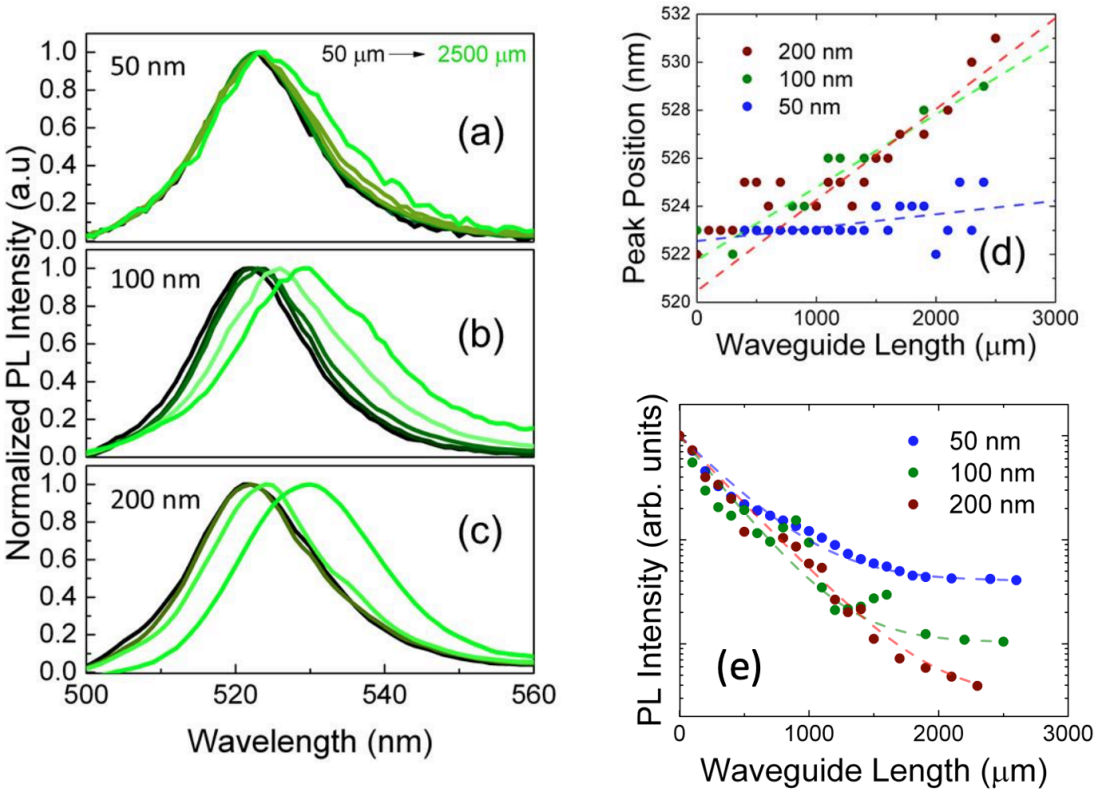

Figure 7.2. (a, b, c) Normalized spectra of the PL spectra plotted in collection of increasing length of the waveguide with 50, 100 and 500 nm thick PNC layers. (d) Peak of the PL spectra as a function of the distance between the stripe and the edge of the sample z. (e) PL intensity as a function of z. Blue, green and brown symbols refer to 50 nm, 100 nm and 300 nm PNC layers. The discontinuous lines represent the fitting to a biexponential decay function.

7.3.2 Photon Recycling Dynamics

Since PR comes from a sequence of multiple (re)absorption, (re)emission and propagation events, there are different physical mechanisms potentially influencing its efficiency and, therefore, its possible applications. For example, this process can be modified by the radiative lifetime, nonradiative channels, Auger recombination, optical path determined by the geometry and diffusion of photons, among other mechanisms [15,20], In this way, a characterization technique able to separate all contributions would

provide the required information to engineer PR in a given device. Here, we propose the application of FD-spectroscopy [33] to determine the elongation of the decay time produced by the PR process. We believe that the analysis of the PL as a function of the frequency can be useful to extract some of the aforementioned mechanisms, in analogy to the impedance spectroscopy often used for the characterization of solar cells. In particular, a finite PL decay time of the sample under study will limit the PL intensity at sufficiently high modulation frequencies. Particularly, the intensity and phase of the collected PL signal exhibit a frequency dependence given by the following low pass filter transfer function [35]:

$$\mathrm{m}(\omega) = (1 + \omega^2\tau^2)^{-1/2} \tag{7.2}$$

$$\phi(\omega) = tan^{-1}(\omega\tau) = cos^{-1}[(1 + \omega^2\tau^2)^{-1/2}] \quad (3) \tag{7.3}$$

Here, $m(\omega)$ is the absolute value of the PL normalized by the response of the laser, $\phi(\omega)$ is the phase difference between the reference signal and the PL, τ is the effective decay time, and $\omega = 2\pi f$, where f is the frequency of the modulation applied to the excitation laser. In order to provide the highest accuracy in the measurements, each experimental point was obtained after five averages and signal was always kept at least one-fold higher than the noise. In addition, it is worth to point out that the maximum modulation frequency of our excitation laser is around 2-3 MHz (while minimum measurable by the lock-in amplifier was 25 kHz), hence the analysis of modulated signal by $m(\omega)$ will only be sensitive to decay times between $\tau \sim 1/\omega \approx 10^{-6}$ s and $4\ 10^{-5}$ s. For this reason, we propose to choose $tan(\phi(\omega))$ as this function is more sensitive to changes in the modulated PL. In this way, τ will be accurately determined from the measured variation of $\phi(\omega)$ by the lock-in amplifier, that has a sensitivity as low as 0.01 radians. Figures 7.3a, 7.3b and 7.3c show representative measurements in optical waveguides incorporating PNC films of thicknesses d_1 = 50 nm, d_1 = 100 nm, and d_1 = 200 nm, respectively, and propagation distances s = 0.2 mm (red symbols), s = 0.7 mm (blue symbols), s = 2 mm (green symbols). In all cases we observe a very low data dispersion and allows an easy extraction of τ by the slope of the $tan(\phi(\omega))$ fitting curve (solid lines).

We obtain τ in the range from τ = 3 ns to τ = 7.5 ns depending on the geometrical parameter s and d_1 (see Figure 7.3d). The smallest PL decay time of 3 - 3,5 ns measured for $s < 100\ \mu m$ in the three waveguides agrees quite well with the average recombination time reported for $CsPbBr_3$ PNCs under low excitation fluencies (< 1 μJ/cm^2) [38]. As

expected, the separation (*s*) enhances the PR process by a longer path for the emitted photons, resulting in an additional delay for the collected photons before reaching the detector. Consequently, τ rises with *s* and reaches τ= 7.5 ns for the longest propagation length studied in this work, *s* = 3000 µm. Similarly, τ also increases with the thickness d_1 of the PNC film in the waveguide due to the fact that TE_0 is more and more confined in the active layer. Indeed, there is a clear correspondence of τ with the red-shift measured in Figure 7.2, as it is shown in Figure 7.3e, where the lifetime is parametrized by the red-shift $\Delta\lambda$ of the samples with d_1 = 100 nm (green symbols) and d_1 = 200 nm (brown symbols). The observed correlation between both parameters implies that photon recycling contributes to the external Stokes Shift measured in our PNC-waveguides, as it was shown in similar studies with perovskite single crystals [9,16].

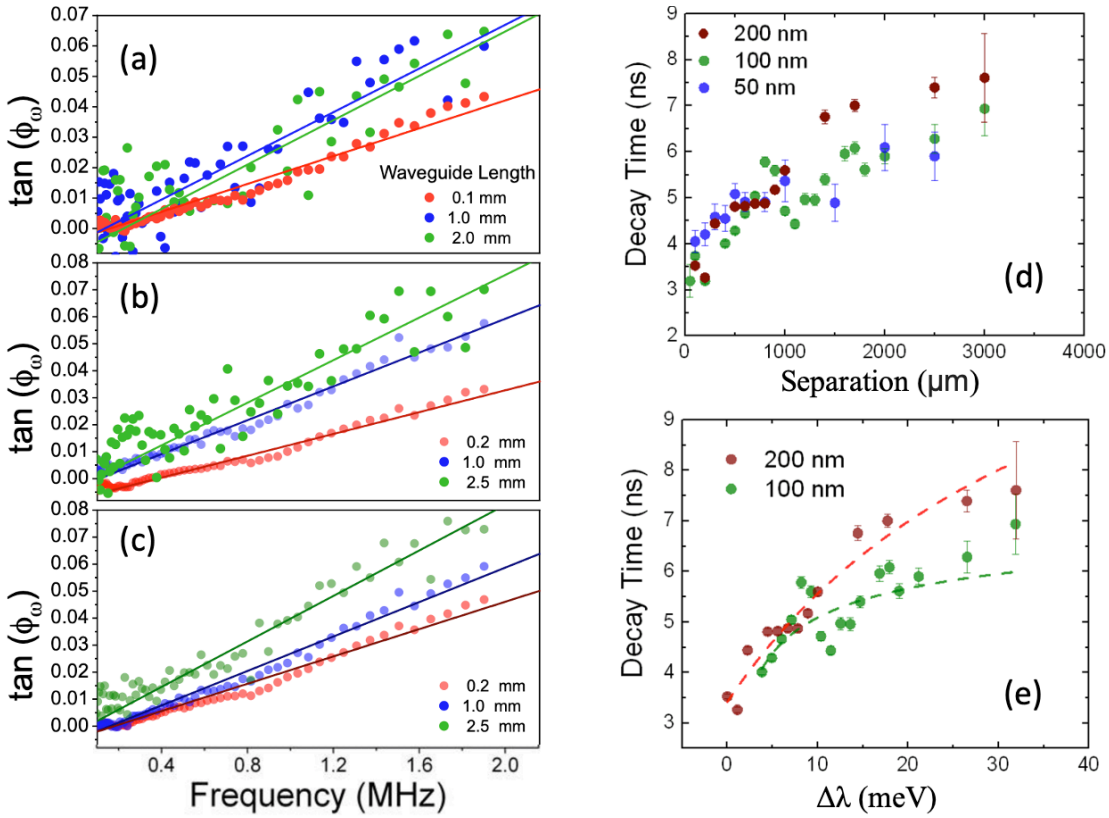

Figure 7.3. Tangent of ϕ(ω) for s=0.2 mm (red symbols), s=0.7 mm (blue symbols), s= 2 mm (green symbols): (a) 50 nm, (b) 100 nm, (c) 300 nm. The data is fitted by Equation 7.2 (solid lines). (d) Decay times extracted in Figure 7.2a-c as a function of *s*. (e) Decay times as a function of the red-shift Δλ.

7.3.2 Modelling of Photon Recycling

The results presented in the previous section clearly indicate the influence on the PR effect in the dynamics of the light propagation along the waveguide. In particular, the photons extracted at the output edge of the sample are influenced by several parameters

that results on a redshift of the spectra and an increase of the lifetime. According the models proposed elsewhere for planar structures, [15,20] we propose the following rate equations to simulate the generation of carriers and propagation of photons along the waveguide:

$$\frac{\partial n}{\partial t} = \sum_\lambda \beta_\lambda \gamma_\lambda - k_x n - k_{xx} n^2 \tag{7.4}$$

$$\frac{d\gamma_\lambda}{dt} = -\beta_\lambda \gamma_\lambda + k_{xx} P_\lambda n^2 \tag{7.5}$$

Here, $\beta_\lambda = c\alpha_\lambda/n_p$ is the rate of photon absorption, P_λ is the probability of emission at the wavelength λ, and the coefficients k_x and k_{xx} are the monomolecular and bimolecular recombination rates, respectively. P_λ is given by the normalized distribution of the experimental PL measured at the shortest waveguide configuration, while $\beta_\lambda = c\alpha_\lambda/n_p$; where c is the speed of light, α_λ the absorption coefficient at the wavelength λ obtained from the experimental curve (Figure 7.1c) and n_{po} is the refractive index. Monomolecular and bimolecular recombination rates of carriers are given by $k_x = 10^9$ s^{-1} and $k_{xx} = 10^{-10}$ cm^3 s^{-1} [15,20]**.** Since the geometry proposed in this work requires including the boundary conditions of the waveguide and the field distribution of the propagating TE_0 (TM_0) mode, Equations 7.4-7.5 were solved by using a Monte Carlo ray-tracing technique [39] based on the following steps: (i) the method introduces the flow of primary photons that are spontaneously generated at the input of the waveguide and calculates independently the trajectory of each photon inside the structure (green arrows in Figure 7.4a); (ii) the algorithm calculates the probability of reabsorption by PNCs embedded inside the structure (yellow circles in Figure 7.4a) as a function of the wavelength and the position z; (iii) the absorbed photons generate carriers that will recombine when triggered by a probabilistic calculation, spawning a secondary flow of emitted photons. The secondary photons are reinjected into the waveguide at the position at which the carrier recombination occurred with an arbitrary direction. The wavelength of the newly photogenerated photon is assigned following the un-redshifted PL curve distribution (as measured in backscattering conditions). The simulation can be executed in discretized time steps between 1 and 100 femtoseconds. Photons and carriers can be counted at every time step to obtain a histogram plot of their densities. When the nanosecond time scale is reached, the simulation reaches a stationary state that reproduce quite well the propagation inside a waveguide of 2500 µm length.

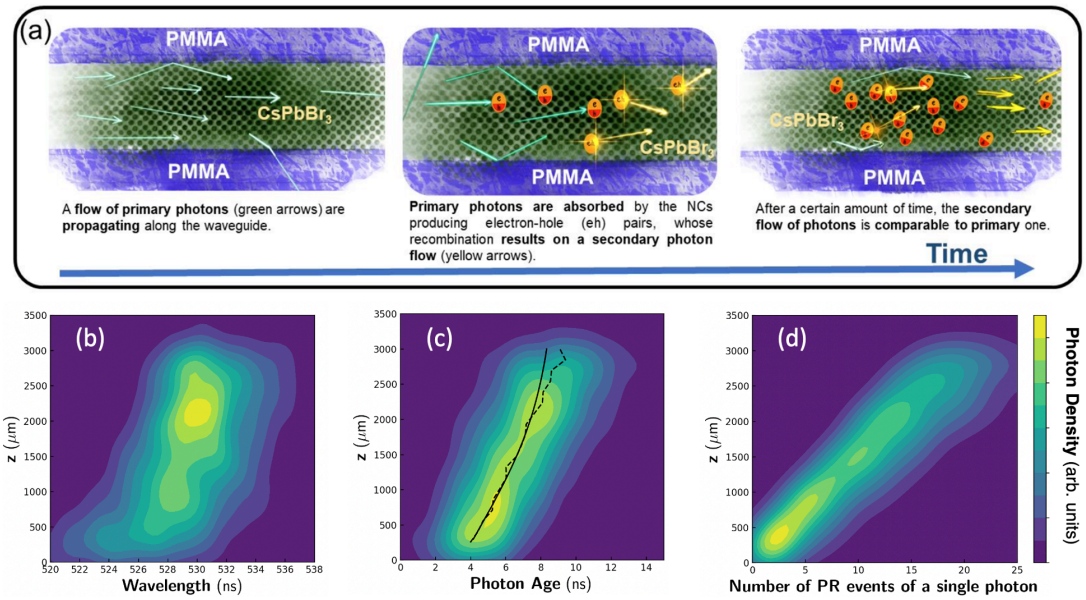

Figure 7.4. Simulation with a Monte Carlo algorithm (a) Steps carried out by the algorithm. (b) Map of the wavelength of the photons inside the waveguide. (c) Map of the lifetime of each photon inside the waveguide (the experimental decay times a 200 nm tick waveguide, extracted from Figure 7.3e, is plotted as a continuous black line while the bin-average tendency curve of the 2D-map is plotted as a black discontinuous line). (d) Map of the number of chained absorption-emission events for each photon inside the waveguide.

The simulation predicts a spectral red-shift of 10 nm (see map in Figure 7.4b), in agreement with the experimental results presented in Figure 7.2c. Also, the simulation allows to predict the maximum number of chained PR events of a single photon (Figure 7.4d). In this particular configuration, the average number of (re)absorption an (re)emission processes that a single photon suffers until it reaches the end of the waveguide (2500 - 3000 μm) is of around 15 - 20 events. This translates into a time delay of around 7 - 10 ns, as can be seen in Figure 7.4c, for photons that have travelled a distance of around 2500 μm after undergoing several PR events, which again is in very good agreement with the measured lifetimes reported in Figure 7.3d.

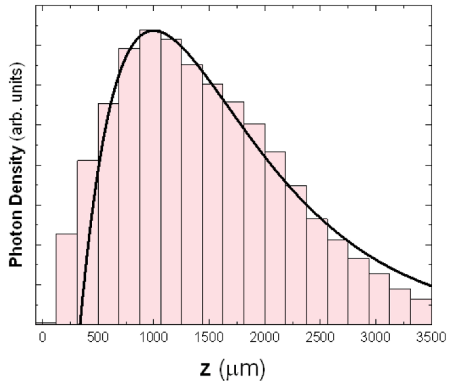

Figure 7.5. Secondary photon population inside the waveguide simulated with the Monte Carlo method (bar histogram). The simulated data is fitted to a rise/decay function (solid black curve).

Finally, the secondary photon population density was fitted to a rise/decay function, $A\left(e^{-z/L_D} - e^{-z/L_R}\right)/(L_D - L_R)$, in which A is the fitting amplitude and the lengths L_D and L_R are the decay and rise propagation lengths, respectively. Thus, the model predicts (from the fittings of the data in Figure 7.5) a rise length of $L_R = 500 \pm 100$ µm, which is the average propagations length that primary photons (those with shorter wavelengths) will travel until being absorbed, and a decay length of $L_D = 900 \pm 100$ µm, which correspond to the propagation length of the secondary photons (those with longer wavelengths) aided by the photon recycling effect. This result is are in agreement with the averaged propagation length obtained from the experimental data shown in Figure 7.2b. Therefore, we can say that our system, which restricts the flux of photons within the plane of the waveguide (and mainly along the direction of the waveguided primary flux), exhibits a behavior which can be described by Fick's laws of diffusion [40]. Hence, we could deduce a diffusion coefficient ($D = L_p^2/\tau$) by considering a photon mean lifetime of $\tau \approx 7.5\, ns$, as extracted from Figure 7.3, and an average propagation length of 700 µm, obtaining a value in the order of 65 m^2/s for this hypothetical photon diffusion propagation mechanism.

7.4 CONCLUSIONS

In this work, PR mechanism is studied in PNC thin films by using a PMMA/PNC/PMMA sandwich waveguide structure. This configuration highly confines the PL within the active material by the TE_0 (TM_0) propagation modes, an optimal strategy to enhance the reabsorption effect necessary to observe the PR. In this way, the geometrical parameters of the structure were optimized to maximize this interaction. Consequently, PL line experiences a redshift with the propagation length up to 10 nm for the best device (thickest PNC film), which indicates the strong reabsorption effect in the structure. The impact of PR is corroborated by a correlation of the redshift with the decay time of the collected photons. For this purpose, a frequency domain spectroscopy technique is developed to properly characterize the decay time together with other intrinsic effects that influences the PR. The influence of each parameter is stablished by Monte Carlo stochastic model. These simulations reproduce and verify the experimental results. Since this effect is carried out along several mm, this elegant configuration provides an enhancement of the waveguide propagation distance due to increased photon lifetimes. Consequently, and making an analogy with the case of carriers

generated and diffusing in a semiconductor slab, we obtain a diffusion length very close to the mm range (340 μm). Therefore, the proposed device is expected to provide potential applications in integrated optics incorporating perovskite materials as active media, but also photovoltaics and light emitting diodes.

7.5 REFERENCES

1. Dumke, W.P. Spontaneous Radiative Recombination in Semiconductors. *Phys. Rev.* **1957**, *105*, 139–144.
2. Xu, Y.; Tennyson, E.M.; Kim, J.; Barik, S.; Murray, J.; Waks, E.; Leite, M.S.; Munday, J.N. Active Control of Photon Recycling for Tunable Optoelectronic Materials. *Adv. Opt. Mater.* **2018**, *6*, 1701323.
3. Science, S. Theory of some effects of photon recycling in semiconductors. *Semicond. Sci. Technol.* **1993**, *8*, 1267–1276.
4. Koc, M.A.; Raja, S.N.; Hanson, L.A.; Nguyen, S.C.; Borys, N.J.; Powers, A.S.; Wu, S.; Takano, K.; Swabeck, J.K.; Olshansky, J.H.; et al. Characterizing Photon Reabsorption in Quantum Dot-Polymer Composites for Use as Displacement Sensors. *ACS Nano* **2017**, *11*, 2075–2084.
5. Stranks, S.D.; Hoye, R.L.Z.; Di, D.; Friend, R.H.; Deschler, F. The Physics of Light Emission in Halide Perovskite Devices. *Adv. Mater.* **2018**, *1803336*, 1–11.
6. Gan, Z.; Wen, X.; Chen, W.; Zhou, C.; Yang, S.; Cao, G.; Ghiggino, K.P.; Zhang, H.; Jia, B. The Dominant Energy Transport Pathway in Halide Perovskites: Photon Recycling or Carrier Diffusion? *Adv. Energy Mater.* **2019**, *9*, 1900185.
7. De Wolf, S.; Holovsky, J.; Moon, S.J.; Löper, P.; Niesen, B.; Ledinsky, M.; Haug, F.J.; Yum, J.H.; Ballif, C. Organometallic halide perovskites: Sharp optical absorption edge and its relation to photovoltaic performance. *J. Phys. Chem. Lett.* **2014**, *5*, 1035–1039.
8. Maes, J.; Balcaen, L.; Drijvers, E.; Zhao, Q.; De Roo, J.; Vantomme, A.; Vanhaecke, F.; Geiregat, P.; Hens, Z. Light Absorption Coefficient of CsPbBr3 Perovskite Nanocrystals. *J. Phys. Chem. Lett.* **2018**, *9*, 3093–3097.
9. Gan, Z.; Chen, W.; Yuan, L.; Cao, G.; Zhou, C.; Huang, S.; Wen, X.; Jia, B. External stokes shift of perovskite nanocrystals enlarged by photon recycling. *Appl. Phys. Lett.* **2019**, *114*.
10. Diab, H.; Arnold, C.; Lédée, F.; Trippé-Allard, G.; Delport, G.; Vilar, C.; Bretenaker, F.; Barjon, J.; Lauret, J.S.; Deleporte, E.; et al. Impact of Reabsorption on the Emission Spectra and Recombination Dynamics of Hybrid Perovskite Single Crystals. *J. Phys. Chem. Lett.* **2017**, *8*, 2977–2983.
11. Xing, G.; Mathews, N.; Lim, S.S.; Yantara, N.; Liu, X.; Sabba, D.; Grätzel, M.; Mhaisalkar, S.; Sum, T.C. Low-temperature solution-processed wavelength-tunable perovskites for lasing. *Nat. Mater.* **2014**, *13*, 476–480.
12. Protesescu, L.; Yakunin, S.; Bodnarchuk, M.I.; Krieg, F.; Caputo, R.; Hendon, C.H.; Yang, R.X.; Walsh, A.; Kovalenko, M. V Nanocrystals of Cesium Lead Halide Perovskites (CsPbX3, X = Cl, Br, and I): Novel Optoelectronic Materials Showing Bright Emission with Wide Color Gamut. *Nano Lett.* **2015**, *15*, 3692–3696.
13. Kirchartz, T.; Staub, F.; Rau, U. Impact of Photon Recycling on the Open-Circuit Voltage of Metal Halide Perovskite Solar Cells. *ACS Energy Lett.* **2016**, *1*, 731–739.

14. Motti, S.G.; Crothers, T.; Yang, R.; Cao, Y.; Li, R.; Johnston, M.B.; Wang, J.; Herz, L.M. Heterogeneous Photon Recycling and Charge Diffusion Enhance Charge Transport in Quasi-2D Lead-Halide Perovskite Films. *Nano Lett.* **2019**, *19*, 3953–3960.
15. Pazós-Outón, L.M.; Szumilo, M.; Lamboll, R.; Ritcher, J.M.; Crespo-Quesada, M.; Ehrler, B.; Pazos-Outon, L.M.; Abdi-Jalebi, M.; Beeson, H.J.; Vrucinie, M.; et al. Photon recycling in lead iodide perovskite solar cells. *Science (80-.).* **2016**, *351*, 1430–1433.
16. Fang, Y.; Wei, H.; Dong, Q.; Huang, J. Quantification of re-absorption and re-emission processes to determine photon recycling efficiency in perovskite single crystals. *Nat. Commun.* **2017**, *8*, 14417.
17. Yamada, T.; Aharen, T.; Kanemitsu, Y. Near-Band-Edge Optical Responses of CH3NH3PbCl3 Single Crystals: Photon Recycling of Excitonic Luminescence. *Phys. Rev. Lett.* **2018**, *120*, 57404.
18. Dursun, I.; Zheng, Y.; Guo, T.; De Bastiani, M.; Turedi, B.; Sinatra, L.; Haque, M.A.; Sun, B.; Zhumekenov, A.A.; Saidaminov, M.I.; et al. Efficient Photon Recycling and Radiation Trapping in Cesium Lead Halide Perovskite Waveguides. *ACS Energy Lett.* **2018**, *3*, 1492–1498.
19. Wang, Y.; Sun, X.; Shivanna, R.; Yang, Y.; Chen, Z.; Guo, Y.; Wang, G.C.; Wertz, E.; Deschler, F.; Cai, Z.; et al. Photon Transport in One-Dimensional Incommensurately Epitaxial CsPbX3 Arrays. *Nano Lett.* **2016**, *16*, 7974–7981.
20. Ansari-Rad, M.; Bisquert, J. Insight into Photon Recycling in Perovskite Semiconductors from the Concept of Photon Diffusion. *Phys. Rev. Appl.* **2018**, *10*, 4062–4073.
21. Abebe, M.G.; Abass, A.; Gomard, G.; Zschiedrich, L.; Lemmer, U.; Richards, B.S.; Rockstuhl, C.; Paetzold, U.W. Rigorous wave-optical treatment of photon recycling in thermodynamics of photovoltaics: Perovskite thin-film solar cells. *Phys. Rev. B* **2018**, *98*, 1–12.
22. Brenes, R.; Laitz, M.; Jean, J.; DeQuilettes, D.W.; Bulovic, V. Benefit from Photon Recycling at Maximum Power Point of the State-of-the-Art Perovskite Solar Cells. *Phys. Rev. Appl.* **2019**, *10*, 1.
23. Saliba, M.; Zhang, W.; Burlakov, V.M.; Stranks, S.D.; Sun, Y.; Ball, J.M.; Johnston, M.B.; Goriely, A.; Wiesner, U.; Snaith, H.J. Plasmonic-Induced Photon Recycling in Metal Halide Perovskite Solar Cells. *Adv. Funct. Mater.* **2015**, *25*, 5038–5046.
24. Staub, F.; Kirchartz, T.; Bittkau, K.; Rau, U. Manipulating the Net Radiative Recombination Rate in Lead Halide Perovskite Films by Modification of Light Outcoupling. *J. Phys. Chem. Lett.* **2017**, *8*, 5084–5090.
25. Richter, J.M.; Abdi-Jalebi, M.; Sadhanala, A.; Tabachnyk, M.; Rivett, J.P.H.; Pazos-Outón, L.M.; Gödel, K.C.; Price, M.; Deschler, F.; Friend, R.H. Enhancing photoluminescence yields in lead halide perovskites by photon recycling and light out-coupling. *Nat. Commun.* **2016**, *7*.
26. Suárez, I.; Larrue, A.; Rodríguez-Cantó, P.J.; Almuneau, G.; Abargues, R.; Chirvony, V.S.; Martínez-Pastor, J.P. Efficient excitation of photoluminescence in a two-dimensional waveguide consisting of a quantum dot-polymer sandwich-type structure. *Opt. Lett.* **2014**, *39*, 4962–4965.
27. Signoretto, M.; Zink-Lorre, N.; Suarez, I.; Font-Sanchis, E.; Sastre-Santos, Á.; Chirvony, V.S.; Fernandez-La zaro, F.; Martínez-Pastor, J.P. Efficient optical amplification in a sandwich-type active-passive polymer waveguide containing perylenediimides. *ACS Photonics* **2017**, *4*.
28. Zhang, X.; Sun, C.; Zhang, Y.; Wu, H.; Ji, C.; Chuai, Y.; Wang, P.; Wen, S.; Zhang, C.; Yu, W.W. Bright Perovskite Nanocrystal Films for Efficient Light-Emitting Devices. *J. Phys. Chem. Lett.* **2016**, *7*, 4602–4610.

29. Yakunin, S.; Protesescu, L.; Krieg, F.; Bodnarchuk, M.I.; Nedelcu, G.; Humer, M.; De Luca, G.; Fiebig, M.; Heiss, W.; Kovalenko, M. V. Low-threshold amplified spontaneous emission and lasing from colloidal nanocrystals of caesium lead halide perovskites. *Nat. Commun.* **2015**, *6*, 1–8.
30. Wang, Y.; Li, X.; Song, J.; Xiao, L.; Zeng, H.; Sun, H. All-Inorganic Colloidal Perovskite Quantum Dots: A New Class of Lasing Materials with Favorable Characteristics. *Adv. Mater.* **2015**, *27*.
31. Navarro-Arenas, J.; Suárez, I.; Chirvony, V.S.; Gualdrón-Reyes, A..; Mora-Seró, I.; Martínez-Pastor, J.P. Single-Exciton Amplified Spontaneous Emission in Thin Films of CsPbX3 (X=Br,I) Perovskite Nanocrystals. *J. Phys. Chem. Lett.* **2019**, *10*, 6389–6398.
32. Akkerman, Q.A.; Gandini, M.; Di Stasio, F.; Rastogi, P.; Palazon, F.; Bertoni, G.; Ball, J.M.; Prato, M.; Petrozza, A.; Manna, L. Strongly emissive perovskite nanocrystal inks for high-voltage solar cells. *Nat. Energy* **2016**, *2*, 16194.
33. Lakowicz, J.R. *Principles of Fluorescence Spectroscopy*; Springer, 2006; ISBN 9780387312781.
34. Ansari-Rad, M.; Bisquert, J. Theory of Light-Modulated Emission Spectroscopy. *J. Phys. Chem. Lett.* **2017**, *8*, 3673–3677.
35. Gordillo, H.; Suarez, I.; Abargues, R.; Rodriguez-Canto, P.; Martinez-Pastor, J.P. Color Tuning and White Light by Dispersing CdSe, CdTe, and CdS in PMMA Nanocomposite Waveguides. *IEEE Photonics J.* **2013**, *5*, 2201412–2201412.
36. Palik, E. Handbook of Optical Constants of Solids 1998.
37. Zhao, M.; Shi, Y.; Dai, J.; Lian, J. Ellipsometric study of the complex optical constants of a CsPbBr3 perovskite thin film. *J. Mater. Chem. C* **2018**, *6*, 10450–10455.
38. Chirvony, V.S.; González-Carrero, S.; Suárez, I.; Galian, R.E.; Sessolo, M.; Bolink, H.J.; Martínez-Pastor, J.P.; Pérez-Prieto, J. Delayed Luminescence in Lead Halide Perovskite Nanocrystals. *J. Phys. Chem. C* **2017**, *121*, 13381–13390.
39. Gopalsamy, K.; Aggarwala, B.D. Monte Carlo Methods for some Fourth Order Partial Differential Equations. *ZAMM - J. Appl. Math. Mech. / Zeitschrift für Angew. Math. und Mech.* **1970**, *50*, 759–767.
40. Fick, A. Ueber Diffusion. *Ann. Phys.* **1855**, *170*, 59–86.

8 Conclusions

The main objective of this Thesis was focused into bringing new materials for photonic integrated circuits (PICs), particularly the use of thin-film processed colloidal nanocrystals, for developing devices that could be embedded into or used together (optical fibers) in PIC systems. For this application, it is necessary the development of active waveguides for optical amplification, lasers, modulators and photodetectors, most of them studied in this work by using $CsPbX_3$ perovskites nanocrystals. These semiconductors present high PLQY and strong absorption in the UV-VIS region, together with a straightforward integration into optical architectures, which are important properties for future integrated photodetectors, light sources and amplifiers, or even more complex systems. The most important results accomplished in this PhD are:

- **Synthesis of PNCs and fabrication of thin films:** The $CsPbX_3$ (X = Br, X = $Br_{0.5}I_{0.5}$, and X = I) nanocrystals used in this Thesis were synthetized following the hot-injection method with the modifications detailed in Chapters 4, 5, 6 and 7. With these colloidal solutions of PNCs, a layer-by-layer deposition method based on doctor blading technique was optimized to produce homogeneous films up to several hundred nanometer thick on a large variety of substrates. This method consisted of a sequential deposition of close packed PNC layers, with precise control of the thickness of the final film by choosing the amount of deposited layers. We used this technology to develop several photonic applications as well as other fundamental investigations PNCs.

- **Fabrication of PNC-based photodetectors**: In Chapter 4 we have presented several photodector devices based on $CsPbBr_3$ PNC thin films. The purpose of this research was to improve the carrier mobility of the PNC film via solid state ligand exchange. In this way, the short inter-particle distance imposed by the supplanting MPA ligands improved the mobility up to $5 \times 10^{-3}\,\mathrm{cm^2/Vs}$, as measured in FET devices, one order of magnitude higher than films based on pristine OA/OLA capped PNCs. This mobility enhancement led to an important 20-fold improvement in the photodetector's figures of merit: Responsivity

increased from 7 to 100 mA/W (corresponding to a detectivity as high as 8 x 10^{10} jones), as measured in our Schottky-based heterojunction photodiodes. We went a step forward with these photodevices by demonstrating the processability a bilayer PbS QDs (lead sulfide semiconductor operating at telecom wavelengths) and PNCs tandem photodiodes. The resulting device had a spectral response ranging from UV to NIR with responsivity levels of 40 mA/W at visible wavelengths and 20 mA/W around the telecom C-band (1525-1565 nm). These results can be basis of future photodiode arrays or CMOS-like cameras operating simultaneously at visible and NIR wavelengths or low-cost applications in the fields of IOT and optical sensing.

- **PNC-doped HC-NCF optical amplifiers:** In an effort to produce optical amplification at room temperature under continuous-wave excitation, in Chapter 5 we have shown a novel all-fiber amplification device by doping a HC-NCF with highly luminescent $CsPbBr_3$ PNCs. The PNCs were infiltrated by capillary forces, producing a thin coating layer on the inner walls of the holes in the fiber, inducing a strong modification in the fiber's modal structure at the PNC resonant wavelengths (510-540 nm). The observed amplification by the PNC-doped HC-NCF was explained by means of a third order non-linear optical mechanism, as the most plausible hypothesis. High optical nonlinearities on PNCs were excited by the high mode confinement allowed by this particular geometry, an idea that can be the starting point for the design of more advanced hollow-core PNC-filled optical fibers. For example, an increase of the effective area of the tube modes can enhance the light-matter interaction inside the fiber, allowing the study of high order optical nonlinearities with perovskite nanomaterials and facilitating the development of new future nonlinear photonic devices.

- **Amplified spontaneous emission with thin films of PNCs:** In Chapter 6, ASE is demonstrated in PNC films with different halide compositions (X = Br, X = $Br_{0.5}I_{0.5}$ and X = I) at liquid Helium temperatures. This study allowed us to determine the physical mechanisms involved in the formation of optical gain in PNCs, and also to stablish the role of different excitonic species to explain the stimulated emission in these nanocrystals. Our experimental data evidences that ASE is produced by single exciton recombination. In addition, we have

established the influence of the size distribution, of the individual PNCs colloids in the layers, as the origin of the inhomogeneous broadening and gain saturation of the ASE spectra under high excitation fluencies. The experimental ASE spectra and its evolution with increasing optical excitation density was explained by a rate equation model. These results allow us to explain the generation of ASE in PNCs, which paves the road towards the future development of emitting devices under continuous wave optical (or electrical) operation. Moreover, random lasing resonances, produced due to the formation of closed loops of scattered light in big nanoparticles or agglomerates, were observed. To fully harness this potential for efficient lasing devices, it will be necessary to develop photonic architectures with high confinement of light, as considered in Chapters 5 and 7, and to reduce the effect of nonradiative recombination of excitons at room temperature.

- **PNC active waveguides**: Once the optical gain was demonstrated, in Chapter 7 PNC films were integrated in a polymer/PNC/polymer sandwich-type waveguide on top of Si/SiO_2 substrates. The high refractive index contrast between the different materials results in the propagation of a highly confined fundamental TE_0 (TM_0) mode in the active layer, specially for PNC-film thicknesses above 100 nm. The strong overlap between the propagating mode and the active film enhances the reabsorption process responsible for stimulated emission. In addition, the top and bottom claddings reduce the losses of the light travelling along the waveguide, therefore allowing the propagation of the light along the whole length of the structure. At these conditions, PL spectra is red-shifted for long separations due to the influence of the (re)absorption/(re)emission of photon events (secondary photons) along the propagation path. The experimental characterization of the recombination time by frequency domain spectroscopy revealed that the red-shift is correlated with the decay, hence with the recycling of photons inside the waveguide. We have evaluated by means of Monte Carlo simulations that the generation of secondary photons (photons generated by the reabsorption of the PL) enhances the light emitted by the structure, indicating that this is a promising configuration for future efficient optical amplification and lasing devices.

Everything considered, we believe that PNCs are promising candidates for future integrated devices. Exploiting light confinement in either a waveguide configuration or a hollow-core fiber, the generation of light was enhanced and can also trigger high order non-linear effects. As a result, PNCs can provide signal amplification with very low (seemingly thresholdless) pump powers at room temperature. However, there is still much room for improvement; it could be very interesting to pursue light confinement in a cavity configuration to demonstrate lasing. Parallel to the experiments shown in this Thesis, some trials were done in this direction; for example, including gratings at the ends of the PNC waveguides or depositing Bragg reflectors enclosing a PNC thin film, yielding promising, but still inconclusive results. Future projects may continue following this objective, eventually achieving more ambitious goals like the development of integrable PNC-based electrically pumped lasers. Concurrently, the implemented PbS-QDs/PNC tandem photodetectors offer interesting perspectives in the development of PIC applications, especially when considering the cost-effectiveness of perovskite nanocrystals and the possibility to fabricate the devices by ink-jet printing techniques.

APPENDIX A RELATED PUBLICATIONS

A.1 RESULTS INCLUDED IN THIS THESIS

A.1.1 Navarro Arenas, J.; Soosaimanickam, A.; Pashaei Adl, H.; Abargues, R.; P. Boix, P.; Rodríguez-Cantó, P.J.; Martínez-Pastor, J.P. Ligand-Length Modification in $CsPbBr_3$ Perovskite Nanocrystals and Bilayers with PbS Quantum Dots for Improved Photodetection Performance. Nanomaterials **2020**, 10, 1297.

ABSTRACT

Nanocrystals surface chemistry engineering offers a direct approach to tune charge carrier dynamics in nanocrystals-based photodetectors. For this purpose, we have investigated the effects of altering the surface chemistry of thin films of $CsPbBr_3$ perovskite nanocrystals produced by the doctor blading technique, via solid state ligand-exchange using 3-mercaptopropionic acid (MPA). The electrical and electro-optical properties of photovoltaic and photoconductor devices were improved after the MPA ligand exchange, mainly because of a mobility increase up to 5×10^{-3} cm^2/Vs . The same technology was developed to build a tandem photovoltaic device based on a bilayer of PbS quantum dots (QDs) and $CsPbBr_3$ perovskite nanocrystals. Here, the ligand exchange was successfully carried out in a single step after the deposition of these two layers. The photodetector device showed responsivities around 40 and 20 mA/W at visible and near infrared wavelengths, respectively. This strategy can be of interest for future visible-NIR cameras, optical sensors, or receivers in photonic devices for future Internet-of-Things technology.

A.1.2 Navarro-Arenas, J.; Suarez, I.; Chirvony, V.S.; Gualdron-Reyes, A.F.; Mora- Seró, I.; Martínez-Pastor, J.P. Single- Exciton Amplified Spontaneous Emission in Thin Films of $CsPbX_3$ (X=Br, I) Perovskite Nanocrystals. J. Phys. Chem. Lett. **2019**, 10, 6389-6398.

ABSTRACT

$CsPbX_3$ perovskite nanocrystals (PNCs) have emerged as an excellent material for stimulated emission purposes, with even more prospective applications than conventional colloidal quantum dots. However, a better understanding of the physical mechanisms responsible for amplified spontaneous emission (ASE) is required to achieve more ambitious targets (lasing under continuous wave optical or even electrical excitation). Here, we establish the intrinsic mechanisms underlying ASE in PNCs of three different band gaps ($CsPbBr_3$, $CsPbBr_{1.5}I_{1.5}$, and $CsPbI_3$). Our characterization at cryogenic temperatures does not reveal any evidence of the biexciton mechanism in the formation of ASE. Instead, the measured shift toward long wavelengths of the ASE band is easily explained by the reabsorption in the PNC layer, which becomes stronger for thicker layers. In this way, the threshold of ASE is determined only by optical losses at a given geometry, which is the single-exciton mechanism responsible for ASE. Experimental results are properly reproduced by a physical model.

A.1.3 Navarro-Arenas, J.; Suárez, I.; Martínez-Pastor, J.P.; Ferrando, A.; Gualdrón-Reyes, A.F.; Mora-Seró, I.; Gao, S.-F.; Wang, Y.-Y.; Wang, P.; Sun. Optical Amplification in Hollow-Core Negative-Curvature Fibers Doped with Perovskite $CsPbBr_3$ Nanocrystals. Nanomaterials **2019**, 9, 868.

ABSTRACT

We report a hollow-core negative-curvature fiber (HC-NCF) optical signal amplifier fabricated by the filling of the air microchannels of the fiber with all-inorganic $CsPbBr_3$ perovskite nanocrystals (PNCs). The optimum fabrication conditions were found to enhance the optical gain, up to +3 dB in the best device. Experimental results were approximately reproduced by a gain assisted mechanism based on the nonlinear optical properties of the PNCs, indicating that signal regeneration can be achieved under low pump powers, much below the threshold of stimulated emission. The results can pave the road for new functionalities of the HC-NCF with PNCs, such as optical amplification, nonlinear frequency conversion and gas sensors.

A.2 Results Partially Included in this Thesis

A.2.1 Andres-Penares, D.; Navarro-Arenas, J.; Sánchez-Alarcón, R.I.; Abargues, R.; Martínez-Pastor, J.P.; Sánchez-Royo, J.F. Enhanced optical response of InSe nanosheet devices decorated with $CsPbX_3$ (X = I, Br) perovskite nanocrystals. Appl. Surf. Sci. **2021**, 536, 147939.

Abstract

The combination of several two-dimensional materials opens the door for the creation of cooperative nanodevices with functionalities that complement to each other and even compensate the weaknesses of the individual components. Two-dimensional indium selenide (InSe) shows one of the largest tunability bandgap found in two-dimensional materials with application in optoelectronics. However, the intrinsic out-of-plane luminescent dipolar nature limits its implementation in devices operating in vertical configuration. All-inorganic $CsPbX_3$ (X = Br, I) cubic nanoparticles offer high absorption and emission quantum yields and great integrability with two-dimensional materials. Combining these two compounds, it is found that InSe-perovskite nano-heterostructures enhances the photoluminescence of the InSe side of the device, as compared to the bare InSe nanosheet, due to the multi-oriented down-shift light conversion mediated by the perovskite-nanocrystals. Similar nanostructures have been prepared by using Molybdenum Selenide ($MoSe_2$), but a reduction of its photoluminescence is observed in this case due to its well-known in-plane dipole orientation.

A.2.2 Abargues, R.; Navarro-Arenas, Juan.; Rodríguez-Cantó, P.J.; Maulu, A.; Sánchez-Royo, J.F.; Martínez-Pastor, J.P. Enhancing the photocatalytic properties of PbS QD solids: the ligand exchange approach. Nanoscale **2019**, 11, 1978–1987

ABSTRACT

Surface engineering of nanomaterials is a promising tool towards the design of new materials for conversion of solar energy into chemical energy. In this work, we examine the influence of ligand exchange on the photocatalytic performance of solution-processed PbS films. We test different ligands such as oleylamine (OAm), 1,2-ethanedithiol (EDT), 3-mercaptopropionic acid (MPA) and tetrabutylammonium iodide (TBAI). The study demonstrates that PbS films capped with MPA and EDT exhibit 3.5-fold enhanced photocatalytic performance for the photodecomposition of methyl orange upon sunlight exposure. Both band energy alignment and charge carrier transport have a strong impact on the generation of reactive oxygen species (ROS), which play a key role in the photodecomposition process. Moreover, the stability and reusability of the photocatalysts are clearly improved after ligand exchange. We prove how both MPA and EDT provide much more stability to PbS QD films to operate very efficiently up to 8 cycles of photocatalysis. As observed in XPS, the oxidation of PbS is prevented after ligand exchange. We demonstrate how surface chemistry engineering of solution-processed QD films can open a new approach towards the design of highly efficient and stable visible-light-driven photocatalysts, which paves the way to low cost and large area fabrication of high-performance photocatalytic devices.

A.2.3 Maulu, A.; Navarro-Arenas, J.; Rodríguez-Cantó, P.; Sánchez-Royo, J.; Abargues, R.; Suárez, I.; Martínez-Pastor, J.P. Charge Transport in Trap- Sensitized Infrared PbS Quantum-Dot-Based Photoconductors: Pros and Cons. Nanomaterials **2018**, 8, 677.

ABSTRACT

Control of quantum-dot (QD) surface chemistry offers a direct approach for the tuning of charge-carrier dynamics in photoconductors based on strongly coupled QD solids. We investigate the effects of altering the surface chemistry of PbS QDs in such QD solids via ligand exchange using 3-mercaptopropionic acid (MPA) and tetrabutylammonium iodide (TBAI). The roll-to-roll compatible doctor-blade technique was used for the fabrication of the QD solid films as the photoactive component in photoconductors and field-effect phototransistors. The ligand exchange of the QD solid film with MPA yields superior device performance with higher photosensitivity and detectivity, which is due to less dark current and lower noise level as compared to ligand exchange with TBAI. In both cases, the mechanism responsible for photoconductivity is related to trap sensitization of the QD solid, in which traps are responsible of high photoconductive gain values, but slow response times under very low incident optical power (<1 pW). At medium-high incident optical powers (>100 pW), where traps are filled, both MPA- and TBAI-treated photodevices exhibit similar behavior, characterized by lower responsivity and faster response time, as limited by the mobility in the QD solid.

A.2.4 Maulu, A.; Rodríguez-Cantó, P .J.; Navarro-Arenas, J.; Abargues, R.; Sánchez-Royo, J.F .; García-Calzada, R.; Martínez Pastor, J.P. Strongly- coupled PbS QD solids by doctor blading for IR photodetection. RSC Adv. **2016**, 6, 80201–80212.

ABSTRACT

Solution-processed QD solids are emerging as a novel concept for high-performance optoelectronic devices. In this work, doctor blading is proposed for the fabrication of strongly-coupled QD solids from a PbS nanoink for photodetection at telecom wavelengths. The key step of this procedure is the solid-state ligand exchange, which reduces the interparticle distance and increases the carrier mobility in the resulting strongly-coupled QD solid. This is accomplished by replacing the original long oleylamine molecules by shorter molecules like 3-mercaptopropionic acid, as confirmed by FTIR, TGA and XPS. Further, a detailed investigation with XPS confirms the air-stability of the QD solids and the extreme reduction of the principal oxidation product, $PbSO_3$, from ligand exchange times of 60 s. Finally, the QD solid is tested as an active layer for the fabrication of a Schottky NIR photodetector. The device shows a maximum responsivity of 0.26 A W^{-1} that corresponds to an internal quantum efficiency higher than 30% at 1500 nm and detectivity around 10^{11} jones.

APPENDIX B RESUMEN EN ESPAÑOL

Los cristales con estructura de red tipo perovskita conforman una gran familia de materiales que comparten la fórmula química general ABX_3. En una celda unidad, las vacantes A y B son cationes y pueden ser ocupadas por un metal o semimetal de la tabla periódica. Los átomos A están ubicados en el centro del cubo mientras que en los vértices se enlazan los átomos del elemento B; los del tipo X son aniones (oxígeno, nitrógeno, halógeno, hidrógeno) que se encuentran octaédricamente coordinados con los átomos del tipo B. Estas estructuras reciben el nombre de perovskita en referencia al mineral del titanato de calcio ($CaTiO_3$), descubierto en los Montes Urales, en Rusia, en 1836 y bautizado en reconocimiento al geólogo Lev Alekseyevich von Perovski. A día de hoy existen muchas subfamilias de perovskita, cada una con con un conjunto de propiedades fisicoquímicas que las hacen más interesantes para su estudio en determinadas regiones de la ciencia de los materiales.

La investigación recogida en esta Tesis se centra en la subfamilia de perovskitas de halogenuros de plomo (del inglés *Lead Halide Perovskites*, LHP). Durante los últimos años se ha demostrado que este tipo semiconductor presenta unas propiedades optoelectrónicas fascinantes, las cuales lo sitúan como un candidato potencial para el desarrollo de una nueva generación de dispositivos fotónicos y fotovoltaicos. En este caso, la estructura está compuesta por un catión monovalente A, que puede ser metilamonio (MA), formamidinio (FA), o cesio (Cs); B es un metal, en este caso Pb; y X es un halógeno (Cl-, Br-, I-) [2]. En particular, en el trabajo desarrollado en la presente Tesis, se han empleado nanocristales de perovskitas de la familia $CsPbX_3$, totalmente inorgánicas. Sus propiedades ópticas incluyen altos coeficientes de absorción, la capacidad de sintonizar el borde de absorción con la composición de halógeno (X), una alta eficiencia de emisión, y altos coeficientes no lineales, entre otras características que hacen de las LHP un semiconductor flexible capaz de ser utilizado tanto en tecnologías fotovoltaicas como en otras aplicaciones dentro del marco la óptica integrada. Estos nanocristales semiconductores se fabrican por medio de una química coloidal sencilla y de bajo coste, que da lugar a nanopartículas con una eficiencia de emisión superior al 90% y anchuras de línea inferiores a 100 meV. Poco después del descubrimiento, en 2014, de sus excepcionales propiedades como medio activo para la generación de ganancia, se empezaron a desarrollar dispositivos láser y diodos LED, entre otras aplicaciones destacadas. Siguiendo con este progreso, se espera que los nanocristales de perovskita (PNCs) con estequiometria $CsPbX_3$ provean un éxito similar en la generación de ganancia óptica. Estas razones justifican que el interés de la comunidad científica por este

material haya crecido rápidamente durante los últimos años. De hecho, según la WOS (*Web of Science*), el tema *halide perovskites* cuenta ya con más de cinco mil artículos científicos publicados desde el año 2017.

El objetivo de la presente Tesis consiste en aprovechar las excelentes propiedades de este material para investigar nuevas aplicaciones dentro del marco de la óptica integrada. En concreto, se han desarrollado dispositivos fotónicos y optoelectrónicos basados en capas delgadas de PNCs en diferentes tipos de estructuras fotónicas, como guías de onda, cavidades o fotodetectores. De esta manera, el trabajo incluye el diseño, fabricación, caracterización y modelado de los dispositivos mencionados, así como su aplicación como láseres, amplificadores o fotodetectores.

Como paso previo al desarrollo de dichos dispositivos, se perfeccionó previamente la síntesis química de las nanopartículas de perovskita, y una tecnología adecuada para el crecimiento de capas delgadas con las mejores propiedades para la generación de ganancia o el transporte de carga. Para ello, en primer lugar, se optimizó la distribución de tamaños, eliminando el exceso de material químico en la solución coloidal a través de una purificación multietapa. Una vez alcanzadas las condiciones reológicas que ha de reunir una dispersión coloidal óptima, que llamaremos nanotinta, se procedió con una técnica de impresión de película delgada conocida como Doctor Blade, cuyo nombre recuerda una pieza mecánica clave en los primeros equipos de hueco grabado. Esta técnica permite una deposición homogénea de las nanotintas sobre una gran variedad de sustratos con un control preciso del espesor (desde decenas de nanómetros hasta algunas micras), y consiste en la imprimación secuencial de varias películas delgadas con un paso intermedio para la evaporación del disolvente de la nanotinta. De esta manera, se fabrican capas compactas aptas para el transporte de carga y la generación de ganancia.

Los primeros dispositivos optoelectrónicos fabricados aprovechando esta técnica de deposición fueron fotoconductores y fotodiodos. El propósito de este primer proyecto fue el de mejorar la movilidad de los portadores en las capas delgadas de PNCs. El núcleo de una PNC se encuentra rodeado en su capa exterior por unas moléculas que reciben el nombre de ligandos, generalmente agrupaciones hidrocarbonadas lineales, que le confieren estabilidad en el medio líquido (el disolvente de la nanotinta) evitando su agregación. Además, dichos ligandos suprimen centros de recombinación superficiales, incrementando la eficiencia cuántica del nanocristal. Puesto que la relación superficie/volumen es relativamente grande en esta clase de nanoestructuras, la química superficial de los nanocristales tiene un impacto crítico en sus propiedades optoelectrónicas. En el caso que nos ocupa, además, los ligandos que rodean los nanocristales también los interconectan cuando están ensamblados en una

película delgada. Por este motivo, en esta clase de materiales la longitud de los ligandos es un factor crítico para la movilidad electrónica de la capa, puesto que el mecanismo de conducción viene dado por efectos como el de Frenkel-Poole. Con el fin de eliminar los ligandos largos heredados de la síntesis, en este trabajo se realiza un cambio de ligando sobre capas compactas PNCs. Para ello, se reemplazan los ligandos originales (oleiamina y acido oleico) por un hidrocarburo alifático (ácido 3-mercaptopropionico) más corto.

En la presente Tesis Doctoral se realizó una caracterización detallada de las propiedades de conducción de los PNCs en diversos dispositivos optoelectrónicos. En primer lugar se diseñó un fotodiodo tipo Schottky (metal-semiconductor) con la estructura ITO/PEDOT:PSS (50 nm)/$CsPbBr_3$ (300 - 400 nm)/MoO_3 (15 nm)/Au (100 nm) con cambio de ligando en la capa de PNCs y una capa de óxido de molibdeno como bloqueador de electrones para mejorar la eficiencia de recolección de cargas del dispositivo. De estos fotodiodos se extrajeron varias propiedades con un modelo de doble heterounión. En concreto, se demostró una mejora de un factor 20 en las figuras mérito del fotodetector, y un incremento de la Responsividad de 7 a 100 mA/W (correspondiente a una Detectividad de 8 x 10^{10} jones). Este tipo de cambio de ligando en estado sólido también pudo aprovecharse para el desarrollo de dispositivos más complejos, como una heterounión tipo tándem de films de PNCs con capas de puntos cuánticos (QDs) de sulfuro de plomo (PbS). Los QDs de PbS operan en la banda C (1525-1565 nm) de las telecomunicaciones mientras que los PNCs tienen el borde de la banda de absorción sobre los 500 nm. El resultado es un fotodetector con una respuesta que se extiende desde el ultravioleta (UV) hasta el infrarrojo cercano (NIR), con niveles de Responsividad de 40 mA/W en el UV y 20 mA/W en el NIR. Finalmente, durante este proyecto se construyeron fotoconductores con arquitectura metal-semiconductor-metal (MSM) y dispositivos tipo FET (del inglés *Field Effect Transistor*) con cambio de ligando. De los FET se extrajo un valor para la movilidad, obteniendo un valor de of 5 × 10^{-3} cm^2/Vs, un orden de magnitud mayor de lo esperado con los ligandos originales.

El siguiente proyecto abarcado en la Tesis se centra en la generación de amplificación de la emisión estimulada (del inglés *Amplified Spontaneous Emission*, ASE) que se obtiene al bombear ópticamente capas de $CsPbBr_3$ con pulsos de femptosegundos (fs) o nanosegundos (ns). Las prestaciones demostradas por este material no alcanzan todavía los umbrales de emisión estimulada y de ganancia óptica obtenidas con las capas policristalinas. De hecho, la generación de ganancia óptica en los PNCs presenta ciertas limitaciones que incluyen su poca estabilidad en condiciones ambientales, la falta de una tecnología establecida para depositar capas, o las trampas no radiativas que limitan la ganancia óptica a temperatura ambiente.

En concreto, en este trabajo se presenta un análisis detallado de las propiedades de emisión de luz y ASE en capas de $CsPbX_3$ con emisión (absorción) a tres longitudes de onda diferentes, sintonizadas con la cantidad de halógeno (X = Br, X = $Br_{0.5}$ $I_{0.5}$, X = I). Para ello, se propone en primer lugar una tecnología de depósito de PNCs en capas que maximicen la generación de luz, como la descrita anteriormente. El depósito óptimo de las capas da lugar a la generación de emisión estimulada con umbrales de ASE alcanzados para las capas de X = Br, X = $Br_{0.5}$ $I_{0.5}$ y X = I de hasta E_{th} =5, E_{th} =80 y E_{th} =20 μJ / cm^2, medidos a temperaturas criogénicas (de esta manera se pretende inhibir las transiciones no radiativas y, con ello, favorecer la generación de ganancia) con pulsos de nanosegundos de bajas potencias (<1 μJ/cm^2). Aquí, cabe destacar que, pese a que en la mayoría de los trabajos previos la generación de ganancia óptica es demostrada con excitaciones de fs, en este trabajo se han obtenido estos resultados con pulsos más largos (ns), lo cual es indicativo de la calidad de las capas fabricadas. Por ejemplo, en publicaciones previas con X = Br era necesario utilizar pulsos de fs para alcanzar umbrales de ASE similares, ya que la excitación con pulsos más largos implicaba en un incremento dramático de la energía umbral. Los mayores umbrales obtenidos con las capas de X = $Br_{0.5}$ $I_{0.5}$ o X=I pueden ser achacados a una menor calidad de las capas o una peor estabilidad de los PNCs que contienen yodo. De hecho, este uno de los primeros trabajos en los que se demuestra ASE en PNCs de $CsPbI_3$, debido probablemente a la peor estabilidad de este tipo de perovskitas, lo cual dificulta su caracterización óptica.

Asimismo, durante este segundo objetivo se realizó una investigación más fundamental para establecer el papel de las diferentes especies (exciton, biexciton y portadores libres) y de los mecanismos físicos (efecto de la reabsorción, ensanchamiento inhomogéneo de la banda PL y saturación de la ganancia) en la generación de ganancia óptica en capas delgadas de PNCs. Aunque la emisión biexcitónica suele ser el mecanismo elegido para explicar la emisión estimulada de estas nanopartículas, nuestros datos experimentales demuestran que la generación de ASE se debe principalmente a las transiciones que implican un solo excitón, y que esta viene influenciada por la reabsorción de la emisión por el propio material. Por otra parte, establecemos la influencia de la distribución de tamaños de los PNC en el fenómeno de la saturación de la ganancia y el ensanchamiento de los espectros. Estos resultados ayudan a entender cómo se genera la ganancia en las capas de PNC, algo que resulta fundamental a la hora de diseñar dispositivos optoelectrónicos funcionales con este tipo de nanopartículas.

Finalmente, es importante resaltar que dado que los resultados obtenidos demuestran la generación de amplificación óptica a tres longitudes de onda diferentes (528 nm, 600 nm y

705 nm, para X = Br, X = $Br_{0.5}$ $I_{0.5}$ y X = I, respectivamente), se puede pensar en futuras aplicaciones derivadas de sintonizar la longitud de onda de ASE con la composición, como por ejemplo el multiplexado en longitud de onda, o la implementación de láseres sintonizables.

De forma paralela a este proyecto se inició el desarrollo de láseres basados en nanotintas de PNCs. El primer dispositivo que se trató de construir fue un VSCEL (*Vertical-Cavity Surface-Emitting Laser*) por bombeo óptico, donde el medio óptico en encuentra embebido en una microcavidad resonante Fabry-Perot (FP) en la que la emisión es perpendicular a los espejos. Los espejos Bragg empleados en la construcción de la cavidad, crecidos mediante la técnica de deposición conocida como ALD (del inglés *Atomic Layer Deposition*), alternan capas de óxidos con alto contraste de índice como TiO_2 y Al_2O_3. Con estos espejos se consiguió una cavidad FP centrada en 520nm, longitud de onda que coincide con el máximo de emisión de los PNCs sintetizados en nuestro laboratorio. Otra de las aproximaciones planteadas para obtener fue la fabricación de un DFB (del inglés *Distributed Feedback Laser*). Para ello, se empleó una técnica de nanolitografía por haz de Electrones (en inglés *Electron-Beam Lithography*, EBL) para trazar una red de difracción en una guía de ondas de Poli(metil metacrilato) o PMMA sobre un sustrato de silicio, sobre la que se depositaron las nanopartículas. La estructura fue configurada para emitir en dirección normal a la superficie, puesto que la emisión paralela a la superficie resultó problemática a la hora de recoger la señal generada por la cavidad, y se demostró que la fotoluminiscencia se acopla a los modos de la cavidad.

Con el objetivo de fabricar un dispositivo capaz de operar a temperatura ambiente y bajo bombeo continuo, finalmente se optó por emplear las novedosas fibras ópticas microestructuradas como estructura confinante del campo electromagnético para favorecer la generación de fotoluminiscencia de los PNCs infiltrados en su interior. Estas fibras están recibiendo gran atención actualmente debido a las ventajas que presentan en comparación con las fibras convencionales. En concreto, dentro del gran abanico que abarca este tipo fibra óptica, cabe destacar las fibras de curvatura negativa (*negative curvature fibers*, NCF), una clase especial de fibras de núcleo hueco en las que el revestimiento está compuesto de una serie de capilares de sílice puro rodeando al núcleo – también hueco – de la fibra. Asimismo, esta variedad puede subdividirse más, aunque mencionaremos sólo las tipo *hollow-core anti-resonant fibers* (HC-ARFs) – las que hemos empleado en los experimentos descritos en este artículo –. El mecanismo responsable del guiado por el interior de estas fibras recibe el nombre de ARROW (del inglés *Antiresonant Reflecting Optical Waveguide*) e inhibe el acoplo

ente los modos que se propagan por el núcleo y el revestimiento donde se encuentran los capilares. Este nuevo tipo de fibras ópticas introducen diversas ventajas con respecto a las ya instituidas PCF (*Photonic Crystal Fibers*). Por ejemplo, puesto que la propagación ARROW no requiere de un revestimiento periódico, la fabricación de los dispositivos se simplifica considerablemente, permitiendo incluso el uso de calcogenuros en sustitución de la sílice de los capilares –posibilidad que es de gran interés para aplicaciones que operan en el infrarrojo– . Por otra parte, introducen una mejora con respecto a las PCF en cuanto al confinamiento de los modos al núcleo de la fibra debido a las opciones de diseño que introduce la curvatura negativa otorgando nuevos grados de libertad para controlar el número y la constante de propagación de los modos guiados. Finalmente, uno de los principales intereses de las fibras HC radica en el hecho de que pueden servir de huésped para alojar otros materiales, facilitando así el estudio de sus propiedades fundamentales o su aplicación como sensor de parámetros químicos o biológicos. Entre diferentes aplicaciones, las HC-ARF resultan muy interesantes para emplearse en el área de las telecomunicaciones, con la introducción de un material activo para o la fabricación de láseres u otros dispositivos fotónicos.

En este contexto se propone la integración de PNCs en fibras tipo HC-ARF para la generación de ganancia óptica. Para ello, la disolución de PNCs se ha optimizado para permitir su infiltración a través de los capilares de la HC-ARF hasta alcanzar longitudes de decenas de centímetros. El primer desafío a resolver en este proyecto fue determinar si la HC-AFR se dopaba uniformemente mediante el proceso descrito en el apartado anterior. Con este propósito, se seccionó la fibra cargada con PNCs para realizar varios mapas de PL (del inglés *photoluminiscence*) de las secciones cruzadas intermedias. En los mapas de PL se aprecia que la emisión de luz se produce en los anillos que conforman los capilares de la HR-ARF, lo que confirma la adherencia de las nanopartículas en las paredes. Estos resultados fueron corroborados mediante una simulación por elementos finitos en el software COMSOL Multiphysics, demostrando que los PNCs formaban capas concéntricas de 55 nm de espesor alrededor de los capilares de la fibra microestructurada.

El dispositivo resultante es capaz de amplificar una señal de prueba de 515 nm cuando la fibra dopada se bombea con un láser de onda continua de 405 nm con potencias de bombeo inferiores a 3 μW. Debido a que, aparentemente, el sistema no presenta un umbral de emisión estimulada, se propone un mecanismo de ganancia basado en las propiedades no lineales de tercer orden de este tipo de nanocristales, reciente reportadas. De esta manera, se propone un modelo basado en la generación de mezcla de cuatro ondas capaz de

reproducir los resultados experimentales con buena precisión. En concreto, los resultados de ganancia obtenidos concuerdan con un mecanismo de amplificación paramétrica.

Debido a la relativa juventud de las HC-ARF, todavía no existen antecedentes de este tipo de dispositivos en la literatura. Únicamente se han encontrado publicaciones basadas en puntos cuánticos coloidales en guías de onda plasmónicas, y dieléctricas, que demuestran amplificación de luz por mecanismos similares. Con todo ello, se espera que estos resultados preliminares sirvan como base de la integración de nuevas funcionalidades ópticas en fibras HC-ARF.

Siguiendo con la estrategia del confinamiento de la PL en las capas de PNCs, se inició un último trabajo basado en una arquitectura de guía de ondas plana con alto contraste de índice. En particular, los dispositivos se diseñaron para demostrar y amplificar un efecto conocido como el reciclaje de fotones (en inglés *photon recycling*, PR), muy frecuente en este tipo de perovskita, que pasa a describirse a continuación.

El PR es mecanismo físico que ocurre cuando una fracción de los fotones generados radiativamente por un semiconductor es absorbida y emitida secuencialmente antes de ser extraída. Los ciclos múltiples de (re) absorción / emisión dan como resultado un gas de "fotones reciclados", densamente concentrados en el medio activo por el que se propagan. En consecuencia, el PR proporciona otro grado de libertad a la hora de controlar la densidad de portadores de un semiconductor, y con ello una forma de controlar sus propiedades optoelectrónicas para obtener dispositivos más eficientes. Las aplicaciones demostradas del PR incluyen diodos semiconductores con voltajes de circuito abierto extremadamente altos, y moduladores de luz y células solares más eficientes.

El efecto del PR cobra especial importancia en el caso de las LHP. De hecho, el gran solapamiento entre la función de absorción y la de absorción en este material, sumado a la alta eficiencia de emisión característica de las LHP, establecen unas condiciones claramente favorables para el PR. Es por que ello que en los últimos 3-4 años han ido publicándose diferentes trabajos experimentales y teóricos que relacionan el mecanismo del PR con las excelentes eficiencias de conversión y las tasas de emisión reportadas para esta familia de semiconductores. Aunque existe una controversia sobre el impacto de la RP en la eficiencia de las células solares, hay estudios recientes con células monocristalinas de perovskita que confirman que el RP es el mecanismo dominante de transporte de energía, y otros trabajos teóricos y experimentales que demuestran que el PR introduce una mejora en el voltaje de circuito abierto de la célula. El diseño óptico de la arquitectura es un factor determinante a la hora de optimizar el impacto del PR. Por ejemplo, algunos dispositivos eficientes hacen uso

de las MHP estructuradas en forma de microhilos. Estos filamentos actúan como guías de onda para la PL generada por el propio semiconductor, con gran eficiencia puesto que se evitan pérdidas por acoplamiento, entre otras ventajas. Otra estrategia sería la de la dispersión de la PL con nanopartículas de plata para aumentar la trayectoria de los fotones, incrementando el tiempo de vuelo de los fotones hasta ser recolectados por el circuito fotovoltaico. Una estructura fotónica ideal, optimizada aprovechar el fenómeno del PR, debería tener una gran distancia de propagación y al mismo tiempo un acoplamiento óptico eficiente.

Este es el caso de la arquitectura fotónica empleada en el presente trabajo, la cual cumple con todas las condiciones necesarias para optimizar PR en capas delgadas de PNCs. Esta estructura consiste en un núcleo activo en forma de capa delgada (50-200 nm) intercalado entre dos capas (pasivas) de PMMA. Esta elegante configuración de guía de onda plana explota de manera eficiente las propiedades de (re)emisión/absorción de luz del semiconductor por el alto confinamiento de los fotones dentro de la capa activa, además de ofrecer una propagación con un coeficiente de atenuación reducido debido a la trasparencia del polímero. Por otra parte, esta clase de guía permite una extracción eficiente de la PL mediante el acoplamiento a lente (*end-fire*). De esta manera, nuestra estructura de guía de onda PMMA / PNC / PMMA resulta ser una excelente configuración para estudiar el PR, demostrando ser capaz de introducir un incremento en los tiempos de vida de los fotones extraídos de la guía de ondas guía de onda, de hasta 10 ns en el caso de un óptimo, tras propagarse una longitud de 3 mm.

Para ello, se ha caracterizado el tiempo de vida de los fotones mediante una técnica de espectroscopia conocida como FDS (del inglés *Frequency Domain Spectroscopy*). Dicha técnica se basa en la modulación del bombeo y en la correspondencia en fase entre la excitación y la fluorescencia, permitiendo extraer el tiempo de recombinación de la muestra, sin necesidad de implementar costosas tarjetas de correlación, a partir del desfase y la modulación de la amplitud de la fluorescencia haciendo uso de un amplificador de corriente síncrono tipo *Lock-In*.

Para finalizar esta investigación se corroboraron los resultados experimentales con una simulación realizada por el método de Monte Carlo en la que la trayectoria de cada fotón, así como su interacción con el medio semiconductor, es calculada individualmente. Con suficiente estadística, el modelo predice un tiempo de retardo para los fotones que atraviesan la guía de ondas que describe bien los resultados experimentales.

En conclusión, los trabajos recogidos en esta Tesis presentan los PNCs como candidatos prometedores para su implementación como medio activo en una generación futura de

dispositivos fotónicos y optoelectrónicos. Con esta finalidad se presentan una serie de estrategias que pueden mejorar el rendimiento y la aplicabilidad de estos nanocristales: (i) una técnica optimizada para el crecimiento de capas compactas de PNCs; (ii) una mejora de la movilidad de los portadores tras un cambio de ligando en estado sólido; (iii) un diseño adecuado para explotar el confinamiento de la luz en una configuración de guía de onda o en una fibra de núcleo hueco, mejorando la generación de luz y desencadenando efectos no lineales; (iv) análisis detallado sobre el mecanismo de generación de ganancia el interior de una capa delgada de PNCs. Los presentes resultados muestran que los PNCs pueden proporcionar amplificación de señal con potencias de bombeo muy bajas, y a temperatura ambiente, si son implementadas en condiciones óptimas. Sin embargo, todavía hay mucho margen para la mejora. Por ejemplo, para alcanzar la emisión láser se ha de mejorar la arquitectura de los dispositivos, optimizando el diseño de la cavidad óptica o haciendo uso de los efectos característicos de este semiconductor, como los efectos ópticos no lineales o el reciclaje de fotones. Un proyecto futuro puede conducirse por esta línea de investigación para finalmente alcanzar objetivos más ambiciosos, como el desarrollo de láseres de bombeo eléctrico. Por otra parte, los fotodetectores tipo tándem fabricados, con la heterounión PbS QDs / PNC, ofrece perspectivas interesantes para el desarrollo de aplicaciones fotodetección/fotoemisión integradas ya que abarca un amplio rango espectral, desde el UV hasta el NIR. Estos dispositivos son especialmente interesantes teniendo en cuenta la rentabilidad de la química coloidal empleada en su síntesis y la posibilidad de construir los dispositivos mediante técnicas de impresión estandarizadas.

APPENDIX C LIST OF ACRONYMS

ARROW: Antiresonant Reflecting Optical Waveguide
ASE: Amplified Spontaneous Emission
BBO: Barium borate (nonlinear crystal)
BNC: Bayonet Neill–Concelman
CB: Conduction Band
CQD: Colloidal Quantum Dot
CW: Continuous Wave
DFB: Distributed Feedback Laser
EBL: Electron Blocking Layer
EDFA: Erbium Doped Fibers Amplifiers
EQE: External Quantum Efficiency
ETL: Electron Transport Layer
FA: Formamidinium
FD: Frequency Domain
FET: Field Effect Transistor
FWHM: Full Width at Half Maximum
FWM: Four Wave Mixing
HBL: Hole Blocking Layer
HC: Hollow-Core
    -ARF: Anti-Resonant Fiber
    -NCF: Negative-Curvature Fiber
    -PCF: Photonic Crystal Fiber
HCF: Hollow-Core Fiber
HTL: Hole Transport Layer
IC: Integrated Circuit
IQE: Internal Quantum Efficiency
ITO: Indium Tin Oxide
LBL: Layer-by-layer
LHP: Lead Halide Perovskite
MA: Methylammonium
MHP: Metal Halide Perovskites
MPA: 3-Mercaptopropionic acid
MSM: Metal-Semiconductor-Metal
NC: Nanocrystal
NEP: Noise Equivalent Power
NIR: Near Infrared
Nd:YAG: Neodymium-doped Yttrium Aluminum Garnet
OA: Oleic Acid
OAm: Oleylamine
OFET: Organic Field Effect Transistor
PEDOT:PSS: poly(3,4-ethylenedioxythiophene) polystyrene sulfonate
PIC: Photonic Integrated Circuits
PL: Photoluminescence
PLQY: Photoluminescence Quantum Yield
PML: Perfectly Matched Layer
PMMA: Poly(methyl methacrylate)
PNC: Perovskite Nanocrystal
PR: Photon Recycling
PV: Photovoltaic
PVD: Physical Vapor Deposition
QD: Quantum Dot
QE: Quantum Efficiency
QY: Quantum Yield
SCLC: Space-Charge-Limited Current
SEM: Scanning Electron Microscopy
SMU: Source Measure Unit
SRH: Shockley–Read–Hall
TE: Transverse Electric
TEM: Transmission Electron Microscopy
TIR: Total Internal Reflection
TM: Transverse Magnetic
TRPL: Time Resolved Photoluminescence
UV: Ultraviolet
VB: Valence Band
VCSEL: Vertical-Cavity Surface-Emitting Laser
VSL: Variable Stripe Length
WDM: Wavelength-Division Multiplexing